2019-04-15

# Buoyancy Driven Flows in Porous Media with Applications to Geological Storage of Carbon Dioxide

Jafari Raad, Seyed Mostafa

UNIVERSITY OF CALGARY

# Buoyancy Driven Flows in Porous Media with Applications to Geological Storage of Carbon Dioxide

by

Seyed Mostafa Jafari Raad

A THESIS

SUBMITTED TO THE FACULTY OF GRADUATE STUDIES

IN PARTIAL FULFILLMENT OF THE REQUIREMENTS FOR THE

DEGREE OF DOCTOR OF PHILOSOPHY

GRADUATE PROGRAM IN CHEMICAL AND PETROLEUM ENGINEERING

CALGARY, ALBERTA

APRIL, 2019

# Abstract

This dissertation presents theoretical analyses and numerical experiments on buoyancy-driven convection in porous media in the context of geological storage of carbon dioxide ($CO_2$) in deep saline aquifers. One of the main focuses of this study is to investigate the role of the concentration dependent base state density profile in the stability criterion of buoyancy-driven convection and hydrodynamics of the associated convective mixing in different fluid systems. In particular, scaling relations, which allow estimation of the onset of the convective instabilities and the generalization of the base state density dependence of the growth of the instabilities are of interest.

Stability criterion of the buoyancy-driven convection in analogue fluid mixtures used in experimental studies of $CO_2$ convective mixing are of particular interest. The density profile dependence of the growth of instabilities in both binary and ternary fluid mixtures is mathematically analyzed and scaling relations that relate the stability criterion of the diffusive boundary layer to the key parameters of the systems is proposed.

It is shown that the characteristic behaviour of the base state density profile plays an important role in stability characteristics of the diffusive boundary layer and convective mixing beyond the onset of instability. The results have shown that the choice of an analogue system is critically important in correct representation of the onset of convective instabilities of $CO_2$/water and design of experiments. In particular, it is shown that there are fundamental differences in the evolution of the buoyancy-driven instability and dynamics of convective mixing between $CO_2$/water and typical EG-MeOH/water and PPG/water analogue systems.

The developed concepts on the role of density profiles in the stability criterion of the buoyancy-driven convection are applied to multi-component fluid systems with applications to impure $CO_2$ storage. The role of permitted impurities on the characteristic shape of the density profile evolved during the dissolution of impure $CO_2$ in water is mathematically analyzed and a parameter space classification, which allows prediction of general stability behaviour of an impure $CO_2$/water system is proposed. Specifically, a linear stability analysis is conducted to investigate the effect of $H_2S$ impurity in $CO_2$ stream on the onset of buoyancy-driven convection associated with impure carbon $CO_2$ storage in deep saline aquifers. Contrary to the common belief, it is shown that an impurity such as $H_2S$ has the potential to accelerate the buoyancy-driven instabilities.

The theoretical analysis is extended, by means of high-resolution numerical simulations, to characterize the long-term behaviour of density-driven convection and the associated mixing. The key features of the convective dissolution beyond the onset is analyzed by evaluating the finger patterns and convective fluxes at different periods of the mixing process. It is shown that an impure $CO_2$ stream may lead to different convective mixing dynamics at early and late periods of dissolution process depending on the fractional composition of the permitted impurity.

Another focus of this study is to develop mathematical models that capture key features of fluid flow and transport in fractured porous media and to characterize the stability criteria of buoyancy-driven convection in fractured aquifers in the context of $CO_2$ storage. Through performing a parametric analysis, by means of a linear stability analysis, the role of physical properties of a fracture network in the stability of the diffusive boundary layer in a saturated fractured porous medium is characterized. Important effects of fracture interporosity flow and fracture storativity on the stability behaviour of the system are demonstrated and scaling relations that can be used to estimate the onset of density-driven instabilities in a dual porosity porous system are reported as a function of the most common physical properties of the fractured porous medium.

These findings improve our understanding of density-driven flow in porous media in the context of $CO_2$ storage and are important in the estimation of potential storage capacity, risk assessment, and storage site characterization and screening.

## Acknowledgments

I would like to express my sincere appreciation to my supervisor Dr. Hassan Hassanzadeh for his outstanding knowledge, supervision, support, guidance, and patience during my research and studies at the University of Calgary. I am grateful to Dr. Hassanzadeh for his trust in me and giving me the opportunity to learn and grow under his guidance, and for always giving me enough independence to pursue my own thoughts. He has been a constant source of inspiration, and it has truly been a great honor for me to work under his supervision.

I want to thank Dr. Johnathan Ennis-King for the hospitality, guidance, and support during my research at the Commonwealth Scientific and Industrial Research Organisation (CSIRO), in Australia. I would also like to thank Dr. Hamid Emami-Meybodi for his support and guidance during my research at Pennsylvania State University.

My gratitude also extends to my dissertation committee members Dr. S.M. Farouq Ali and Dr. Jalal Abedi for their invaluable guidance and feedback through this research. I would also like to thank Dr. Steven Bryant, Dr. Yuri Leonenko, and Dr. Jeffrey Priest for serving on my examining committee.

I am thankful to my friends and fellow graduate students at University of Calgary for their support and help during my research. I would also like to thank all the faculty and staff of the Chemical and Petroleum Engineering Department as well as fellow colleagues at Pennsylvania State University and Commonwealth Scientific and Industrial Research Organisation (CSIRO) for making my graduate studies and my research pleasant and enjoyable.

I acknowledge the financial support from the Natural Sciences and Engineering Research Council of Canada (NSERC), the support of the Australian Government Department of Education through the Endeavour Research Fellowship, the Alberta Innovates – Technology Futures (AITF) through Alberta Innovates Graduate Student Scholarship, NOVA Chemicals, Estate of Ursula O. and Herbert Zandmer, Schulich School of Engineering, the Faculty of Graduate Studies at the University of Calgary as well as the Department of Chemical and Petroleum Engineering at the University of Calgary. This research project was enabled in part by the computing support provided by WestGrid and Compute Canada Calcul Canada. I also gratefully acknowledge the Commonwealth Scientific and Industrial Research Organisation (CSIRO) and John and Willie

Leone Family Department of Energy and Mineral Engineering at the Pennsylvania State University for their hospitality.

I warmly thank and appreciate my parents and my brothers for all the support and encouragement I have received over the years.

*To my life's best ever teacher; my mother.*

## Table of Contents

**List of Tables**



**List of Figures**

## Nomenclature

### *Letters*

| | |
|---|---|
| C | Concentration [$ML^{-3}$] |
| $CO_2$ | Carbon dioxide [-] |
| Cr | Courant number [-] |
| $d$ | Diameter [L] |
| $D$ | Diffusion coefficient [$L^2T^{-1}$] |
| EG-MeOH | Ethylene glycol and methanol |
| J | Probability density function |
| $g$ | Gravity acceleration [$LT^{-2}$] |
| $H$ | Height [L] |
| $k$ | Permeability [$L^2$] |
| $l$ | Characteristic thickness of the matrix block [L] |
| $L$ | Length [L] |
| $P$ | Pressure [$ML^{-1}T^{-2}$] |
| Pe | Peclet number [-] |
| PPG | Propylene glycol |
| Ra | Rayleigh number [-] |
| Sh | Sherwood number [-] |
| $t$ | Time [T] |
| $u$ | Velocity component in x-direction [$LT^{-1}$] |
| $v$ | Velocity component in z-direction [$LT^{-1}$] |
| v | Velocity [$LT^{-1}$] |
| **v** | Velocity vector [$LT^{-1}$] |
| $x$ | x-coordinate direction [-] |
| $y$ | y-coordinate direction [-] |
| $z$ | z-coordinate direction [-] |

### *Greek letters*

| | |
|---|---|
| ω | Storativity coefficient [-] |
| α | Dimensionless exponential distribution constant [-] |
| $\alpha$ | Decline factor [-] |

| | |
|---|---|
| $\beta$ | Coefficient of density increase [-] |
| $\kappa$ | Perturbation number [-] |
| $\sigma$ | Perturbation growth rate [-] |
| $\lambda$ | Fracture interporosity flow coefficient [L] |
| $\mu$ | Viscosity [$ML^{-1}T^{-1}$] |
| $\rho$ | Density [$ML^{-3}$] |
| $\tau$ | Dimensionless time [-] |
| $\phi$ | Porosity [$L^3L^{-3}$] |
| $\chi$ | Mole fraction |

***Superscripts***

| | |
|---|---|
| s | Equilibrium |
| ' | Perturbed property |
| ^ | Dimensionless |

***Subscripts***

| | |
|---|---|
| 0 | Base state |
| b | Brine |
| c | Critical value |
| Conv | Convection |
| Diff | Diffusion |
| e | Equivalent |
| f | fracture |
| m | Matrix |
| max | Maximum |
| min | Minimum |

# Chapter 1: Introduction

## 1.1 Background

Worldwide emission of carbon dioxide ($CO_2$) due to utilization of fossil fuels is one of the important human concerns. It is believed that such anthropogenic emissions has caused climate change over the past decades and is expected to continue in the upcoming years (Metz et al., 2005). Immediate reduction of greenhouse gas emissions is one of the most imperative environmental policies that has been proposed for global warming mitigation (EPA, 2014). Capture and geological storage of $CO_2$ in deep geological formations has been recognized as an operative choice and a viable short term option to reduce $CO_2$ emissions over the next decades until new technologies play an important role in significant reduction of the emissions (NACAP, 2012). At the national level, geostorage is a key opportunity that offers the possibility of sustaining access to fossil fuels such as oil sands in Alberta while reducing emissions.

$CO_2$ in a dense phase can be injected into deep subsurface formations (more than 800 meters below the surface where the ambient pressures and temperatures will usually result in $CO_2$ being in a supercritical state). Within these formations, oil fields, depleted gas fields, deep coal seams, and saline formations are all possible options (Orr, 2009a). Deep saline aquifers have been identified as the best alternative among geological formation for $CO_2$ storage due to their high capacity, proximity to emission sources, and worldwide availability (Metz et al., 2005).

The injected $CO_2$ can be effectively trapped in aquifers by several mechanisms such as structural (Gaus et al., 2008), residual gas (Boot-Handford et al., 2014), solubility (Benson and Cole, 2008), and mineral trapping (Firoozabadi and Myint, 2010), as briefly described below. In a typical geological storage most likely all mechanisms are active with different time scales. The focus of

this work is on solubility trapping of $CO_2$, which is an important trapping mechanism. In this dissertation, the role of buoyancy-driven convection and the associated convective mixing on solubility trapping of $CO_2$ in saline aquifers are studied.

### 1.2 Buoyancy-driven Convection Principles

Buoyancy-driven convection in porous media is of great importance for wide range of applications related to groundwater, soil contamination, chemical engineering, $CO_2$ capture or sequestration, and petroleum and geothermal reservoirs (Carballido-Landeira et al., 2013; Lindeberg and Wessel-Berg, 1997; Nield and Bejan, 2006). Buoyancy-driven convection can develop due to a buoyantly unstable density stratification in the gravity field, which can be attributed to either temperature and/or concentration gradient. The conditions under which buoyancy-driven convection develops in the concentration field have received great attention in the past decade (Ennis-King and Paterson, 2005; Hassanzad et al., 2005; Loodts et al., 2014; Myint and Firoozabadi, 2013; Trevelyan et al., 2011). Buoyancy-driven convection involved in geological sequestration of $CO_2$ into deep saline aquifers is a good example of the current interest. Much attention has been paid to the modelling of the convective dissolution of $CO_2$ in deep saline aquifers over the past two decades, since the role of density-driven convection on solubility trapping of $CO_2$ has been identified (Lindeberg and Wessel-Berg, 1997; Weir et al., 1996; Weir et al., 1995).

Once injected, $CO_2$ spreads as a free phase under a seal called cap rock since it is more buoyant than resident brine. While in free phase, there is always risk of leakage through pathways such as fractures, abandoned wells, and faults. Interestingly, gifted by Mother Nature, dissolution of $CO_2$ into brine increases the brine density at the top of aquifer. Depending on aquifer properties, the denser brine saturated with $CO_2$ at the top tends to sink down and is replaced with fresh brine. This leads to buoyancy-driven instabilities in an aquifer. This process can result in enhanced dissolution of $CO_2$ into brine and consequently reduces the volume of free (or mobile) phase $CO_2$ under the seal leading to decrease of the $CO_2$ risk of leakage (Ennis-King and Paterson, 2005; Hassanzadeh et al., 2005). Figure 2 shows the schematic of the described phenomenon.

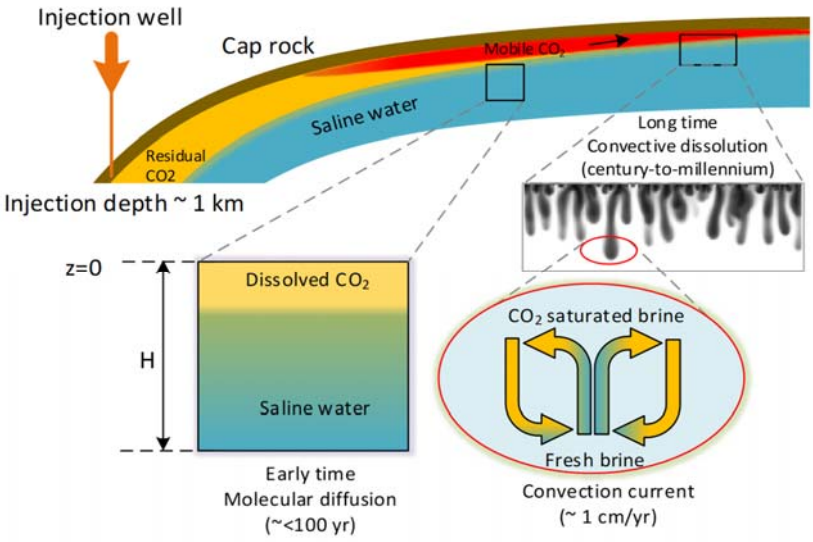


**Figure 1.1:** Schematic of mechanisms involved in long-term sequestration of $CO_2$ in deep saline aquifers (Jafari Raad and Hassanzadeh, 2016).

### 1.3 Motivation and Research Objective

The rate of decrease in $CO_2$ free phase and hence reduction of risk of leakage depends on the rate of transfer of $CO_2$ from the free phase to the underlying brines by convection, diffusion and geo-hydrological characteristics of aquifers. Solubility trapping of $CO_2$ as a result of the convective dissolution has been recognized as one of the main mechanisms in reduction of free phase $CO_2$ and thus reducing risk of leakage from storage sites. This $CO_2$ trapping mechanism has received emerging attention as it significantly affects the trapping efficiency, storage capacity and long-term storage security (Gilfillan et al., 2009).

Most of the previous studies on the buoyancy-driven convection are mainly concerned with pure $CO_2$ injection and there are relatively few works that considered injection of impure $CO_2$ into deep saline aquifers and the potential impact of impurities on the fate of the injected $CO_2$ has remained unexamined. One of the hindrances to progress in large scale implementation of $CO_2$ storage has been high cost of $CO_2$ capture from impure anthropogenic sources. Sequestering less pure $CO_2$ can potentially reduce the cost of capture process (Bachu et al., 2003; Ji and Zhu, 2013; Li et al., 2013; Nicot et al., 2013; Talman, 2015; Wong et al., 2003). However, before large scale implementation of geological storage, risk associated with the long-term storage needs to be assessed and

mechanisms which contribute to the permanent storage should be identified. These are necessary steps to avoid catastrophic consequences of possible leakage of the injected $CO_2$ from subsurface geological formations.

Permitted impurities in $CO_2$ streams can potentially impact the physical properties of $CO_2$/water system and hence stability criterion of the buoyancy-driven convection. Since the stability criterion of the buoyancy-driven convection is significantly influenced by the dynamics of the base state density profile, it should be of primary importance to have a good understanding of the concentration dependent base state density behaviour during dissolution process. This study investigates the role of the concentration dependent base state density profile on the stability of the buoyancy-driven convection and hydrodynamics of the associated convective mixing in different fluid pair systems. Stability criterion of the buoyancy-driven convection in binary and ternary fluid pair systems used in experimental studies of $CO_2$ convective mixing are of particular interest. The developed concepts on the role of density profiles in the stability of buoyancy-driven convection are extended to multi-component systems with applications to impure $CO_2$ and acid gas storage. One of the main objectives of this research is to determine the effect of permitted impurities in $CO_2$ streams on the fate of the injected $CO_2$ in subsurface formations and investigate ways to engineer or control the involved convective mixing mechanism.

An important class of geological formations suitable for storage of $CO_2$ and acid gases are fractured aquifers. Understanding the density-driven convection involved in dissolution of $CO_2$ in fractured formations is important since fractured aquifers are widespread and are gaining importance for their potential to host captured $CO_2$ for storage. The majority of previous works have been focused on $CO_2$ storage process in deep single porosity saline aquifers. This work also discusses stability criterion of the buoyancy-driven convection in dual porosity porous systems in the context of $CO_2$ storage in fractured aquifers. There is relatively less work focused on stability criterion involved in $CO_2$ sequestration process in fractured aquifers while fluid flow properties in a fractured formation can be completely different from those of in a conventional one. Understanding the effect of geological formation characteristics on the dynamics of dissolution and consequently effectiveness of $CO_2$ trapping is of great importance for long-term storage and risk assessment. We also study the effect of interface boundary excitation on the stability of diffusive boundary layers in porous media. Stability of fluids in porous media with boundary excitation is of particular interest, especially in connection with the geophysical and environmental

problems. The objective of this part of my study is to perform an analysis of the instability and the associated dynamics of solutal natural convection in a saturated porous medium in the presence of boundary excitation. The presented analysis and results in this study provide fundamental understanding of natural convection in the presence of boundary excitation.

In summary, the objectives of this research are (i) to perform theoretical studies related to the role of the base state density profile in dynamics of buoyancy-driven convection in different fluid pair systems as analogue to pure and impure $CO_2$/water systems, (ii) study the buoyancy-driven convection and the associated convective dissolution involved in impure $CO_2$ sequestration in deep saline aquifers, (iii) study the role of the gas/brine interface boundary condition on the stability of the diffusive boundary layer in geological flows with applications to geological storage of $CO_2$, and (iv) stability of diffusive boundary layers in fractured geological formations.

This study provides fundamental understanding on the role of fluid mixture physical properties as well as geological formation characteristics in hydrodynamics of convective mixing and the efficiency of solubility trapping mechanisms. In particular, the developed scaling relationships that characterize the long-term behaviour of the mixing process can be used as a useful tool for estimation of potential storage capacity, risk assessment and site screening purposes. The result from this research will also provide insight into a wide range of applications in various aspects of mixing encountered in engineering and science.

### 1.4 Dissertation Outline

This dissertation is comprised of nine chapters, which seven of them cover the core materials with an introduction chapter at the beginning and a summary chapter at the end. The core material chapters 2, 3, 4, 5, 6, 7 and 8 have been published in seven peer reviewed journals.

Chapter 2 presents a parametric analysis on the stability criteria of buoyancy-driven convection and hydrodynamics of the associated convective mixing in binary fluid pair systems. This study offers a quantitative description of the role of base state density profile evolve during dissolution process on the stability criteria of fluid pair systems with general form of the mixture density function and dynamic density profiles. In particular, stability criterion of analogue fluid systems such as water-propylene glycol used in experiments of convective dissolution of $CO_2$ in brine are discussed. This chapter is a modified version of the article entitled “Onset of dissolution-driven

instabilities in fluids with nonmonotonic density profile" that has been published in the journal of *Physical Review E*[*]. Chapter 3 extends the analysis provided in Chapter 2 to ternary analogue fluid systems. This chapter is a modified version of the article entitled "On the choice of analogue system in $CO_2$ convective dissolution experiments" that has been published in the journal of *Water Resources Research*[†]. This study addresses the evolution of the buoyancy-driven instability and dynamics of convective mixing in EG-MeOH/water analogue system. This study examines the ability of EG-MeOH/water system in resembling the dynamics of $CO_2$/water system and proposes scaling relations for the onset of convective instabilities that incorporate the effects of the concentration dependency of density of the analogue system at different mixture compositions.

Chapter 4 discusses the effect of permitted impurities in a $CO_2$ stream on the onset of buoyancy-driven convection associated with impure carbon dioxide ($CO_2$) storage in deep saline aquifers. In particular, impact of permitted $H_2S$ contaminants in a $CO_2$ stream on the stability criteria of the diffusive boundary layer associated with dissolution of $CO_2$ in brine is discussed through analytical developments. This Chapter offers a general parameter classification of dynamic density profiles evolve in impure $CO_2$/water systems based on key physical properties of impure systems and makes predictions for the stability behaviour of impure systems based on the buoyancy ratio and diffusivity contrast of permitted impurities and $CO_2$ species. This chapter is a modified version of the article entitled "Does impure $CO_2$ impede or accelerate convective mixing in geological storage?" that has been published in the *International Journal of Greenhouse Gas Control*[‡].

---

[*] Jafari Raad, S. M., Hassanzadeh, H. (2015). Onset of dissolution-driven instabilities in fluids with nonmonotonic density profile. *Physical Review E, Statistical, Nonlinear, and Soft Matter Physics*, *92*(5–1), 053023. https://doi.org/10.1103/PhysRevE.92.053023.

[†] Jafari Raad, S. M., Emami-Meybodi, H., Hassanzadeh, H. (2016). On the choice of analogue fluids in $CO_2$ convective dissolution experiments. *Water Resources Research*, *52*(6), 4458–4468. https://doi.org/10.1002/2015WR018040.

[‡] Jafari Raad, S. M., Hassanzadeh, H. (2016). Does impure $CO_2$ impede or accelerate the onset of convective mixing in geological storage? *International Journal of Greenhouse Gas Control*, *54*, 250–257. https://doi.org/10.1016/j.ijggc.2016.09.011.

Chapter 5 extends the analysis provided in Chapter 4 through numerical experiments to examine the dynamics of convective mixing and the total rate of dissolution involved in impure $CO_2$ storage. It also demonstrates the effect of permitted $H_2S$ impurities on the distribution of $CO_2$ concentration through the host aquifer. This chapter is a modified version of the article entitled "Prospect for storage of impure carbon dioxide streams in deep saline aquifers-A convective dissolution perspective" that has been published in the *International Journal of Greenhouse Gas Control*[*].

Chapter 6 presents the influence of the diffusion contrast between species in a two-component partially miscible system on the dynamics of Rayleigh–Bénard (RB) convection in porous media. This chapter is a modified version of the article entitled "On the dynamics of two-component convective dissolution in porous media" that has been published in the journal of *Water Resources Research*[†]. This study offers an inclusive parametric analysis on the stability criteria of two-component partial miscible systems, which allows distinction of regions with different stability criteria and convective dissolution dynamics. This study provides new insight into the effect of diffusion contrast and can be used to develop strategies for acceleration and deceleration of buoyancy-driven instabilities.

Chapter 7 presents a detailed parametric analysis on the stability of a diffusive boundary layer in porous media subject to time-dependent boundary conditions. This chapter is a modified version of the article entitled "Impact of boundary excitation on stability of a diffusive boundary layer in porous media" that has been published in *Advances in Water Resources*[‡]. This study offers scaling relations that incorporate the effect of the boundary parameters on the stability criteria and the dynamics of the buoyancy-driven mixing.

---

[*] Jafari Raad, S. M., Hassanzadeh, H. (2017). Prospect for storage of impure carbon dioxide streams in deep saline aquifers-A convective dissolution perspective. *International Journal of Greenhouse Gas Control*, *63*, 350–355. https://doi.org/10.1016/J.IJGGC.2017.06.011.

[†] Jafari Raad, S. M., Hassanzadeh, H., Ennis-King, J. (2018). On the dynamics of two-component convective dissolution in porous media. *Water Resources Research*, (In Press).

[‡] Jafari Raad, S. M., Emami-Meybodi, H., Hassanzadeh, H. (2019). Impact of boundary excitation on stability of a diffusive boundary layer in porous media. *Advances in Water Resources*, 126, 40-54. https://doi.org/10.1016/J.ADVWATERES.2019.02.005

Chapter 8 presents analytical analysis on the effect of physical properties of fracture network on the stability criteria of buoyancy-driven convection in a dual porosity system in the context of $CO_2$ storage in fractured aquifers. This chapter suggests scaling relations for the onset of convective instability that relate the onset of density-driven instabilities to the key physical properties of the fractured rocks in dual porosity systems. This chapter is a modified version of the article entitled "Onset of density-driven instabilities in fractured aquifers" that has been published in the journal of *Physical Review E*[*].

Finally, Chapter 9 summarizes the important findings and contributions of this study and makes recommendations for future works.

[*] Jafari Raad, S. M., Hassanzadeh, H. (2018). Onset of density-driven instabilities in fractured aquifers. *Physical Review E*, *97*(4), 043109. https://doi.org/10.1103/PhysRevE.97.043109.

# Chapter 2: Onset of Dissolution-driven Instabilities in Fluids with Non-monotonic Density*

## 2.1 Abstract

Analogue systems have recently been used in several experiments in the context of convective mixing of $CO_2$. We generalize the non-monotonic density dependence of the growth of instabilities and provide a scaling relation for the onset of instability. The results of linear stability analysis and direct numerical simulations show that these fluids do not resemble the dynamics of $CO_2$/water convective instabilities. A typical analogue system, such as water/propylene glycol, is found to be less unstable than $CO_2$/water. These results provide a basis for further research and proper selection of analogue systems and are essential to the interpretation of experiments.

## 2.2 Introduction

It is believed that anthropogenic carbon dioxide ($CO_2$) emissions are the main cause of the current global temperature trend over the past decades and is expected to continue in the upcoming years (Metz et al., 2007). Capture and storage of $CO_2$ (CCS) in deep geological formations has been suggested as an option to reduce $CO_2$ atmospheric emissions (NACAP, 2012). Deep saline aquifers have been identified as the best alternative among geological formations for $CO_2$ storage, due to their high capacity, proximity to emission sources, and worldwide availability (Metz et al., 2005).

*Jafari Raad, S. M., Hassanzadeh, H. (2015). Onset of dissolution-driven instabilities in fluids with nonmonotonic density profile. *Physical Review E, Statistical, Nonlinear, and Soft Matter Physics*, *92*(5–1), 053023. https://doi.org/10.1103/PhysRevE.92.053023.

In the storage process, $CO_2$ is compressed and injected in deep saline aquifers, where it comes into contact with brine and starts dissolving. The dissolution of $CO_2$ and solubility trapping in formation brine has been identified as one of the key mechanisms in the permanent storage process (Gilfillan et al., 2009).

The injected $CO_2$ is less dense than the brine and remains buoyant above it under a cap rock (or seal), but slowly diffuses into the underlying brine. Dissolution of most gases in water reduces the aqueous phase density, with the exceptions of sulfur dioxide ($SO_2$), $CO_2$, argon (Ar) and krypton (Kr) (Ennis-King and Paterson, 2005). The $CO_2$-saturated brine is slightly denser than the pure brine and becomes gravitationally unstable, leading to a convective dissolution process that enhances the flux of $CO_2$ into the brine. Such a slight density increase has been shown to be a linear function of the $CO_2$ concentration (Yang and Gu, 2006). Depending on aquifer properties, the denser brine saturated with $CO_2$ at the top tends to sink down and is replaced with fresh brine. As a result of buoyancy-driven flow or so-called convective dissolution, the volume of free-phase $CO_2$ under the seal decreases significantly compared to pure diffusion, thereby reducing the leakage risk of the $CO_2$ (Ennis-King and Paterson, 2005; Hassanzadeh et al., 2005).

Much attention has been paid to the modelling of the convective dissolution of $CO_2$ in deep saline aquifers over the past two decades, since the role of density-driven convection on solubility trapping of $CO_2$ has been identified (Lindeberg and Wessel-Berg, 1997; G. Weir et al., 1996; G. J. Weir et al., 1995). Difficulty in attaining a laboratory setting to study convective dissolution using $CO_2$ and water at actual storage conditions has inspired researchers to propose the use of analogue systems, which retain some properties of the $CO_2$/water system and allow experiments at normal laboratory conditions and length and time scales (MacMinn et al., 2012). A few studies have investigated the convective dissolution of $CO_2$ in water using analogue systems. Analogue systems, such as propylene glycol (PPG) / water (Agartan et al., 2015; Backhaus et al., 2011; MacMinn and Juanes, 2013; Tsai et al., 2013), mixtures of ethylene glycol and methanol (EG-MeOH) / water (MacMinn et al., 2012; Neufeld et al., 2010), potassium permanganate / water (Slim et al., 2013) and phenolphthalein dissolved in 4-methyl-2-pentanone (commonly known as methyl isobutyl ketone or MIBK) / sodium hydroxide (for reactive systems) (Cardoso and Andres, 2014), have been used as analogue systems. Water/PPG and EG-MeOH/water systems have been used to mimic dynamics of free-phase $CO_2$ relative to water as well as the dynamics of $CO_2$

dissolved in water (Hidalgo et al., 2013); whereas potassium permanganate /water has been utilized to capture the latter (Slim et al., 2013).

Analogue systems have some differences. In particular, analogue fluids and water are fully miscible, whereas $CO_2$ is partially soluble in water. Therefore, analogue systems cannot capture the capillary impacts on the convective dissolution of a $CO_2$/water system. Some of these systems have substantial viscosity variations: i.e., in water/PPG, PPG is ~50 times more viscous than water (Sun and Teja, 2004); and, in EG-MeOH/water, water is ~4 times less viscous than EG-MeOH (Tsierkezos and Molinou, 1999). A fundamental difference between $CO_2$/water and analogue systems, such as EG-MeOH/water and PPG/water, is that dissolution of EG-MeOH or PPG in water results in non-monotonic density behaviour with concentration, whereas a $CO_2$/water system shows a monotonic density-concentration dependence.

The objective of our study was not the simulation of these experiments, but the parameterization of the role of the non-monotonic density profile on the onset of dissolution-driven instabilities, which has not been studied in the past. In addition, inconsistencies reported for the scaling of convective flux in recent experimental studies with the classic scaling of the Rayleigh-Bénard convection (Backhaus et al., 2011; Hidalgo et al., 2013; MacMinn et al., 2012; MacMinn and Juanes, 2013; Neufeld et al., 2010; Tsai et al., 2013) have motivated us to study the role of density behaviour of analogue systems at the onset of instabilities.

Non-monotonic density profiles arise in several physical and chemical processes, such as natural convection of water near its density maximum (Kim and Choi, 2014; Moore and Weiss, 1973), buoyancy-driven flows induced by chemical reactions and/or diffusion in multi-species miscible or immiscible systems (Loodts et al., 2014; Trevelyan et al., 2011, 2015). A recent study attempted to demonstrate the role of non-monotonic density profile (Kim, 2014); however, the analysis did not permit scaling and generalization of the non-monotonic dependence of the growth of the convective instabilities. It was concluded that water/PPG is more unstable than a $CO_2$/water system. This conclusion was partly made since the onset time of a moving interface problem was compared with a fixed interface one. Nevertheless, it is well-known that a moving interface results in a faster onset of instabilities (Daniel and Riaz, 2014; Elenius et al., 2012; Elenius et al., 2014; Emami-Meybodi and Hassanzadeh, 2015; Emami-Meybodi and Hassanzadeh, 2013; Myint and Firoozabadi, 2013; Slim and Ramakrishnan, 2010). Therefore, a comparison between $CO_2$/water

and water/PPG systems can only be made when the boundary conditions for both systems are the same and more importantly when both systems are governed by the same dimensionless scaling group (i.e. Ra). In other words, the Rayleigh numbers that govern the system stability of the monotonic and non-monotonic profiles are not the same as will be shown in our stability analysis formulation. Nonetheless, when scaling groups are similar the moving interface is always more unstable than the fixed interface for a fixed Rayleigh number, which has been widely discussed in the literature (Emami-Meybodi et al., 2015).

In addition, for a monotonic system such as $CO_2$/water the onset time can be scaled based on the linear behaviour of the density as a function of concentration of the diffusing species. For such a system $\rho = \rho_i(1+\beta c)$ and the maximum density difference is given by $\Delta\rho = \rho_i \beta c$, where $\rho_i$ is the density of the initial fluid with zero concentration of the diffusion species. Therefore, the behaviour of the density profile (its linearity) is captured in the definition of the scaled time. Similarly, for a non-monotonic system such as water/PPG the behaviour of the analogue fluid should appear in the definition of the scaled time and the scaled onset time cannot be independent from the characteristics of the density function. However, in the analysis reported in (Kim, 2014) the onset time is scaled based on an the density difference between pure PPG and pure water, which does not resemble the non-monotonic behaviour of the density of water/PPG mixture. Therefore, the scaled times of $CO_2$/water and water/PPG reported in (Kim, 2014) are not comparable. In this paper, we have shown that the density difference used in the scaling of time should capture the non-monotonic behaviour of the fluid to have a proper comparison of the onset times for the two systems.

In this study, we report results of both linear stability analysis (LSA) and direct numerical simulations of a gravitationally unstable boundary layer to address these issues. In particular, we present a universal scaling relation, which allows estimation of the onset of the convective instabilities and generalization of the non-monotonic dependence of the growth of the instabilities.

## 2.3 Mathematical Formulation

### 2.3.1 Governing equations

We started with a two-dimensional, laterally infinite, homogeneous, isotropic, isothermal, vertical cross-section of a porous layer of constant thickness, H, saturated with quiescent fluid, as shown in Figure 2.1 (adopted from Hewitt et al. (Hewitt et al., 2013)). The quiescent fluid was initially free of the diffusing species. Boundary conditions for the flow (pressure) and mass transport were set as follows: No flow boundaries were set at the top and bottom of the domain, the bottom boundary was set at no mass flux, and the top boundary was set at a constant concentration of the diffusing species for fixed interface problems.

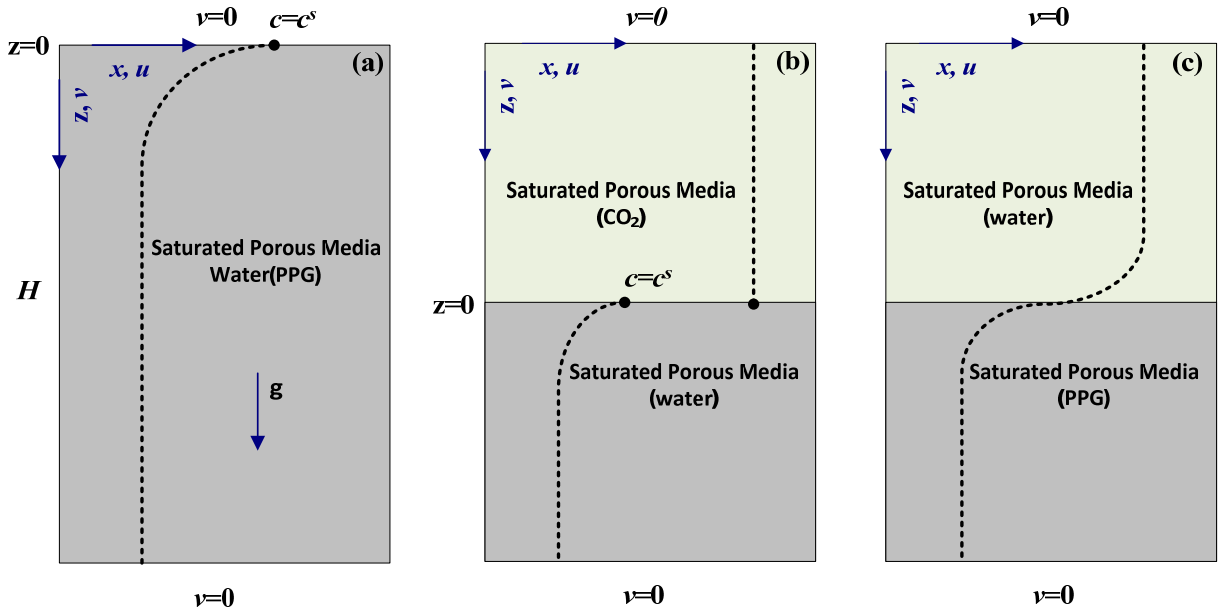


**Figure 2.1**: Geometry and boundary condition for three different systems (a) fixed interface problem, (b) moving interface problem (immiscible system), and (c) moving interface problem (miscible system) used in this study. The base state concentration profile versus depth is also shown by the dotted lines (adopted from Hewitt et al.(Hewitt et al., 2013)).

In the context of geological storage of $CO_2$ and in the absence of capillary pressure, the interface between $CO_2$ and water remains sharp (i.e., an immiscible system); therefore, a constant concentration at the top (fluids interface) was deemed to be more appropriate (Emami-Meybodi

and Hassanzadeh, 2015). However, the moving interface is more compatible for a miscible system. We performed LSAs for both fixed and moving interface problems. Our study was focused on the fixed interface problem since it is more comparable with a $CO_2$/water system. The results of the moving interface are presented for comparison. A detailed discussion on various boundary conditions is provided elsewhere (Hewitt et al., 2013).

Assuming that the Boussinesq approximation and Darcy's law are valid, the governing equations of non-reactive flow and transport for an incompressible fluid, in the absence of viscosity variation and dispersion effects, can be written as (Bear, 1972):

$$D\phi\nabla^2 c - \mathbf{v}\cdot\nabla c = \phi\frac{\partial c}{\partial t}; \tag{2.1a}$$

$$\nabla\cdot\mathbf{v} = 0; \tag{2.1b}$$

$$\mathbf{v} = -\frac{k}{\mu}(\nabla p - \rho\mathbf{g}\nabla z), \tag{2.1c}$$

where $\rho = f(c)$, $\mathbf{v}(u,v)$ is a vector of the Darcy velocity, $t$ is time, $k$ is the porous medium permeability, $\mu$ is the viscosity, $p$ is the pressure, $g$ is the gravitational acceleration, $z$ is the vertical coordinate (positive downwards), $\rho$ is the mixture density, $\phi$ is the porosity, $c$ is the concentration, and $D$ is the effective molecular diffusion coefficient of the diffusing species in porous media and is assumed to be independent of concentration for dilute solutions.

### 2.3.2 Base state solution

The system is initially stagnant; thus, the molecular diffusion is the dominant mechanism involved in the mass transfer of the dissolved species prior to the onset of convection. In this case, the governing equation for the base state reads as:

$$\frac{\partial^2\hat{c}_0}{\partial\hat{z}^2} = \frac{\partial\hat{c}_0}{\partial\hat{t}}, \tag{2.2}$$

where subscript 0 stands for the base state.

We scaled the vertical coordinate $z$ by $H$ (the thickness of the porous layer), time with the diffusion time scale, $H^2/D$, and the species concentration by the maximum concentration of the diffusing

species at the top boundary, $C^s$ ($\hat{c}_0 = c_0 / c^s$). The initial and boundary conditions for the base state were $\hat{c}_0(\hat{z},\hat{t}=0)=0$ and, $\hat{c}_0(0,\hat{t})=1$, $\partial\hat{c}_0(1,\hat{t})/\partial\hat{z}=0$, respectively. The base state solution can be written as:

$$\hat{c}_0 = \left[1 - \frac{2}{\pi}\sum_{n=1}^{\infty}\frac{1}{\lambda_n}\sin(\lambda_n \pi \hat{z})\exp\left(-\lambda_n^2 \pi^2 \hat{t}\right)\right], \tag{2.3}$$

where $\lambda_n=(2n-1)/2$.

A second-order polynomial, given by $\rho=\rho_i(1+\beta_1\hat{c}+\beta_2\hat{c}^2)$, is used to describe the density-concentration relationship. This second-order polynomial closely fits the water/PPG density experimental data with a coefficient of determination of approximately one ($R^2\approx1$) (Sun and Teja, 2004). This density relation can be expressed in dimensionless form as $\hat{\rho}=\hat{c}+r_\beta\hat{c}^2$, where $\hat{\rho}=(\rho-\rho_i)/\beta_1\rho_i$, $\rho_i$ is the initial fluid density and $r_\beta=\beta_2/\beta_1$. Parameter $r_\beta$ controls the shape of the density function. The dimensionless initial fluid density is $\hat{\rho}=0$ and the dimensionless density at the upper boundary is $\hat{\rho}_{in}=1+r_\beta$.

For $r_\beta$<-1/2 (e.g. water/PPG), there is an intermediate density maximum, $\hat{\rho}(\hat{c}_m)=-1/(4r_\beta)$, where $\hat{c}_m=-1/(2r_\beta)$; thus, diffusion of the diffusing species from the top boundary creates a mixing zone, which at some depth is slightly denser than the initial fluid and may trigger the convective instability. Note that for $r_\beta\geq$-1/2 (e.g. $CO_2$/water), the mixing zone is always denser than the initial fluid. For water/PPG systems, PPG and water are considered as initial fluid and diffusing species, respectively; and, $\hat{c}$ denotes the concentration of water (diffusing species); whereas water and $CO_2$ are considered as initial fluid and diffusing species, respectively, for $CO_2$/water systems, and $\hat{c}$ represents the concentration of $CO_2$ (diffusing species). It should be noted that $r_\beta$ is zero for $CO_2$/water systems.

We studied the effect of the shape of density function on the evolving base state density profile to describe the possible instability of the system. Using the early time solution of the base state concentrations given by $\hat{c}_0=erfc(\hat{z}/\sqrt{4\hat{t}})$, the density gradient in the z-direction ($\hat{\rho}_z$) in the porous layer can be obtained as:

$$\frac{\partial \hat{\rho}}{\partial \hat{z}} = -\frac{e^{-\frac{\hat{z}^2}{4\hat{t}}}}{\sqrt{\pi \hat{t}}}\left(1 + 2r_\beta erfc\left(\frac{\hat{z}}{\sqrt{4\hat{t}}}\right)\right). \tag{2.4}$$

Equation (2.4) indicates that the density gradient at the top boundary has negative or positive values for $r_\beta \geq -1/2$ and $r_\beta < -1/2$, respectively; hence, the density profile may have extremum (local minimum or maximum). Therefore, the behaviour of the density profile with depth needed to be inspected. By setting $\hat{\rho}_z = 0$ in Equation (2.4), we obtain $1 + 2r_\beta erfc(\hat{z}/\sqrt{4\hat{t}}) = 0$. For $r_\beta > 0$, this equation has no root, and the density profile remains monotonic and without an inflection point. However, for $r_\beta < 0$, there exists one root, indicating the likelihood of an extremum.

As discussed, system with monotonic or non-monotonic density profiles are distinguished based on character of their density profiles with depth. Systems with extremum in density profile are known as non-monotonic systems. Systems with non-monotonic density profile can be divided into two different categories based to the sign of the interface density differences ($\hat{\rho}_{in} = 1 + r_\beta$) and density gradient, $\hat{\rho}_z$ at the interface. These evolving non-monotonic density profiles are characterized by regions denoted by $r_\beta < -1$ an $-1 < r_\beta < -1/2$. A monotonic density profile is characterized by $-1/2 < r_\beta < 0$. Figure 2.2 shows the mixture densities with various $r_\beta$ values and their corresponding dynamic density profiles. For instance, system (V) with $r_\beta = -0.7$ resulted in a positive density differences while water/PPG system, (VI) with $r_\beta = -1.68$ reveals a negative interface density difference. These two systems demonstrate the non-monotonic density behaviour with depth. The interface density differences values are the main differences between these two systems. Zero interface density is shown by dashed line in Figure 2.2. Systems with a profile such as (I), (II), (III), and (IV) show different density- concentration behaviour. However, these systems reveal a monotonic density profile with depth but with a different interface density difference corresponding to their $r_\beta$ value. The dissimilarity that exists between these density profiles has a great impact on the evolution of convective instabilities, as discussed in Section 2.4.

These results demonstrate the base state density profiles during the evolution of the boundary layer, which may potentially become unstable, and is very informative in the detailed LSA in the following section.

### 2.3.3 Linear stability analysis

We performed a LSA based on the quasi-steady-state approximation (QSSA) to study the growth of perturbations and determine the onset of convective instabilities. The pressure, velocity, concentration and density fields that appeared in the governing equations of flow and transport (Equation (2.1)) are subjected to small perturbations using the general linearization form of $\mathbf{s}=\mathbf{s}_0+\mathbf{s}'$, where $\mathbf{s}$=$\mathbf{s}$[p,v,c,ρ], and subscript 0 stands for the base state. Since the fluid is initially quiescent, and the transport occurs by pure diffusion, the base state for concentration is given by Equation (2.2), where the base state velocity is $\mathbf{v}_0$=0 and the base state density is $\hat{\rho}_0=\hat{c}_0+r_\beta\hat{c}_0^2$. After substitution for the perturbed variables in the flow and transport equations, linearizing in the perturbations, simplification and dropping of the hats (^) for convenience, we obtain:

$$\nabla^2 v' = \mathrm{Ra}\left(1+f(2c_0-1)\right)\frac{\partial^2 c'}{\partial x^2}, \tag{2.5a}$$

$$\nabla^2 c' - v'\frac{\partial c_0}{\partial z} = \frac{\partial c'}{\partial t}, \tag{2.5b}$$

where the velocity perturbation is scaled by ϕD/H, $\nabla^2=\nabla_x^2+\nabla_z^2$, $f=r_\beta/(1+r_\beta)$ and Rayleigh number Ra, which is the ratio of buoyancy strength to the dissipative effects of viscosity and diffusion, is defined as $\mathrm{Ra}=kg\rho_i H\beta_i(1+r_\beta)/\mu\phi D$.

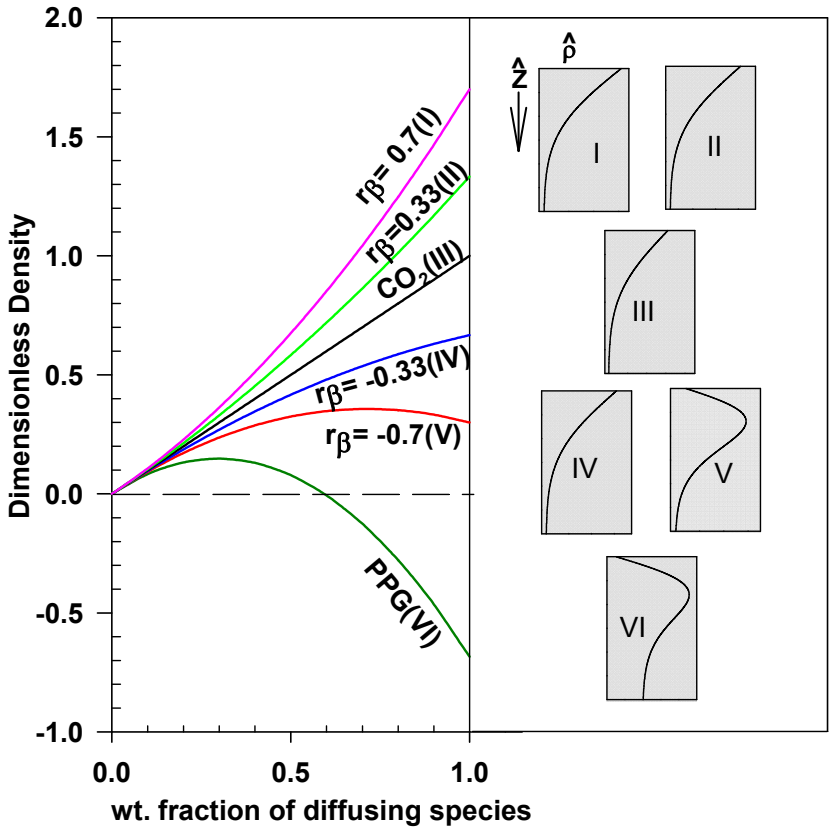


**Figure 2.2**: (color online). Density versus weight fraction of diffusing species for mixtures with various density functions. The right panel shows the base state dynamic density profile versus depth for the fixed interface problem.

Using the Fourier decomposition method, the perturbed velocity and concentration can be expressed as $[c',v']=[c^*,v^*](z,t_0)e^{-i\kappa x+\omega t}$, where $\kappa$ and $\omega$ are the perturbation wavenumber and growth rate, respectively. Using Equation (2.5), we obtain:

$$\frac{\partial^2 v^*}{\partial z^2}-\kappa^2 v^* = (-\kappa^2)\,\mathrm{Ra}\left(1+f(2c_0-1)\right)c^*, \tag{2.6a}$$

$$\frac{\partial^2 c^*}{\partial z^2}-\kappa^2 c^* - v^*\frac{\partial c_0}{\partial z} = \omega c^*. \tag{2.6b}$$

The boundary conditions for the perturbed flow and concentration are given by: $c^*(0)=0$, $\partial c^*(1)/\partial z=0$, $v^*(0)=v^*(1)=0$.

It is worth noting that the time scale represented by $t$ refers to the fast growing perturbations, while the other time-scale, $t_0$, corresponds to the molecular diffusion, which is a very slow phenomenon. Therefore, it seems reasonable to assume that $\partial c_0/\partial z$ is evaluated at time $t_0$ or the so-called frozen time during the growth of perturbations. Knowing that the molecular diffusion is a very slow process, this approach is applicable since the growth of perturbations is much faster than the evolution of the base state density profile. This approach is known as the (QSSA) (Tan and Homsy, 1986) and has been extensively used in LSA (Ghesmat et al., 2011; Riaz et al., 2006; Tan and Homsy, 1986; Trevelyan et al., 2011). The limits of the validity of the QSSA have been discussed elsewhere (Trevelyan et al., 2011).

Equation (2.6a) converts to the $CO_2$/water case for $r_\beta$=0. To find the growth rate, ω, for an assigned wavenumber, $\kappa$, the above system of Equations (2.6a) and (2.6b) are solved numerically using a second-order finite difference method. For each value of $\kappa$, the discretized equations lead to an eigenvalue problem given by:

$$[\mathbf{A}_v][\mathbf{v}^*]=(-\kappa^2)\mathrm{Ra}\left(1+f(2c_0-1)\right)\mathbf{c}^*, \tag{2.7a}$$

$$[\mathbf{A}_c][\mathbf{c}^*]-[\mathbf{v}^*]\frac{\partial \mathbf{c}_0}{\partial z}=[\boldsymbol{\omega}][\mathbf{c}^*]\ , \tag{2.7b}$$

where $\mathbf{A}_v=\left(\mathbf{D}_v-\kappa^2\mathbf{I}\right)$, $\mathbf{A}_c=\left(\mathbf{D}_c-\kappa^2\mathbf{I}\right)$, $\mathbf{D}_v$, and $\mathbf{D}_c$ are coefficient matrices based on central discretization of the second derivatives, and **c** and **v** are vectors containing the unknown variables at the discrete nodes. Solutions to Equations (2.7a) and (2.7b) can be written as:

$$[\mathbf{v}^*]=(-\kappa^2)\mathrm{Ra}\left(1+f(2c_0-1)\right)[\mathbf{A}_v]^{-1}[\mathbf{c}^*], \tag{2.8a}$$

$$[\mathbf{A}_c][\mathbf{c}^*]-\left((-\kappa^2)\,\mathrm{Ra}\left(1+f(2c_0-1)\right)[\mathbf{A}_v]^{-1}[\mathbf{c}^*]\right)\left[\frac{\partial \mathbf{c}_0}{\partial z}\right]=[\boldsymbol{\omega}][\mathbf{c}^*]\ . \tag{2.8b}$$

This eigenvalue problem is solved numerically, and the maximum eigenvalue of the coefficient matrix is considered as the growth rate, $\omega$, corresponding to the assigned wavenumber, $\kappa$, and $Ra$ at a certain $t_0$. The same numerical procedure reported by Emami-Meybodi and Hassanzadeh

(Emami Meybodi and Hassanzadeh, 2013) was used to solve the eigenvalue problem. The obtained growth rate of the initial perturbations for given wavenumbers are evaluated for detection of the onset of instability using dispersion curves. A positive growth rate at a particular time is an indication of instability. Thus, the onset time can be detected using a zero maximum growth rate: i.e., the time at which the growth rate first becomes positive represents the actual time of the instability. Negative values for the growth rate of large wavenumbers imply that the system remains stable.

We validated our computational algorithm using the early time analytical solution ($t \rightarrow 0$) for the special case of a step change in the concentration profile. For this case, it can be shown that $\omega = -\kappa^2$ (Riaz et al., 2006; Tan and Homsy, 1986). The results shown by open circles in Figure 2.3a indicate that the developed algorithm recovers the special case of $\omega = -\kappa^2$ when time approaches zero, suggesting the validity of the developed numerical code.

We used the traditional QSSA (or the normal z-domain) (Tan and Homsy, 1986) to solve the system of equations given in Equation (2.8); however, previous studies have shown that the onset times obtained using QSSA in self-similar coordinates are larger than those obtained using the traditional QSSA (Kim, 2014; Tilton et al., 2013). Recently, a comprehensive study addressed some concerns in this area using a comparison of the traditional QSSA and QSSA in self-similar coordinated with initial value problem (IVP) as well as full numerical simulations (Tilton et al., 2013). According to these studies, the disagreement concerning the critical time is attributed to the sensitivity of different analyses to how the perturbation growth is measured. It is worth noting that both the selected perturbation field (concentration or velocity) and the norm used to measure the perturbation amplitude impact the measured growth rates. The traditional QSSA supports smaller initial amplitudes compared to other noted methods that consider larger initial perturbations. However, previous studies (Tan and Homsy, 1986; Tilton et al., 2013) have shown that the qualitative behaviour of the resulted scaling for time of onset for all analysis methods remains the same.

For more clarification, we tested the stability criterion using QSSA in self-similar coordinates for both water/PPG and $CO_2$/water systems. Since the formulation of QSSA in the self-similar coordinates has been presented in the previous publications (Daniel and Riaz, 2014; Riaz et al., 2006; Tilton et al., 2013), we have provided this formulation in Appendix A.

## 2.4 Results and Discussion

### 2.4.1 Fixed interface problem

We studied the effect of the mixture density function on the growth of convective instabilities. Figure 2.3 shows the dispersion curves at different times for $CO_2$/water and water/PPG systems with linear and non-monotonic mixture density functions, respectively. The results shown in Figure 2.3 demonstrate a clear difference between linear and non-monotonic density functions, suggesting that the onset of convective instabilities for the two systems can be different. To verify this hypothesis, we investigated the onset of the convective instabilities versus *Ra* for various mixtures' density functions. The results for the fixed interface problem using the traditional QSSA, as shown in Figure 2.4, recover the well-known scaling of $\hat{t} = \mathrm{aRa}^{-2}$. The results for $CO_2$/water are also shown in Figure 2.4 with a solid black line. These results for $CO_2$/water are in close agreement with the previous findings (Bestehorn and Firoozabadi, 2012; Ennis-King et al., 2005; Hassanzadeh et al., 2006; Meulenbroek et al., 2013; Slim, 2014), which supports the validity of the analysis.

Figure 2.4 shows that prefactor *a* is a strong function of the mixture density function. An analogue system with $r_\beta \approx -1.68$ (Sun and Teja, 2004) resembles the PPG, which has been used in several recent experiments (Agartan et al., 2015; Backhaus et al., 2011; MacMinn and Juanes, 2013; Tsai et al., 2013). This mixture results in a non-monotonic density profile during the growth of the diffusive boundary layer, as indicated in Figure 2.2 (case VI). For a $CO_2$/water system where the interface is fixed, the traditional QSSA and the self-similar formulations result in scaling prefactor values of ~56 and ~167, respectively. This is in agreement with previous studies (Kim and Choi, 2012; Riaz et al., 2006; Tilton et al., 2013). For a water/PPG system where the interface is fixed, the traditional QSSA and self-similar formulations result in scaling prefactor values of ~80 and ~1791, respectively. The results reveal that the qualitative behaviour of the growth of perturbations remains similar for the self-similar and traditional QSSA formulations.

For the case of $r_\beta$=-1, $\hat{\rho}_{in} = \hat{\rho}(\hat{z}=0)$; thus, $\mathrm{Ra} = 0$. In this case, it can be shown that Equation (2.5a) can be written as $\nabla^2 v' = \mathrm{Ra}^*(1+2r_\beta c_0)\partial^2 c'/\partial x^2$; and, the linear scaling for the onset of instabilities follows $\hat{t} \approx 92/\mathrm{Ra}^{*2}$, where $\mathrm{Ra}^* = kg\rho_i H\beta_i / \mu\phi D$. Dependency of the scaling prefactor to $r_\beta$ for

the fixed interface problem using the traditional QSSA is shown in Figure 2.5. The results show that, while a non-monotonic profile results in the same scaling for the onset of convective instabilities, it gives a prefactor that is a strong function of the mixture density function. The results also reveal that an analogue system with $r_\beta$=-1.58 closely resembles the onset of convective instabilities for $CO_2$/water systems. However, the dynamics of the system beyond the onset for the two systems may be quite different.

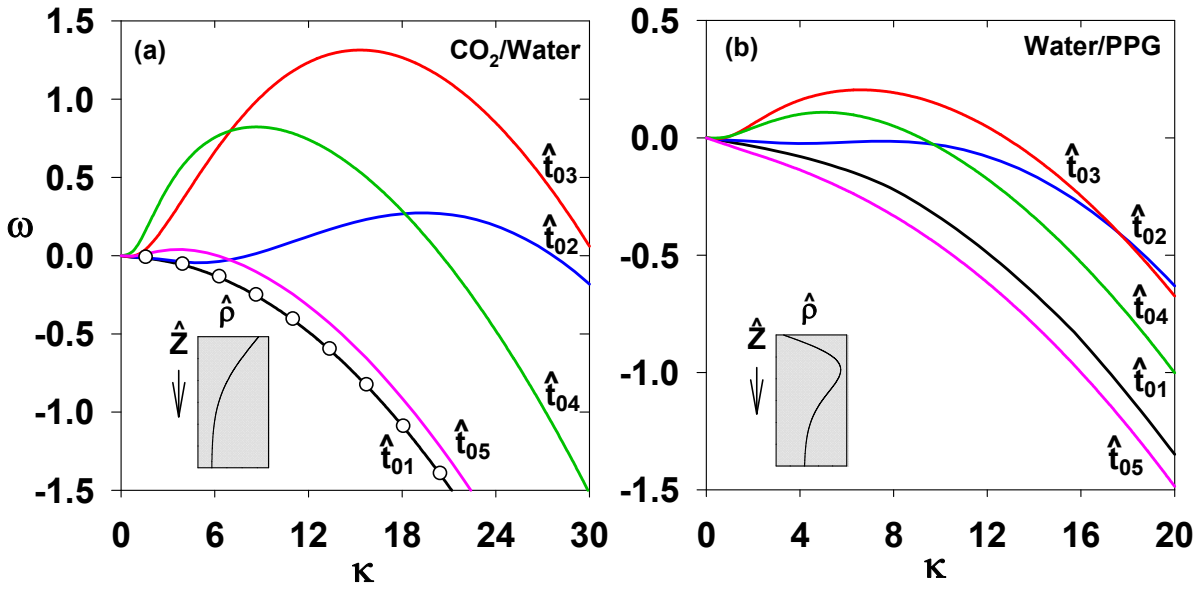


**Figure 2.3**: (color online). Rate of growth of perturbations versus the wavenumber for systems with |Ra|=300, at different frozen times of $\hat{t}_{01}=8\times10^{-5}$, $\hat{t}_{02}=8\times10^{-4}$, $\hat{t}_{03}=8\times10^{-3}$, $\hat{t}_{04}=8\times10^{-2}$, $\hat{t}_{05}=8\times10^{-1}$ (a) $CO_2$/water with $r_\beta$=0 and (b) water/PPG with $r_\beta$=-1.68. Open circles are the results of the analytical solution ($\omega$=-$\kappa^2$) compared with the results of the stability analysis shown by the line.

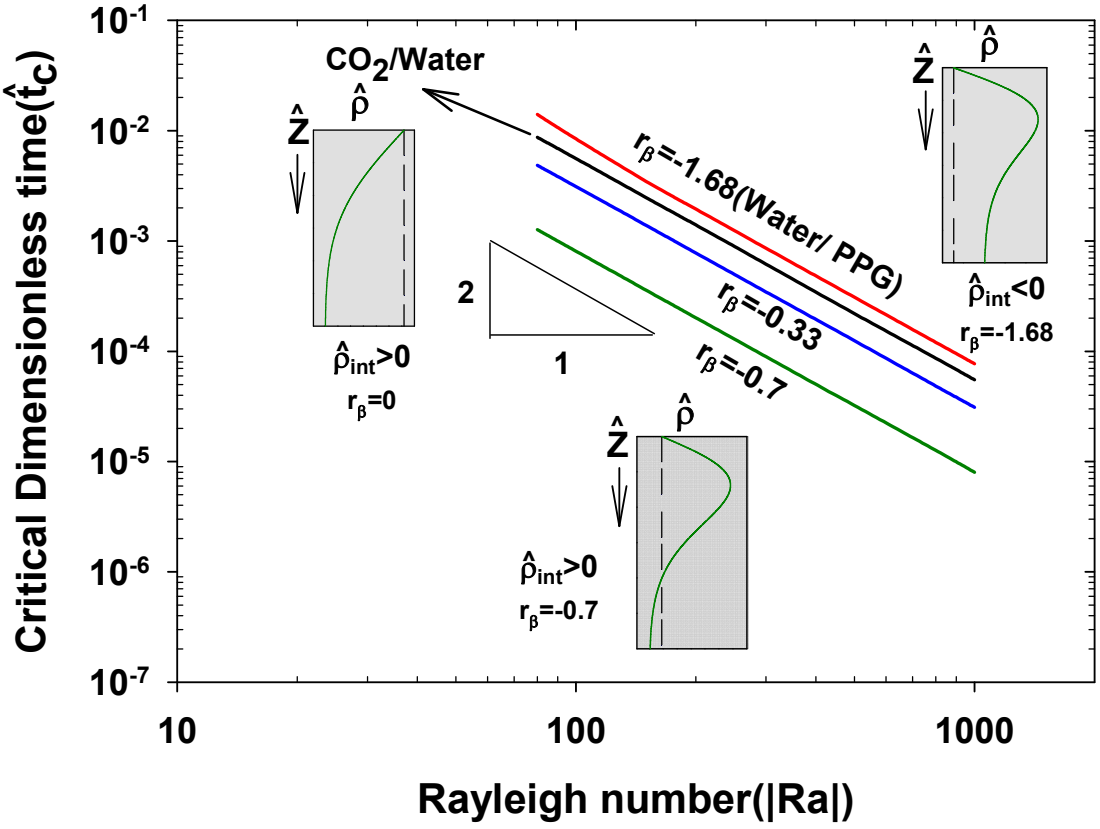


**Figure 2.4**: (color online). Onset of convective instabilities versus |Ra| for various mixture density functions including $r_\beta$=0 ($CO_2$/water), $r_\beta$=-0.33, $r_\beta$=-0.7, $r_\beta$=-1.68 (water /PPG).

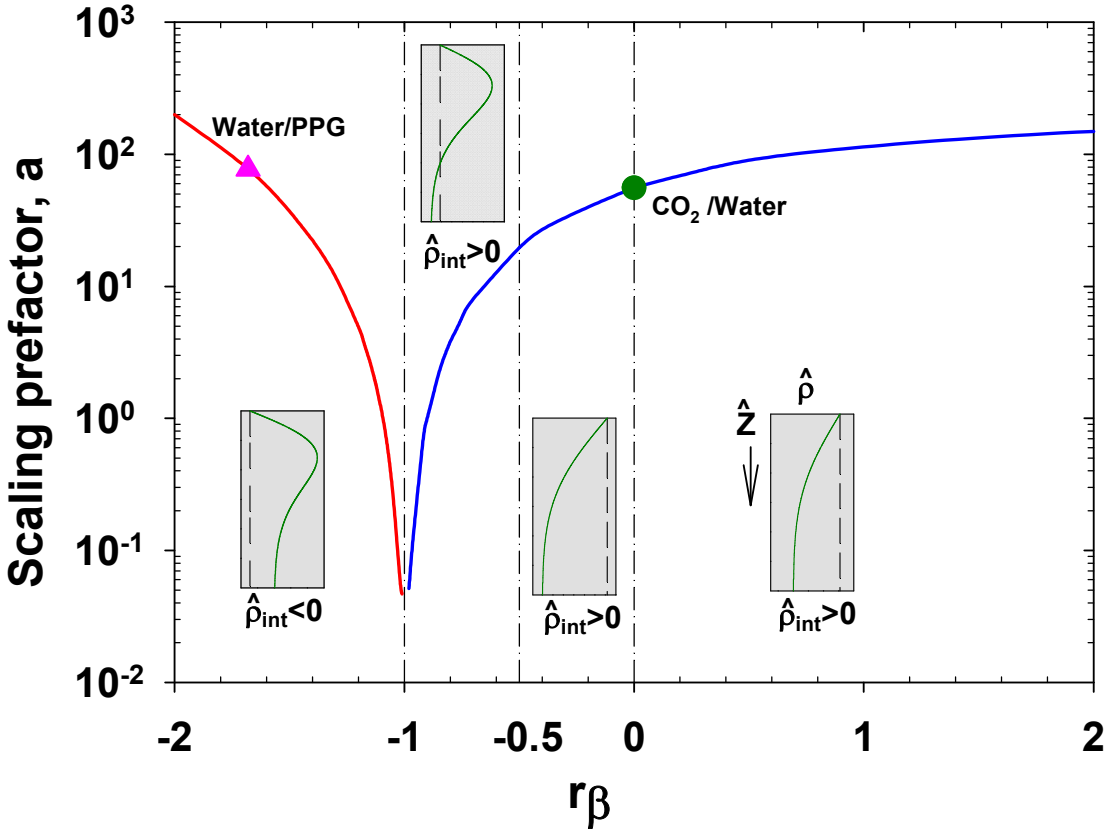


**Figure 2.5**: (color online). Prefactor of scaling relation, $a$, for the onset of convective instabilities ($\hat{t}=a/\mathrm{Ra}^2$) for various mixture density functions with different $r_\beta$. Water/PPG and $CO_2$/water systems are shown by a circle and triangle, respectively. Base state density profiles with depth are also shown for different regions.

### 2.4.2. Moving interface problem

As discussed previously, we used the fixed interface setup to make our results comparable to $CO_2$/water, which may be considered a fixed interface problem. Furthermore, not all non-monotonic density profiles shown in Figure 2.2 allow a moving interface problem, since the system is initially unstable for cases such as I, II, IV. In order to be able to use the moving interface formulation for miscible systems, an initially stable system is necessary, which is only possible for cases V and VI. It is well known that the moving interface problem results in a faster onset of instabilities (Daniel and Riaz, 2014; Elenius et al., 2012; Elenius et al., 2014; Emami-Meybodi

and Hassanzadeh, 2015; Emami Meybodi and Hassanzadeh, 2013; Myint and Firoozabadi, 2013; Slim and Ramakrishnan, 2010). The same trend can also be imagined for the water/PPG system, as shown in Table 2.1.

We present the results of the moving interface problem for a water/PPG system to obtain the critical time using the same parameters defined for the fixed interface problem. For the water/PPG system, the moving interface problem using the traditional QSSA and self-similar formulations results in scaling prefactors of ~57 and ~1296, respectively. For the $CO_2$/water system, the moving interface problem with the traditional QSSA formulation results in a scaling prefactor of ~46, while the prefactor for the self-similar formulation is reported to be ~153. Therefore, the results for the moving interface problem also reveal that the water/PPG system is less unstable than $CO_2$/water.

The results of our analysis are summarized in Table 2.1, which shows that, independent of the formulation and the nature of interface (fixed or moving), the water/PPG system is always less unstable than $CO_2$/water.

**Table** Error! No text of specified style in document..**1**: Summary of the obtained scaling prefactor for the fixed and moving interface problems using traditional QSSA and QSSA with self-similar formulations.

| Formulation | Fixed interface | Moving interface |
|---|---|---|
| Traditional QSSA | $a_{CO2/water}$ ~56 | $a_{CO2/water}$ ~ 46 |
| | $a_{water/PPG}$~80 | $a_{water/PPG}$~57 |
| QSSA in self-similar | $a_{CO2/water}$ ~167 | $a_{CO2/water}$ ~153 |
| | $a_{water/PPG}$~1791 | $a_{water/PPG}$~1296 |

### 2.4.3. Nonlinear simulations

We have conducted the non-linear simulations for both water/PPG and $CO_2$/water systems to confirm the results of the stability analysis. In order to examine the behaviour of $CO_2$/water and water/PPG systems, Equations (2.1a- 2.1c) were solved numerically. Details of the numerical approach and controls on accuracy of the numerical solutions have been reported in previous publications (Coats, 1969; Emami-Meybodi and Hassanzadeh, 2015; Emami Meybodi and

Hassanzadeh, 2013). The 2D numerical solutions were conducted to evaluate the concentration distribution associated with convective mixing for the two systems. The same fluid properties used in the linear stability analysis are employed in the direct numerical simulations. The nonlinear development of convective dissolution is investigated at Ra = 800 for both systems. Figure 2.6 shows the concentration distribution for $CO_2$/water and water/PPG systems at different times. For the moving interface problem, the height of the system above and below the interface is considered to be the same and equal to the height of the domain in the fixed interface problem. For the moving interface case (right panel), only concentration disturbances below the interface are shown for better comparison.

Consistent with the results of our linear stability analysis, the $CO_2$/water system results in faster development of the boundary layer instabilities, such that the growth rate of fingers are significantly stronger than those in the water/PPG systems. Furthermore, the fingering pattern in the $CO_2$/water system is more vigorous than those in the water/PPG system where the fingers develop with less interaction with neighbouring fingers. In addition, the wavelength of the density-driven fingers in the $CO_2$/water system is much smaller than those in the water/PPG. A strong merging of fingers was observed in the $CO_2$/water system while the growth of fingers in the water/PPG system is nearly independent from each other with minimal interaction. In the water/PPG system fingers growth in the form of sluggish plumes due to damping effect of upper stable region. These direct numerical simulation results are in qualitative agreement with the results of the linear stability analysis, which shows that water/PPG system is less unstable than $CO_2$/water system.

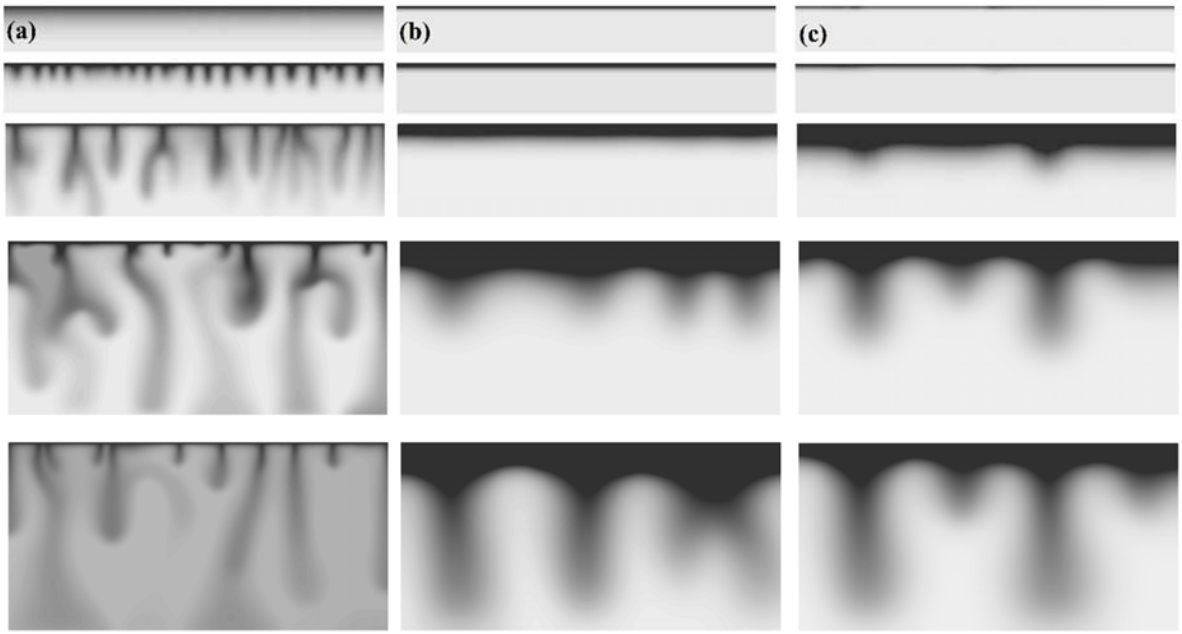


**Figure 2.6**: (Color online) Concentration distribution at the different times of $\hat{t}_{01} = 1.2\times10^{-3}$, $\hat{t}_{02} = 2.4\times10^{-3}$, $\hat{t}_{03} = 4.8\times10^{-3}$, $\hat{t}_{04} = 9.6\times10^{-3}$, $\hat{t}_{05} = 1.44\times10^{-2}$ for Ra=800 representing (a) $CO_2$/water system with the fixed interface, (b) water/PPG system with the fixed interface, and (c) water/PPG system with the moving interface. For the moving interface case (right panel), only concentration distributions below the interface are shown for better comparison.

## 2.5 Summary and Conclusions

We used a general form of the mixture density function combined with the dynamic density profile to characterize the stability behaviour of a gravitationally unstable diffusive boundary layer. Using both LSA and direct numerical simulations, we have shown that the choice of the analogue system is important in the design of experiments for proper representation of the convective instabilities in $CO_2$/water system. In particular, it was shown that water/PPG system is less unstable than $CO_2$/water and does not mimic the dynamics of $CO_2$/water system. Furthermore, a scaling relation for the onset of convective instabilities was developed that incorporates the effects of the concentration dependency of density of the analogue system. Our results form a basis for proper

selection of an analogue system and are necessary to interpret $CO_2$ convective dissolution experiments.

It was shown that an analogue system with $r_\beta$=-1.58 resembles the onset of convective instabilities for $CO_2$/water systems. However, the dynamics of the system beyond the onset of instabilities may be quite different. This is an important research question and calls for further studies. In particular, determination of the reason behind inconsistencies found in the scaling of the convective flux in recent experimental studies with the classic scaling of the Rayleigh-Bénard convection merits further studies. In addition, in the context of geological storage of $CO_2$, the onset time is typically shorter than the time necessary to dissolve all of the $CO_2$. Therefore, even large changes to the onset time are unlikely to have a major impact on the fate of the injected $CO_2$ into the subsurface. The development of the instability once triggered is much more important, as is the subsequent rate at which $CO_2$ dissolves.

### 2.6 Acknowledgments

The authors would like to thank two anonymous reviewers for their constructive comments, which have greatly improved our paper. The authors would also like to thank Hamid Emami-Meybodi of the Pennsylvania State University for fruitful discussions. This work was supported by a Discovery Grant from the Natural Sciences and Engineering Research Council of Canada (NSERC). This research was enabled in part by support provided by WestGrid (www.westgrid.ca) and Compute Canada Calcul Canada (www.computecanada.ca).

### 2.8 Appendix 2.A: Self-similar Coordinate Formulation of The Stability Analysis Equations

The linearized form of the perturbations can be written as:

$$\nabla^2 v' = \mathrm{Ra}\left(1 + f(2c_0 - 1)\right)\frac{\partial^2 c'}{\partial x^2}, \tag{2.A1a}$$

$$\nabla^2 c' - v'\frac{\partial c_0}{\partial z} = \frac{\partial c'}{\partial t}, \tag{2.A1b}$$

where the base states for the fixed and the miscible moving interface problems are given by $c_0 = erfc(z/\sqrt{4t})$, and $c_0 = \frac{1}{2}erfc(z/\sqrt{4t})$, respectively.

Using the Fourier decomposition method, the perturbed velocity and concentration are expressed as:

$$c' = c^*(z,t_0)e^{-i\kappa x+\omega t}, \tag{2.A2a}$$

$$v' = v^*(z,t_0)e^{-i\kappa x+\omega t}, \tag{2.A2b}$$

The time-dependent variable $\zeta(z,t) = z/\sqrt{4t}$ is used to transform the z-domain equations into the self-similar coordinates as given by:

$$\lambda^2 \frac{\partial^2 v^*}{\partial \zeta^2} - k^2 v^* = \mathrm{Ra}\left(1+f(2c_0-1)\right)\left(-\kappa^2\right)c^*, \tag{2.A3a}$$

$$\lambda^2 \frac{\partial^2 c^*}{\partial \zeta^2} - \kappa^2 c^* - \lambda \frac{\partial c_0}{\partial \zeta} v^* + \frac{\zeta}{2t}\frac{\partial c^*}{\partial \zeta} = \omega c^*, \tag{2.A3b}$$

where $\lambda = 1/\sqrt{4t}$.

Discretization of Equations (2.A3a) and (2.A3b) results in the following system of equations:

$$[\mathbf{A}_v][v^*] = (-\kappa^2)\,\mathrm{Ra}\left(1+f(2c_0-1)\right)c^*, \tag{2.A4a}$$

$$[\mathbf{A}_c][c^*] - \lambda\frac{\partial c_0}{\partial \zeta}[v^*] = [\boldsymbol{\omega}][c^*], \tag{2.A4b}$$

where $\mathbf{A}_v = \left(\lambda^2\mathbf{D}_{2v} - \kappa^2\mathbf{I}\right)$, $\mathbf{A}_c = \left(\lambda^2\mathbf{D}_{2c} - \kappa^2\mathbf{I} + \frac{\zeta}{2t}\mathbf{D}_{1c}\right)$, $\mathbf{D}_{2v}$, $\mathbf{D}_{2c}$ and $\mathbf{D}_{1c}$ are coefficients of matrices based on the central difference of the second and first derivatives; and, **c** and **v** are vectors containing the unknown variables at the discrete nodes.

Solutions to Equations (2.A4a) and (2.A4b) can be written as:

$$[v^*] = (-\kappa^2)\,\mathrm{Ra}\left(1+f(2c_0-1)\right)[\mathbf{A}_v]^{-1}[c^*], \tag{2.A5a}$$

$$[\mathbf{A}_c][c^*] - \lambda\left((-\kappa^2)\,\mathrm{Ra}\left(1+f(2c_0-1)\right)[\mathbf{A}_v]^{-1}[c^*]\right)\left[\frac{\partial c_0}{\partial \zeta}\right] = [\boldsymbol{\omega}][c^*]\ . \tag{2.A5b}$$

The same procedure described in the main text was used to find the eigenvalues of the system of equations.

# Chapter 3: On the Choice of Analogue Fluids in $CO_2$ Convective Dissolution Experiments*

## 3.1 Abstract

Mixtures of ethylene glycol and methanol (EG-MeOH) have been used as an analogue system (i.e., EG-MeOH/water) in recent experiments in the context of convective dissolution of $CO_2$ in deep saline aquifers. We have conducted a linear stability analysis of a gravitationally unstable diffusive boundary layer as well as direct numerical simulation of convective mixing involved in dissolution of EG-MeOH species in water. We provide new evidences that EG-MeOH does not resemble the dynamics of convective instabilities and subsequent mixing associated with dissolution of $CO_2$ in water. It is found that there are fundamental differences in the evolution of the buoyancy-driven instability and dynamics of convective mixing between $CO_2$/water and a typical EG-MeOH/water analogue system. Our results show that for a constant Rayleigh number the onset of convective instabilities for EG-MeOH/water can be different by an order of magnitude as compared with $CO_2$/water. In addition, EG-MeOH/water system reveals different dynamics associated with the convective mixing as compared to $CO_2$/water system. This study improves our understanding of the instability behaviour of analogue systems, their proper selection, and motivates further experiments.

* Jafari Raad, S. M., Emami-Meybodi, H., Hassanzadeh, H. (2016). On the choice of analogue fluids in $CO_2$ convective dissolution experiments. *Water Resources Research*, *52*(6), 4458–4468. https://doi.org/10.1002/2015WR018040

## 3.2 Introduction

Solubility trapping of carbon dioxide ($CO_2$) in formations brine has been recognized as a dominant sink (Gilfillan et al., 2009). The density of the aqueous phase in contact with the injected $CO_2$ slightly increases as a result of $CO_2$ dissolution leading to natural convection. Accelerated $CO_2$ dissolution into the aqueous phase due to such a favourable process results in reduction of the volume of free phase $CO_2$ and thus reduces the risk of leakage of $CO_2$ from storage formations (Emami-Meybodi et al., 2015; Ennis-King and Paterson, 2005; H. Hassanzadeh et al., 2005; Islam and Sun, 2015; Lindeberg and Wessel-Berg, 1997). This problem has been widely studied theoretically in the past decade. Maintaining actual storage conditions in laboratory studies of convective dissolution of $CO_2$ is challenging due to time and length scale limitations and has motivated application of analogue systems. In addition, operation of experiments at actual subsurface condition using water and $CO_2$ requires high pressure and high temperature experimental setup.

A handful of studies have recently reported the use of analogue system in experimental studies in the context of geological storage of $CO_2$. analogue systems such as propylene glycol (PPG)/water (Agartan et al., 2015; Backhaus et al., 2011; MacMinn and Juanes, 2013; Tsai et al., 2013), mixtures of methanol and ethylene glycol (EG-MeOH)/water (MacMinn et al., 2012; Neufeld et al., 2010), potassium permanganate/water (Slim et al., 2013), and phenolphthalein dissolved in 4-methyl-2-pentanone (commonly known as methyl isobutyl ketone or MIBK)/ sodium hydroxide (for reactive systems) (Cardoso and Andres, 2014) have been used in the recent studies. Analogue systems such as water/PPG and EG-MeOH/water have been used to resemble the dynamics of free-phase $CO_2$ relative to water and also to mimic the convective dissolution of $CO_2$ in water (Hidalgo et al., 2013) while the potassium permanganate/water system has been utilized to only capture the convective dissolution (Slim et al., 2013). Although these analogue systems allow experiments at normal laboratory conditions and length and time scales (MacMinn et al., 2012) and represent some features of the $CO_2$/water, there are some fundamental differences between the two systems. Presence of a density maximum at intermediate concentrations is one of the main features of EG-MeOH/water mixture while $CO_2$/water system shows a monotonic density-concentration behaviour (Jafari Raad and Hassanzadeh, 2015). In addition, there is a significant viscosity variation in some of analogue systems (Sun and Teja, 2004; Tsierkezos and Molinou,

1999). Furthermore, analogue fluids and water are fully miscible and hence cannot capture the impacts of capillarity on the convective dissolution of $CO_2$/water system, which is a partially miscible system.

One of the analogue systems that has been recently used to mimic $CO_2$/water is a mixture of methanol and ethylene glycol (EG-MeOH)/water (MacMinn et al., 2012; Neufeld et al., 2010). EG-MeOH/water mixtures used in the experimental studies of the convective dissolution result in non-monotonic density profiles. Stability behaviour of fluids with non-monotonic density profiles has been addressed in several physical and chemical processes such as buoyancy-driven flows induced by chemical reaction and/or diffusion in multi-species miscible or immiscible systems (Loodts et al., 2014; Trevelyan et al., 2011, 2015) and natural convection of water near its density maximum (Kim and Choi, 2014; Moore and Weiss, 1973). However, none of the previous studies presented scaling relations for onset of convective instabilities for a diffusive boundary layer of binary species.

Important questions that need to be addressed with regard to the EG-MeOH/water system are: does EG-MeOH/water resemble hydrodynamics of $CO_2$/water system? How does the growth of the convective instabilities depend on the composition of EG-MeOH? In this study, we report results of the linear stability analysis (LSA) of a gravitationally unstable diffusive boundary layer and perform direct numerical simulations of the convective dissolution involved in solubility trapping mechanism to address these questions. Using linear stability analysis and direct numerical simulations we have shown that the onset of convective instabilities and the mixing dynamics of $CO_2$/water and EG-MeOH/water systems are different. In particular, it is shown that the binary nature of EG-MeOH and the time evolution of the mixture density profile during the dissolution need to be considered.

## 3.3 Mathematical Formulation

### 3.3.1 Governing equations

We consider a two-dimensional, homogeneous and isotropic porous layer of thickness, $H$, saturated with quiescent pure water. The model is considered to be laterally infinite and flow and solute transport are assumed to take place at isothermal condition. No-flow boundary conditions are considered at the top and bottom of the domain with respect to pressure. A no-flux boundary

condition is maintained at the bottom of the domain while a constant concentration of EG-MeOH is set at the top of the domain with respect to the mass transport. Under the assumption of single-phase flow the interface between $CO_2$ and water has been considered sharp with a constant concentration (Riaz et al. 2006, Emami-Meybodi and Hassanzadeh, 2015). Using the Boussinesq approximation, assuming an incompressible fluid, and neglecting viscosity variability, cross diffusion of species and dispersion, the governing equations of non-reactive single phase flow and transport in a porous medium can be written as follows (Bear, 1972):

$$D_i \phi \nabla^2 \chi_i - \mathbf{v} \cdot \nabla \chi_i = \phi \frac{\partial \chi_i}{\partial t}; \tag{3.1a}$$

$$\nabla \cdot \mathbf{v} = 0; \tag{3.1b}$$

$$\mathbf{v} = -\frac{k}{\mu}(\nabla p - \rho g \nabla z), \tag{3.1c}$$

where $\mathbf{v}(u,v)$ is the Darcy velocity vector, $p$ is the pressure, $\chi$ is the mole fraction, $\mu$ is the viscosity, $t$ is the time, $k$ is the permeability, $\phi$ is the porosity, $g$ is the gravitational acceleration, $z$ is the vertical coordinate and positive downwards, $D$ is the effective molecular diffusion coefficient in porous media and assumed to be independent of concentration for dilute solutions, and subscript $i$ denotes the species index with $i = 1$ for ethylene glycol (EG) and $i = 2$ for methanol (MeOH). The aqueous phase density is therefore a function of both species concentration (i.e, $\rho = f(\chi_1, \chi_2)$).

For a purely diffusive process as a base state and prior to the onset of convection, the following governing equation can be obtained from the general mass conservation Equation (3.1a):

$$r_{Di} \frac{\partial^2 \hat{\chi}_{0i}}{\partial \hat{z}^2} = \frac{\partial \hat{\chi}_{0i}}{\partial \hat{t}}, \tag{3.2}$$

where subscript 0 denotes the base state condition. Vertical coordinate $z$, time, and species mole fractions are scaled by thickness of the porous layer ($H$), EG diffusion time scale ($H^2/D_1$) and mole fraction of EG in the EG-MeOH solution, $\chi_1^s$ ($\hat{\chi}_{0i} = \chi_{0i}/\chi_1^s$), respectively. We also scaled the effective molecular diffusion coefficient by EG molecular diffusion coefficient ($r_{Di}=D_i/D_1$).

The base state solution can be obtained using the initial and boundary conditions $\hat{\chi}_{0i}(\hat{z}, \hat{t}=0) = 0$ and, $\hat{\chi}_{0i}(0,\hat{t}) = \chi_i^s / \chi_1^s = r_{ci}$, $\partial \hat{\chi}_{0i}(1,\hat{t})/\partial \hat{z} = 0$, respectively, as given by:

$$\hat{\chi}_{0i} = r_{ci}\left[1 - \frac{2}{\pi}\sum_{n=1}^{\infty}\frac{1}{\lambda_n}\sin\left(\lambda_n \pi \hat{z}\right)\exp\left(-\lambda_n^2 \pi^2 r_{Di}\hat{t}\right)\right], \tag{3.3}$$

where $\lambda_n=(2n\text{-}1)/2$, $r_{c1}=1$, $r_{c2}=r_c$, $r_{D1}=1$, $r_{D2}=r_D$. For the system of interest (i.e., EG-MeOH/water) $r_D=1.38$ can be obtained from experimental data (Derlacki et al., 1985; Fernández-Sempere et al., 1996; Ternström et al., 1996).

### 3.3.2 Base state density profiles

Mixtures of EG-MeOH solutions with 60-70 wt.% of EG (at 25°C) when mixed with water result in mixture that is heavier than the original EG-MeOH solution and pure water. This range varies depending on temperature. This property of EG-MeOH solutions with water has been used to utilize EG-MeOH/water mixtures as an analogue system for experimental studies of $CO_2$ convective dissolution (MacMinn et al., 2012; Neufeld et al., 2010).

Experimental density data of EG-MeOH/water ternary system at 25°C (Conrad et al., 1952; Lee et al., 1990; Mikhail and Kimel, 1961; Ray and Nemethy, 1973) can be correlated using $\rho = \rho_b(1+\sum_{j=1}^{3}\sum_{i=1}^{2}\beta_{ij}\chi_i^j)$ where $\rho_b$ is the pure water density and $\beta_{ij}$ values are the coefficients of density variation with concentration given by: $\beta_{11}$= 0.381016, $\beta_{21}$= –0.251612, $\beta_{12}$= –0.446894, $\beta_{22}$=0.037877, $\beta_{13}$=0.184493, $\beta_{23}$=0.002322. This density function predicts the mixture density with a maximum error of less than 1%. Figure 3.1 shows density of various EG-MeOH solutions with different EG wt.% mixed with water versus EG-MeOH weight fraction at 25°C obtained using the above mentioned density function.

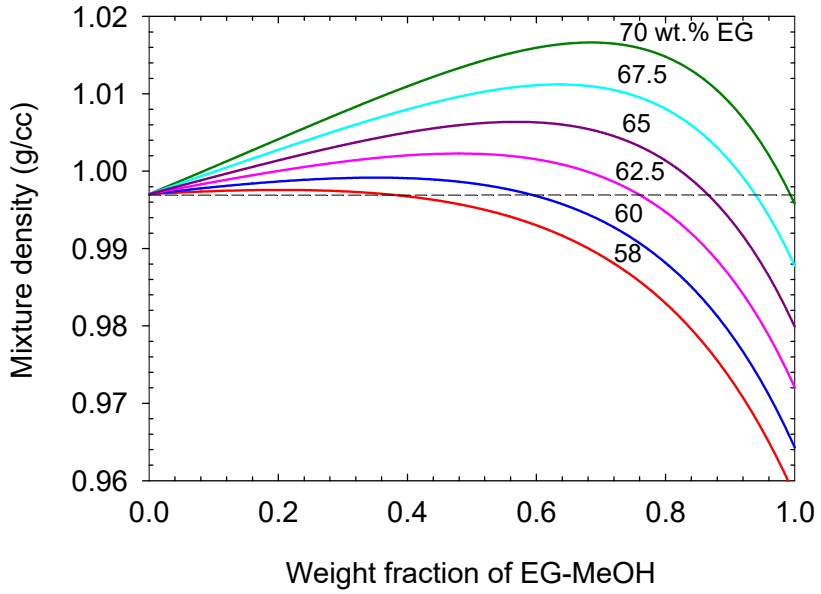


**Figure 3.1**: Density of EG-MeOH solutions mixed with water versus weight percent of EG-MeOH for various EG wt.% at 25°C.

The ternary density function can be written in dimensionless form as given by $\hat{\rho}=\sum_{j=1}^{3}\sum_{i=1}^{2} r_{\beta ij}\hat{\chi}_i^j$ where $\hat{\rho}=(\rho-\rho_b)/\beta_1\chi_1^s\rho_b$ and $r_{\beta 11}=1$, $r_{\beta 21}=\beta_{21}/\beta_{11}$, $r_{\beta 12}=\beta_{12}/\beta_{11}\chi_1^s$, $r_{\beta 22}=\beta_{22}/\beta_{11}\chi_1^s$, $r_{\beta 13}=\beta_{13}/\beta_{11}\chi_1^{s2}$, and $r_{\beta 23}=\beta_{23}/\beta_{11}\chi_1^{s2}$. The interface density is defined as the density difference at $z$=0 and the original water as described by: $\hat{\rho}_{\text{int}}=\sum_{j=1}^{3}\sum_{i=1}^{2} r_{\beta ij}r_{ci}^i$.

The vertical density gradient ($\partial\hat{\rho}/\partial\hat{z}$) can be obtained using the base state solutions at the early time, $\hat{\chi}_{0i}=r_{ci}erfc(\hat{z}/\sqrt{4r_{Di}\hat{t}})$, as given by:

$$\frac{\partial\hat{\rho}}{\partial\hat{z}}=-\sum_{j=1}^{3}\sum_{i=1}^{2}\frac{jr_{\beta ij}r_{ci}^j}{\sqrt{\pi r_{Di}^{i-1}\hat{t}}}\exp\left(-\frac{\hat{z}^2}{4r_{Di}^{i-1}\hat{t}}\right)\left\{erfc\left(\frac{\hat{z}}{\sqrt{4r_{Di}^{i-1}\hat{t}}}\right)\right\}^{j-1}, \tag{3.4}$$

where $r_c$=$r_{c2}$ and $r_D$=$r_{D2}$.

For a mixture of EG-MeOH /water, the evolution of the base state density profile may have extremum (local minimum or maximum). Therefore, the behaviour of the density profile with depth needs to be examined using Equation (3.4). The dimensionless density ( $\hat{\rho}$ ) and its gradient ( $\partial\hat{\rho}/\partial\hat{z}$ ) at the interface, and roots of the first and second derivatives of the density profile determine the shape of the density profile. The interface density, $\hat{\rho}(z=0)$, for all EG wt.% shown in Figure 3.1 is negative while $\partial\hat{\rho}/\partial\hat{z}$ at $\hat{z}=0$ is positive. This suggests a stable diffusive layer on the top of the domain (see Figure 3.2). The first derivative of the density profiles has no roots for 58 and 60 wt.% of EG while it has two roots for the other EG solutions (62.5-70%) signifying occurrence of two extrema as shown in Figure 3.2. While at some concentration of EG-MeOH mixture densities for 58 and 60 wt.% of EG is larger than both water and EG-MeOH (see Figure 3.1) the associated dynamic density profiles do not demonstrate extremum since $r_D$ >1. The second derivative of the density profile has two roots for all EG wt.% indicating presence of two inflection points. Figure 3.2 shows density profiles versus depth for different EG wt.%. Density profile for $CO_2$/water is also shown for comparison. The local maximum (first peak from top) in the density profiles shown in Figure 3.2 is as a result of formation of a stable diffusive boundary layer. The local minimum (second peak from top) occurs due to higher value of diffusion coefficient for MeOH compared with EG ($r_D$=1.38). Thus, the diffusion front of MeOH is ahead of EG decreasing the local solution density. The density profile for $CO_2$/water lacks these features and later, we will show that the dissimilarity between the density profiles can have a great impact on the onset of convective instabilities and subsequent mixing.

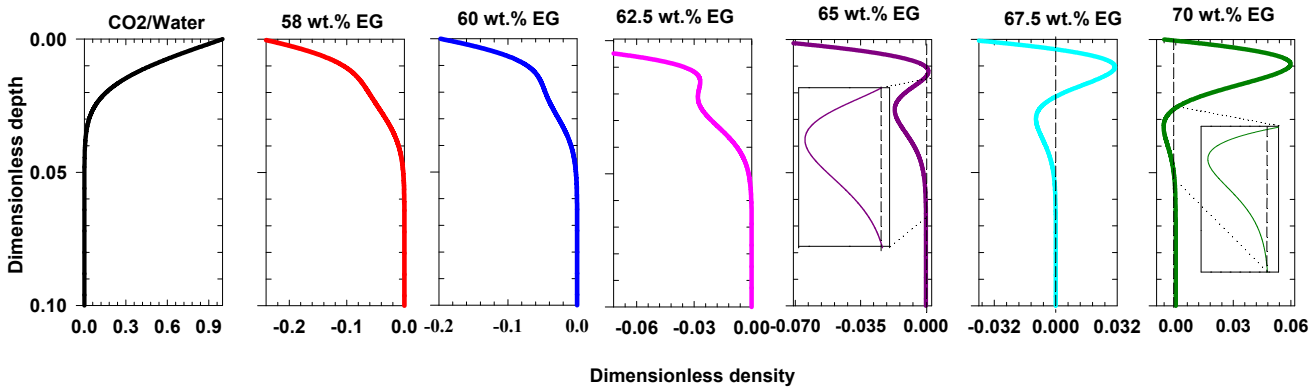


**Figure 3.2**: Density profiles for different EG wt. % in EG-MeOH solutions as analogue systems at $\hat{t} = 1 \times 10^{-4}$. Density profile for $CO_2$/water is also shown for comparison; for $CO_2$/water $r_{\beta ij}$=0, except $r_{\beta 11}$=1.

### 3.3.3 Linear stability analysis

A linear stability analysis using quasi-steady state approach (QSSA) is used to study the growth of perturbation and consequently to determine the onset of convective instabilities. To conduct a linear stability analysis, the governing equations of flow and transport given in Equation (3.1) are perturbed using $\mathbf{s} = \mathbf{s}_0 + \mathbf{s}'$ where $\mathbf{s}$=$\mathbf{s}$[p,$\mathbf{v}$,$\chi_1$,$\chi_2$,ρ]. The fluid is stationary at the early time and the concentrations, velocity, and density base states can be described by $\partial^2 \hat{\chi}_{0i} / \partial \hat{z}^2 = r_{Di} \partial \hat{\chi}_{0i} / \partial \hat{t}$, $\mathbf{v}_0$=0, and $\hat{\rho}_0 = \sum_{j=1}^{3} \sum_{i=1}^{2} r_{\beta ij} \hat{\chi}_{0i}^{j}$, respectively. Substituting the perturbed variables into the flow and transport equations, linearizing in perturbations and after simplification, we obtain the following perturbed equations:

$$\nabla^2 v' = Ra \frac{1}{\sum_{j=1}^{3} \sum_{i=1}^{2} r_{\beta ij} r_{ci}^{j}} \sum_{j=1}^{3} \sum_{i=1}^{2} j r_{\beta ij} \chi_{0i}^{j-1} \frac{\partial^2 \chi_i'}{\partial x_D^2}, \tag{3.5a}$$

$$r_{Di} \nabla^2 \chi_i' - v' \frac{\partial \chi_{0i}}{\partial z} = \frac{\partial \chi_i'}{\partial t}, \tag{3.5b, c}$$

where the velocity perturbation is scaled by $\phi D_1/H$, $\nabla^2 = \nabla_{xy}^2$, Ra is the Rayleigh number $\mathrm{Ra} = \dfrac{kgH\rho_b\beta_{11}}{\mu_0\varphi D_1}\sum_{j=1}^{3}\sum_{i=1}^{2} r_{\beta ij} r_{ci}^{j}$ and the hats (^) are dropped for convenience.

The perturbed velocity and concentration are expressed as $[\chi'_1, \chi'_2, v'] = [\chi_1^*, \chi_2^*, v^*](z,t_0)e^{-i\kappa x+\omega t}$ where $\kappa$ and $\omega$ are the perturbation wave-number and growth rate, respectively. Using Equation (3.5) we obtain

$$\frac{\partial^2 v^*}{\partial z^2} - \kappa^2 v^* = \mathrm{Ra}(-\kappa^2)\frac{1}{\sum_{j=1}^{3}\sum_{i=1}^{2} r_{\beta ij} r_{ci}^{j}}\sum_{j=1}^{3}\sum_{i=1}^{2} j r_{\beta ij}\chi_{0i}^{j-1}\chi_i^*, \tag{3.6a}$$

$$r_{Di}\frac{\partial^2 \chi_{Di}^*}{\partial z_D^2} - \kappa^2 c_{Di}^* - v_D^*\frac{\partial \chi_{0i}}{\partial z} = \omega\chi_i^*, \tag{3.6b, c}$$

where $r_{D1}$=1 and $r_{D2}$=$r_D$. The boundary conditions for the perturbed flow and concentration are given by $\chi_i^*(0) = 0$, $\partial\chi_i^*(1)/\partial z = 0$, and $v^*(0) = v^*(1) = 0$.

The growth of perturbation can be assumed to be much faster than the development of the base state and thus the quasi-steady-state approximation (QSSA) (Tan and Homsy, 1986) is applicable. This approach has been widely used in the linear stability analysis of gravitationally unstable diffusive boundary layers (Ghesmat et al., 2011; Riaz et al., 2006; Trevelyan et al., 2011). Limitations of the QSSA have been discussed elsewhere (Trevelyan et al., 2011). Using QSSA, $\partial\chi_{0i}/\partial z$ in Equations (3.6b) and (3.6c) can be evaluated at time $t_0$ or so called "frozen time" during the growth of perturbations.

It is worth noting that Equation (3.6a) recovers $CO_2$/water system when $r_{\beta ij}$=0, except $r_{\beta 11}$=1. The above system of Equations (3.6a-c) are solved numerically using a second-order finite difference method to find the growth rate, ω, as a function of wave-number, $\kappa$. The following eigenvalue problem can be obtained using the discretized equations.

$$[\mathbf{A}_v][\mathbf{v}^*] = \mathrm{Ra}(-\kappa^2)\frac{1}{L}\sum_{i=1}^{2} M_i\chi_i^*\ , \tag{3.7a}$$

$$r_{Di}[\mathbf{A}_c][\boldsymbol{\chi}_i^*] - [\mathbf{v}^*]\frac{\partial\boldsymbol{\chi}_{0i}}{\partial z} = [\boldsymbol{\omega}][\boldsymbol{\chi}_i^*]\ , \tag{3.7b,c}$$

where $M_i = \sum_{j=1}^{3} j r_{\beta ij} \chi_{0i}^{j-1}$, $L = \sum_{j=1}^{3}\sum_{i=1}^{2} r_{\beta ij} r_{ci}^{j}$, $\mathbf{A}_v = (\mathbf{D}_v - \kappa^2 \mathbf{I})$, $\mathbf{A}_c = (\mathbf{D}_c - \kappa^2 \mathbf{I})$, $\mathbf{D}_v$, and $\mathbf{D}_c$ are coefficient matrices based on central discretization of the second derivatives and **c** and **v** are vectors containing the unknown variables at the discrete nodes. The subscripts *v* and *c* refer to vertical velocity and concentration, respectively. Equations (3.7a-c) can be rearranged to obtain:

$$[\mathbf{v}^*] = \mathrm{Ra}(-\kappa^2)[\mathbf{A}_v]^{-1}\left[\frac{M_1}{L}\chi_1^* + \frac{M_2}{L}\chi_2^*\right], \tag{3.8a}$$

$$r_{Di}[\mathbf{A}_c][\chi_i^*] - \left\{\mathrm{Ra}(-\kappa^2)[\mathbf{A}_v]^{-1}\left[\frac{M_1}{L}\chi_1^* + \frac{M_2}{L}\chi_2^*\right]\right\}\left[\frac{\partial \chi_{0i}}{\partial z}\right] = [\boldsymbol{\omega}][\chi_i^*]. \tag{3.8b,c}$$

The eigenvalue Equations (3.8b) and (3.8c) can be rewritten in matrix form;

$$\begin{bmatrix} [\mathbf{A}_c] + \frac{M_1 \mathrm{Ra}\,\kappa^2}{L}[\mathbf{A}_v]^{-1}\left[\frac{\partial \chi_{01}}{\partial z}\right] & \frac{M_2 \mathrm{Ra}\,\kappa^2}{L}[\mathbf{A}_v]^{-1}\left[\frac{\partial \chi_{01}}{\partial z}\right] \\ \frac{M_1 \mathrm{Ra}\,\kappa^2}{L}[\mathbf{A}_v]^{-1}\left[\frac{\partial \chi_{02}}{\partial z}\right] & r_D[\mathbf{A}_c] + \frac{M_2 \mathrm{Ra}\,\kappa^2}{L}[\mathbf{A}_v]^{-1}\left[\frac{\partial \chi_{02}}{\partial z}\right] \end{bmatrix}\begin{bmatrix}\chi_1^* \\ \chi_2^*\end{bmatrix} - [\boldsymbol{\omega}]\begin{bmatrix}\chi_1^* \\ \chi_2^*\end{bmatrix} = 0. \tag{3.9}$$

To find the growth rate, ω, for an assigned wave-number, $\kappa$, and Ra number at time $t_0$, the above problem is solved numerically using the same procedure addressed in previous studies (Emami-Meybodi and Hassanzadeh, 2013). The maximum eigen-value of the coefficient matrix for given wavenumbers is considered as the growth rate, ω. The onset of instability is evaluated based on the obtained growth rate of the initial perturbations for given wave-numbers, using dispersion curves. The time at which the growth rate turns positive at a given wave-number represents the onset of instability.

Analytical solution at the early time ($t \to 0$) for the special case of a step change in the concentration profile was used to verify the computational algorithm. For such a case, it can be shown that $\omega = -\kappa^2$ (Ghesmat et al., 2011; Tan and Homsy, 1986). The good agreement between results of the developed algorithm and the analytical solution $\omega = -\kappa^2$ at $\hat{t}_{01} = 8\times10^{-5}$, shown by open circles in Figure 3.3(a), indicates validity of the analysis.

## 3.4 Results and Discussion

### 3.4.1 Stability analysis

We present results of linear stability analysis for $CO_2$/water and EG-MeOH/water systems characterized by monotonic and non-monotonic density profiles, respectively. Figure 3.3 shows the growth rate of perturbations for $CO_2$/water and EG-MeOH/water mixtures at different times. The results shown in Figure 3.3 demonstrate a clear difference between EG-MeOH/water and $CO_2$/water systems. These results suggest that the onset of convective instabilities for the two systems can be different. To further clarify this finding, results of the onset of the convective instabilities versus *Ra* for various mixtures of EG-MeOH are shown in Figure 3.4. The results for different compositions of EG-MeOH recover the well-known scaling of $\hat{t}_c = aRa^{-2}$, in which the prefactor a is a constant. The result for $CO_2$/water is also shown in Figure 3.4, which is in close agreement with previous findings (Bestehorn and Firoozabadi, 2012; Ennis-King et al., 2005; Hassanzadeh et al., 2006; Meulenbroek et al., 2013; Slim, 2014). Figure 3.4 shows that the prefactor a depends on the composition of the EG-MeOH solution. The results reveal that an EG-MeOH mixture with 62.5 wt.% EG results in a scaling relation with a prefactor of a ~ 870 as compared to $a \sim 56$ for $CO_2$/water pair, indicating a significant delay in the onset of instabilities at a given Rayleigh number. This mixture results in a marginally non-monotonic density profile during the growth of the diffusive boundary layer with a negative peak density (see Figure 3.2). On the other hand, a mixture of EG-MeOH with 67.5 wt.% EG results in non-monotonic density profile with a positive peak density (see Figure 3.2) with scaling prefactor of a ~ 6 suggesting a much faster onset of the convective instabilities. At a given Rayleigh number, the onset of instabilities for a mixture of EG-MeOH with 67.5 wt.% appears to be around one order faster than $CO_2$/water pair. An EG-MeOH mixture with 65 wt.% EG results in a non-monotonic density profile with a peak dimensionless density close to zero and scaling prefactor of a ~ 82. It is worth noting that an EG-MeOH mixture with 65.39 wt.% EG results in the same scaling prefactor as of $CO_2$ while the base state density profile for $CO_2$ is evidently different. However, this resemblance does not guarantee the same dynamic for the two systems beyond the onset time. These findings highlight the importance of the proper choice of an analogue system in experimental studies for representation of $CO_2$ convective dissolution behaviour. In particular, inconsistencies reported in

scaling of convective flux in several experimental studies (Backhaus et al., 2011; Hidalgo et al., 2012; MacMinn et al., 2012; MacMinn and Juanes, 2013; Neufeld et al., 2010; Tsai et al., 2013) with the classical scaling (Hidalgo et al., 2012; Nield and Bejan, 2006; Slim et al., 2013) highlight the importance of choice of analogue fluids.

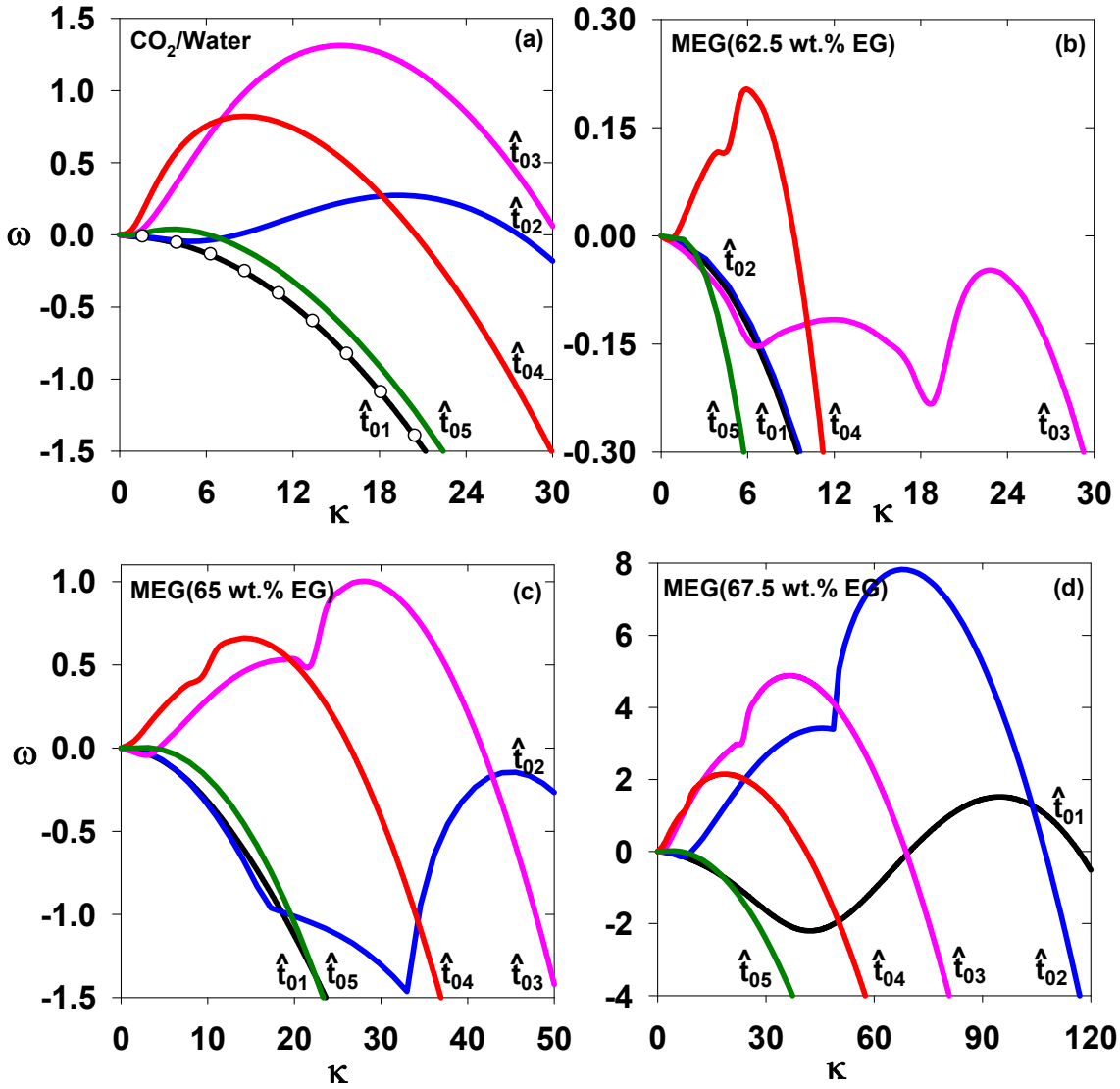


**Figure 3.3**: Rate of growth of perturbations versus wave-number at different frozen times of $\hat{t}_{01}=8\times10^{-5}$, $\hat{t}_{02}=8\times10^{-4}$, $\hat{t}_{03}=8\times10^{-3}$, $\hat{t}_{04}=8\times10^{-2}$, $\hat{t}_{05}=8\times10^{-1}$ (a) $CO_2$/water, and (b), (c), and (d) EG-MeOH/water with EG wt.% of 62.5, 65, and 67.5, respectively. Open circles are the results of the analytical solution ($\omega=-\kappa^2$) as compared with the results of the stability analysis shown by line.

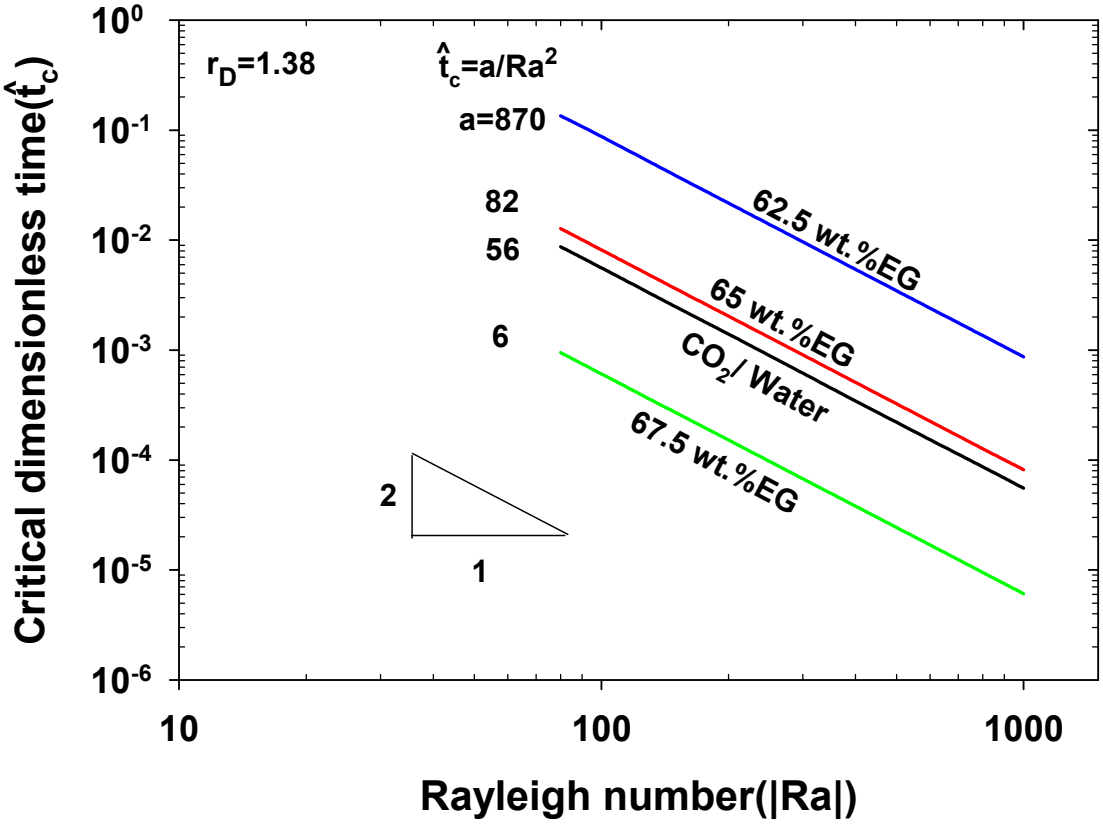


**Figure 3.4**: Onset of convective instabilities versus Rayleigh number for different compositions of EG wt.% in EG-MeOH mixture.

### 3.4.2 Nonlinear simulations

Direct numerical simulations have been conducted to examine the nonlinear behaviour of convective mixing in $CO_2$/water and the analogue systems. Equations. (3.1a-c) were solved numerically using a well-known IMPEC approach where pressure is considered implicit while mole fractions are treated explicitly. Details of the numerical approach and controls on accuracy of the numerical solutions have been reported in previous publications (Coats, 1969; Emami-Meybodi and Hassanzadeh, 2015; Emami Meybodi and Hassanzadeh, 2013).

The 2D numerical simulations were conducted to evaluate the nonlinear dynamics of mixing for $CO_2$/water and analogue systems. The direct numerical simulations were performed at |Ra|=600,

using the same parameters defined in the linear stability analysis section. Figure 3.5 shows the time evolution of concentration distribution for the $CO_2$/water system and EG-MeOH/water systems with 65 wt. % and 67.5 wt. % of EG. As predicted by the linear stability analysis, these three systems exhibit different instability behaviour followed by different fingering pattern. Consistent with the results of the stability analysis, the dynamics of EG-MeOH/water systems change significantly as the mass fraction of EG in EG-MeOH mixture is increased. The EG-MeOH/water systems with 67.5 wt. % of EG results in faster development of the boundary layer instabilities such that the growth rate of fingers is significantly stronger than those in EG-MeOH/water system with 65 wt.% of EG and $CO_2$/water system. Furthermore, it can be observed that the fingering pattern in the EG-MeOH/water systems with 67.5 wt. % of EG is significantly vigorous than those in the EG-MeOH/water system with 65 wt. % of EG and $CO_2$/water system. In the EG-MeOH/water system with 65 wt. % of EG fingers evolve in the form of sluggish convective fingers due to damping effect of the upper thick stable region. In this system fingers grow nearly independent from each other with minimal interaction.

Numerical simulations for three different mixtures of EG-MeOH/water with 62.5 wt. %, 65 wt. % and 67.5 wt. % of EG have been conducted and consistent with the results of stability analysis in all cases a linear scaling was obtained for the onset time. As it was expected and has been previously reported (Emami-Meybodi et al., 2015; Hassanzadeh et al., 2007) the linear stability analysis shows smaller onset time as compared to the numerical simulations. This deviation originates from the fact that definition of the onset time in linear stability analysis and numerical simulation approaches are different. In the case of linear stability analysis, the onset time is based on the growth rate of perturbations once turn positive. While, the onset time in numerical simulation has been defined as the time when growth of perturbations is visible in the form of fingers of dense fluid penetrating into less dense fluid or sometimes when pure diffusive mixing and convective mixing curves deviates from each other.

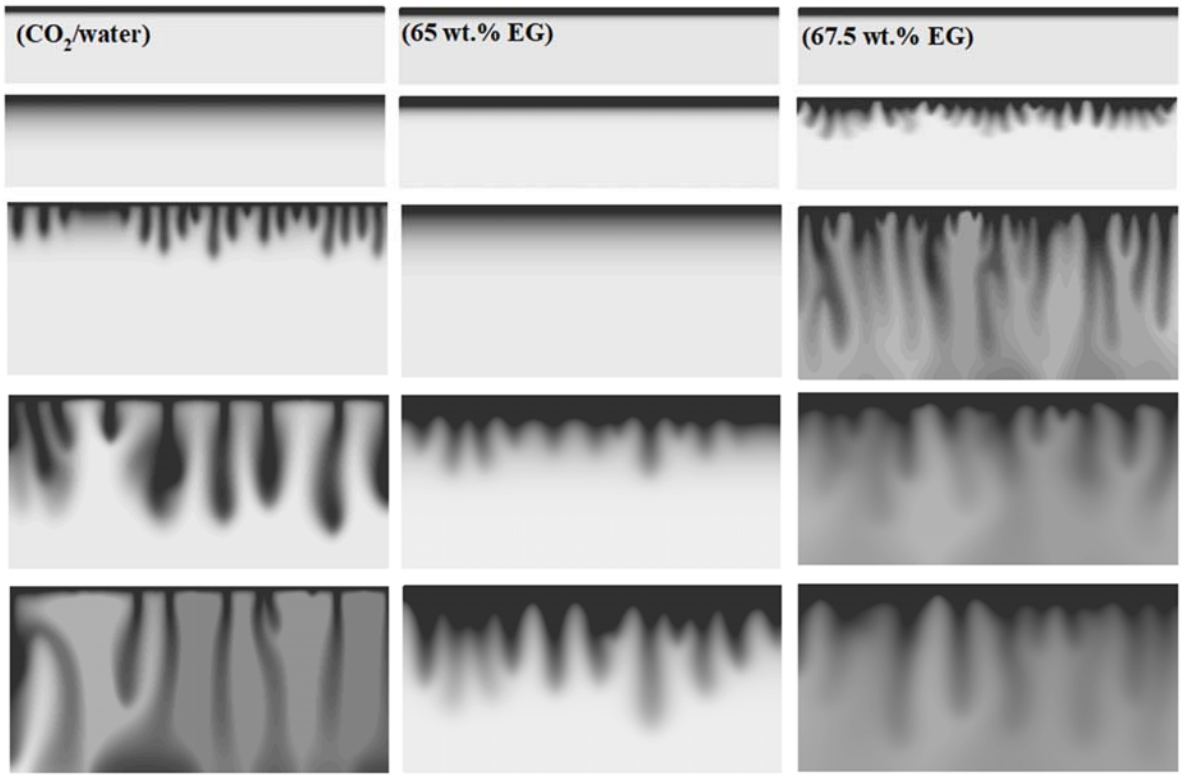


**Figure 3.5**: Concentration distribution at different times of $\hat{t}_{01} = 0.0013$ , $\hat{t}_{02} = 0.004$, $\hat{t}_{03} = 0.011$, $\hat{t}_{04} = 0.018$, and $\hat{t}_{05} = 0.025$ for |Ra|=600 representing $CO_2$/water system (left panel), EG-MeOH/water system with 65 wt. % of EG. (middle panel), and EG-MeOH/water system with 67.5 wt. % of EG. (right panel).

To better understand dynamics of the mixing process beyond the onset of instability, we studied the dissolution flux of the four cases considered in the stability analysis section. Figure 3.6 shows the numerical measurement of dissolution flux as a function of time, both in dimensionless form. The dissolution flux per unit area is expressed as the cumulative dissolution of mass in water (Emami-Meybodi et al., 2015):

$$F(\hat{t}) = \frac{1}{A}\frac{d}{d\hat{t}}\int_V C(\hat{t})dV \ , \tag{3.10}$$

where $V$ is the domain pore volume, $A$ is the cross sectional area of the interface and $C$ is total concentration of species (EG and MeOH) in the entire domain.

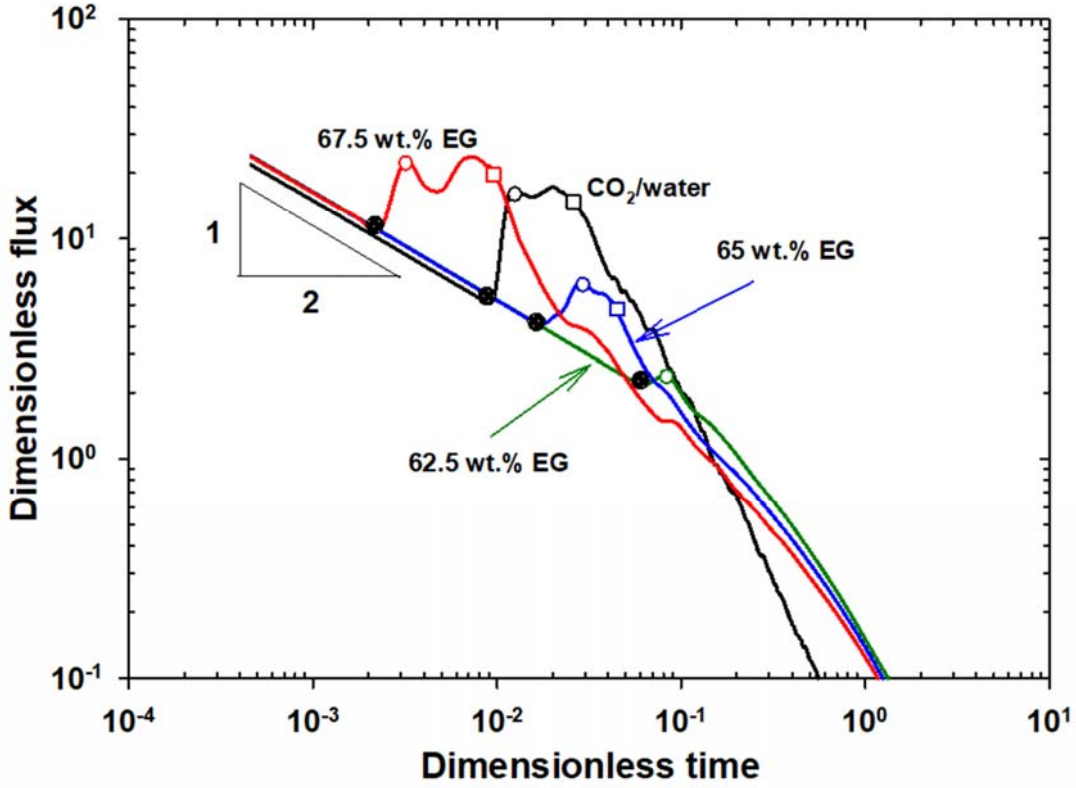


**Figure 3.6**: Dimensionless dissolution flux versus dimensionless time for $CO_2$/water and the EG-MeOH/water systems with |Ra|=600.

Consistent with the results of the stability analysis, the dissolution flux for $CO_2$/water system are clearly different than those of the analogue systems. As illustrated by concentration distribution maps (see Figure 3.5), the time of the onset of convection when the finger like structures form (solid black circle symbols shown in Figure 3.6) is significantly different for various systems. For EG-MeOH/water systems, the time of the onset of convection, which is marked by a sharp increase in the dissolution flux, increases as EG fraction of EG-MeOH solution decreases. Furthermore, the maximum flux values (open circle symbols shown in Figure 3.6) strongly depend on the EG fraction of EG-MeOH solution such that the systems with higher EG fraction results in a larger maximum flux. In addition, the start of shutdown regime (open square symbols shown in Figure 3.6) where the convective fingers touch the bottom boundary and the domain begins to saturate is accelerated by increase of EG fraction. As it was expected, $CO_2$/water system and the EG-MeOH/water systems show different dynamics especially in the onset of convection and the

maximum flux. These results are in qualitative agreement with the results of the linear stability analysis and assert that the EG-MeOH/water systems neither resemble the onset of instability nor the nonlinear mixing of $CO_2$/water system.

### 3.5 Summary and Conclusions

Stability behaviour of a gravitationally unstable diffusive boundary layer for EG-MeOH/water was studied. Possible base state densities during the growth of a gravitationally unstable diffusive layer for various EG wt.% were identified. Using the linear stability analysis and nonlinear simulations, we have shown that the composition of EG-MeOH mixture has a significant effect on the stability characteristics of the diffusive boundary layer and convective mixing beyond the onset of instability. Furthermore, scaling relations were developed that consider the effect of the composition of EG-MeOH on the onset of convective instabilities. The results have shown that the choice of an analogue system is critically important in correct representation of the onset of convective instabilities of $CO_2$/water and design of experiments. In particular, it was shown that EG-MeOH mixtures do not resemble the dynamics of $CO_2$/water system. The onset of convective instabilities for common EG-MeOH mixtures used in experiments was found to be strong function of the composition of EG in the EG-MeOH solution. These findings form a basis for further investigations in relation with the proper choice of analogue systems for design of the convective dissolution experiments.

### 3.6 Acknowledgements

The authors would like to thank two anonymous reviewers and the Associate Editor for their constructive comments, which have greatly improved our paper. This work was supported by a Discovery Grant from the Natural Sciences and Engineering Research Council of Canada (NSERC) and was enabled in part by support provided by WestGrid (www.westgrid.ca) and Compute Canada Calcul Canada (www.computecanada.ca). All data used in this work are available in open literature.

# Chapter 4: Does Impure $CO_2$ Impede or Accelerate the Onset of Convective Mixing in Geological Storage?*

## 4.1 Abstract

We have conducted a linear stability analysis to investigate the effect of impurity in $CO_2$ stream on the onset of convective mixing associated with impure carbon dioxide ($CO_2$) storage in deep saline aquifers. It has been generally thought that injecting impurities such as hydrogen sulphide ($H_2S$) and nitrogen ($N_2$) along with carbon dioxide impedes the buoyancy-driven instabilities resulting in less efficient $CO_2$ solubility trapping. In this work, we have for the first time shown that contrary to the original thought informed inclusion of an impurity such as $H_2S$ has a potential to accelerate the onset of buoyancy-driven instabilities and possibly leading to more effective solubility trapping. This result improves our understanding of the storage of impure $CO_2$ streams in deep saline aquifers and uncovers a new area for further research.

## 4.2 Introduction

Immediate reduction of greenhouse gas emissions is one of the most imperative environmental policies that has been proposed for global warming mitigation (EPA, 2014). It is believed that

* Jafari Raad, S. M., Hassanzadeh, H. (2016). Does impure $CO_2$ impede or accelerate the onset of convective mixing in geological storage? *International Journal of Greenhouse Gas Control*, *54*, 250–257. https://doi.org/10.1016/j.ijggc.2016.09.011.

anthropogenic carbon dioxide ($CO_2$) emissions level as a primary greenhouse gas, has caused climate change over the past decades and is expected to continue in the upcoming years (Metz et al., 2007). Capture and geological storage of $CO_2$ in deep geological formations has been recognized as an operative choice and a viable short term option to reduce $CO_2$ emissions over the next decades until new technologies can play an important role in significant reduction of the emissions (NACAP, 2012). Deep saline aquifers have been identified as the best alternative among geological formation for $CO_2$ storage due to their high capacity, proximity to emission sources, and worldwide availability (Metz et al., 2005). Once injected $CO_2$ spreads under a sealing rock or so called cap rock due to its buoyancy, gradually dissolving into the underlying formation brines. The formation brines saturated with $CO_2$ on top of an aquifer beneath a cap rock (or seal) is slightly denser than the original brine. This leads to buoyancy-driven instabilities in an aquifer. The $CO_2$ saturated brine sinks down due to gravitational instabilities and is continuously replaced by fresh brine from the bottom of the aquifer giving rise to convective dissolution. This process can result in enhanced dissolution of $CO_2$ into brine and consequently reduces the volume of free (or mobile) phase $CO_2$ under the seal leading to decrease of the $CO_2$ risk of leakage (Ennis-King and Paterson, 2005; Hassanzadeh et al., 2005). Figure 4.1 shows the schematic of the described phenomenon.

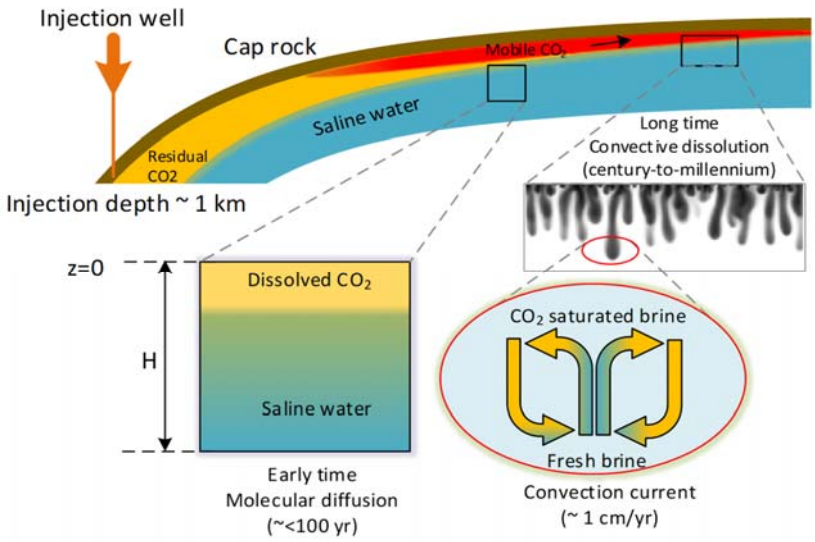


**Figure 4.1:** Schematic of mechanisms involved in long-term sequestration of $CO_2$ in deep saline aquifers.

Long term risk of leakage of free phase $CO_2$ is a great concern. Solubility trapping of $CO_2$ as a result of the convective dissolution has been recognized as one of the main mechanisms in reduction of free phase $CO_2$ and thus reducing risk of leakage from storage sites. The majority of previous works have been focused on pure $CO_2$ streams. One of the hindrances to progress in large scale implementation of $CO_2$ storage has been high cost of $CO_2$ capture from impure anthropogenic sources. Sequestering less pure $CO_2$ can potentially reduce the cost of capture process (Bachu et al., 2003; Ji and Zhu, 2013; Li et al., 2015; Nicot et al., 2013; Talman, 2015). However, transportation and compression of impure $CO_2$ streams continue to be challenging. Two abundant species which exist in impure anthropogenic $CO_2$ streams are $H_2S$ (oil and gas production) and $N_2$ (power plants). Dissolution of the both species ($N_2$ and $H_2S$) in water results in density decrease while $CO_2$ dissolution increases the aqueous phase density. Permitting impurities into $CO_2$ injection steams influences the density and viscosity of the mixture and then the shape of $CO_2$ migrating plume in subsurface (IEAGHG, 2011; Ji and Zhu, 2013). A few studies have been conducted to consider the effect of co-injection of some popular impurities with $CO_2$. However, recent interpretations and findings, which are merely based on the overall density reduction effect of such impurities, have led to an incorrect proposition that impure $CO_2$ stream leads to lower solubility trapping (Bachu, 2008; Ji and Zhu, 2013; Li et al., 2015; Wang et al., 2011). The notion of density reduction as a results of dissolution of impurities such as $H_2S$ and $N_2$ has been used to conclude that co-injection of $CO_2$ with impurity considerably retards the convective mixing and thus lowers the solubility trapping (Ji and Zhu, 2013; Li et al., 2015; Zhang et al., 2011).

An important physical mechanism that has been unnoticed in the previous studies is the role of molecular diffusion of impurities such as $H_2S$ and $N_2$ during the long-term storage process. Experimental data of molecular diffusion has indicated that diffusion of $H_2S$ and $N_2$ are different than $CO_2$. Such a difference in the molecular diffusion gives rise to a non-monotonic density profile during the dissolution process. Here we have shown that a diffusive boundary layer with a non-monotonic density profile resulted from the contrast in the diffusion of coefficients of species of an impure stream can become more unstable than that of pure $CO_2$ stream, leading to a faster onset of convective instability. Non-monotonic density profiles are known to arise in numerous physical and chemical settings. Examples are natural convection of water near its density maximum (Blake et al., 1984; Kim and Choi, 2014; Moore and Weiss, 1973) and density-driven

flows as a result of chemical reaction and/or diffusion in multi-component miscible or immiscible flows (Loodts et al., 2014, 2015, Trevelyan et al., 2011, 2015; Wylock et al., 2014). However, the important character of non-monotonic density profile in the context of impure $CO_2$ storage has not been discussed in the literature.

Precise determination of the effect of impurities on the fate of the injected $CO_2$ in subsurface requires investigations that take into account the hydrodynamics of the system. Does impure $CO_2$ impede the onset of convective dissolution? How does the growth of these convective instabilities depend on the impurities? Are we able to control the onset of convective dissolution in aquifers by proper selection of impurities? These are the questions that need further investigations. In particular, the time evolution of the non-monotonic density profile during dissolution of impure $CO_2$ in deep saline aquifers needs to be considered. In this work, we report results of linear stability analysis of a gravitationally unstable diffusive boundary layer to address some of these questions.

## 4.3 Mathematical Formulation

### 4.3.1 Governing equations

We consider a two-dimensional, homogeneous and isotropic physical porous model of thickness, H (see Figure 4.1 for domain geometry), saturated with quiescent water. The model is assumed to be laterally infinite and isothermal. No-flow boundary conditions are considered at the top and bottom of the domain with respect to pressure. A no-flux boundary condition is maintained at the bottom of the domain while constant concentrations of species are set at the top of the domain with respect to the mass transport.

Under the assumption of single-phase flow and consequently in the absence of capillarity, the interface between $CO_2$ and water has been considered sharp with a constant concentration (Emami-Meybodi and Hassanzadeh, 2015; Jafari Raad and Hassanzadeh, 2015; Riaz et al., 2006). Using the Boussinesq approximation and assuming an incompressible fluid and in the absence of viscosity variation, cross diffusion of species, and dispersion, the governing equations of non-reactive single phase flow and transport in a porous medium can be written as follows (Bear, 1972):

$$D_i\phi\nabla^2\chi_i - \mathbf{v}\cdot\nabla\chi_i = \phi\frac{\partial\chi_i}{\partial t}; \tag{4.1a}$$

$$\nabla\cdot\mathbf{v} = 0; \tag{4.1b}$$

$$\mathbf{v} = -\frac{k}{\mu}(\nabla p - \rho\mathbf{g}\nabla z), \tag{4.1c}$$

where, $\mathbf{v}(u,v)$, $p$, $\chi$, $\mu$ and $t$ are vector of Darcy velocity, pressure, mole fraction, viscosity and time, respectively. $k$ is the porous medium permeability, $\phi$ porosity, g the gravitational acceleration and z is the vertical coordinate and positive downwards. $D$ is the effective molecular diffusion coefficient in the porous media and assumed to be independent of concentration for dilute solutions. $i$ is the species index with $i$=1 for $CO_2$ and $i$=2 for impurity species. The aqueous phase density as a function of both species mole fraction (i.e, $\rho = f(\chi_1, \chi_2)$) is obtained from the linear regression of the predicted aqueous phase density using a thermodynamics model (Tsivintzelis et al., 2010; Zirrahi et al., 2012). The gas mixture composition range is chosen based on the licensed acid gas injection sites in western Canada. The licensed composition for acid gas injection varies between 2 to 85 mole % $H_2S$ with the rest being $CO_2$ (Stefan Bachu et al., 2003, 2008). According to the licensed disposal conditions of the injection sites, we assume representative temperature and pressure of 40°C and 100 bar, respectively. Figure 4.2 shows the aqueous phase density as a function of species mole fractions in the aqueous phase for three impure $CO_2$ streams, which clearly shows the linear behaviour. The mixture density can be expressed by $\hat{\rho} = \hat{\chi}_1 + r_\beta\hat{\chi}_2$ where $\hat{\rho} = (\rho - \rho_b)/\chi_1^s\beta_1\rho_b$, $\hat{\chi}_i = \chi_i/\chi_1^s$, $\chi_i$ is the species mole fraction with respect to total moles in the aqueous phase, and $\chi_1^s$ is the equilibrium mole fraction of $CO_2$ in the aqueous phase. $\rho_b$ is the water density, $\beta$ is expansion coefficient, which is defined as $\beta_i = \frac{1}{\rho_b}d\rho/d\chi_i$, and $r_\beta = \beta_2/\beta_1$ is the ratio of the coefficients of density variation of $H_2S$ (or $N_2$) to $CO_2$. The density at the interface ($z$=0) between the impure $CO_2$ and water is given by $\hat{\rho}_{\text{int}} = 1 + r_\beta r_c$, where $r_c = \chi_2^s/\chi_1^s$ and $\chi_2^s$ is the equilibrium mole fraction of $H_2S$ in the aqueous phase.

Values of $r_\beta$ corresponding to the above mentioned linear relation of aqueous phase density are obtained for a given operating temperature and pressure conditions. The density data for $CO_2$-$H_2S$/water fluid pair at 40 °C and 100 bar results in $r_\beta \approx -0.57$. Figure 4.3 shows $r_\beta$ values as a

function of temperature and pressure for the system of $CO_2$-$H_2S$/water. The density data for $CO_2$-$N_2$/water system at the above mentioned operational condition result in $r_\beta \approx$-1.53. It is worth noting that solubility of $N_2$ into water is significantly lower than that of $CO_2$. It will be shown that while $r_\beta$ for $CO_2$-$N_2$/water is high, the equilibrium mole fraction ratio, $r_c$, is very small leading to low $r_\beta r_c$ values where the hydrodynamic of the system remains very close to pure $CO_2$. Therefore, our focus in this work is on impure $CO_2$ streams containing $H_2S$.

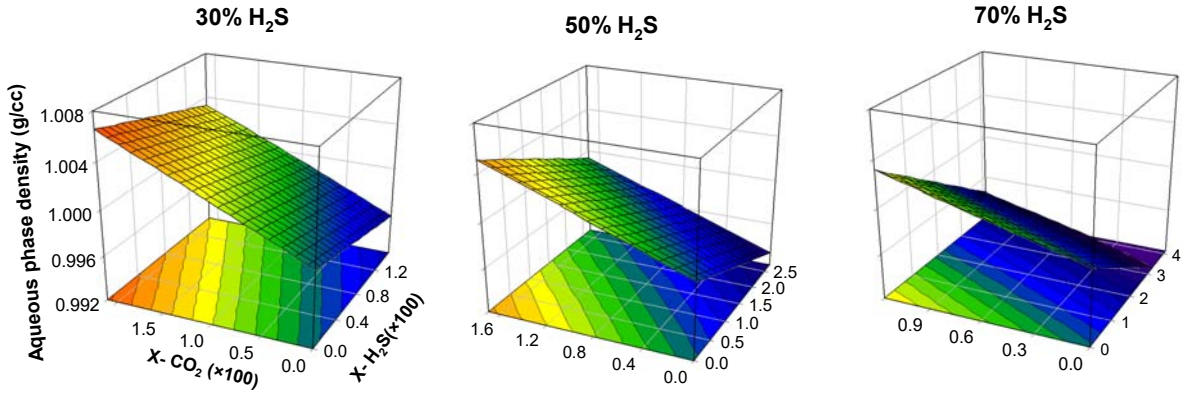


**Figure 4.2:** Aqueous phase density as a function of species mole fraction for three impure $CO_2$ streams at 40 °C and 100 bar, which can be described by $\rho = 0.998 + 0.3681\chi_{CO_2} - 0.2099\chi_{CO_2}$.

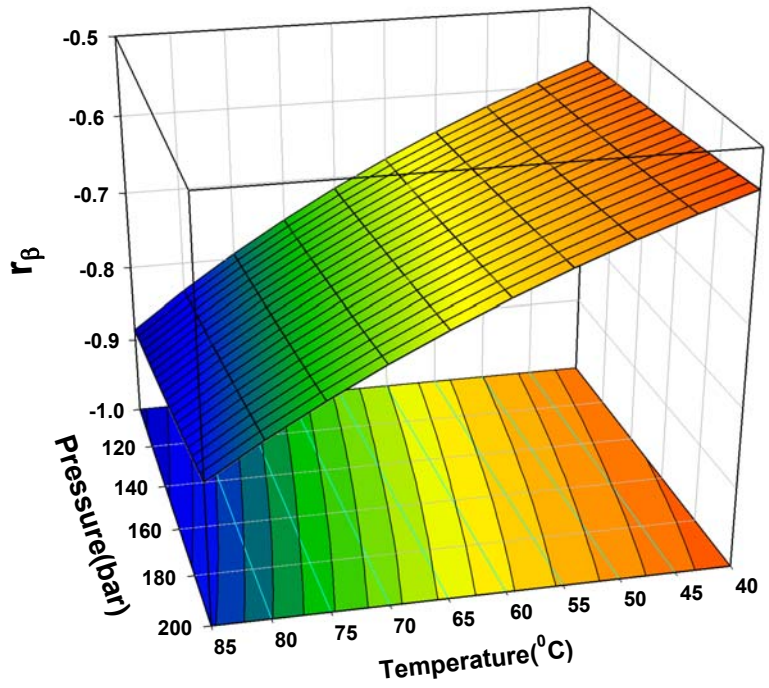


**Figure 4.3***:* $r_\beta$ as a function of temperature and pressure for $CO_2$-$H_2S$/water system, which can be described by $r_\beta = -5.283\times10^{-1} + 3.834\times10^{-4}T + 1.39\times10^{-4}P - 5.549\times10^{-5}T^2 + 8.833\times10^{-7}P^2$, where P is in bar and T in °C.

### 4.3.2 Base state density profiles

Dissolution of $CO_2$ in water slightly increases the aqueous phase density. Such a density increase creates a gravitationally unstable diffusive boundary layer on top of an aquifer, which may lead to convective dissolution resulting in improved storage efficiency. Presence of impurities in the injected stream affects stability of the boundary layer and consequently the $CO_2$ dissolution in aquifers. We study the time-dependent base state density profile as a function of the binary system physical properties to classify the regions with possibility of the boundary layer instability. Prior to the onset of convection, the system is initially stagnant ( $\mathbf{v} = 0$ ) and molecular diffusion is the dominant mechanism involved in the mass transfer of the dissolved species. For the diffusive mass

transfer mechanism as a base state of dissolution process the following dimensionless governing equation can be obtained from the general mass conservation Equation (4.1a):

$$\frac{\partial \hat{\chi}_{0i}}{\partial \hat{t}} = r_{Di} \frac{\partial^2 \hat{\chi}_{0i}}{\partial \hat{z}^2} \ , \tag{4.2}$$

where subscript 0 denotes the base state condition. Vertical coordinate $z$, time and species concentration are scaled by thickness of the porous layer (H), $CO_2$ diffusion time scale ($H^2/D_1$) and the concentration of $CO_2$ at the interface, $\chi_1^s$ ($\hat{\chi}_{0i} = \chi_{0i}/\chi_1^s$), respectively. We also scaled the effective molecular diffusion coefficient by $CO_2$ molecular diffusion coefficient ($r_{Di}=D_i/D_1$).

The base state solution can be obtained using the initial and boundary conditions $\hat{\chi}_{0i}(\hat{z},\hat{t}=0)=0$ and, $\hat{\chi}_{0i}(\hat{z}=0,\hat{t})=r_{ci}$, $\partial\hat{\chi}_{0i}(1,\hat{t})/\partial\hat{z}=0$, respectively, as given by:

$$\hat{\chi}_{0i} = r_{ci}\left[1-\frac{2}{\pi}\sum_{n=1}^{\infty}\frac{1}{\lambda_n}\sin(\lambda_n\pi\hat{z})\exp\left(-\lambda_n^2\pi^2 r_{Di}\hat{t}\right)\right], \tag{4.3}$$

where $\lambda_n=(2n-1)/2$, $r_{c1}=1$, $r_{c2}=r_c$, $r_{D1}=1$, $r_{D2}=r_D$.

The vertical density gradient can be obtained using the proposed density concentration relationship and the associated base state concentrations solutions for both species (e.g. $CO_2$ and $H_2S$) at the early time, $\hat{\chi}_{0i} = r_{ci}erfc(\hat{z}/\sqrt{4r_{Di}\hat{t}})$, as given by:

$$\frac{\partial\hat{\rho}}{\partial\hat{z}} = -\frac{1}{\sqrt{\pi\hat{t}}}\left\{\exp\left(-\frac{\hat{z}^2}{4\hat{t}}\right)+\frac{r_\beta r_c}{\sqrt{r_D}}\exp\left(\frac{\hat{z}^2}{4r_D\hat{t}}\right)\right\}, \tag{4.4}$$

For $CO_2$-$H_2S$ /water system $r_\beta<0$ ($\beta_1>0$, $\beta_2<0$), the density profile can have extremum (local minimum or maximum). Therefore, the behaviour of the density profile with depth needs to be inspected. By setting $\partial\hat{\rho}/\partial\hat{z}=0$ in Equation (4.4), rearranging and taking natural log of the resulting expression we arrive at $(1-r_D)\hat{z}^2/4r_D\hat{t}-\ln(-r_\beta r_c/r_D^{1/2})=0$. This is a quadratic equation in $\hat{z}$ with discriminant $\Delta=(1-r_D)\ln(-r_\beta r_c/r_D^{1/2})/r_D\hat{t}$. The existence of extremum in the density profile then can be identified using sign of the discriminant. In addition, for cases that results in a monotonic density profile possibility of an inflection point also needs to be determined. In such a

case, the second derivative of the density profile needs to be evaluated to determine the existence of an inflection point in the density profile. This again leads to a quadratic equation given by $(1-r_D)\hat{z}^2/4r_D\hat{t}-\ln(r_\beta r_c/r_D^{3/2})=0$ with $\Delta=(1-r_D)\ln(-r_\beta r_c/r_D^{3/2})/r_D\hat{t}$. The inflection point exists when $\Delta>0$. Table 1 shows a summary of various stability states arise for the evolving base state density profile. The interface density $\hat{\rho}_{\text{in}}$, is defined as the density difference at $z$=0 and the original water as described by: $\hat{\rho}_{\text{int}}=1+r_\beta r_c$. We study binary systems that cover six potentially unstable regions in the parameter space ($-r_\beta r_c$, $r_D$) shown in Figure 4.4. The entire parameter space is divided into two categories based on the molecular diffusion ratio, ($r_D$<1 and $r_D$>1). A case with $r_D$<1 represents an impurity with a molecular diffusion coefficient less than that of $CO_2$, while $r_D$>1 denotes an impurity with a molecular diffusion larger than that $CO_2$. Reported experimental molecular diffusion coefficients data for $CO_2$-$H_2S$/water system reveals that $r_D$ is always less than unity and varies from 0.66 to 0.99 for the given temperature range of 293-368 K (Tamimi et al., 1994).

Therefore, for a typical storage condition of 40 °C and 100 bar, the density profile can be defined using ($r_\beta$=-0.57, $r_D$~0.87). Figure 4.4 shows parameter space ($-r_\beta r_c$, $r_D$) for various stability regions and the associated density profiles. For binary systems with various $H_2S$ composition, the system density profile demonstrates both monotonic and non-monotonic behaviour, which cover the space parameter regions I, VII, II and III corresponding to their physical properties, as shown in Figure 4.4. The parameter space for $CO_2$/water system is given by ($-r_\beta r_c$, $r_D$) = (0,1) with a monotonic density profile similar to region I. Later, we will show that the dissimilarity exists between the two density profiles has a great impact on the evolution of convective instabilities.

Table **Error! No text of specified style in document.**1: Characteristics of various parameter space regions shown in Figure 4.4

| Region | $r_D$ | $\hat{\rho}_z\big\|_{\hat{z}=0}$ | Density profile | Stability | $\hat{\rho}_{int}$ |
|---|---|---|---|---|---|
| I | $(-r_\beta r_c)^2 < r_D \leq 1$ | decreasing | monotonic | unstable | + |
| II&III | $r_D<1$, $r_D<(-r_\beta r_c)^2$ | increasing | non-monotonic | unstable | ± |
| IV | $1 \leq r_D<(-r_\beta r_c)^2$ | increasing | monotonic | stable | - |
| V&VI | $r_D>1$, $r_D>(-r_\beta r_c)^2$ | decreasing | non-monotonic | unstable | ± |
| VII | $(-r_\beta r_c)^2<r_D<(-r_\beta r_c)^{2/3}$ | decreasing | monotonic/INF | unstable | + |
| VIII | $(-r_\beta r_c)^{2/3}<r_D<(-r_\beta r_c)^2$ | increasing | monotonic/INF | unstable | - |

In all non-monotonic cases with an extremum, the peak in the density profile occurs at $\hat{z}_p = 2\sqrt{r_D \hat{t}\, \ln(-r_\beta r_c / r_D^{1/2})/(1-r_D)}$ and the peak density is given by $\hat{\rho}_p = erfc\sqrt{r_D \ln(-r_\beta r_c / r_D^{1/2})/(1-r_D)} + r_\beta r_c erfc\sqrt{\ln(-r_\beta r_c / r_D^{1/2})/(1-r_D)}$, which is independent of time. It is expected that for large values of $-r_\beta r_c$ or $r_D$ the peak in density diminishes resulting in a monotonically increasing or decreasing density profiles, respectively. For an impure system with $r_\beta>0$ (e.g. $SO_2$, Ar, Kr), the density profile remains always monotonically decreasing with an inflection point at the interface.

The above classification demonstrates the important role of physical properties of impure streams on the growth of the diffusive boundary layer, which may potentially become unstable as discussed in the following section

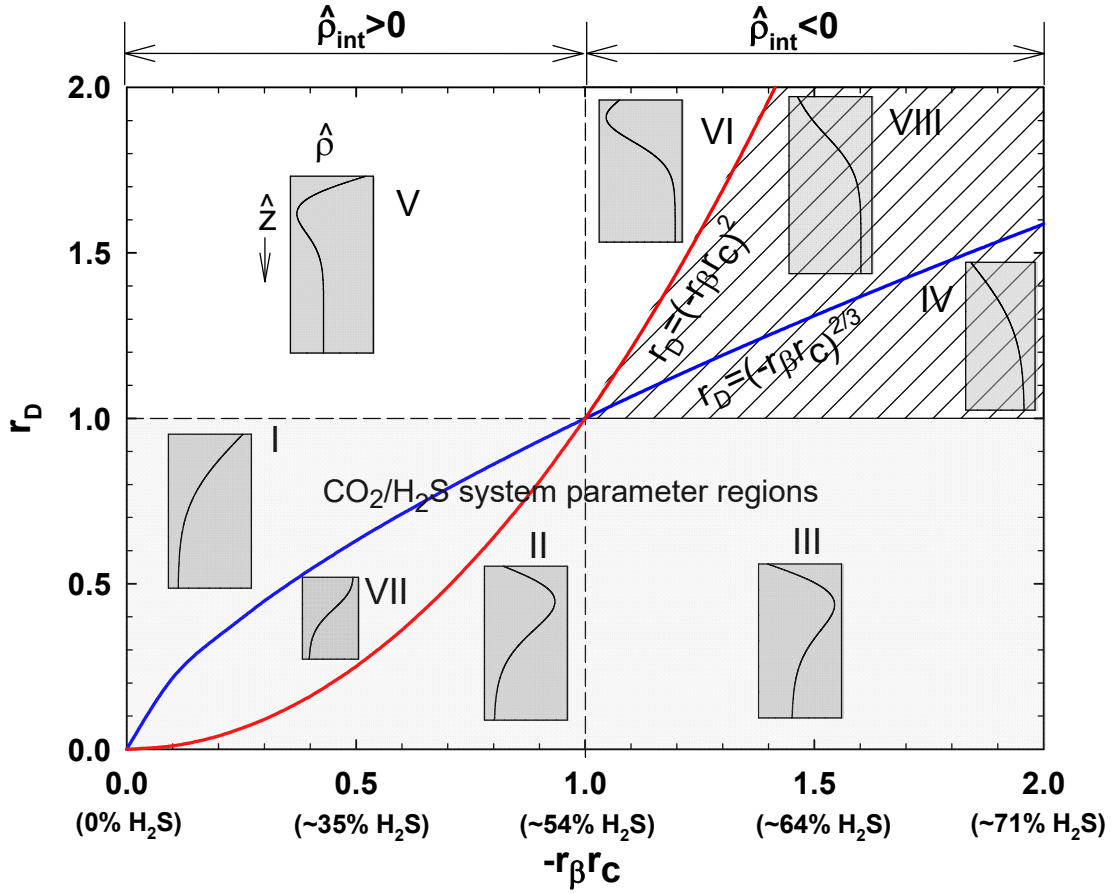


**Figure 4.4:** Parameter space ($-r_\beta r_C$, $r_D$) classification shows various stability regions. Inset plots are the base state density profiles with depth. Dashed space (IV) demonstrate the stable regions. Gray color highlighted spaces (I, VII, II& III) indicate the possible parameters regions for aqueous $CO_2/H_2S$ system. $H_2S$ compositions correspond to a typical storage temperature of 40°C and a pressure of 100 bar.

### 4.3.3 Linear stability analysis

The base state density profiles parametrized in the previous section may become unstable and lead to convective dissolution, which is favorable in the context of geological storage of $CO_2$. The linear stability analysis determines the time at which these instabilities occur and is important for impure injection streams and screening of storage sites. A linear stability analysis using quasi-steady state approximation (QSSA) is used to study the growth of instabilities and consequently to determine their time of onset. To conduct a linear stability analysis, the governing equations of flow and

transport given in Equation (4.1) are perturbed using $\mathbf{s}=\mathbf{s}_0+\mathbf{s}'$ where s=s[p,v,$\chi_1$,$\chi_2$,ρ]. The fluid is stationary at the early time and the concentrations, velocity, and density base states can be described by $\partial\hat{\chi}_{0i}/\partial\hat{t}=r_{Dt}\partial^2\hat{\chi}_{0i}/\partial\hat{z}^2$, $\mathbf{v}_0$=0, and $\hat{\rho}_0=\hat{\chi}_{01}+r_\beta\hat{\chi}_{02}$, respectively. Substituting the perturbed variables into the flow and transport equations, eliminating the higher order terms and after simplification, we obtain the following perturbed equations.

$$\nabla_2^2 v' = \mathrm{Ra}\,\frac{\nabla_1^2\chi_1' + r_\beta\nabla_1^2\chi_2'}{1+r_\beta r_c}; \tag{4.5a}$$

$$r_{Di}\nabla_2^2\chi_i' - v'\frac{\partial\chi_{0i}}{\partial z} = \frac{\partial\chi_i'}{\partial t}\ , \tag{4.5b, c}$$

where the velocity perturbation is scaled by $\phi D_1/H$, $\nabla_1^2=\nabla_x^2, \nabla_2^2=\nabla_{xz}^2$, $\mathrm{Ra}=kg\rho_b\beta_1\chi_1^s H(1+r_\beta r_c)/\mu\varphi D$ and i=1,2, and the hats (^) are dropped for convenience.

The perturbed velocity and concentration are expressed as $[\chi_1',\chi_2',v']=[\chi_1^*,\chi_2^*,v^*](z,t)e^{-i\kappa x+\omega t}$ where $\kappa$ and $\omega$ are the perturbation wave-number and growth rate, respectively. Using Equation (4.5) we obtain

$$\frac{\partial^2 v^*}{\partial z^2} - \kappa^2 v^* = \mathrm{Ra}(-\kappa^2)\frac{\chi_1^* + r_\beta\chi_2^*}{1+r_\beta r_c}, \tag{4.6a}$$

$$r_{Di}\frac{\partial^2\chi_i^*}{\partial z^2} - \kappa^2\chi_i^* - v^*\frac{\partial\chi_{0i}}{\partial z} = \omega\chi_i^*; \tag{4.6b, c}$$

where $i$=1,2, $r_{D1}$=1 and $r_{D2}=r_D$. The boundary conditions for the perturbed flow and mass transfer are given by $\chi_i^*(0)=0$, $\partial\chi_i^*(1)/\partial z=0$, $v^*(0)=v^*(1)=0$. For the special case of $-r_\beta r_c=1$, $\Delta\hat{\rho}_{\mathrm{int}}=0$; thus, Ra =0. In this case, it can be shown that Equation (5a) is reduced to $\nabla_2^2 v' = \mathrm{Ra}^*\left(\nabla_1^2\chi_1' + r_\beta\nabla_1^2\chi_2'\right)$ where $\mathrm{Ra}^* = kg\rho_b\beta_1\chi_1^s H/\mu\phi D$.

The growth of perturbations can be assumed to be much faster than the development of the base state and thus the quasi-steady-state approximation (QSSA) (Tan and Homsy, 1986) is applicable.

This approach has been widely used in the linear stability analysis of gravitationally unstable diffusive boundary layers (Ghesmat et al., 2011; Riaz et al., 2006; Trevelyan et al., 2011). Limitations of the QSSA have been discussed elsewhere (Trevelyan et al., 2011). Using QSSA, $\partial\chi_{0i}/\partial z$ in Equations (4.6b, c) can be evaluated at time $t_0$ or the so called "frozen time" during the growth of perturbations.

It is worth noting that Equation (4.6a) recovers $CO_2$/water system when $r_\beta$=0. The above system of Equations (4.6a-c) are solved numerically using a second-order finite difference method to find the growth rate, ω, as a function of wave-number, $\kappa$. The following eigenvalue problem can be obtained using the discretized equations.

$$[\mathbf{A}_v][\mathbf{v}^*] = \mathrm{Ra}(-\kappa^2)\left[\frac{\boldsymbol{\chi}_1^* + r_\beta \boldsymbol{\chi}_2^*}{1 + r_\beta r_c}\right], \tag{4.7a}$$

$$r_{Di}[\mathbf{A}_c][\boldsymbol{\chi}_i^*] - [\mathbf{v}^*]\frac{\partial \boldsymbol{\chi}_{0i}}{\partial z} = [\boldsymbol{\omega}][\boldsymbol{\chi}_i^*], \tag{4.7b,c}$$

where $\mathbf{A}_v = (\mathbf{D}_v - \kappa^2\mathbf{I})$, $\mathbf{A}_c = (\mathbf{D}_c - \kappa^2\mathbf{I})$, $\mathbf{D}_v$, and $\mathbf{D}_c$ are coefficient matrices based on central discretization of the second derivatives and **c** and **v** are vectors containing the unknown variables at the discrete nodes. Solutions to Equations (4.7a-c) can be written as:

$$[\mathbf{v}^*] = \mathrm{Ra}(-\kappa^2)[\mathbf{A}_v]^{-1}\left[\frac{\boldsymbol{\chi}_1^* + r_\beta \boldsymbol{\chi}_2^*}{1 + r_\beta r_c}\right], \tag{4.8a}$$

$$r_{Di}[\mathbf{A}_c][\boldsymbol{\chi}_i^*] - \left\{\mathrm{Ra}(-\kappa^2)[\mathbf{A}_v]^{-1}\left[\frac{\boldsymbol{\chi}_1^* + r_\beta \boldsymbol{\chi}_2^*}{1 + r_\beta r_c}\right]\right\}\left[\frac{\partial \boldsymbol{\chi}_{0i}}{\partial z}\right] = [\boldsymbol{\omega}][\boldsymbol{\chi}_i^*]. \tag{4.8b,c}$$

The eigenvalue Equations (4.8b) and (4.8c) can be rewritten in matrix form;

$$\begin{bmatrix} [\mathbf{A}_c] + \dfrac{\mathrm{Ra}\,\kappa^2}{1 + r_\beta r_c}[\mathbf{A}_v]^{-1}\left[\dfrac{\partial \boldsymbol{\chi}_{01}}{\partial z}\right] & \dfrac{\mathrm{Ra}\,\kappa^2 r_\beta}{1 + r_\beta r_c}[\mathbf{A}_v]^{-1}\left[\dfrac{\partial \boldsymbol{\chi}_{01}}{\partial z}\right] \\ \dfrac{\mathrm{Ra}\,\kappa^2}{1 + r_\beta r_c}[\mathbf{A}_v]^{-1}\left[\dfrac{\partial \boldsymbol{\chi}_{02}}{\partial z}\right] & r_D[\mathbf{A}_c] + \dfrac{\mathrm{Ra}\,\kappa^2 r_\beta}{1 + r_\beta r_c}[\mathbf{A}_v]^{-1}\left[\dfrac{\partial \boldsymbol{\chi}_{02}}{\partial z}\right] \end{bmatrix}\begin{bmatrix} \boldsymbol{\chi}_1^* \\ \boldsymbol{\chi}_2^* \end{bmatrix} - [\boldsymbol{\omega}]\begin{bmatrix} \boldsymbol{\chi}_1^* \\ \boldsymbol{\chi}_2^* \end{bmatrix} = 0. \tag{4.9}$$

The above eigenvalue problem was solved numerically using the same numerical procedure reported by Emami-Meybodi and Hassanzadeh (Emami Meybodi and Hassanzadeh, 2013). The maximum eigenvalue of the coefficient matrix corresponding to given parameters of $\kappa$, $t$ and Ra number is considered as the growth rate, ω. Onset time is defined as the time at which the growth rate of perturbation first becomes positive. Thus, the onset time can be detected using dispersion curves given a zero maximum growth rate.

For the special case of a step change in concentration profile, analytical solution at the early time ($t \rightarrow 0$) results in $\omega = -\kappa^2$ (Ghesmat et al., 2011; Tan and Homsy, 1986). This analytical solution was used to verify the computational algorithm. Growth rates of the perturbations obtained by the analytical solution ($\omega = -\kappa^2$) at $\hat{t}_{01} = 8 \times 10^{-5}$, shown by open circles in Figure 4.5(a), are in close agreement with results of the developed algorithm indicating validity of the analysis.

## 4.4 Results and Discussion

### 4.4.1 Stability analysis

Figure 4.5 shows rate of growth of perturbations for pure $CO_2$ stream and three other streams of impure $CO_2$ at different times. The results shown in Figure 4.5 demonstrate a clear difference between $CO_2$/water system and the impure $CO_2$/water systems. These results suggest that the onset of convective instabilities for each stream can be different. This figure shows clearly that an impure stream with 52% $H_2S$, which corresponds to ($-r_\beta r_c$, $r_D$) ~ (0.96, 0.87) (see region II in Figure 4.4), has a maximum growth rates as compared to the other streams. The non-monotonic density profile associated with the positive interface density difference ($\hat{\rho}_{int} > 0$) implies that impure $CO_2$ streams fall in region II of Figure 4.4 are gravitationally more unstable than pure $CO_2$ and other streams. In other words, the presence of impurity leads to faster onset of instability. In contrast, an impure stream with 56% $H_2S$, which corresponds to ($-r_\beta r_c$, $r_D$) ~ (1.04, 0.87) (see region III in Figure 4.4), demonstrates the lowest growth rate of the convective instabilities. This behaviour is attributed to the negative interface density difference ($\hat{\rho}_{int} < 0$), which corresponds to excessive $H_2S$ concentration in the impure stream. To further clarify these findings, results of the onset of the convective instabilities versus Ra for various impure streams are shown in Figure 4.6.

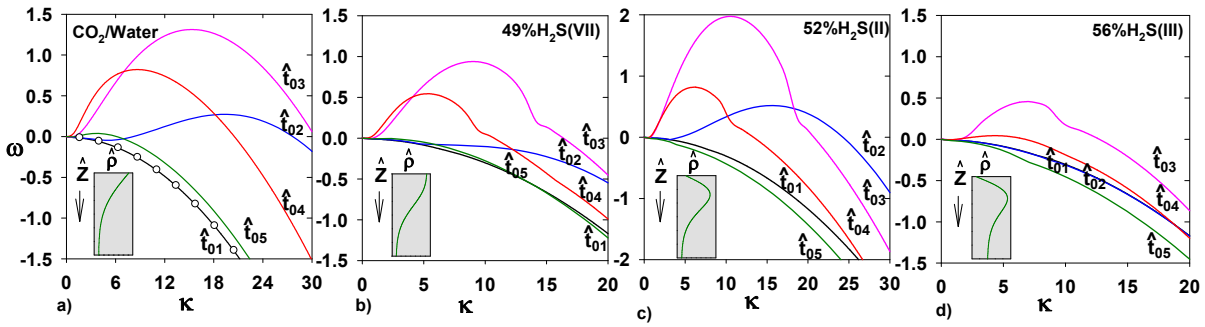


**Figure 4.5:** Rate of growth of perturbations versus wave-number at different frozen times of $\hat{t}_{01}=8\times10^{-5}$, $\hat{t}_{02}=8\times10^{-4}$, $\hat{t}_{03}=8\times10^{-3}$, $\hat{t}_{04}=8\times10^{-2}$, $\hat{t}_{05}=8\times10^{-1}$ for a system with Ra=300, (a) pure $CO_2$ stream with ($-r_\beta r_c$, $r_D$) = (0, 1), (b) impure stream with 49% $H_2S$ [($-r_\beta r_c$, $r_D$) ~ (0.9,0.87)], (c) impure stream with 52% $H_2S$ [($-r_\beta r_c$, $r_D$) ~ (0.96,0.87)], and (d) impure stream with 56% $H_2S$ [($-r_\beta r_c$, $r_D$) ~ (1.04,0.87)] where $H_2S$ compositions correspond to a typical storage temperature of 40° C and a pressure of 100 bar. Open circles are the results of the analytical solution ($\omega=-\kappa^2$) as compared with the results of the stability analysis shown by line.

Figure 4.6 shows the onset of instabilities as a function of Rayleigh number for pure stream of $CO_2$ and four possible impure streams. Rayleigh number is used to compare the onset of instability of systems with different rock and fluid properties based on the scaled onset time. According to the definition of Rayleigh number ($\mathrm{Ra}=kg\rho_b\beta_1\chi_1^s H(1+r_\beta r_c)/\mu\phi D$), a constant Ra for different $r_\beta r_c$ can be achieved by varying other properties including thickness of porous layer, permeability or porosity. The results shown in Figure 4.6 reveal that an impure stream with 52% $H_2S$ ($r_\beta r_c$ =-0.96), which falls in region II of the parameter space (see Figure 4.4) leads to a faster onset of instability as compared to the pure $CO_2$. This system represents a non-monotonic density profile with a positive interface density differences ($\hat{\rho}_{int}>0$) during the growth of the diffusive boundary layer. Results shown in Figure 4.6 clearly indicate the important role of density profile on the onset of instability. Results also show that in all cases the onset of instability can be scaled with the inverse of $Ra^2$, implying the onset time is independent of the porous layer thickness, which is in agreement with previous findings (Bestehorn and Firoozabadi, 2012; Ennis-King et al., 2005; Hassanzadeh

et al., 2006; Meulenbroek et al., 2013; Slim, 2014). The scaling prefactor (a) for each system is also given in Figure 4.6. The results reveal that a mixture with $-r_\beta r_c$=0.96 (52% $H_2S$) results in a scaling relation with a prefactor of a ≈40 suggesting a faster onset of the convective instabilities as compared to a ≈56 for a pure stream of $CO_2$. It is worth noting that $H_2S$ compositions reported in Figure 4.6 correspond to a typical storage temperature of 40° C and a pressure of 100 bar. In the other words, $H_2S$ composition that leads to a faster onset depends on the storage temperature and pressure conditions. These findings show that the composition of impurity for storage sites can be engineered to control and accelerate the evolution of convective mixing.

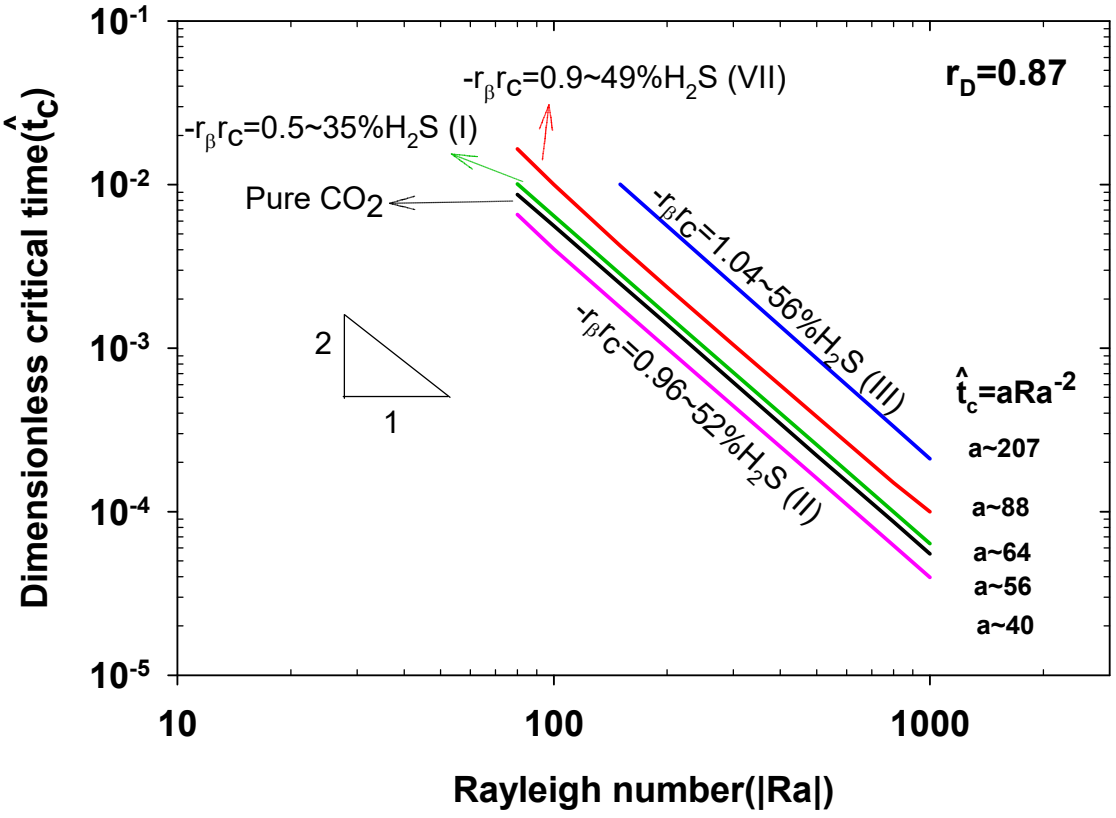


**Figure 4.6:** Onset of instability scaled with Ra for various regions of the parameter space where $H_2S$ compositions correspond to a typical storage temperature of 40° C and a pressure of 100 bar.

Figure 4.7 shows the dependency of the onset of convective instability to the equilibrium concentration ratio ($r_c$) of impure $CO_2$ streams for different Rayleigh numbers. The corresponding parameter space is also shown on this figure. Positive interface densities $(\hat{\rho}_{int} > 0)$ generally tend to create a monotonically decreasing density profile (unstable system) while negative interface densities $(\hat{\rho}_{int} < 0)$ result in a monotonically increasing density profile (stable system). Once the interface density is not strong enough, the contrast in molecular diffusion of $CO_2$ and $H_2S$ (represented by $r_D$) comes into play and forms a non-monotonic density profile. A non-monotonic density profile caused by such a contrast with positive interface density can accelerate the onset of convective instability significantly, which needs to be considered for geological storage of acid gases.

The results shown in Figure 4.7 reveal that as the composition of $H_2S$ in an impure $CO_2$ stream increases the onset time gradually increases up to an equilibrium ratio of ~1.51, which corresponds to an impurity composition of ~51% $H_2S$. This gradual increase in the onset time corresponds to parameter space regions I and VII shown in Figure 4.4 where the density profile is monotonic with $(\hat{\rho}_{int} > 0)$. Further addition of $H_2S$ to the impure stream decreases the interface density leading to deceleration of the onset of convective instabilities. Although $CO_2$ molecular diffusion is greater than that of $H_2S$ ($r_D$<1), the effect of higher equilibrium ratio ($r_c$) is dominant in controlling the shape of density profile. Therefore, the density profile remains monotonic. For larger $H_2S$ impurities in acid gas streams between ~51-55 mole%, which corresponds to the parameter space region II, the interface density is still positive but diminishes by further increase in the composition of $H_2S$. Since $CO_2$ is more diffusive than $H_2S$ ($r_D$<1), it penetrates deeper into the formation and generates a non-monotonic density profile with positive interface density $(\hat{\rho}_{int} > 0)$. It is worth noting that $CO_2$ increases the aqueous phase density while $H_2S$ decreases the density upon dissolution. Figure 4.7 shows that impure streams with positive interface density and non-monotonic density profile (region II) may have a faster onset of instability as compared to a pure stream of $CO_2$. This finding is in agreement with the behaviour of the growth of perturbations described in Figure 4.5. For $H_2S$ compositions beyond 55% the interface density differences take negative values (region III). While the density remains non-monotonic in region III, the effect of negative interface density is dominant over the diffusion contrast leading to more stable system as compared to pure $CO_2$ stream. The peak in the density profile diminishes rapidly beyond $r_\beta r_c$>~1.5

leading to a monotonically increasing and stable profile. These results are not applicable to the special case of $-r_\beta r_c = 1$ since the Rayleigh number for this case is different than the one used in our analysis. In the following section, the optimum storage pressure and temperature that lead to faster onset of convective dissolution will be discussed.

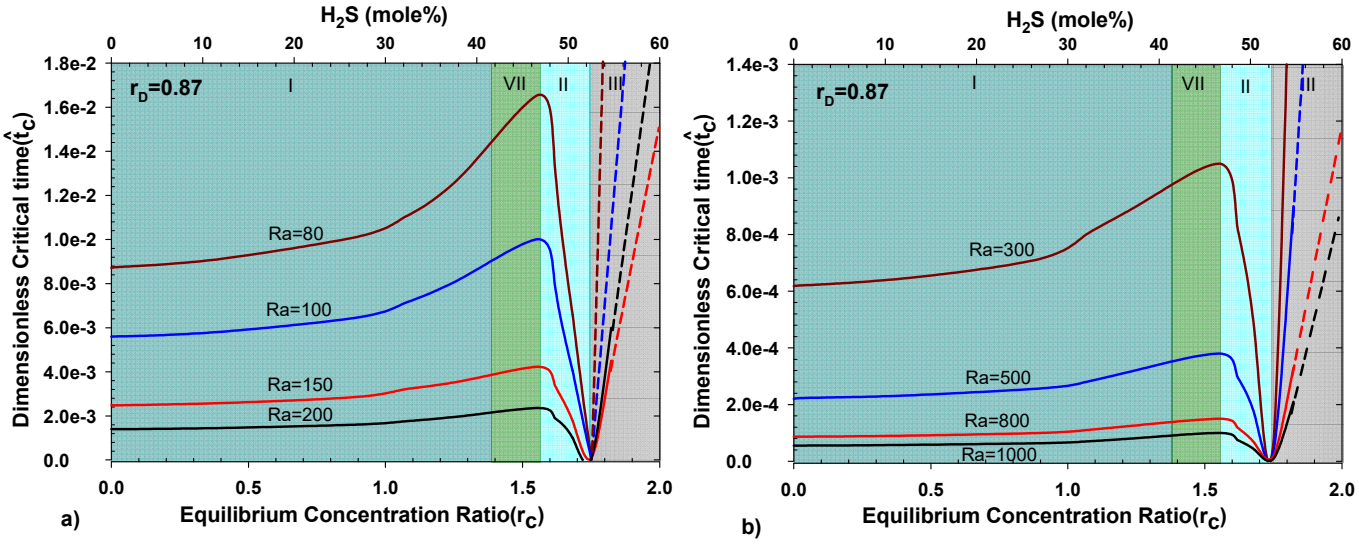


**Figure 4.7:** Onset of instability versus composition of impurity for various regions of the parameter space at a) Ra<200 and b) 300<Ra<1000, binaries with $r_B$=-0.57 and $r_D$=0.87 where $H_2S$ compositions correspond to a typical storage temperature of 40° C and a pressure of 100 bar.

### 4.4.2 Implication for acid gas disposal

Site screening is an important step in pilot scale and as well as field scale implementation of acid gas disposal to improve storage efficiency and reduce risk of leakage. Pressure and temperature of disposal sites are among important parameters required for site screening purposes. The parameter space ($-r_\beta r_c$, $r_D$) classification developed earlier was used to find the optimum $H_2S$ compositions leading to faster onset of convective dissolution. Results are shown in Figure 4.8 as a function of pressure and temperature of storage sites. The optimum $H_2S$ content of $CO_2$ stream that leads to faster onset of convective dissolution can be represented by a linear function of pressure and

temperature as given in Figure 4.8. This simple relationship can be used to choose composition of $H_2S$ in the impure storage stream for acid gas disposal and simplify the site screening process.

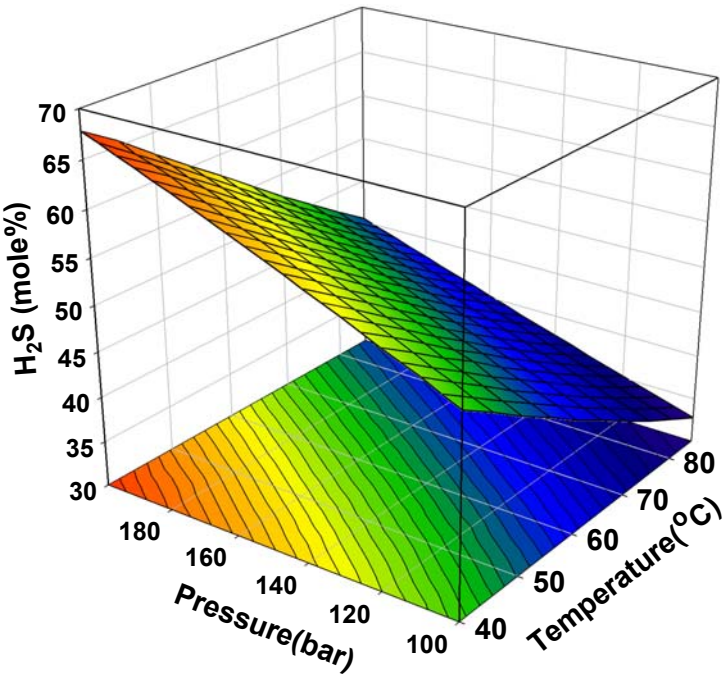


**Figure 4.8:** Optimum $H_2S$ composition (mole %) leading to faster onset as a function of storage temperature and pressure. Dependency of optimum $H_2S$ composition can be expressed as a linear relationship of $x_{H_2S}(\%) = 0.147P - 0.4695T + 56.466$ where $P$ is in bar and $T$ in °C.

Information related to the onset of instabilities such as the scaling relations (see Figure 4.6) and the parameter space (See Figure 4.4) developed in this study are important in proper design, site screening, characterization and safety of geological storage. This information can be used to either identify future geological candidates for acid gas disposal or reviewing the current operating conditions of licensed sites. For example, large-scale injection of acid gas into geological formations has been approved for more than 47 operation sites in Western Canada (Alberta and British Colombia) operating over a wide range of acid-gas composition, pressure and temperature (Bachu et al., 2003, 2008; Bachu and Carroll, 2005). Deep saline aquifers with 26 injection sites, depleted oil and/or gas reservoirs with 17 injection sites and underlying water leg of depleted oil and gas reservoir with 4 injection sites are the main hosting geological formation for acid gas

injection in Western Canada. Storage sites such as those are possible candidates for reviewing the operating conditions to control the onset of convective dissolution.

### 4.5 Acknowledgments

The authors would like to thank reviewers for their constructive comments. This work was supported by a Discovery Grant from the Natural Sciences and Engineering Research Council of Canada (NSERC) and was enabled in part by support provided by WestGrid (www.westgrid.ca) and Compute Canada Calcul Canada (www.computecanada.ca).

# Chapter 5: Prospect for Storage of Impure Carbon Dioxide Streams in Deep Saline Aquifers-A Convective Dissolution Perspective*

## 5.1 Abstract

Secure and permanent storage of $CO_2$ in deep saline aquifers by solubility trapping depends highly on the rate at which it dissolves in formation brine by convective dissolution. A commonly-held belief is that injection of impurities along with $CO_2$ retards the evolution of convective dissolution, thereby, negatively impacting solubility trapping of $CO_2$. Injection of impurities along with $CO_2$ provides an exceptional prospect for low-cost Carbon Capture and Storage (CCS) technologies and can potentially accelerate large scale implementation of geological storage of $CO_2$. In this study, convective dissolution of $CO_2$ streams with different portion of $H_2S$ impurities, which leads to solubility trapping of $CO_2$ in deep saline aquifers, is studied using non-linear numerical simulations. We have shown that the rate of dissolution of an impure $CO_2$ stream with $H_2S$ impurities less than 30 mol.% is nearly similar to that of a pure $CO_2$ stream. It was also shown that an impure $CO_2$ stream may lead to different convective mixing dynamics at early and late periods of dissolution process. These findings suggest that an impure $CO_2$ stream can be engineered to improve the rate of dissolution and thus solubility trapping of $CO_2$ leading to higher storage security and efficiency.

* Jafari Raad, S. M., Hassanzadeh, H. (2017). Prospect for storage of impure carbon dioxide streams in deep saline aquifers-A convective dissolution perspective. *International Journal of Greenhouse Gas Control*, *63*, 350–355. https://doi.org/10.1016/J.IJGGC.2017.06.011

## 5.2 Introduction

It is believed that the effects of our increase reliance on fossil fuels and subsequent carbon dioxide ($CO_2$) emissions are becoming an ever present threat to global climate change (Metz et al., 2007; Pacala and Socolow, 2004). Storage of $CO_2$ into deep saline aquifers has been considered as an operative choice and a viable short term option offsetting anthropogenic emissions of $CO_2$ (Benson and Cole, 2008; Boot-Handford et al., 2014; EPA, 2014; Firoozabadi and Cheng, 2010; Lackner, 2003; Metz et al., 2005; Orr, 2009a). Most gases (e.g. $H_2S$, $N_2$, $O_2$), when dissolve in water decrease the aqueous phase density. However, $CO_2$ and a few other gases ($SO_2$, Kr, Xe) increase density of the aqueous phase (Ennis-King et al., 2005). Solubility trapping of $CO_2$ in deep saline aquifers favors from such a density increase since it leads to higher rate of dissolution of $CO_2$ in water and thus a more secure sequestration process can be achieved.

Once $CO_2$ is injected into an aquifer, it migrates upwards to the top of reservoir due to its buoyancy and spreads under caprock from where it gradually dissolves into the underlying brine (Lindeberg and Wessel-Berg, 1997). Dissolution of $CO_2$ into brine slightly increases the density of brine phase. Setting the negative density gradient in gravity field leads to sink down and consequently replacement of the $CO_2$-rich brine phase by underlying fresh brine, giving rise to a buoyancy-driven flow or so-called convective dissolution process. This mechanism significantly accelerates the solubility trapping of the injected $CO_2$ and consequently increases security of storage (Ennis-King and Paterson, 2005; Hassanzadeh et al., 2005; Hassanzadeh et al., 2007; Orr, 2009b).

Secure and permanent storage of $CO_2$ in deep saline aquifers by solubility trapping depends highly on the rate at which it dissolves in formation brine by convective dissolution. Intuitively, one may infer that injection of impurities, which reduce the aqueous phase density, such as those found in flue gases (e.g. $N_2$) and oil and gas production operations (e.g. $H_2S$) along with $CO_2$ impedes the development of convective dissolution; thus, undesirably influencing the trapping of $CO_2$ in deep saline aquifers. However, here we will show that this is not always the case.

Capture of $CO_2$ from impure streams is an expensive and energy intensive process (Markewitz et al., 2012). Injection of impurities along with $CO_2$ provides an exceptional prospect for competitive CCS technologies and can potentially accelerate implementation of large scale geological storage of $CO_2$. On the other hand, potential risk for impure $CO_2$ injection process and its subsequent environmental impact is higher than those for pure $CO_2$. Furthermore, impurities could pose risk of excessive corrosion of carbon storage infrastructures such as compression, transportation, and

injection facilities. However, compression, transportation, and injection of acid gases have been practiced in oil and gas industry for subsurface disposal to avoid flaring of $H_2S$ and expensive sulphur recovery units as well as in oil reservoirs for enhanced oil recovery (EOR) purposes for a long time all around the world. These operations have demonstrated the practicality of impure $CO_2$ injection in subsurface (Bachu and Gunter, 2005; Bachu et al., 2003; Carroll and Maddocks, 1999; Moshfeghian et al., 2002; Rahimi and Griffin, 2004; Wall and Kenefake, 2005; Wang et al., 2011; Whatley, 2000).

Convective dissolution that leads to permanent storage of $CO_2$ is of great importance. This $CO_2$ trapping mechanism has received emerging attention as it significantly affects the trapping efficiency, storage capacity and long-term storage security (Gilfillan et al., 2009). Previous studies of convective dissolution in the context of $CO_2$ sequestration have addressed the stability analysis (Ennis-King et al., 2005; Hassanzadeh et al., 2006; Jafari Raad et al., 2015; Myint and Firoozabadi, 2013; Riaz et al., 2006) and full numerical simulation of the process (Emami-Meybodi and Hassanzadeh, 2015; Farajzadeh et al., 2007; Hidalgo et al., 2012; Jafari Raad et al., 2016; Meulenbroek et al., 2013; Neufeld et al., 2010), and experiments to represent the dynamics of the process (Agartan et al., 2015; Backhaus et al., 2011; Cardoso and Andres, 2014; Loodts et al., 2014; MacMinn and Juanes, 2013; Tsai et al., 2013). These studies improved our understanding of convective dissolution of pure $CO_2$ streams. However, the majority of previous works have been focused on pure $CO_2$ streams and there are relatively few works that considered injection of impure $CO_2$ while the potential impact of impurities on fate of the injected $CO_2$ has been unnoticed. Understanding the effect of permitted impurities on the dynamics of dissolution and consequently effectiveness of $CO_2$ trapping is of great importance for long-term storage and risk assessment.

Impure $CO_2$ streams containing significant portion of hydrogen sulphide ($H_2S$) produced from sour hydrocarbon pools has been one of the main concern of oil and gas producers as well as environmentalists over the past decades (Metz et al., 2005). While the high cost of $CO_2$ capture from impure sources and purification process have been major challenges to the large scale implementation of $CO_2$ storage, co-injection of $CO_2$ with impurities has been suggested as a cost-effective option to reduce the cost of carbon capture and storage (Bachu et al., 2003; Ji and Zhu, 2013; Q. Li et al., 2013; Nicot et al., 2013; Talman, 2015; Wong et al., 2003).

Impurities in $CO_2$ steams are known to influence the fluid mixture thermophysical properties and consequently the sequestration process (IEAGHG, 2011; Ziabakhsh-Ganji and Kooi, 2012, 2014a, 2014b). Impurities such as $H_2S$ and $N_2$ decrease the density of aqueous phase, which may have an undesirable effect on solubility trapping of $CO_2$ (Stefan Bachu, 2008; Ji and Zhu, 2013; Lei et al., 2016; D. Li et al., 2015; Nicot et al., 2013; Wang et al., 2011). Co-injection of $H_2S$ with $CO_2$ may also affect mineral trapping of $CO_2$. Previous studies indicated that injection of $H_2S$ with $CO_2$ results in different mineral alteration patterns, precipitation types and $CO_2$ mineral trapping than injection of pure $CO_2$ (Xu et al., 2004, 2007). It was reported that $H_2S$ and $CO_2$ mineral trapping depends highly on PH and host rock type (Zhang et al., 2011). Since the time scale of mineral trapping is believed to be much longer than convective dissolution, undrestanding of the solubility trapping of impure $CO_2$ is worthy of consideration. Although great acheivements have been made through the prevouis studies on solubility trapping, the role of impurities on convective dissolution and their impact on solubility trapping of impure $CO_2$ remains poorly understood. In a most recent study (Jafari Raad and Hassanzadeh, 2016), linear stability analysis was conducted to investigate the effect of $H_2S$ as an impurity on the onset of convective dissolution. It was shown that difference in the molecular diffusion of $H_2S$ and $CO_2$ species may give rise to a non-monotonic density profile during the dissolution process, which can significantly affect the instability behaviour of diffusive boundary layer and consequently the onset of convective dissolution. It was shown that the impure $H_2S$ streams have potential to accelerate the onset of convective dissolution (Jafari Raad and Hassanzadeh, 2016). Nevertheless, the long-term fate of the injected $CO_2$ in subsurface is dictated by the mixing process after the onset. Therefore, from the storage security standpoint, the fate of the impure $CO_2$ beyond the onset is significantly more important than the onset, which has not been studied in the past. The understanding developed in this analysis may provide an opportunity to engineer injection streams to accelerate solubility trapping.

A detailed numerical simulation of convective dissolution by considering the effect of impurities could reveal possibility of injecting impure $CO_2$ streams, which eventually leads to significantly lower carbon capture cost. This study is designed to answer important questions related to the role of impurities on solubility trapping of impure $CO_2$ streams in subsurface. Does the dynamic of onset hold valid beyond the onset? What is the impurity range that results in similar dynamics as of pure $CO_2$ stream? Is it possible to engineer impure streams to improve solubility trapping of $CO_2$? In the following sections, we intend to answer these questions.

## 5.3 Model Description

We consider a two-dimensional (2D) saturated porous layer of thickness H, and length L, where the domain is impervious to flow from the top and bottom as well as its sides. The top boundary is exposed to constant concentration of species ($CO_2$ and impurity) where the interface between diffusing species and water has been considered sharp under the assumption of single-phase flow and consequently in the absence of capillarity (Emami-Meybodi and Hassanzadeh, 2015; Jafari Raad and Hassanzadeh, 2015; Riaz et al., 2006). The porous layer is assumed to be homogeneous, isotropic, and isothermal. Schematic of the considered system and the associated boundary conditions are shown in Figure 5.1.

Under the assumption of incompressible flow coupled with the Boussinesq approximation and in the absence of viscosity variation, cross diffusion of species, and velocity-based dispersion, the governing equations of non-reactive single-phase flow and transport in a porous medium can be expressed by (Bear, 1972)

$$D_i\phi\nabla^2\chi_i - \mathbf{v}\cdot\nabla\chi_i = \phi\frac{\partial\chi_i}{\partial t}; \tag{5.1a}$$

$$\nabla\cdot\mathbf{v} = 0; \tag{5.1b}$$

$$\mathbf{v} = -\frac{k}{\mu}(\nabla p - \rho\mathbf{g}\nabla z), \tag{5.1c}$$

where, index $i$ is the species index with $i$=1 for $CO_2$ and $i$=2 for impurity, $\mathbf{v}=(u,v)$ is the vector of Darcy velocity when $u$ and $v$ are the horizontal and vertical components of components of Darcy velocity, respectively, and $p$, $\chi$, $\mu$ and t are pressure, mole fraction, viscosity, and time, respectively. $k$ is the porous medium permeability, $\phi$ is the porosity, $g$ is the gravitational acceleration and $z$ is the vertical coordinate and positive downwards. $D$ is the effective molecular diffusion coefficient of species in the porous media and assumed to be independent of concentration for dilute solutions. It is worth noting that $H_2S$ has smaller molecular diffusion coefficient in water than $CO_2$ (Tamimi et al., 1994).

The aqueous phase density as a function of species mole fractions in the aqueous phase for $CO_2$-$H_2S$/water fluid pair can be expressed by $\rho = \rho_b(1+\beta_1\chi_{CO_2}+\beta_2\chi_{H_2S})$ (Jafari Raad and

Hassanzadeh, 2016), where χ is the species mole fraction with respect to total moles in the aqueous phase, $\rho_b$ is the water density, and $\beta$ is expansion coefficient, which is defined as $\beta_i = \frac{1}{\rho_b} d\rho / d\chi_i$.

A thermodynamics model developed based on the Cubic-Plus-Association equation of state (CPA-EoS) was used to predict the aqueous phase density. This relation was obtained using thermodynamics analysis of solubility limits for mixture of $CO_2$-$H_2S$ in brine under the licensed operating disposal conditions for acid gas injection sites in Western Canada at a typical temperature and pressure of 40°C and 100 bar, respectively (Bachu et al., 2003, 2008; Jafari Raad and Hassanzadeh, 2016). Detailed thermodynamics model and the behaviour of the aqueous phase density for acid gas-brine systems has been reported elsewhere (Jafari Raad and Hassanzadeh, 2016; Tsivintzelis et al., 2010; Zirrahi et al., 2015).

The expansion coefficient values for $CO_2$-$H_2S$/water fluid pair for the given temperature and pressure condition are given by $\beta_1 = 0.368$ and $\beta_2 = -0.21$. In the following section, nonlinear simulations are presented.

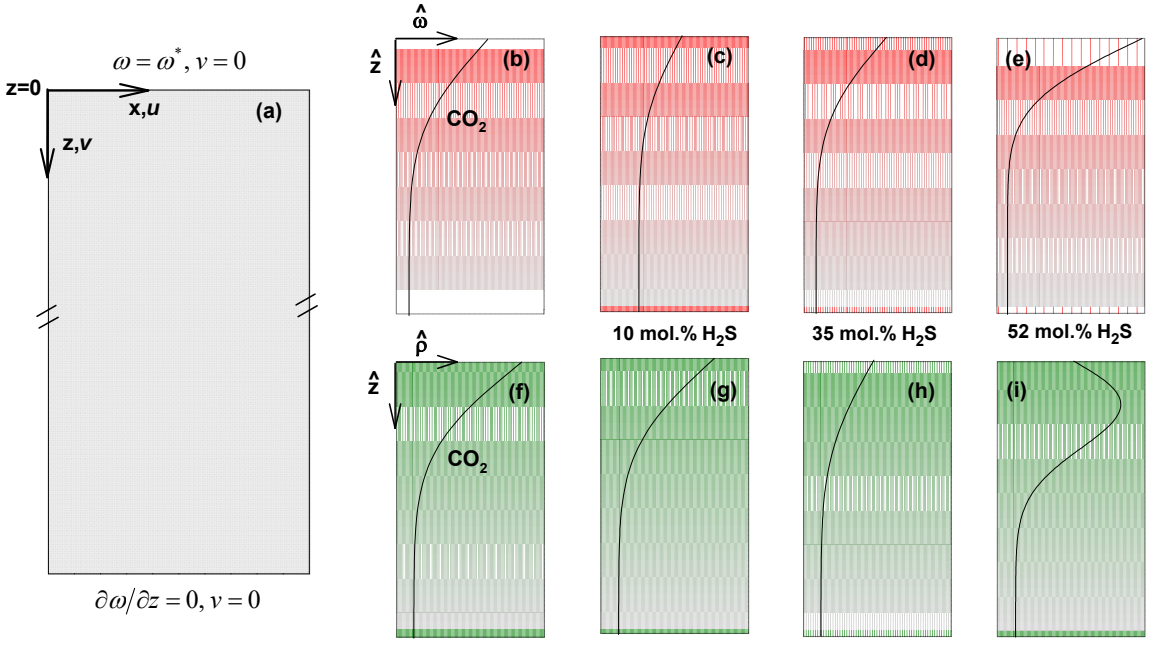


**Figure 5.1:** (a) Geometry and boundary conditions used in this study. The considered brine-rich porous layer is initially free of the diffusing species. No flow boundaries are set at the top and bottom as well as its sides. The top boundary is exposed to a constant concentration where the

species ($H_2S$ and $CO_2$) with finite solubilities in water at the interface diffuse downward, (b-e) $CO_2$ dimensionless base state concentration ( $\chi_i / \chi_1^s$ ) profiles versus depth for pure $CO_2$, and impure streams with 10, 35 and 52 mol.% $H_2S$ in water, respectively. The base state concentrations are found using mass conservation Equation (5.1a) at pure diffusive state ( $\mathbf{v} = 0$ ) (Jafari Raad and Hassanzadeh, 2016). (f-i) dimensionless base state density profiles versus depth for pure $CO_2$, and impure streams with 10, 35 and 52 mol.% $H_2S$, respectively.

### 5.4 Nonlinear Simulations

We have conducted full numerical simulations to gain an insight into the nonlinear dynamics of mixing for impure $CO_2$ streams with various fractions of $H_2S$ impurities. The basic framework of the developed numerical model is based on a well-known IMPEC approach where the implicit scheme is used to discretize flow Equations (5.1b) and (5.1c) while the transport Equations (5.1a) are treated explicitly (Settari, 2001). Governing Equations (5.1a-c) are discretized using the finite difference approach in a block-centred Cartesian grid system for a two-dimensional domain where equal horizontal and vertical meshes are employed. The numerical model has been benchmarked against single and multi-component systems (Emami-Meybodi and Hassanzadeh, 2015; Emami-Meybodi and Hassanzadeh, 2013; Jafari Raad et al., 2016; Jafari Raad and Hassanzadeh, 2015). For brevity, we refer the reader to the previous publications for more details of the numerical approach and controls on accuracy of the numerical solutions.

Here, we investigate the onset of convective dissolution and the associated dynamics for pure $CO_2$ and impure $CO_2$ streams with 10, 35 and 52 mol.% of $H_2S$. These cases are chosen based on a detailed parameter space classification representing dynamics of density profiles during dissolution of acid gas ($H_2S$-$CO_2$) in brine reported in our recent study (Jafari Raad and Hassanzadeh, 2016). It was shown that dissolution of acid gas in brine leads to four main family of density profiles depending on the fraction of $H_2S$ impurities and operating conditions. Using linear stability analysis, it was previously shown that an impure $CO_2$ stream corresponding to each parameter space region shows its unique stability behaviour (Jafari Raad and Hassanzadeh, 2016). We have chosen these cases with the purpose of making a consistent comparison between the results of the numerical simulations and the linear stability analysis relating dynamics of buoyancy driven instability and subsequent mixing to the dynamics of base state density profiles.

The dimensionless scaling group, $\mathrm{Ra} = kg\rho_b\beta_1\chi_1^s H(1+r_\beta r_c)/\mu\phi D_1$ is used to make a proper comparison of the convective dissolution of $CO_2$-$H_2S$/water system considered in the nonlinear simulations, where, $r_c = \chi_2^s / \chi_1^s$, $r_\beta = \beta_2 / \beta_1$, and $\chi_i^s$ is equilibrium mole fraction of specie *i* in the aqueous phase. All numerical simulations were performed at |Ra|=600. The concentration distributions, fractional ultimate dissolution of acid gas and dissolution fluxes as the most practical measures of convective dissolution are considered in analysis that follows.

**5.5 Results and Discussion**

The 2D numerical solutions were conducted to evaluate the concentration distribution associated with convective dissolution for pure and impure $CO_2$/water systems. An impurity such as $H_2S$ decreases the density of the aqueous phase, which one may intuitively conclude that it impedes the convective dissolution. However, the lower molecular diffusion of $H_2S$ compared to $CO_2$ leads to double diffusive convection that makes evolution of convective instabilities associated with an impure $CO_2$ stream similar to or in some cases more vigorous than a pure $CO_2$ stream. This phenomenon, which has not been noticed in previous studies of convective dissolution, provides a unique feature of impure systems that can be used to engineer impure $CO_2$ streams to optimize storage condition. Figure 5.2 shows the time evolution of concentration distribution for pure $CO_2$ and impure $CO_2$ streams with 10, 35 and 52 mol.% of $H_2S$. It can be observed that, these systems exhibit different instability behaviour followed by different fingering pattern. Concentration distributions show that the $CO_2$/water system leads to fingering pattern with shorter wavelength compared to all impure streams. Results of the concentration distributions show that lateral spreading and merging of the developed fingers in the $CO_2$/water system is more vigorous than those in the impure systems. However, the impure $CO_2$/water systems with 52 mol.% of $H_2S$ results in faster development of the instabilities in form of finger structures representing the onset of convective dissolution, which is in agreement with the results of stability analysis (Jafari Raad and Hassanzadeh, 2016).

The numerical results show that impure systems with a large portion of $H_2S$ impurities (52 mol.%) lead to sluggish form of fingers associated with low rate of convective mixing due to the presence of less dense mixture on the upper layer compared to pure $CO_2$. Furthermore, $H_2S$ impurity significantly affects the wavelength of the density-driven fingers in the impure $CO_2$/water system such that systems with higher impurities result in fingers with longer wavelengths.

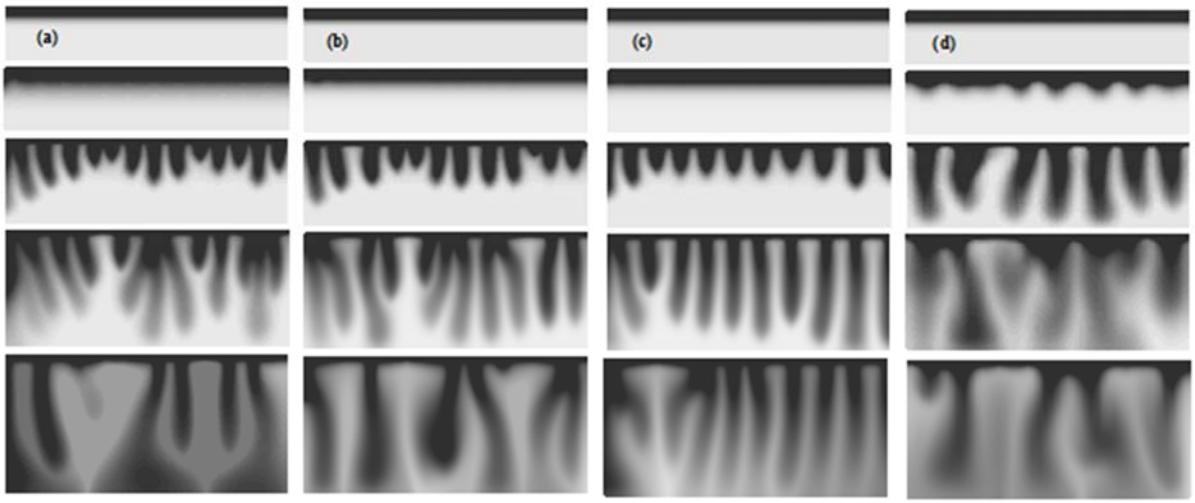


**Figure 5.2:** Concentration distribution of $CO_2$/water systems with |Ra|=600 at different times of $t = 0.75(yr)$, $t = 1.35(yr)$, $t = 1.80(yr)$, $t = 2.25(yr)$, and $t = 2.85(yr)$, including (a) pure $CO_2$ streams [$(\chi_1^s, \chi_2^s)$~( 0.0256,0.0)], (b) impure $CO_2$ with 10 mol.% $H_2S$ [$(\chi_1^s, \chi_2^s)$~( 0.0242,0.0048)], (c) impure $CO_2$ with 35 mol.% $H_2S$ [$(\chi_1^s, \chi_2^s)$~( 0.0202, 0.0181)], and (d) impure $CO_2$ with 52 mol.% $H_2S$ [$(\chi_1^s, \chi_2^s)$~( 0.0166, 0.0285)]. Equilibrium mole fraction of dissolved species in the aqueous phase were evaluated at the typical storage temperature of 40°C and a pressure of 100 bar.

Figure 5.3 shows the fractional ultimate dissolution of acid gas ($CO_2$+$H_2S$) as a function of time for the considered cases. The results shown in Figure 5.3 clearly show that the impure $CO_2$ stream with 52 mol.% of $H_2S$ results in faster onset of convective dissolution compared to $CO_2$ stream, while the impure $CO_2$ streams with 10 and 35 mol.% of $H_2S$ show a delayed onset compared to pure $CO_2$. Furthermore, numerical simulation results show that an impure stream with 57 mol.% or higher $H_2S$ impurities leads to stable system and denotes the pure diffusion as a dominant mechanism during the sequestration process. These non-linear simulation results are in agreement with the results of the linear stability analysis reported in our previous study (Jafari Raad and Hassanzadeh, 2016). The instability behaviour is attributed partly to the magnitude of interface density differences and the shape of base state density profile under the consequence of the contrast in the molecular diffusions of $CO_2$ and $H_2S$.

It is worth noting that an impure $CO_2$ stream with 52 mol.% of $H_2S$ results in a non-monotonic density profile with positive density difference at the interface while the impure $CO_2$ stream with 10 and 35 mol.% of $H_2S$ lead to monotonic density profiles (Jafari Raad and Hassanzadeh, 2016). These results show the important role of double diffusion on evolution of unstable density profiles and dynamics of convective dissolution. Comparison of mixing curves beyond the onset time reveal a unique mixing behaviour for an impure $CO_2$ stream with 52 mol.% of $H_2S$. While an impure $CO_2$ stream with 52 mol.% of $H_2S$ reveals a faster development of convective dissolution, its mixing rate is significantly less than pure $CO_2$ as well as impure $CO_2$ streams with less $H_2S$ impurities. Higher convective dissolution rate in $CO_2$/water system is attributed to the strong interaction and merging of fingers as they propagate downward (see concentration distribution shown in Figure 5.2). At the same time, the growth of fingers in the case of impure $CO_2$/water systems with 52 mol.% of $H_2S$, is nearly independent from each other with less interaction as compared to the pure $CO_2$/water system.

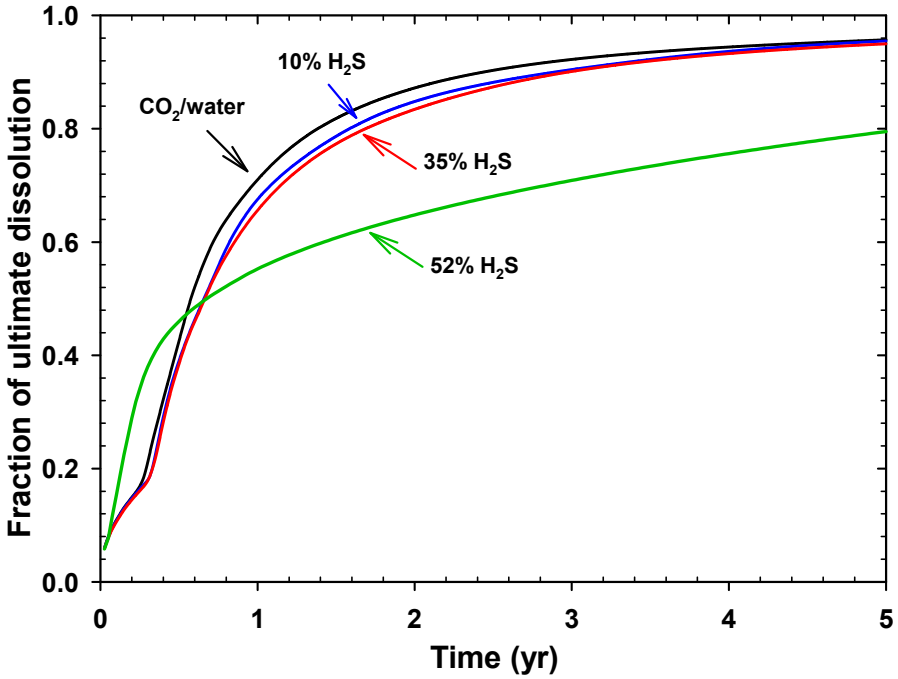


**Figure 5.3:** Dissolution curves representing convective mixing for pure and impure $CO_2$/water systems with |Ra|=600. For $CO_2$-$H_2S$/water systems, ultimate dissolution denotes fraction of acid gas ($CO_2$+$H_2S$) dissolved in water.

To gain a better understanding of the dynamics of the mixing process beyond the onset of instability, we studied the dissolution flux of systems with different level of impurities. The dissolution flux is measured directly from the numerical simulations taking the cumulative dissolution of mass in water. The dissolution flux per unit area can be expressed by:

$$F(\hat{t}) = \frac{1}{A}\frac{d}{d\hat{t}}\int_V C(\hat{t})dV \ , \tag{5.2}$$

where $V$ indicates the domain pore volume, $A$ is the cross-sectional area of the interface and $C$ is total concentration of species ($CO_2$+$H_2S$) in the entire domain.

Figure 5.4 shows the numerical measurements of dissolution flux as a function of time. It can be observed that impurity of $CO_2$ stream significantly influences the convective onset marked by the sharp increase of dissolution flux and consequently, the nonlinear dynamics of convective mixing beyond the onset.

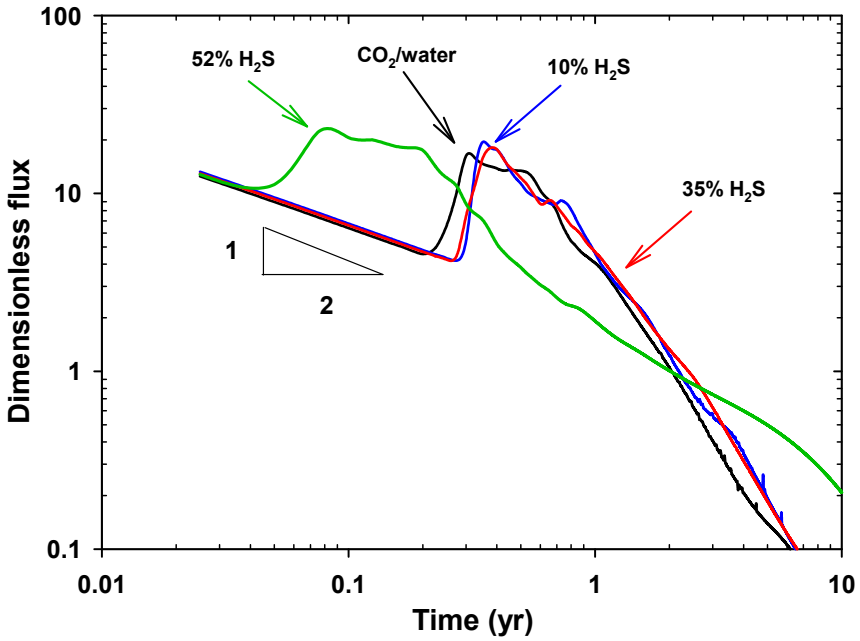


**Figure 5.4:** Dimensionless dissolution flux versus time for pure $CO_2$ and the impure $CO_2$ streams with 10, 35 and 52 mol.% $H_2S$ at |Ra|=600.

Examination of the convective flux beyond the onset show that an impure $CO_2$ stream with 52 mol.% of $H_2S$ leads to lower convective flux at the late period of mixing as compared to other cases with lower $H_2S$ impurities as well as pure $CO_2$ stream. Even though this system shows the fastest onset of convective instabilities, it reveals a sluggishly mixing process. This behaviour can be credited to the accumulation of less dense mixture below the interface on the top layer. In other words, convective dissolution homogenizes the concentrations within the mixing zone, which would counteract the effect of double diffusion on the density stratification and consequently the mixing behaviour. Interestingly, the impure $CO_2$ streams with 10 and 35 mol.% of $H_2S$ reveal a close mixing dynamics and consequently nearly equivalent dissolution flux to the pure $CO_2$ stream. These results show that while an impurity such as $H_2S$ is prone to impede the convective dissolution, an informed choice of impurity can lead to similar convective dissolution as of pure $CO_2$ stream. The results clearly indicate the important role of the composition of the injected stream on the evolution of convective dissolution. Due to these facts, well-designed operating conditions in acid gas injection operations may have a significant effect on the onset of convective

instability and consequently long-term fate of the injected acid gases. These findings improve our understanding of mixing mechanisms involved in large scale sequestration of acid gases in deep saline aquifers.

### 5.6 Summary and Conclusions

Co-injection of carbon dioxide ($CO_2$) with impurities such as hydrogen sulphide ($H_2S$) into deep saline aquifers has been suggested as a potential cost-effective option for geological sequestration of acid gases. We studied the effect of $H_2S$ impurity exists in $CO_2$ streams on the convective dissolution of $CO_2$ and impurities using direct numerical simulations. It was found that permitting $H_2S$ impurities significantly affects the dynamics of convective dissolution. The results clearly indicated the important role of the composition of the injected stream on the evolution of convective dissolution. Numerical simulation results showed that the dynamic of the system at the onset of convective dissolution does not hold beyond the onset, such that an impure stream with an earlier onset of convective dissolution develops a slower dynamic at the late time of the process. While an impurity such as $H_2S$ is prone to impede the convective dissolution, it was shown that an informed choice of impurity can lead to similar convective dissolution as of pure $CO_2$ stream. An impure $CO_2$ stream with 52 mol.% $H_2S$ was shown to demonstrate an earlier onset of convective dissolution. It was shown that the rate of dissolution of an impure $CO_2$ stream with $H_2S$ impurity less than ~30 mol.% is nearly similar to the pure $CO_2$ stream. These findings form a basis for further research in this area and engineering of impure streams to improve security and efficiency of impure $CO_2$ storage in deep saline aquifers. However, the hazardous nature of $H_2S$, leakage risk and its subsequent environmental impact should be considered in large scale implementation of impure $CO_2$ storage.

### 5.7 Acknowledgments

The authors would like to thank two anonymous reviewers for their constructive comments and suggestions which greatly improved the quality of the paper. This work was supported by a Discovery Grant from the Natural Sciences and Engineering Research Council of Canada (NSERC), Alberta Innovates - Technology Futures (AITF) foundation and was enabled in part by support provided by WestGrid (www.westgrid.ca) and Compute Canada Calcul Canada (www.computecanada.ca).

# Chapter 6: On the Dynamics of Two-component Convective Dissolution in Porous Media*

## 6.1 Abstract

We studied the influence of the diffusion contrast between species on the dynamics of Rayleigh–Bénard (RB) convection in porous media. The onset time of buoyancy-driven instabilities and convective dissolution flux were quantified using linear stability analysis (LSA) and direct numerical simulations (DNS). The parametric analysis indicates eight distinct instability regions. Different stability mechanisms were characterized over the given range of diffusivity and relative buoyancy ratios. In particular, transition from instabilities solely by double diffusion to Rayleigh–Bénard (RB) convection was identified using linear stability analysis and confirmed using nonlinear simulations. The parametric analysis on the onset also indicates that double diffusion has a potential to accelerate or slow down the RB convection depending on the solutes diffusion contrast. This study provides new insight into the effect of diffusion contrast and can be used to develop strategies for acceleration and deceleration of buoyancy-driven instabilities.

* Jafari Raad, S. M., Hassanzadeh, H., Ennis-King, J. (2018). On the dynamics of two-component convective dissolution in porous media. *Water Resources Research*, (In Press).

## 6.2 Introduction

Buoyancy-driven convection in porous media is of great importance for a wide range of applications related to geophysical and environmental fluid dynamics. Rayleigh–Bénard (RB) convection is a fundamental mechanism for the buoyancy-driven flows leading to nonlinear dynamics of mixing (Lemaigre et al., 2013; Trevelyan et al., 2011). RB instability develops due to negative density stratifications when a heavy solution lies on top of a light one in the gravity field (Trevelyan et al., 2011; Wooding, 1969). RB convection in porous media is observed in applications as diverse as groundwater hydrology (Van Dam et al., 2009; Diersch and Kolditz, 2002; Simmons, 2005), carbon dioxide sequestration (Ennis-King and Paterson, 2005; Hassanzadeh et al., 2005; Lindeberg and Wessel-Berg, 1997; Riaz et al., 2006), soil contamination and waste disposal (Gao et al., 2013; Liu and Dane, 1996; Mao et al., 2006; Schincariol and Schwartz, 1990; Shen and Chengji, 2015; Truex et al., 2015; Xie et al., 2010; Yang and Edwards, 2000), and crystallization processes and magma chambers (Holness et al., 2006; Kuritani et al., 2007; Worster et al., 1990).

Buoyancy-driven instabilities can also develop in an initially stable stratifications due to development of vertically adverse density gradient as a consequence of diffusivity contrast of diffusing components (chemical species or heat/mass) (Radko, 2013; Turner, 1979). Double diffusion (DD) phenomenon is for instance the origin of thermohaline convective motions in oceans (Schmitt, 1994), and magma chamber (Huppert and Sparks, 1984), where both heat and mass diffuse and instabilities develop due to the heat and mass transfer diffusivity contrast. DD instabilities can also occur in binary or multicomponent systems where solutes with different diffusion coefficients establish density gradients in an initially stable density stratification (Griffiths, 1981; Huppert and Turner, 1981; Pringle and Glass, 2002; Trevelyan et al., 2011). Despite numerous studies on RB convection and DD instabilities, the interplay of DD instabilities on dynamics of such systems remains largely unexplored. The potential of the DD mechanism to influence the initiated instabilities in a RB problem has been previously demonstrated in miscible (Carballido-Landeira et al., 2013; Lemaigre et al., 2013; Trevelyan et al., 2011), immiscible (Eckert et al., 2004; Eckert and Grahn, 1999) and, more recently, in a partially miscible systems (Jafari Raad and Hassanzadeh, 2016; Loodts et al., 2018).

Trevelyan et al., 2011, have analysed the differential diffusion effects on buoyancy-driven instabilities in miscible systems with initially step function density profile. Their analysis deals with a two-component miscible system where a denser solution containing a solute A overlies a less dense one containing a solute B. Solutes B and A diffuse with different rates and their relative contribution to the density is positive. Using investigation of time evolving base state density profiles, analytical and numerical experiments, they have classified various Rayleigh–Taylor (RT), double diffusive (DD), diffusive-layer convection (DLC) and delayed-double diffusive (DDD) instability mechanisms in a parameter space characterized by the relative contribution of solutes to the density and their diffusion coefficient ratio. They have shown that the domain of instability obtained from analysis of time-evolving base state density profiles is much larger than the one predicted from linear base state profiles.

A recent study on miscible systems show that DD can lead to a mixed mode dynamic in which the two DD instabilities act cooperatively (Carballido-Landeira et al., 2013). This is the case when upper solution contains a solute A which diffuses sufficiently faster than a solute B which is initially in the underlying less dense solution ($r_D$<1), where $r_D$ is the ratio of diffusion coefficient of solutes A and B, $r_D = D_B/D_A$. More recently, Gopalakrishnan et al., 2018, have renewed interest in understanding the influence of DD mechanisms on the onset of instabilities and fingering pattern in RB convection. It was reported that the onset of instability and rate of advancement of the mixing front in system with $r_D$>1 can be scaled by the maximum density jump around the interface (called dynamic density) due to diffusion contrast. Their study deals with a case with $r_D$>1, where solute B diffuses faster than a solute A.

DD can be encountered in many practical applications in the presence of RB convection and are able to influence the mixing process. Therefore, understanding the role of diffusion contrast on the stability of partially miscible systems is of importance. There are relatively very few studies available in the literature that look into the interplay of DD and RB convection in partially miscible systems. Recently, Jafari Raad and Hassanzadeh (Jafari Raad and Hassanzadeh, 2016, 2017) have studied the impact of DD and its effects on instability of RB convection in the context of impure $CO_2$ sequestration, where dissolved $CO_2$ and $H_2S$ make opposing contributions to the vertical density profile in the aqueous phase. They have shown that the contrast in diffusion coefficients of $CO_2$ and $H_2S$ may give rise to a non-monotonic density profile during the dissolution process depending on the solutes buoyancy ratio $r_\beta r_c = (\beta_B C_{sB}/\beta_A C_{sA})$, where $\beta_i$ and $C_{si}$ are coefficients in

density relation and equilibrium concentration of the solute $i$=A, B, respectively. It was suggested that the buoyancy-driven convection modes can be systematically classified in the ($r_\beta r_c$, $r_D$) parameter space based on the type of the developed base state density profile. In our previous study we have introduced the ($r_\beta r_c$, $r_D$) parameter space merely based on the time-evolving density profile. However, the previous analysis is limited to a special case of $CO_2$/$H_2S$/water system where a fixed diffusion ratio at various mixture compositions was considered. In particular, the stability and dynamics of convective dissolution for the major part of the ($r_\beta r_c$, $r_D$) parameter space emphasizing the differential diffusion effects remained unexplored.

In this work, we examine both stabilizing and destabilizing effects of the diffusion coefficient contrast on RB instabilities and the associated convective dissolution in systems with different diffusivity ratios and opposing contribution of dissolving solutes to the mixture density.

In contrast to the work of (Trevelyan et al., 2011) where they studied a two-component miscible system with positive buoyancy ratios (both solutes A and B increase mixture density upon dissolution), we study another class of buoyancy-driven problems where for a partially miscible system the two chemical species have opposing effect on mixture density. This leads to another interesting dynamics which have not been explored in previous studies.

Our objective is to understand how the onset and the associated convective dissolution can be controlled by altering the diffusion contrast of the chemical species. To achieve this, we consider partially miscible systems with a sharp interface where two solutes A and B with diffusion contrast and opposing effect on density diffuse into the underlying less dense fluid. While dissolution of solute A increases the density of the host fluid layer, solute B decreases the density. First, we examine the effect of diffusion contrast where unstable density evolves in the gravity field upon dissolution and the net contribution of the solutes A and B to the density is positive ($-r_\beta r_c<1$). Using linear stability analysis (LSA) and direct numerical simulation (DNS), we have quantified the interplay of DD instabilities and RB convection in terms of the onset time and convective dissolution flux. Our parametric analysis on the onset indicates that double diffusion has a potential to accelerate or slow down the RB convection depending on the solutes diffusion contrast.

We also discuss the possible enhancement of DD effects in systems with negative net density contribution of the solutes, where the effect of solute A on increasing density is lower than the effect of solute B in decreasing the density ($-r_\beta r_c>1$) and instabilities occur solely due to a locally

unstable density gradient that results from the diffusion contrast. Our results show that for a given buoyancy ratio ($r_\beta r_c$), this system can be either stabilized or destabilized depending on the diffusion contrast of the diffusing species, allowing a possible control on the onset and associated convective dissolution. Parametric analysis for this system reveals a transition from pure DD instabilities to RB convection at relatively high diffusion contrast, leading to significantly earlier onset of convective instability and higher dissolution flux. It is shown that the key point to distinguish whether the diffusion contrast has a stabilizing or destabilizing effect on buoyancy-driven instabilities depends on the relative contribution of the two species to the density. Although, the focus of this study is on solutal natural convection, the insight developed here can be applied equally to thermohaline problems.

This paper is organized as follows. In section 6.3, we describe the problem of interest by presenting the governing equations, initial and boundary conditions followed by base state solutions for the diffusive mass transfer and the density profile. In sections 6.4 and 6.5, mathematical formulation and description of linear stability analysis and direct numerical simulations are presented, respectively. Results and discussion are presented in section 6.6 followed by section 6.7, which is the conclusion of this study.

## 6.3 Mathematical Formulation

### 6.3.1 Governing equations

We consider a two-dimensional, homogeneous and isotropic porous layer of thickness, *H*, saturated with quiescent fluid initially free of solute. No-flow boundary conditions are considered at the top and bottom of the domain with respect to pressure. A no-flux boundary condition is maintained at the bottom of the domain while a constant concentrations of solutes A and B are set at the top of the domain with respect to the mass transport. The porous layer is assumed to be laterally infinite and flow and solute transport are considered to take place at isothermal conditions.

Using the Boussinesq approximation, and neglecting rock and fluid compressibility effects, viscosity variability, cross diffusion and dispersion effects, the convective transport of non-reactive single phase flow in a porous medium is described as follow (Bear, 1972):

$$D_i \phi \nabla^2 C_i - \mathbf{v} \cdot \nabla C_i = \phi \frac{\partial C_i}{\partial t}; \tag{6.1a}$$

$$\nabla \cdot \mathbf{v} = 0; \tag{6.1b}$$

$$\mathbf{v} = -\frac{k}{\mu}(\nabla p - \rho \mathbf{g} \nabla z), \tag{6.1c}$$

where $\mathbf{v}(u,v)$ is the Darcy velocity vector, $p$ is the pressure, $C$ is the solute concentration, $\mu$ is the water viscosity, $t$ is the time, $k$ is the permeability, $\phi$ is the porosity, $g$ is the gravitational acceleration, $z$ is the vertical coordinate and positive downwards, $D_i$ is the effective molecular diffusion coefficient in porous media and assumed to be independent of concentration for dilute solutions, and subscript $i$ denotes the species index with $i$ =A , B.

Mass conservation equations of solutes A and B (6.1a) is coupled to Darcy's law (6.1c) through a constitutive relation for the density as $\rho=\rho_b(1+\beta_A C_A+\beta_B C_B)$ where $\rho_b$ is the fluid density at $C = 0$, and $\beta$ is coefficient of density variation, which is defined as $\beta_i = \frac{1}{\rho_b} d\rho / dC_i$, and has positive and negative values for solute A and B, respectively.

The governing equations are nondimensionalized using the thickness of the porous layer ($H$) as the length scale, $H^2/ D_A$ as the time scale, and equilibrium solubility of solute A as the concentration scale, $C_A^s$. We also scaled the effective molecular diffusion coefficients using the molecular diffusion coefficient of solute A as $r_{Di}=D_i/D_A$. In nondimensional form, the diffusive mass transfer mechanism as a base state of the dissolution process, prior to the onset of convection ( $\mathbf{v} = 0$ ) is described as

$$r_{Di} \frac{\partial^2 c_{0i}}{\partial \hat{z}^2} = \frac{\partial c_{0i}}{\partial \hat{t}} \ , \tag{6.2}$$

where subscript 0 denotes the base state condition.

Given the initial and boundary conditions $c_{0i}(\hat{z},\hat{t}=0)=0$ and, $c_{0i}(0,\hat{t}) = C_i^s / C_A^s = r_{ci}$ , $\partial c_{0i}(1,\hat{t}) / \partial \hat{z} = 0$, respectively, the diffusive base state solution is given by:

$$c_{0i} = r_{ci}\left[1 - \frac{2}{\pi}\sum_{n=1}^{\infty}\frac{1}{\lambda_n}\sin(\lambda_n \pi \hat{z})\exp\left(-\lambda_n^2 \pi^2 r_{Di}\hat{t}\right)\right], \tag{6.3}$$

where $\lambda_n=(2n\text{-}1)/2$, $r_{cA}=1$, $r_{cB}=r_c$, $r_{DA}=1$, $r_{DB}=r_D$.

Using the proposed density-concentration relationship, the vertical density profile is given by:

$$\hat{\rho}=1-\frac{2}{\pi}\sum_{n=1}^{\infty}\frac{1}{\lambda_n}\sin\left(\lambda_n\pi\hat{z}\right)\exp\left(-\lambda_n^2\pi^2\hat{t}\right)+r_c r_\beta\left[1-\frac{2}{\pi}\sum_{n=1}^{\infty}\frac{1}{\lambda_n}\sin\left(\lambda_n\pi\hat{z}\right)\exp\left(-\lambda_n^2\pi^2 r_D\hat{t}\right)\right], \quad (6.4)$$

where $\hat{\rho}=(\rho-\rho_b)/C_A^s\beta_A\rho_b$, and $r_\beta=\beta_B/\beta_A$ is the ratio of the coefficients of density variation of solute B to solute A.

Depending on the values of $r_\beta r_c$ and $r_D$, the base state concentration profiles imply various density profiles (Jafari Raad and Hassanzadeh, 2016). Here, we study the effect of diffusion contrast on dynamics of the system for $-r_\beta r_c<1$ and $-r_\beta r_c>1$. For the first case ($-r_\beta r_c<1$), the net density contribution of solutes is positive, and instabilities can develop due to the negative density gradient in the gravity field. The interface density $\hat{\rho}_{\text{int}}$, is defined as the density difference from the original fluid density at $z=0$, and is given by, $\hat{\rho}_{\text{int}}=1+r_\beta r_c$.

For the second case ($-r_\beta r_c>1$), the net density contribution of the solutes is negative, and instabilities develop solely due to locally negative density stratifications induced by the double diffusion mechanism. We will show how the DD affect the RB convection in these two different types of density configurations, and how differential diffusion of diffusing solutes affect the instability criterion of the system and nonlinear dynamic of convective dissolution.

### 6.3.2 Linear stability analysis

A linear stability analysis using quasi-steady state approach (QSSA) was conducted to study the growth of perturbation and consequently to determine the onset of convective instabilities. To conduct a linear stability analysis, the governing equations of flow and transport given in Equation (6.1) are perturbed using $\mathbf{s}=\mathbf{s}_0+\mathbf{s}'$ where $\mathbf{s}=\mathbf{s}[p,\mathbf{v},c_A,c_B,\rho]$ and $s'$ are the base state and infinitesimal perturbations of pressure, velocities, concentration and density, respectively.

Substituting the perturbed variables into the flow and transport equations, implementing the base state quantities, linearizing in perturbations and after simplification, we obtain the following perturbed equations:

$$\nabla_2^2 v' = \mathrm{Ra}\,\frac{\nabla_1^2 c_A' + r_\beta \nabla_1^2 c_B'}{1 + r_\beta r_c}; \tag{6.5a}$$

$$r_{Di}\nabla_2^2 c_i' - v'\frac{\partial c_{0i}}{\partial z} = \frac{\partial c_i'}{\partial t}\ , \tag{6.5b, c}$$

where the velocity perturbation is scaled by $\phi D_A/H$, $\nabla_1^2 = \nabla_x^2$, $\nabla_2^2 = \nabla_{xz}^2$, $\mathrm{Ra} = kg\rho_b\beta_A C_A^s H(1+r_\beta r_c)/\mu\phi D_A$ and $i$=A, B, and the hats (^) are dropped for convenience.

For cases with $-r_\beta r_c = 1$ ($\hat{\rho}_{\mathrm{int}} = 0$), Equation (6.5a) is reduced to $\nabla_2^2 v' = \mathrm{Ra}^*\left(\nabla_1^2 c_A' + r_\beta \nabla_1^2 c_B'\right)$, where $\mathrm{Ra}^* = kg\rho_b\beta_A C_A^s H/\mu\phi D_A$.

The perturbed velocity and concentration are expressed as $[c'_A, c'_B, v'] = [c_A^*, c_B^*, v^*](z,t)e^{-i\kappa x+\omega t}$ where $\kappa$ and $\omega$ are the perturbation wave-number and growth rate, respectively. Using Equation (6.5) we obtain

$$\frac{\partial^2 v^*}{\partial z^2} - \kappa^2 v^* = \mathrm{Ra}(-\kappa^2)\frac{c_A^* + r_\beta c_B^*}{1 + r_\beta r_c}; \tag{6.6a}$$

$$r_{Di}\frac{\partial^2 c_i^*}{\partial z^2} - \kappa^2 c_i^* - v^*\frac{\partial c_{0i}}{\partial z} = \omega c_i^*, \tag{6.6b, c}$$

The perturbed flow and mass transfer boundary conditions are given as $v^*(0) = v^*(1) = 0$, and $c_i^*(0) = 0, \partial c_i^*(1)/\partial z = 0$, respectively.

Conducting quasi-steady-state approximation (QSSA) (Tan and Homsy, 1986), $\partial c_{0i}/\partial z$ in Equations (6.6b) and (6.6c) can be evaluated at time $t_0$ or the so called "frozen time" during the growth of perturbations. For the sake of brevity, we refer the reader to the previous studies for more details on QSSA approach (Jafari Raad et al., 2016) and its limitations (Trevelyan et al., 2011).

The system of perturbed Equations (6.6a-c) are discretized using a second-order finite difference method and then solved numerically to find the growth rate, ω, as a function of assigned wave-

number, $\kappa$. The following matrix form eigenvalue problem can be obtained using the discretized equations after some rearrangements (Jafari Raad et al., 2016).

$$\begin{bmatrix} [\mathbf{A}_c]+\dfrac{\mathrm{Ra}\,\kappa^2}{1+r_\beta r_c}[\mathbf{A}_v]^{-1}\left[\dfrac{\partial c_{0A}}{\partial z}\right] & \dfrac{\mathrm{Ra}\,\kappa^2 r_\beta}{1+r_\beta r_c}[\mathbf{A}_v]^{-1}\left[\dfrac{\partial c_{0A}}{\partial z}\right] \\ \dfrac{\mathrm{Ra}\,\kappa^2}{1+r_\beta r_c}[\mathbf{A}_v]^{-1}\left[\dfrac{\partial c_{0B}}{\partial z}\right] & r_D[\mathbf{A}_c]+\dfrac{\mathrm{Ra}\,\kappa^2 r_\beta}{1+r_\beta r_c}[\mathbf{A}_v]^{-1}\left[\dfrac{\partial c_{0B}}{\partial z}\right] \end{bmatrix}\begin{bmatrix} c_A^* \\ c_B^* \end{bmatrix}-[\boldsymbol{\omega}]\begin{bmatrix} c_A^* \\ c_B^* \end{bmatrix}=0\,. \tag{6.7}$$

where $\mathbf{A}_v=(\mathbf{D}_v-\kappa^2\mathbf{I})$, $\mathbf{A}_c=(\mathbf{D}_c-\kappa^2\mathbf{I})$, $\mathbf{D}_v$, and $\mathbf{D}_c$ are coefficient matrices based on central discretization of the second derivatives and **c** and **v** are vectors containing the unknown variables at the discrete nodes.

This eigenvalue problem is solved numerically, and the maximum eigenvalue of the coefficient matrix is considered as the growth rate corresponding to the assigned wavenumber, $\kappa$ and *Ra* number at certain diffusive time, $t_0$. A positive growth rate at a particular time is an indication of instability. Thus, the time at which the growth rate turns positive at a given wave-number represents the onset of instability. The onset of instability is evaluated based on the obtained growth rate of the initial perturbations for given wave-numbers, using dispersion curves. For brevity, we refer the reader to (Emami Meybodi and Hassanzadeh, 2013; Jafari Raad and Hassanzadeh, 2015; Riaz et al., 2006; Tan and Homsy, 1986) for more details on the numerical procedure and the validity of the computational algorithm

### 6.4 Numerical Simulations

We have conducted direct numerical simulations (DNS) to gain further insights into the effects of diffusion contrast on instability behaviour and the nonlinear dynamics of mixing beyond the onset. We solved the nonlinear problem with a high accuracy numerical model developed based on a well-known IMPEC approach where the implicit scheme is used to discretize flow Equations (6.1b) and (6.1c) while the transport Equations (6.1a) are treated explicitly (Settari, 2001). The developed numerical model is based on a uniform Cartesian grid and second order finite difference discretization of the governing Equations (6.1a-c). The numerical model considers the same physical domain and the boundary conditions described in section 6.3. The reader may refer to (Coats, 1969; Emami-Meybodi and Hassanzadeh, 2015; Hassanzadeh et al., 2005) for further

details on the numerical model and controls on the accuracy and convergence of the numerical solutions.

## 6.5 Results and Discussion

### 6.5.1 Systems with ($-r_\beta r_c < 1$)

The density profile in a binary system demonstrates both monotonic and non-monotonic behaviour, depending on the relative buoyancy ($r_\beta r_c$) and diffusion coefficient ratio ($r_D$) (Jafari Raad and Hassanzadeh, 2016). Our objective here is to examine the onset and associated nonlinear dynamics in systems with $-r_\beta r_c < 1$ over the given range of diffusivity ratio, $0.1 < r_D < 100$. Figure 6.1 shows the effect of solutes diffusion coefficient ratio on the growth rate of perturbations at the given buoyancy ratio ($-r_\beta r_c = 0.5$) and (a) $t$ = 0.0002 and (b) 0.0001. The results shown in Figure 6.1(a) demonstrate clear dissimilarities in stability behaviour of systems with $r_D < 1$ and those with $r_D > 1$. While the growth rate increases by increasing diffusion contrast when $r_D > 1$, systems with $r_D < 1$ do not follow the same behaviour. The results show that a system with $r_D = 0.1$ leads to higher growth rates as compared to systems with $r_D = 0.2$, 0.5 and 1. This behaviour is mainly attributed to the shape of the density profile in each system which varies significantly with diffusion coefficient ratio, $r_D$. While systems with $r_D = 0.1$ and 0.2 lead to non-monotonic density profiles with a local maximum at the diffusive boundary layer, systems with $r_D = 1$(no differential diffusion effects) and 0.5 show monotonic, and monotonic with an inflection point density profiles, respectively.

These results suggest that systems with non-monotonic density profile associated with local maximum (systems with $r_D = 0.1$ and 0.2) are gravitationally more unstable than those with monotonic one (systems with $r_D = 0.5$ and 1). However, the distinction between the two systems with non-monotonic density profiles is still not clear. We will show how the shape of a non-monotonic density profile controls the growth rates and consequently onset of convection. Figure 6.1(b) shows the growth rate of perturbations for systems with $r_D \geq 1$. In the case of $r_D > 1$, the density profile features a nonmonotonic behaviour with a local minimum (Jafari Raad and Hassanzadeh, 2016). As it is seen, the growth rate of perturbations increases as the diffusivity ratio increases

over the given range of $r_D$. The results also suggest that the effect of diffusion contrast on the instability of the system reaches a plateau for $r_D$~≥50.

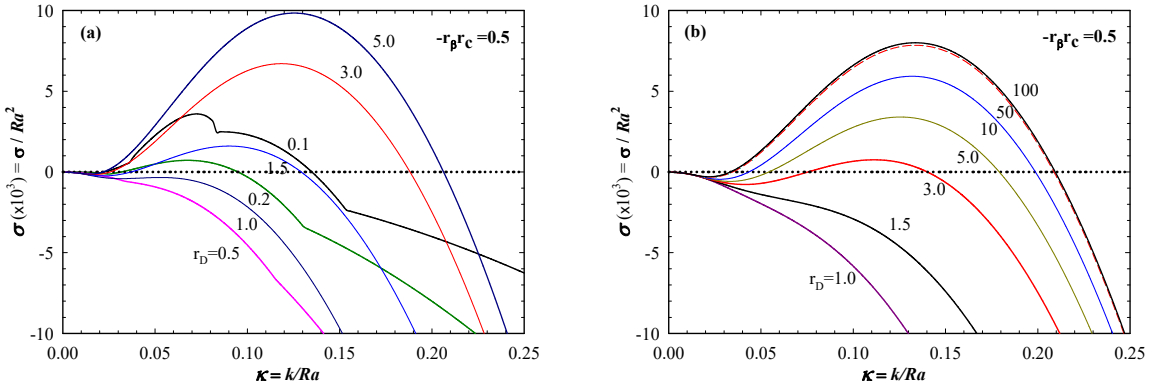


**Figure 6.1:** Growth rates versus dimensionless wavenumber for a system with $-r_\beta r_c$=0.5 at Ra=|500| and different diffusivity ratios (a) $t$ = 0.0002 and $r_D$=0.1, 0.2, 0.5,1, 1.5, 3,5, and (b) $t$ = 0.0001 and $r_D$=0.5, 1.5, 3, 5, 10, 50,100.

To further clarify the results of growth rate, we investigated the onset of instabilities in systems with various diffusion contrasts. Results for the onset recover the well-known scaling of $\hat{t} = aRa^{-2}$ at a given diffusion ratio. The results show that, while systems with different diffusivity contrasts result in the same scaling relations for the onset of convective instabilities, they give a prefactor that is a strong function of the diffusion ratio, $r_D$. The dependence of the scaling prefactor on $r_D$ for the system with $-r_\beta r_c$=0.5 is shown in Figure 6.2(a). The inset plots represent the base state density profiles corresponding to each region. It can be seen that the scaling prefactor for the onset is strongly controlled by the diffusion ratio. The results show that the scaling prefactor increases as the diffusivity ratio increases for systems with small and intermediate values of diffusivity ratio ($0.1<r_D<0.63$) suggesting delayed onset by increasing the diffusivity ratio. This refers to region I ($r_D<(-r_\beta r_c)^2$) and II ($(-r_\beta r_c)^2<r_D<(-r_\beta r_c)^{2/3}$) in Figure 6.2 where the double diffusive mechanism leads to non-monotonic density profile with a local maximum and monotonic density profile with an inflection point, respectively. The scaling prefactor shows a maximum at $r_D$~0.63 ($r_D=(-r_\beta r_c)^{2/3}$),

based on the previously developed space parameter reported by (Jafari Raad and Hassanzadeh, 2016)), and then decreases monotonically leading to a constant value of ~14 for $r_D$~≥50. The same scaling prefactor is obtained for systems where $r_D \rightarrow 0$.

Careful inspection of the base state density profiles in systems with different diffusivity ratios, shown in Figure 6.2(b), reveals that a favorable density difference (dynamically unstable density profile) acts as a driving force of instabilities and is controlled by $r_D$. For a non-monotonic density profile with a local maximum (region I), the driving density difference ($\Delta\rho_u$) decreases as the diffusivity ratio increases. In this case, the local maximum occurs due to higher diffusion coefficient of solute A compared with solute B. In such a case, the diffusion front of solute A is ahead of solute B increasing the local solution density such that the density at the diffusion front of solute A is higher than both interface density and fresh fluid density. The driving density difference ($\Delta\rho_u$) in regions II ($(-r_\beta r_c)^2 < r_D < (-r_\beta r_c)^{2/3}$ with monotonic density profile with inflection point) and III ($(-r_\beta r_c)^{2/3} < r_D < 1$ with monotonic density profile) remains almost constant. However, it can be shown that the density gradient decreases with the diffusivity ratio in region II. In contrast, the density gradient increases with the diffusivity ratio in region III.

It can be also observed that the driving density difference ($\Delta\rho_u$) increases with the diffusivity ratio in region IV ($r_D > 1$ with non-monotonic density profile with a local minimum) and approaches unity at high diffusion ratios where the extremum diminishes, and density follows a monotonic density profile. In this case, the diffusion front of solute B is ahead of solute A decreasing the local solution density such that the density at the diffusion front of solute B is lower than interface density. Comparison of the results of scaling prefactor for the onset and the driving density differences as a function of diffusivity ratio is shown in Figures 6.2(a) and (b) reveals the important role of diffusion contrast on evolution of the unstable density profile.

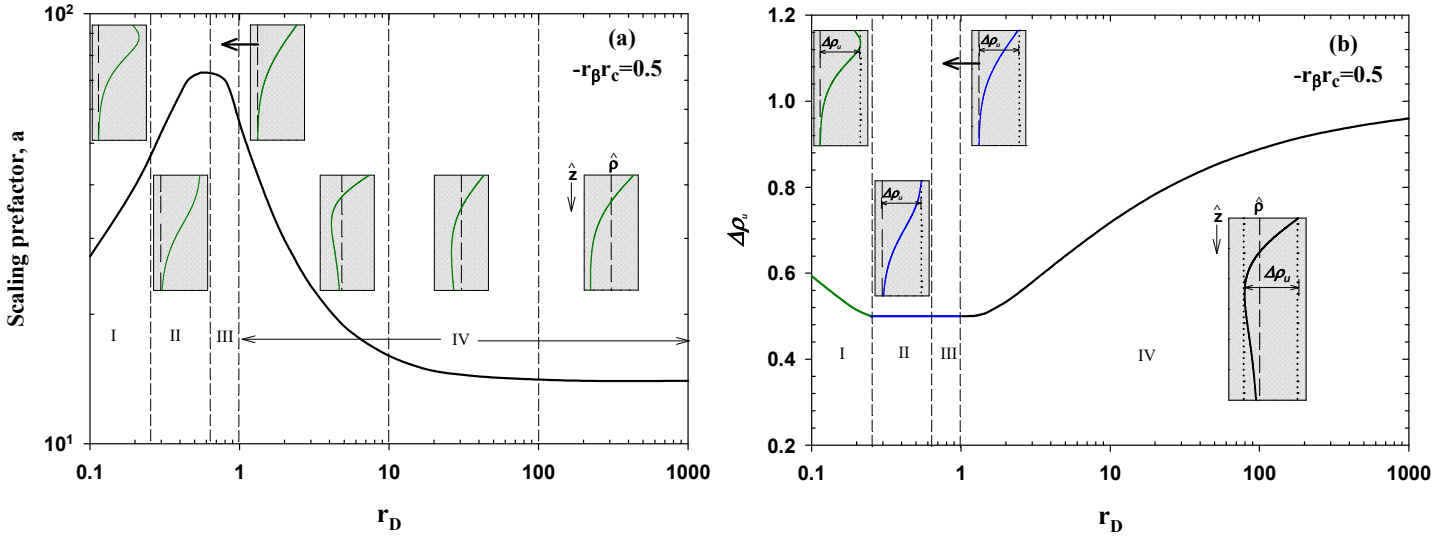


**Figure 6.2:** (a) Scaling prefactor *a,* and (b) driving density difference as a function of diffusion coefficient ratio ($r_D$) for systems with $-r_\beta r_c=0.5$. The inset plots represent the base state density profiles corresponding to each region.

For further insight, we examine the dependence of the scaling prefactor for the onset on the driving density difference induced by the diffusion contrast. Figure 6.3 shows the scaling prefactor for the onset as a function of the driving density difference for non-monotonic density profiles with (a) local maximum and (b) local minimum. The density profile with local maximum shown in Figure 6.3(a), reveals a prefactor which scales inversely with $\Delta\rho_u$ leading to $a=10.552\,\Delta\rho_u^{-1.869}$. Figure 6.3(b) shows the dependency of scaling prefactor to $\Delta\rho_u$ for systems with a local minimum. It can be observed that the scaling prefactor decreases with $\Delta\rho_u$. This system leads to a constant prefactor at high diffusivity ratio suggesting a unified instability behaviour similar to RB. This is the case when the second species (B) diffuses much faster than solute A, and its diffusive front is far ahead of that of solute A.

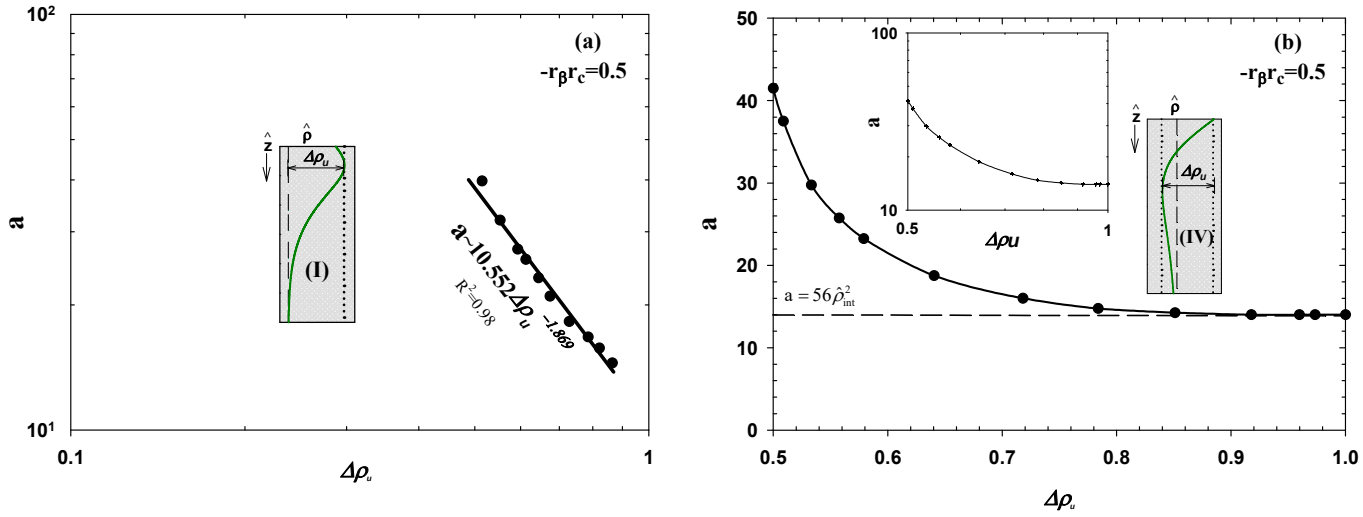


**Figure 6.3:** Scaling prefactor for the onset as a function of the driving density difference ($\Delta\rho_u$) for systems representing nonmonotonic density profile with (a) region I ($r_D<(-r_\beta r_c)^2$) with local maximum and (b) region IV ($r_D>1$) with local minimum at a constant interface density, $-r_\beta r_c=0.5$.

To further support these findings and to understand the dynamics of mixing beyond the onset of instability, we inspected the dissolution flux of diffusing species through direct numerical simulations. 2D numerical simulations were conducted to evaluate the nonlinear dynamics of mixing and convective dissolution flux in various regions with different density profiles, marked in Figure 6.2.

All numerical simulations were performed at |Ra|=500, using the same parameters defined in the linear stability analysis. Figure 6.4 shows the numerical measurement of dissolution flux as a function of time. The dissolution flux per unit area is expressed as the time derivative of cumulative dissolution as given by:

$$F(\hat{t}) = \frac{1}{A}\frac{d}{d\hat{t}}\int_{V_p} \overline{C}(\hat{t})dV \ , \tag{6.8}$$

where $Vp$ indicates the domain pore volume, $A$ is the cross-sectional area of the interface and $\overline{C}$ is the average concentration of both species in the entire domain.

As predicted by the LSA, the onset of convection (open circle symbols shown in Figure 6.4) is significantly different for systems with different diffusion coefficient ratios. Consistent with the

results of the stability analysis, a system with $r_D = 0.1$ (falls in region I) leads to an earlier onset as compared to systems with $r_D = 0.5$ (fall in region II). For systems with $r_D$>0.5 (regions III and IV), the onset of convection (marked by a sharp increase in the dissolution flux) decreases as $r_D$ increases. It can be observed that a higher diffusivity ratio results in a larger maximum flux and earlier shutdown regime. In agreement with results of LSA, systems with $r_D$>20 (region IV) lead to very similar onset times. However, the dynamics of the system beyond the onset of instabilities is different. Inspection of the convective dissolution flux for each species with $r_D$=50, shown in the inset plot (b), reveals that while dissolution of solute A is controlled by both diffusion and convective dissolution, solute B is transported and dissolved merely by diffusion. However, this is not the case for systems with lower diffusivity ratios, as it seen from the inset plot (a) for the system with $r_D$=0.1. The same observation can be made from the concentration distributions, shown as inset contours for systems with (a) $r_D$=0.1 and (b) $r_D$=50. The concentration distribution also shows the significant differences in development of diffusive boundary layer and associated fingering patterns in these systems. This analysis shows that diffusion contrast has a great impact on the RB convection, allowing a possible control of the onset and the associated convective dissolution in partially miscible systems.

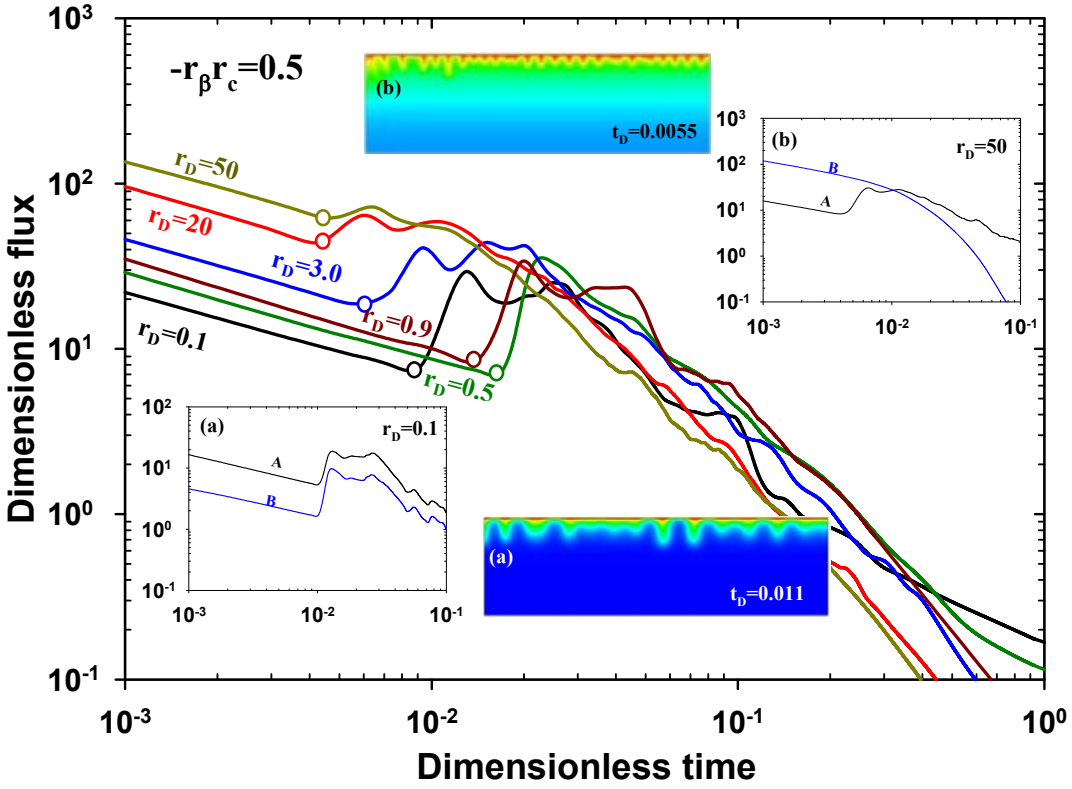


**Figure 6.4:** Dimensionless dissolution flux versus dimensionless time for the cases with $-r_\beta r_c$=0.5, at |Ra|=500 and different diffusivity ratios $r_D$=0.1, 0.5, 3.0, 20 and 50. Inset plots show convective dissolution flux for each species in cases with (a) $r_D$=0.1 and (b) $r_D$=50. The inset maps show the corresponding concentration distribution of diffusing species (A+B) in cases with (a) $r_D$=0.1 and (b) $r_D$=50, at the given diffusive times.

### 6.5.2 Systems with ($-r_\beta r_c$ >1)

Here, we examine the effect of diffusion contrast on stability criterion and the dynamics of connective dissolution in systems with negative interface density where the increasing density effect of solute A is lower than the decreasing density effect of solute B ($-r_\beta r_c$ >1) and instabilities occur due to locally unstable density profile as a result of double diffusion mechanism. Our objective is to investigate the possible enhancement of instabilities and convective dissolution in systems with different diffusion coefficient ratios.

Figure 6.5 shows LSA results of scaling prefactors for the onset in system with $-r_\beta r_c$=1.5, at different diffusivity ratios ($r_D$). Inset plots represent the base state density profiles corresponding to each region. Results shows that for systems with $r_D$<1 the scaling prefactor increases as the diffusivity ratio increases, suggesting a delayed onset at a higher diffusivity ratio. This refers to region V ($r_D$<1) in Figure 6.5 where diffusion contrast leads to a non-monotonic density profile with a local maximum. Inspection of the base state density profile in this region shows that as the diffusion ratio increases the locally unstable density profile induced by double diffusion shrinks gradually toward the stable one at $r_D$=1.

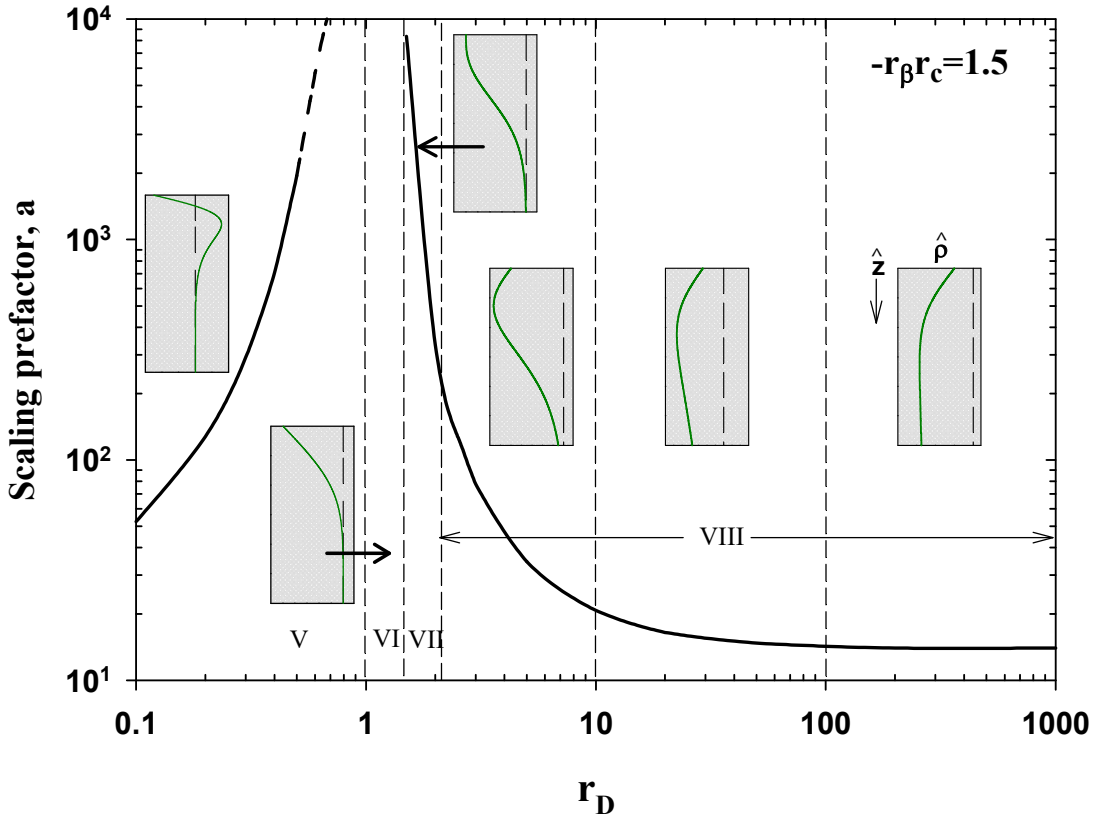


**Figure 6.5:** Scaling prefactor as a function of diffusion coefficient ratio ($r_D$) for systems with $r_\beta r_c$=-1.5. The inset plots represent the base state density profiles corresponding to each region.

As discussed earlier, there is a direct relation between the magnitude of the driving density difference and the instability criteria for the system. Figure 6.6(a) shows the dependency of the scaling prefactor to the driving density difference ($\Delta\rho_u$) in systems with a non-monotonic density profile and a local maximum. The results show that the prefactor scales inversely with the driving density difference, $\Delta\rho_u$, leading to $\mathbf{a}=9.652\ \mathbf{\Delta\rho_u}^{-2.25}$.

For systems with $1<r_D<(-r_\beta r_c)^{2/3}$ (region VI) LSA suggests a stable diffusive boundary layer where diffusion is the only mechanism controlling the dissolution process. In this case, the density profile remains always monotonically increasing downward (Jafari Raad and Hassanzadeh, 2016). It interesting to note in region VII where $(-r_\beta r_c)^{2/3}<r_D<(-r_\beta r_c)^2$ while the base density profile is increasing downward monotonically and one may intuitively expect a stable system, the LSA results show that the system is in fact unstable due to the double diffusive effect. In this region, the scaling factor decreases as the diffusion ratio increases. It worth noting that while the base density profile provides an insight into possibility of evolution of instabilities, it does not provide information on the growth of perturbations and the consequences of the double diffusion effect. It can be also observed that the prefactor decreases as the diffusivity ratio increases over the given range of $r_D>(-r_\beta r_c)^2$ (region VIII) suggesting an earlier onset time. In this case, the density profile is nonmonotonic. The scaling prefactor results, shown in Figure 5, also suggest that DD does not play a significant role on the instability of the system with $r_D>50$. From the inset plot, it can be observed that for large values of $r_D$ the peak in density diminishes resulting in a monotonically decreasing density profile.

Figure 6.6(b) shows the dependency of the onset time to the driving density difference for system with $r_D>r_\beta r_c^2$. The results show that the scaling prefactor scales inversely to the driving density difference ($\Delta\rho_u$) leading to $\mathbf{a}=12.263\mathbf{\Delta\rho_u}^{-0.543}$. It can be observed that the scaling prefactor decreases as the driving density difference increases leading to a unified stability criterion similar to the single component problem in a RB convection at $\Delta\rho_u\sim1$ for $r_D>50$. The same observation was made for systems with $-r_\beta r_c<1$ and $r_D>50$ discussed in section 6.6.1. In this case, solute B diffuses much faster than solute A and decreases the density of underlying fluid layers far ahead of diffusion front of solute A providing a favorable density profile between the upper A-rich dense layer and lower less dense B-rich fluid layer. This observation will be further elaborated in the following using numerical simulations.

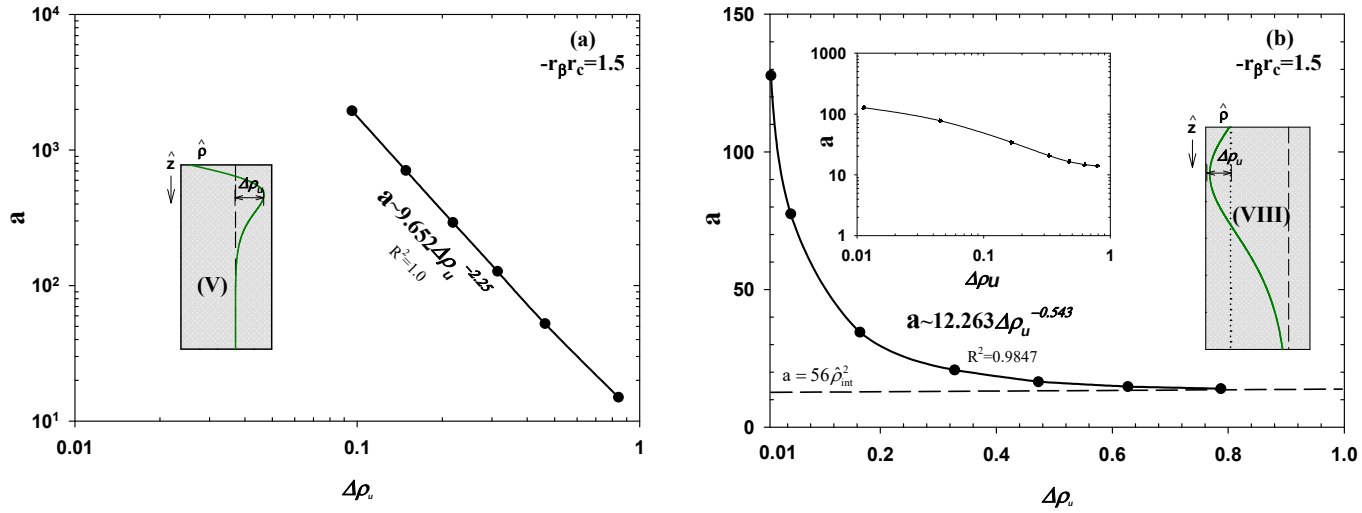


**Figure 6.6:** Scaling prefactor for the onset as a function of the driving density difference for systems representing nonmonotonic density profile with (a) region V ($r_D$<1) with local maximum and (b) region VIII ($r_D$>$(-r_\beta r_c)^2$) with local minimum at constant interface density, $-r_\beta r_c$=1.5.

Figure 6.7 shows the results of numerical for dissolution flux in systems with $-r_\beta r_c$>1 for different diffusion coefficient ratios. As predicted by linear stability analysis, a system with $r_D$=0.1 (region V) leads to an earlier onset, marked by a sharp increase in the dissolution flux, as compared to systems with $r_D$=0.5 (region V), $r_D$=2 (region VII) and $r_D$=3 (region VIII). Examination of the convective flux beyond the onset, however, shows that a system with $r_D$=0.1 leads to lower convective dissolution flux and experiences a delayed shutdown regime as compared to the system with $r_D$ =2 and $r_D$=3. This behaviour can be credited to the accumulation of less dense B-rich mixture below the interface on the top layer due to smaller diffusivity of species B. In other words, the initiated convective motion homogenizes the concentrations gradient within the mixing zone, which would counteract the effect of double diffusion on the density stratification and consequently the mixing behaviour.

In the case of $r_D$>$(-r_\beta r_c)^{2/3}$(regions VII and VIII), systems with higher diffusivity ratio result in larger maximum flux and show earlier shutdown regime. In agreement with results of LSA, systems with $r_D$>20 lead to very similar onset times. However, the dynamics of the system beyond the onset of instabilities is quite different. Inspection of individual dissolution flux of solutes A

and B in this system, shown in the inset plot (b) in Figure 6.7, confirms that at high diffusion ratio solute A is the only component which contributes to the convective dissolution representing similar dissolution dynamics to those in a single component system. The inset concentration maps show the concentration distributions of diffusing species (A+B) for systems with (a) $r_D$=0.1 and (b) $r_D$=50. The separate frontal diffusive boundary layer for solutes A and B is clearly observed from the inset contour (b). It can be also observed that these two systems lead to different diffusive boundary layers and the associated fingering patterns.

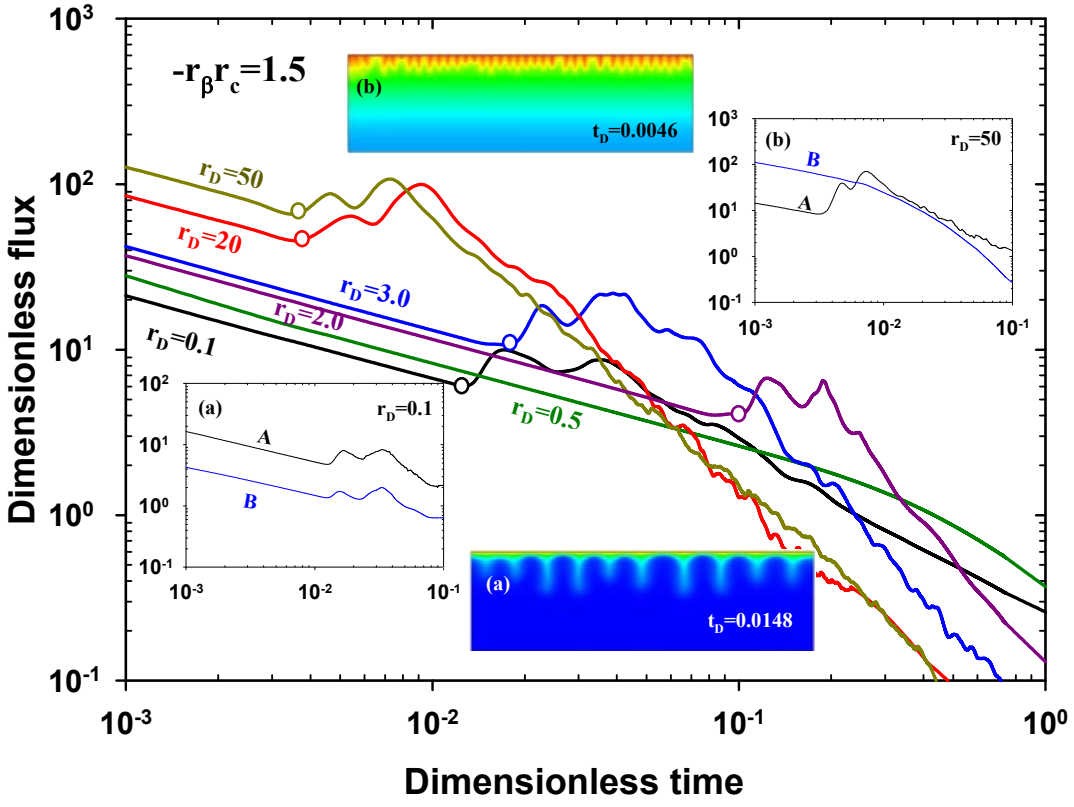


**Figure 6.7:** Dimensionless dissolution flux versus dimensionless time for the cases with $-r_\beta r_c$=1.5, at |Ra|=500 and different diffusivity ratios $r_D$=0.1, 0.5, 2, 3.0, 20 and 50. Inset plots show convective dissolution flux for each species in cases with (a) $r_D$=0.1 and (b) $r_D$=50. The inset contours show the corresponding concentration distribution in cases with (a) $r_D$=0.1 and (b) $r_D$=50, at the given scaled diffusive time.

Figure 8 summarizes the above discussed stability regions in form of the parameter space ($-r_\beta r_c$, $r_D$), the associated density profiles, and the typical fingering patterns for each region. Detailed theory on construction of the parameter space classification has been reported elsewhere (Jafari Raad and Hassanzadeh, 2016). This figure shows how the characteristic shape of density profiles control the evolution of convective instabilities and fingering patterns in different parameter space regions. It can be observed that the shape of fingers, their growth rates and spreading patterns in different space parameter regions are changed and highly controlled by the buoyancy and diffusivity ratio parameters. It interesting to note in region VII where $(-r_\beta r_c)^{2/3}<r_D<(-r_\beta r_c)^2$ while the characteristic shape of base density profile suggests a stable system, numerical simulations in accordance with the LSA suggest an unstable system.

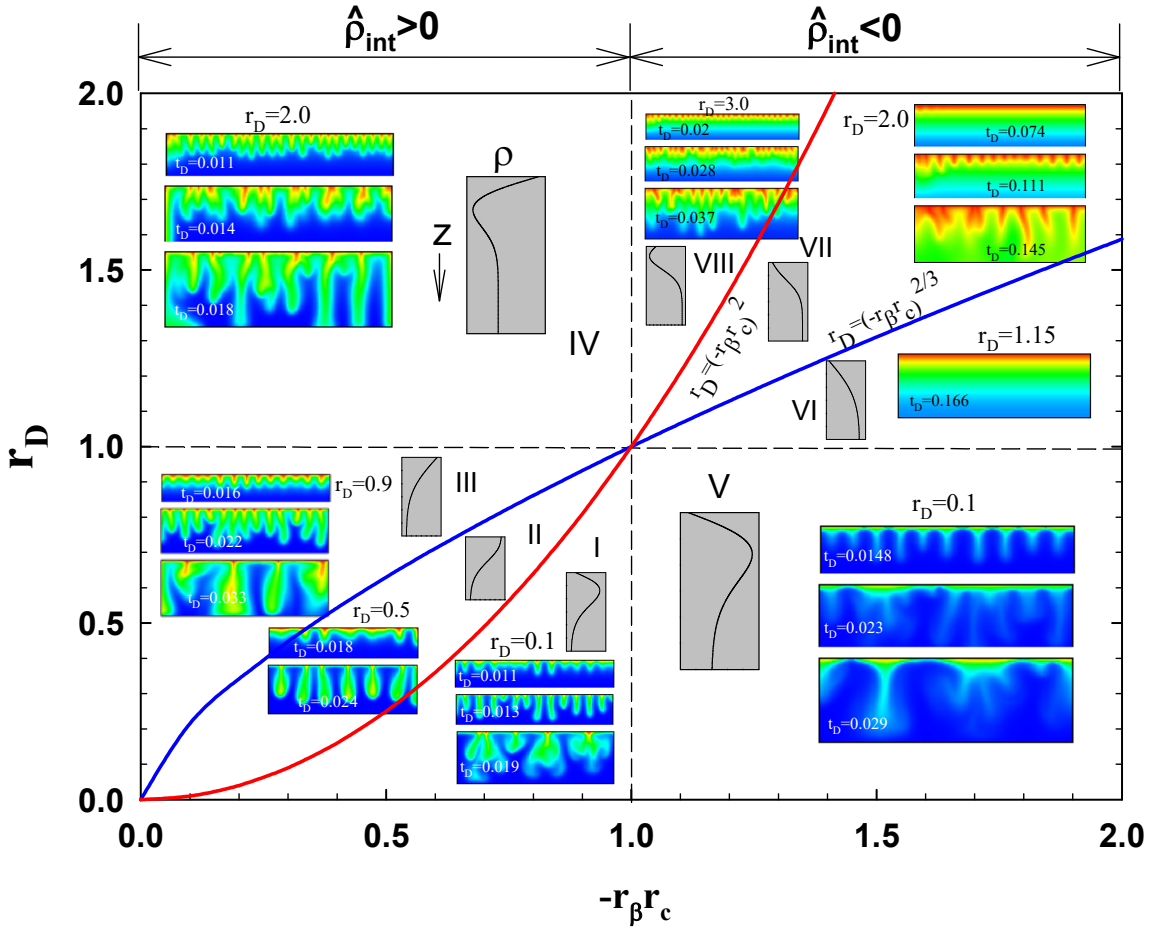


**Figure 6.8:** Parameter space ($-r_\beta r_c$, $r_D$) classification shows various stability regions. Inset plots are the base state density profiles with depth. Inset 2D concentration maps show fingering patterns for systems with |Ra| =500, at the given diffusivity ratio and the scaled diffusive time.

### 6.6 Summary and Conclusions

We studied stabilizing and destabilizing effects of diffusion contrast on the onset of Rayleigh–Bénard (RB) convection and the associated mixing in partially miscible systems. Using linear stability analysis and direct numerical simulations, we have quantified the role of diffusion contrast on convective instabilities in terms of onset time and convective dissolution flux. In particular, two important categories of $-r_\beta r_c$ <1 and $-r_\beta r_c$ >1 were studied. In both categories, dissolution of solute A increases the mixture density while solute B decreases the density. In the first category ($-r_\beta r_c$ <1), the impact of solute A on density increase is greater than the effect of solute B on density

reduction while in the second category ($-r_\beta r_c > 1$), the impact of solute B on density reduction is greater than the effect of solute A on density increase. It was shown that when $-r_\beta r_c < 1$ the system always remains unstable while for the other class it can be stable or unstable depending on the ratio of diffusivities. In both cases, it was shown that the diffusion contrast effect has a potential to accelerate or slow down the convective instabilities depending on the solutes diffusivities. This feature could be used to control the onset and the associated dynamics of convective dissolution.

The relevance of the base state density profile in the control of onset was characterised by analyzing the favorable driving density difference in systems with different diffusivity contrasts. We have proposed scaling relations for the onset as a function of the driving density difference. The presented parametric analysis provides new insights into differential diffusion effects and can be used to control instabilities in partially miscible systems. This study also finds application in solutal and thermal natural convection problems in porous media including geological sequestration of $CO_2$ in deep saline aquifers, enhanced oil recovery, contaminant transport and waste disposal, geophysical fluid dynamics, groundwater hydrology, and convection in magma chamber. In particular, purposeful inclusion of nanoparticles or other materials that are able to modify the density profile could enable accelerating or decelerating of convective dissolution.

### 6.7 Acknowledgments

The authors would like to thank two reviewers for their constructive comments. This work was supported by the Natural Sciences and Engineering Research Council of Canada (NSERC) Discovery Grant and the support of the Australian Government Department of Education through the Endeavour Research Fellowship, the Alberta Innovates – Technology Futures (AITF) through Alberta Innovates Graduate Student Scholarship and was enabled in part by the computing support provided by WestGrid and Compute Canada Calcul Canada. The first author also gratefully acknowledges the Commonwealth Scientific and Industrial Research Organisation (CSIRO) for their hospitality. All data used in analytical and numerical modelling are available in open literature and are cited in this paper.

# Chapter 7: Impact of Boundary Excitation on Stability of a Diffusive Boundary Layer in Porous Media*

## 7.1 Abstract

We study the effects of boundary excitation on the onset of natural convection and the dynamics of subsequent convective mixing by conducting linear stability analysis (LSA) and direct numerical simulations (DNS). A detailed parametric analysis on the stability of a diffusive boundary layer in porous media subject to three different types of linear decline, linear decline followed by constant concentration, and symmetric flat floored valley shape boundary conditions is presented. We propose scaling relations based on results of LSA to describe the critical time and the associated wavenumber of convective instabilities that incorporate the effect of the boundary parameters. The LSA results show that the classic onset criterion is applicable when decline factors ($\alpha$) is smaller than $10^{-4}$. The results also demonstrate that $\alpha$ does not play a significant role in the instability of the system unless it is greater than $10^{-4}$. The results show that in systems with linear concentration decline followed by constant concentration, the impact of decline on the stability of the system decreases as $\alpha$ increases. Based on the LSA results, a system with $\alpha>10^{-2}$ leads to unified stability criteria at different constant concentration ($\chi$) similar to the classic problem, when

* Jafari Raad, S. M., Emami-Meybodi, H., Hassanzadeh, H. (2019). Impact of boundary excitation on stability of a diffusive boundary layer in porous media. *Advances in Water Resources*, 126, 40-54.https://doi.org/10.1016/J.ADVWATRES.2019.02.005

the transient time ($\tau$) and the wavenumber ($\kappa$) are rescaled by $\chi$ as $\tau\chi^2$ and $\kappa/\chi$, respectively. Our results also show that the duration of the flat portion in symmetric flat floored valley shape boundary condition is the main factor controlling the stability behaviour of the system. The DNS results reveal that the dynamics of the buoyancy-driven mixing is also significantly influenced by the temporal variation of concentration at the boundary. These findings improve our understanding of buoyancy-driven instabilities in the presence of boundary excitation and finds applications in thermal and solutal convection in porous media.

## 7.2 Introduction

Solutal and thermal convection in porous media has wide range of applications in a number of fields such as geological flows, groundwater hydrology (Van Dam et al., 2009; Diersch and Kolditz, 2002; Simmons, 2005), waste disposal (Liu and Dane, 1996; Mao et al., 2006; Schincariol and Schwartz, 1990; Yang and Edwards, 2000), carbon dioxide sequestration (Emami-Meybodi et al., 2015; Lindeberg and Wessel-Berg, 1997; Riaz et al., 2006), petroleum reservoir engineering, and geothermal reservoirs (Coumou et al., 2008; Horton and Rogers, 1945; Zhao et al., 2008). Solutal and thermal convection can develop due to negative density gradients in the gravity field resulted from temperature and/or concentration (Landau and Lifshitz, 2004; Nield and Bejan, 2006). Evolution of natural convection in porous media enables efficient heat/solute transport over larger spatial and time scales than those achieved by molecular diffusion. Theoretical basis and importance of natural convection in porous media have been very well discussed in the book by ( Nield and Bejan, 2006).

Stability of the diffusive boundary layer in porous media with different types of boundary conditions such as step change boundary condition (Elder and W., 1967; Ennis-King et al., 2005; Nield and Bejan, 2013), constant flux boundary (Ingham and Pop, 2005; Pop and Ingham, 2001; Vafai, 2005), partially permeable boundary (Elenius et al., 2012; Slim, 2014; Slim and Ramakrishnan, 2010), and moving boundary condition (Meulenbroek et al., 2013; Myint and Firoozabadi, 2013) has been widely discussed in the literature. However, these investigations are mainly concerned with systems with either fully developed or time independent base state (Ingham and Pop, 2005; Donald A. Nield and Bejan, 2013; Pop and Ingham, 2001; Vafai, 2005) or constant boundary type problems (Elenius et al., 2012; Ennis-King et al., 2005; Meulenbroek et al., 2013;

Myint and Firoozabadi, 2013; Slim, 2014; Slim and Ramakrishnan, 2010), where the imposed boundary is independent of time.

Stability of fluids in porous media with boundary excitation is of particular interest, especially in connection with the geophysical and environmental problems. There are relatively very few studies available that look into the effect of interface boundary excitation on the stability of diffusive boundary layers in porous media. Hassanzadeh et al. (Hassanzadeh et al., 2006) studied the effect of linear decline (negative ramp) in concentration at the top boundary on the onset of convection in a transient diffusive layer using a linear stability analysis. They found that the decline factor significantly affects the stability of the diffusive boundary layer in systems with low Ra number (Ra<250). It was reported that the growth of the perturbations in systems with low Ra number attenuates as the decline factor increases. It was also observed that the effect of decline factor on the stability of systems with large Ra number (R=500) can be negligible. More recently, Wen et. al. (Wen et al., 2018) studied the dynamics of convective mixing in a closed porous system in the context of $CO_2$ sequestration. It was shown that the pressure drop in the gas phase during dissolution of gas in water negatively affect both diffusive and convective mass transport of $CO_2$. It was reported that the pressure drop in a closed system decreases the dissolution flux and limits the convection before the underlying brine begins to saturate. However, these studies were either concerned with the dynamics of convective mixing in a finite domain (Wen et al., 2018) or restricted to a simplified form of a time-dependent boundary condition (Hassanzadeh et al., 2006). These studies do not present any parametric analyses on the stability criterion of the system. The objective of the present study is to perform an inclusive analysis of the instability and the associated dynamics of solutal natural convection in saturated porous media in the presence of boundary excitation. The presented analysis and results in this study provide fundamental understanding of natural convection in the presence of boundary excitation. Three different types of time-dependent boundary conditions are used to simulate the concentration excitation at the interface. The effect of boundary excitation on the onset of instabilities and subsequent convective mixing is discussed. A linear stability analysis using quasi-steady-state approximation (QSSA) is conducted to study the effect of time-dependent concentration boundary on the instability behaviour of a gravitationally unstable diffusive boundary layer. We present new scaling relations for the onset of convective instabilities in systems with linear decline, linear decline followed by constant concentration, and symmetric flat floored valley shape boundary conditions.

The developed scaling relations can be used to estimate the onset of density-driven instabilities as a function of the characteristics of the boundary condition and the physical properties of the porous layer. The dynamics of the system beyond the onset time is also studied using direct numerical simulations. Although, we focus on solutal natural convection, the insight developed here can be applied equally to thermal problems.

This paper is organized as follows. In Section 7.3, we describe the problem of interest via presenting the governing equations and boundary conditions followed by a base state solution for the diffusive mass transfer with time-dependent boundary condition. In Section 7.4, mathematical formulation of linear stability analysis is presented. Results and discussion are presented in Section 7.5 followed by Section 7.6, which is summary and conclusion of this study.

## 7.3 Mathematical Formulation

### 7.3.1 Governing equations

We consider a two-dimensional, homogeneous, isotropic, isothermal, vertical cross-section of a porous layer with thickness $H$ as shown in Figure 7.1(a). The porous layer is saturated with a quiescent fluid, which is initially free of solute. A Cartesian coordinate system was chosen with the z-axis pointing downward. The porous layer is assumed to be infinite in the $x$-direction.

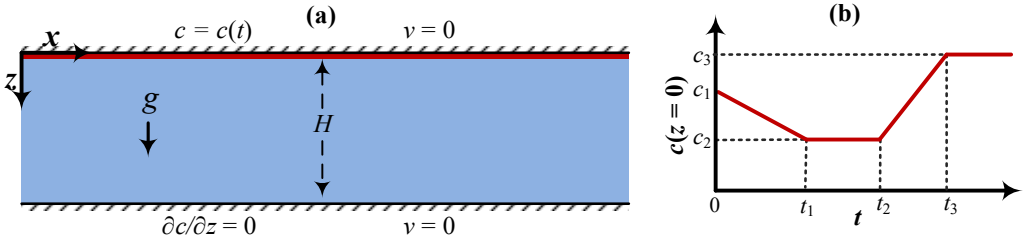


**Figure 7.1:** (a) Geometry and boundary conditions of the porous system. (b) The time-dependent concentration profile imposed on the upper boundary of the porous layer.

The bottom boundary is assumed to be impermeable to flow with zero mass flux. The top boundary is also assumed impermeable to flow but is imposed to a time-dependent concentration as shown in Figure 7.1(b). The time-dependent concentration at the top boundary is defined as:

$$c\big|_{z=0} = c_2 + (c_1 - c_2)\frac{t_1 - t}{t_1}\mathbf{H}(t_1 - t) + (c_3 - c_2)\frac{t - t_2}{t_3 - t_2}\mathbf{H}(t - t_2) + \left[(c_3 - c_2)(1 - \frac{t - t_2}{t_3 - t_2})\right]\mathbf{H}(t - t_3), \quad (7.1)$$

where $c$ is the concentration of the diffusing species, $t$ is the time, $c_1$, $c_2$, $c_3$, are the concentration at $z = 0$ for $t = 0$, $t_1 < t \leq t_2$ , and $t \geq t_3$, respectively, **H** is the Heaviside step function (**H**($t$) = 1 if $t \geq 0$ and **H**($t$) = 0 if $t < 0$).

Assuming the Boussinesq approximation is valid and rock and fluid compressibility effects are negligible, and in the absence of viscosity variation, and dispersion effects, the governing equations of non-reactive single phase flow and transport can be written as (Bear, 1972):

$$D\phi\nabla^2 c - \mathbf{v}\cdot\nabla c = \phi\frac{\partial c}{\partial t}; \quad (7.2)$$

$$\nabla\cdot\mathbf{v} = 0; \quad (7.3)$$

$$\mathbf{v} = -\frac{k}{\mu}(\nabla p - \rho\mathbf{g}\nabla z), \quad (7.4)$$

where **v**($u,v$) is the Darcy velocity vector, $u$ and $v$ are the horizontal and vertical components of the velocity vector, respectively, $p$ is the pressure, $k$ is the porous medium permeability, $\mu$ is the viscosity, $g$ is acceleration due to gravity, $z$ is the vertical coordinate (positive downwards), $\rho$ is the density, $\phi$ is the porosity, and $D$ is the effective molecular diffusion coefficient of the diffusing species in porous media and is assumed to be independent of concentration for dilute solutions.

It was assumed that density is a linear function of the local concentration of the dissolved species,

$$\rho = \rho_0(1 + \beta c), \quad (7.5)$$

where $\rho_0$ is the fluid density at $c = 0$, and $\beta = (1/\rho)\partial\rho/\partial c$, which can be obtained from an equation of state.

The governing equations were nondimensionalized by choosing $c_1$ as the concentration scale, the buoyancy velocity $u_B = k\Delta\rho g / \mu$ as the velocity scale, $l = D\phi\mu / k\Delta\rho g$ with $\Delta\rho=\beta\rho_0 c_1$ as the length scale, and $D/l^2$ as the time scale. It is worth noting that using height of the domain as the length scale would make it difficult if not impossible to distinguish the effect of top and bottom boundary in the finite domain and parameterize the role of the top boundary on the onset of convection. In fact, the defined decline rate ($\alpha$) in H-scaled system such as those used by

(Hassanzadeh et al., 2006) and (Wen et al., 2018) contains H meaning that both alpha ($\alpha$) and Ra change with the height of the domain. In this case, depending on Ra both top and bottom boundary would affect the behaviour of diffusive flux and consequently onset of instability in a same fashion. In other words, for H-scaled system, change in $\alpha$ ($\Pi$ in Wen et al., 2018) could mean either change in the decline rate for the concentration at the top boundary or change in H (which may involve the bottom boundary effect). Therefore, the used scaling may lead to misleading results, especially in systems with low Ra numbers. Here, we intentionally use $l$ as the length scale to avoid this scaling problem and let $\alpha$ to only capture the top boundary features. In other words, time dependent nature of top boundary is isolated from the size of the domain.

Accordingly, the dimensionless form of the governing equations for flow and transport can be expressed as

$$\frac{\partial^2 V}{\partial \eta^2}+\frac{\partial^2 V}{\partial \xi^2}=\frac{\partial^2 C}{\partial \eta^2}, \tag{7.6}$$

$$\frac{\partial C}{\partial \tau}=\frac{\partial^2 C}{\partial \eta^2}+\frac{\partial^2 C}{\partial \xi^2}-U\frac{\partial C}{\partial \eta}-V\frac{\partial C}{\partial \xi}. \tag{7.7}$$

### 7.3.2 Base state solution

At the early times, when the thickness of the diffusive boundary layer ($\delta \approx \sqrt{4Dt}$) (Bird et al., 2002) is very small compared to the height of the porous layer ($\delta \ll H$), the domain can be considered as a semi-infinite medium in the $z$-direction. Eqs. (6) and (7) are subject to the following conditions:

$$V(\xi=0)=V(\xi\to\infty)=0, \tag{7.8a}$$

$$C(\xi\to\infty)=0, \tag{7.8b}$$

$$C(\xi=0)=\chi_2+(\chi_1-\chi_2+\alpha_1\tau)\mathbf{H}\left(\frac{\chi_2-\chi_1}{\alpha_1}-\tau\right)+\alpha_2\left(\tau-\frac{\chi_2-\chi_1}{\alpha_1\theta}\right)\mathbf{H}\left(\tau-\frac{\chi_2-\chi_1}{\alpha_1\theta}\right)+\left((\chi_3-\chi_2)-\alpha_2\left(\tau-\frac{\chi_2-\chi_1}{\alpha_1\theta}\right)\right)\mathbf{H}\left(\tau-\frac{\chi_3-\chi_2}{\alpha_2}-\frac{\chi_2-\chi_1}{\theta\alpha_1}\right), \tag{7.9}$$

where $\chi_i=c_i/c_1$, $\alpha_1 = (\chi_2 - \chi_1)/\tau_1$, $\alpha_2=(\chi_3-\chi_2)/(\tau_3-\tau_2)$, and $\theta=\tau_1/\tau_2$. Figure 7.2 shows the dimensionless form of the time-dependent concentration profile imposed at the upper boundary of the porous layer.

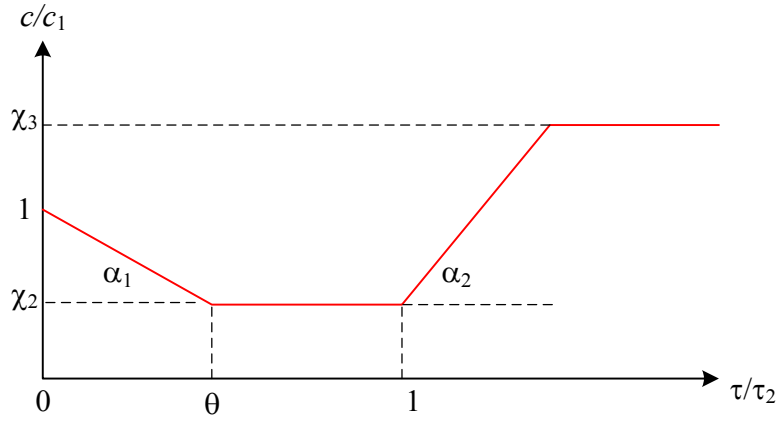


**Figure 7.2**: Dimensionless time-dependent concentration profile at the upper boundary.

Since the system is motionless prior to the onset of instabilities, the bases state velocity is zero. At the early times prior to the onset of instabilities, the molecular diffusion is the dominant transport mechanism. Therefore, Equation (7.7) can be written as

$$\frac{\partial C_b}{\partial \tau} = \frac{\partial^2 C_b}{\partial \xi^2}. \tag{7.10}$$

The time-dependent base state solution of Equation (7.10) subjects to the initial condition $C_b$ ($\tau$ = 0) = 0 and the boundary conditions given in Equation (7.9) can be obtained using Duhamel's theorem (Carslaw and Jaeger, 1959):

$$\begin{aligned} C_b(\xi,\tau) = erfc\left(\frac{\xi}{\sqrt{4\tau}}\right) + \alpha_1(\Omega_0 - \Psi_0) + \alpha_1(\Psi_1 - \Omega_1)\mathbf{H}\left(\tau - \frac{\chi_2 - \chi_1}{\alpha_1}\right) \\ + \alpha_2(\Omega_2 - \Psi_2)\mathbf{H}\left(\tau - \frac{\chi_2 - \chi_1}{\alpha_1\theta}\right) + \alpha_2(\Psi_3 - \Omega_3)\mathbf{H}\left(\tau - \frac{\chi_3 - \chi_2}{\alpha_2} - \frac{\chi_2 - \chi_1}{\theta\alpha_1}\right) \end{aligned}, \tag{7.11}$$

where

$$\Omega_i(\xi,\tau)=\left(\frac{\xi^2}{2}+\tau-\tau_i\right)erfc\left(\frac{\xi}{2\sqrt{\tau-\tau_i}}\right), \tag{7.12a}$$

$$\Psi_i(\xi,\tau)=\xi\sqrt{\frac{\tau-\tau_i}{\pi}}\exp\left(\frac{-\xi^2}{4(\tau-\tau_i)}\right). \tag{7.12b}$$

For the limiting case of $\alpha_2 = -\alpha_1 = \alpha$, $\chi_3=\chi_1=1$, and considering $\chi=\chi_2$, i.e., the time-dependant bouandry, Equation (7.9) can be expressed as:

$$C(\xi=0)=\chi+(1-\alpha\tau-\chi)\mathbf{H}\left(\frac{1-\chi}{\alpha}-\tau\right)+\left(\alpha\tau-\frac{1-\chi}{\theta}\right)\mathbf{H}\left(\tau-\frac{1-\chi}{\alpha\theta}\right)+\left(1-\chi-\alpha\tau+\frac{1-\chi}{\theta}\right)\mathbf{H}\left(\tau-\frac{(1-\chi)(\theta+1)}{\alpha\theta}\right), \tag{7.13}$$

and the base state solution, Equations (7.11) and (7.12), is given as:

$$C_b(\xi,\tau)=erfc\left(\frac{\xi}{\sqrt{4\tau}}\right)+\alpha\left(\begin{array}{l}\Psi_0-\Omega_0+(\Omega_1-\Psi_1)\mathbf{H}\left(\tau-\frac{1-\chi}{\alpha}\right)\\+(\Omega_2-\Psi_2)\mathbf{H}\left(\tau-\frac{1-\chi}{\alpha\theta}\right)\\+(\Psi_3-\Omega_3)\mathbf{H}\left(\tau-\frac{(1-\chi)(\theta+1)}{\alpha\theta}\right)\end{array}\right). \tag{7.14}$$

The dissolution flux per unit area at the interface ($z = 0$) can be obtained as:

$$F(t)=-D_0\phi\int\frac{\partial c(0,t)}{\partial z}dx\,. \tag{7.15}$$

Using the diffusive time and length scales, the non-dimensional form of the flux can be expressed by

$$J(\tau)=\frac{F}{u_B c_1}, \tag{7.16}$$

According to Equations (7.14) – (7.16), the diffusive flux at $\xi=0$ can be written as:

$$J_{diff} = \frac{1}{\sqrt{\pi}}\left(\frac{1}{\sqrt{\tau}} - \Lambda_0 + \mathbf{H}\left(\tau - \frac{1-\chi}{\alpha}\right)\Lambda_1 + \mathbf{H}\left(\tau - \frac{1-\chi}{\alpha\theta}\right)\Lambda_2 - \mathbf{H}\left(\tau - \frac{(1-\chi)(\theta+1)}{\theta\alpha}\right)\Lambda_3\right), \quad (7.17)$$

where $\Lambda_i = 2\alpha\sqrt{(\tau - \tau_i)}$.

Figure 7.3 shows the diffusive flux at the interface ($\xi$ = 0) for systems imposed to the time-dependent concentration boundary. Figure 3(a) presents the diffusive flux for the system with a linear decline concentration boundary at different $\alpha$ = $10^{-5}$, $10^{-4}$, $10^{-3}$, $10^{-2}$, and 0.1 followed by a constant concentration of $\chi$ = 0. A case with $\alpha$ =0 ($\chi$ = 1) is also shown for comparison. The inset plot in Figure 3(a) shows the boundary condition. It can be observed that the decline factor significantly influences the diffusive flux. The linear decline boundary condition with small values of decline factor resembles gas absorption and $CO_2$ dissolution in water. Later, in Appendix it is shown that the linear decline boundary condition with a low decline factor is able to reasonably resemble the early time behaviour of diffusive flux in a close system where the boundary is coupled with a finite gas cap (Wen et al., 2018).

Figure 3(b) shows the log-log scale of the same results. While for a system with a constant boundary condition ($\alpha$ = 0.0, $\chi$ = 1), the diffusive flux declines as $\tau^{-1/2}$ at the early times, the diffusive flux in systems with time-dependent boundary condition ($\alpha \neq 0$, $\chi$ = 0) does not follow the same trend. The results show that the diffusive flux decreases as the decline factor, $\alpha$ increases. Figure 3(b) reveals that at higher decline factors the diffusive flux departs earlier from $\tau^{-1/2}$ and declines much faster compared to the constant concentration boundary condition ($\alpha$ = 0.0, $\chi$ = 1). At very high decline factors, the diffusive flux turns to shut down even before the domain becomes saturated. In this case, due to the positive concentration gradient at the interface, system may even lead to an out-flux regime with a negative diffusive flux and act like a discharge problem (see diffusive flux for systems with $\alpha$ = $10^{-3}$, $10^{-2}$, and 0.1). In other words, the interface may reach a concentration lower than those of its underlying saturated fluid layers in systems with large decline factors. This leads to a non-uniform concentration distribution through the penetration depth of the diffusive front, which negatively slows down the rate of dissolution.

The diffusive flux for a system with a linear decline ($\alpha$ = 0.01) followed by a constant concentration boundary at $\chi$ = 0.0, 0.1, 0.3, 0.5, 0.7, 1 is shown in Figure 2(c). The log-log plot of the same results is shown in Figure 3(d). The inset plot in Figure 3(c) shows the boundary condition. The

diffusive flux for low values of $\chi$ follows a deep shut down during the decline of the interface concentration and then recovers after the decline is completed. Systems with $\chi$ = 0.0, 0.1, and 0.3 show a negative diffusive flux around their bounce back point. As discussed earlier, this behaviour is attributed to the establishment of a positive concentration gradient at the interface, where the effect of constant concentration boundary is not large enough to compensate the effect of the high decline rate and the interface reaches a lower concentration than that of the underlying fluid. The diffusive flux deviates from the shutdown path and starts to recover as a consequence of establishment of the constant concentration boundary following the linear decline of the interface concentration. The diffusive flux reaches a maximum and then declines and approaches the trend of the constant concentration boundary condition. The results show that as $\chi$ increases the diffusive flux bounces back earlier and leads to a higher diffusive flux at the late time.

Figure 3 (e) shows the diffusive flux for a system with a linear decline ($\alpha_1$ =-0.01) followed by a constant concentration of $\chi$ = 0.5 at the boundary, succeeded by a linear positive ramp at $\alpha_2$ = 0.01 at $\theta$ = 0.1, 0.25, 0.5, 0.75, 1.0 and followed by a constant concentration of $\chi$ = 1. A case with $\theta$ =1 is also shown for comparison. The log-log plot of the same results is shown in Figure 3(f). The inset plot in Figure 3(e) shows the boundary condition. During the early time, the diffusive flux goes to a deep shut down until the linear decline in the concentration of the top boundary is terminated. It can be seen from Figure 3 (e) that the diffusive flux experiences its bounce back just after the linear decline is over and the boundary profile turns flat at constant value of $\chi$ = 0.5. The second bounce back occurs at the end of constant concentration period just after the linear ramp begins. The diffusive flux then approaches the trend of a constant concentration boundary ( $\tau^{-1/2}$) at late time when the linear positive ramp is over and a constant concentration of $\chi$ = 1 is established again. The results demonstrate that as the time ratio ($\theta$) decreases the second bounce back in the diffusive flux is delayed. Later, we will show that how the dependency of the diffusive flux to the time dependent boundary condition may impact the onset and associated dynamics of convective dissolution.

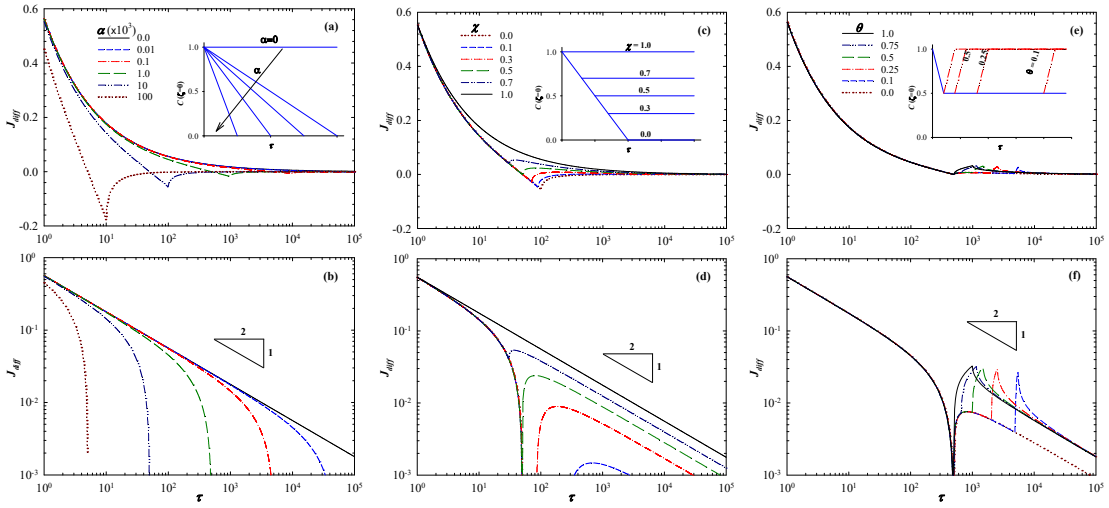

**Figure 7.3:** Diffusive flux versus time, (a and b (log-log)) flux for a linear decline at $\alpha = 10^{-5}$, $10^{-4}$, $10^{-3}$, $10^{-2}$, and 0.1 followed by a constant concentration of $\chi = 0$; a case with $\alpha = 0$ ($\chi = 1$) is also shown for comparison , (c and d (log-log)) flux for a linear decline at $\alpha = 0.01$ followed by constant concentrations of $\chi = 0.0, 0.1, 0.3, 0.5, 0.7$; a case with $\alpha = 0$ ($\chi = 1$) is also shown for comparison, (e and f (log-log)) flux for a linear decline at $\alpha = 0.01$ followed by a constant concentrations of $\chi = 0.5$, succeeded by a linear positive ramp at $\alpha = 0.01$ at $\theta = 0, 0.1, 0.25, 0.5, 0.75$, followed by a constant concentration of $\chi = 1$; a cases with $\theta = 1$ is also shown for comparison.

### 7.3.3 Linear stability analysis

To conduct linear stability analyis the base state is purturbed using $\Re = \Re_b + \Re$ where $\Re = [\mathbf{v}, C]$, and $\Re(\eta,\xi,\tau) = \varepsilon_{\Re}(\xi,\tau)\exp(i\kappa\eta)$ are the infinitesimal perturbations of velocities and concentration where $i$ is the imaginary unit and $\kappa$ is the dimensionless horizontal wavenumber with a very small amplitude $\varepsilon$. After substituting the perturbed variables into the flow and transport equations, implementing the base state quantities, linearizing the perturbations, the following perturbed equations can be obtained:

$$\frac{\partial^2 V'}{\partial \xi^2} - \kappa^2 V' = -\kappa^2 C', \tag{7.18}$$

$$\frac{\partial C'}{\partial \tau} = \frac{\partial^2 C'}{\partial \xi^2} - \kappa^2 C' - \frac{\partial C_b}{\partial \xi} V'. \tag{7.19}$$

The linearized Equations (7.18) and (7.19) were solved using a quasi-steady-state approximation (QSSA), in which the disturbance quantities were assumed to have the following forms (Tan and Homsy, 1986).

$$\begin{bmatrix} V'(\xi,\tau) \\ C'(\xi,\tau) \end{bmatrix} = A(\tau_0) \begin{bmatrix} V^*(\xi) \\ C^*(\xi) \end{bmatrix}, \tag{7.20}$$

where variables defined by asterisks represent the perturbation eigenfunctions. Therefore, the dimensionless growth rate, $\sigma$, reads

$$\sigma(\tau_0) = \frac{1}{A(\tau_0)} \frac{dA}{d\tau}. \tag{7.21}$$

The time scales represented by $\tau$ and $\tau_0$ denote to the fast-growing perturbations and the molecular diffusion time scales, respectively.

Using Equation (7.20), Equations (7.18) and (7.19) can be written as:

$$\left( \frac{\partial^2}{\partial \xi^2} - \kappa^2 \right) V^* + \kappa^2 C^* = 0, \tag{7.22}$$

$$-\frac{\partial C_b}{\partial \xi} V^* + \left( \frac{\partial^2}{\partial \xi^2} - \kappa^2 \right) C^* - \sigma C^* = 0, \tag{7.23}$$

subject the following boundary conditions:

$$V^*(\xi = 0) = V^*(\xi \to \infty) = 0, \tag{7.24}$$

$$C^*(\xi = 0) = C^*(\xi \to \infty) = 0. \tag{7.25}$$

To obtain the growth rate corresponding to an assigned wavenumber the system of perturbed Equations (7.22) and (7.23) are discretized using a second-order finite difference method and then solved numerically. The resulting discretized equations can be expressed by a system of linear equations

$$\mathbf{a}_1\mathbf{V}+\mathbf{a}_2\mathbf{C}=0, \tag{7.26a}$$

$$\mathbf{a}_3\mathbf{V}+\left(\mathbf{a}_4-\sigma\mathbf{I}\right)\mathbf{C}=0 \tag{7.26b}$$

where **V** and **C** are the eigenvectors for vertical velocity and concentration, respectively, $\mathbf{a_1}$–$\mathbf{a_4}$ are the coefficient matrices based on central discretization of the second derivatives related to the eigenfunctions, and **I** is the identity matrix. By substituting $\mathbf{V}=(-\mathbf{a}_1^{-1}\mathbf{a}_2)\mathbf{C}$ into the concentration stability equations, Equation (7.26) can be reduced to

$$\left[\mathbf{a}_4-\mathbf{a}_3\mathbf{a}_1^{-1}\mathbf{a}_2-\sigma\mathbf{I}\right]\mathbf{C}=0. \tag{7.27}$$

This eigenvalue problem is solved numerically, and the maximum eigenvalue of the coefficient matrix is considered as the growth rate corresponding to the assigned wavenumber at a certain diffusive time, $\tau_0$. A positive growth rate at a particular time is an indication of instability. Thus, the onset time can be detected using a zero maximum growth rate (i.e., the time at which the growth rate turns positive at a given wave-number represents the onset of instability). Negative growth rate for every wavenumber suggests a stable system. For brevity, we refer the reader to the previous studies for more details on numerical procedure and validity of the computational algorithm (Riaz et al., 2006; Tan and Homsy, 1986).

## 7.5 Results and Discussion

### 7.5.1 Stability analysis

#### 7.5.1.1 Linear decline

Linear stability analysis (LSA) was conducted to parameterize the effect of the time-dependent boundary condition on the growth rate of perturbations and consequently, the onset of natural convection. The LSA was conducted for a wide range of physical parameters of the time-dependent boundary condition. First, we study the stability of a system imposed to a linear decline followed by a constant concentration of $\chi = 0$ at the upper boundary. The stability analysis on the linear decline boundary condition is important not only in convective dissolution of $CO_2$ into brine in a sequestration process (Akhbari and Hesse, 2017; Hassanzadeh et al., 2006) but also in contaminant

transport and waste disposal (Gao et al., 2013; Shen and Chengji, 2015; Truex et al., 2015; Xie et al., 2010), and crystallization processes and magma chambers (Holness et al., 2006; Kuritani et al., 2007; Worster et al., 1990).

LSA results show that the behaviour of such a system is controlled by the concentration decline factor. The perturbation growth rates for a system with constant concentration boundary ($\alpha = 0, \chi = 1$) is shown in Figure 7.4 (a). For this limiting case, the stability analysis predicts the negative perturbations growth rates at early times, $\tau_0$=25 and 37.5, suggesting an unconditionally stable system at these times. As time increases, the perturbations grow such that growth rates turn positive at critical time $\tau_c$ =56 at the corresponding wavenumber of $\kappa_c$=0.064, representing the onset of instability. Similar stability criterion has been reported in previous studies for systems with the same configuration and boundary conditions (Jafari Raad and Hassanzadeh, 2015; Meulenbroek et al., 2013; Tilton et al., 2013).

Figure 7.4(b) shows dispersion curves for the same system imposed to linear decline in concentration at the upper boundary with various decline factors at $\tau_0 = 62.5$. Perturbations growth rate for the system with constant concentration boundary ($\alpha$=0, $\chi$ = 1) at the similar time is also shown for comparison. The results reveal that increase of decline factor slows down the growth of perturbations, suggesting more stable diffusive boundary layer. In other words, increasing the decline factor has a stabilizing effect in a system with a linear decline boundary. As discussed earlier, this is attributed to a lower interface concentration at higher decline factor. The same observations has been reported in earlier studies (Hassanzadeh et al., 2006; Wen et al., 2018).

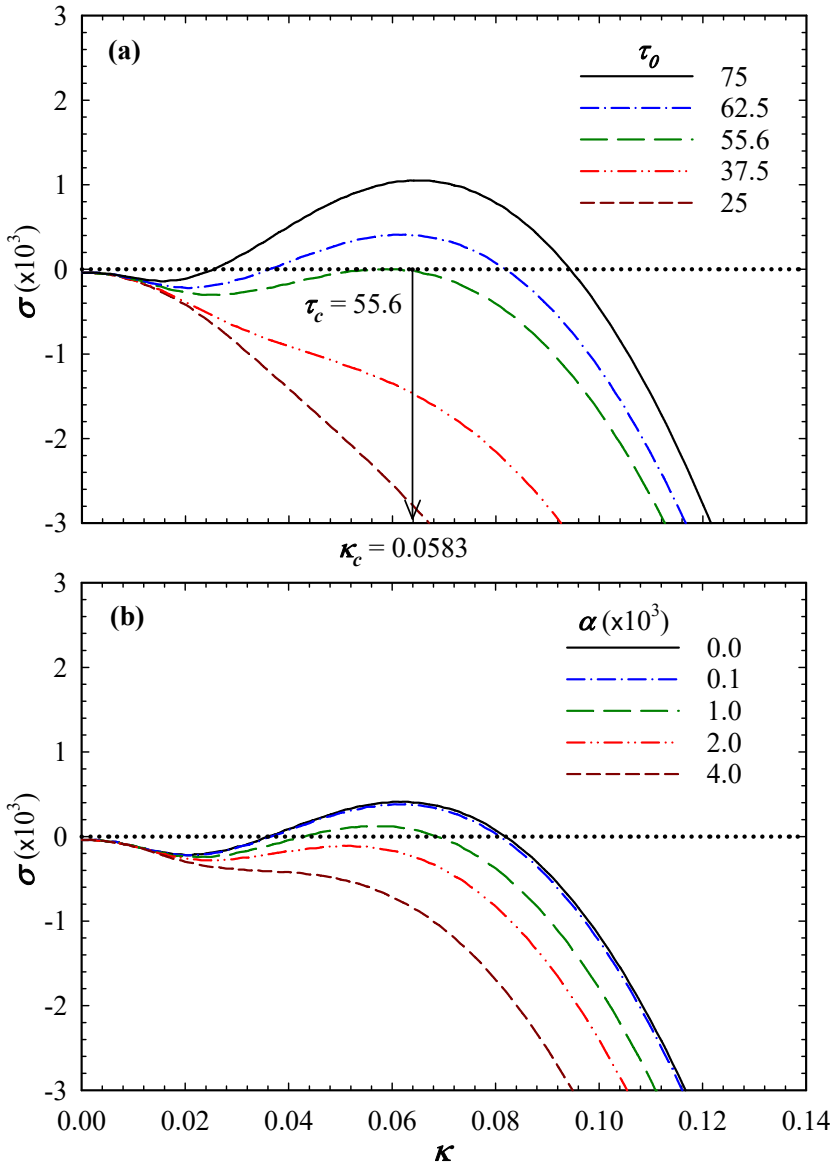


**Figure 7.4:** Growth rates versus dimensionless wavenumber for (a) a system imposed to a constant concentration at the top boundary ($\alpha = 0$, $\chi = 1$) at different dimensionless times and (b) systems imposed to a linearly declining concentration boundary with different decline factors, $\alpha = 0.0001$, 0.001, 0.002, and 0.004, followed by a constant concentration of $\chi = 0$, at a constant dimensionless time $\tau_0 = 62.5$, a case with $\alpha = 0$ ($\chi = 1$) is also shown for comparison.

The general effect of decline factor can be seen from Figure 7.5 where the maximum growth rates, ($\sigma_{max}$) and the corresponding wavenumbers, ($\kappa_{max}$) are shown for systems with different decline factors $\alpha$=0, 0.0001, 0.001, 0.002, 0.003 and 0.004. Inspection of the maximum growth rates obtained for systems with different decline factors, shown in Figure 7.5(a) indicates the significant impact of decline factor. The effect of a large decline factor is to reduce the maximum growth rate significantly suggesting the stabilizing effect of the decline factor.

It can be seen that the maximum growth rate increases rapidly, reaches a maximum and decreases. The results show that systems with larger decline factor lead to higher attenuation of the instabilities. While the late-time evolution of the maximum growth rate scales with $\tau^{-1/4}$ for the system with constant concentration at the upper boundary ($\alpha$=0) the maximum growth rate scales with $\tau^{-5/8}$ in system with $\alpha$=0.003.

Figure 7.5(b) shows that the maximum wavenumber is also controlled by the decline factor. While evolution of the maximum wavenumbers (the most dangerous wavenumber) for the constant boundary system ($\alpha$=0) decays as $\tau^{1/4}$, it decays faster as $\tau^{1/3.2}$ for system with $\alpha$=0.003.

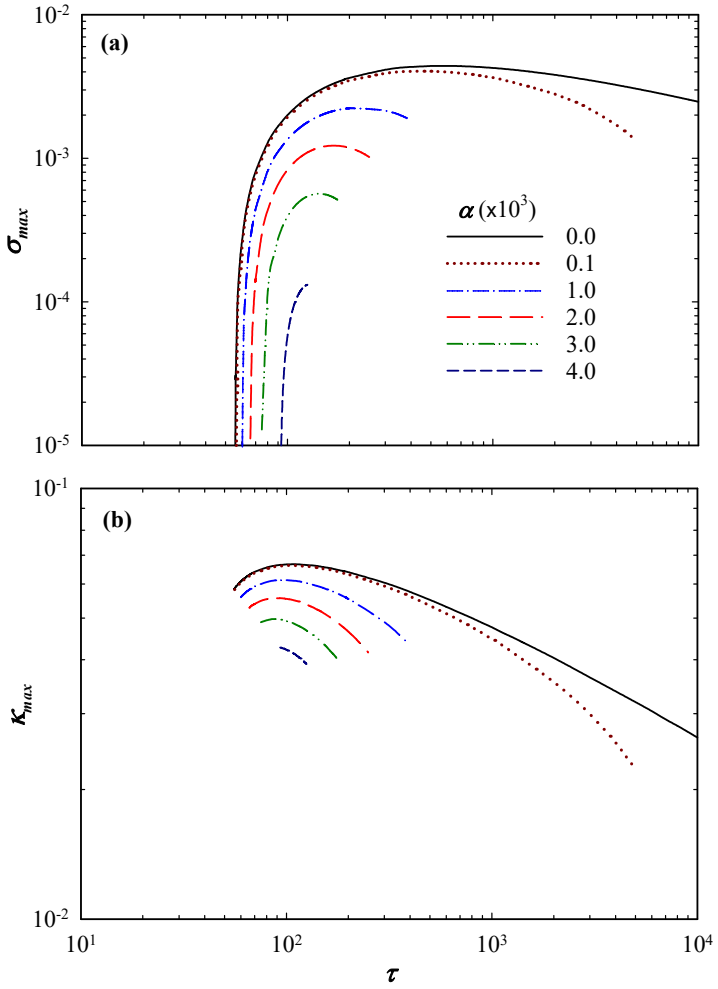


**Figure 7.5:** (a) Maximum growth rate and (b) the corresponding wavenumber as a function of dimensionless time for systems with different decline factors of $\alpha$ = 0, 0.0001, 0.001, 0.002, and 0.004.

A more general overview of the impact of the decline factor on the stability behaviour of the diffusive boundary layer is provided using the neutral stability curves. Figure 7.6 shows the neutral stability curves for different decline rate. The results for the system with a $\alpha$=0 is also shown for comparison. The neutral stability curves clearly show that the decline factor negatively affects the instability of the systems. The instability limit shrinks and moves upward as the decline factor increases, suggesting increase of the critical time. This observation suggests that the system turns more stable at a higher decline factor. It can be observed that the shrinkage effect is significant for a system with a large decline factor such as $\alpha$= 0.004. This behaviour is mostly attributed to the

lower mass flux at the interface at higher decline factor (see Figure 7.3(b)). As the decline factor increases the support of the concentration source at the interface to the underlying diffusive boundary layer decreases. This leads to small penetration depth of the diffusive front, the weak buoyancy force, and a delayed onset. This may also result in attenuation of the already initiated instabilities at earlier times.

It can be also observed that the loci of the critical times, marked by filled circles moves toward smaller wavenumbers as the decline factor increases. It is worth noting that minimum of the neutral stability curve indicates the critical time ($\tau_c$).

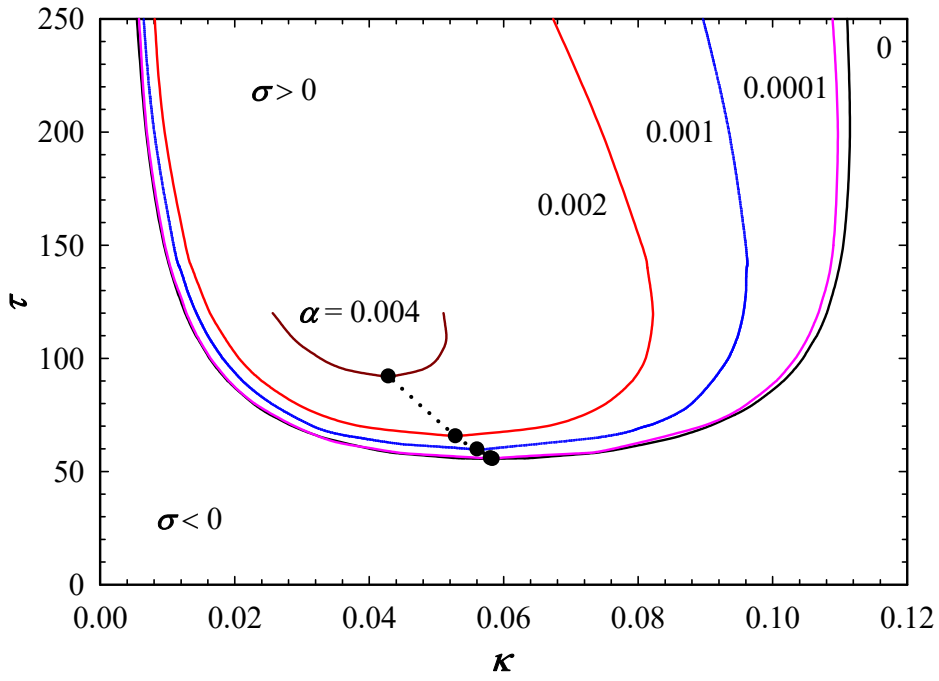


**Figure 7.6:** Neutral stability curves for systems exposed to a linear decline of concentration at the top boundary at different decline factors, $\alpha$ = 0, 0.0001, 0.001, 0.002, and 0.004. The dotted lines show the loci of the critical time and the corresponding wavenumbers that maximize the growth rate ($\sigma$).

To further clarify the effect of decline factor on the stability criteria of the diffusive boundary layer, results of LSA for the scaled critical time and the corresponding wavenumber as a function of decline factor are shown in Figure 7.7. The results show that the scaled critical time increases as the decline factor increases, suggesting a more stable diffusive boundary layer. The results reveal that the critical time and the corresponding wavenumbers are not sensitive to the decline of concentration when the decline factor is less than $10^{-4}$. For systems with decline factors less than $10^{-4}$, the scaled critical time and the corresponding wavenumber recover the scaling relations $\tau_c$ = 55.6 and $\kappa_c$ = 0.0583, respectively. These scaling relations are similar with those reported for the case of constant boundary condition ($\alpha$=0). For this particular case, Tilton et al., (Tilton et al., 2013) reported $\tau_c$ = 55.62 and $\kappa_c$ =0.058, which are quite close to those predicted in our analysis. The critical time and wavenumber both reveal a non-linear dependence for decline factors greater that $10^{-4}$. The scaled critical time (and the corresponding wavenumbers) increases (decreases) monotonically with the decline factor for the intermediate decline factor values of $10^{-4} \leq \alpha \leq 4.4\times10^{-3}$ followed by a sharp increase of the critical time suggesting an unconditionally stable system. The results of LSA imply that both the onset and the wavelength of instabilities are controlled by the decline factor for $10^{-4} \leq \alpha \leq 4.4\times10^{-3}$).

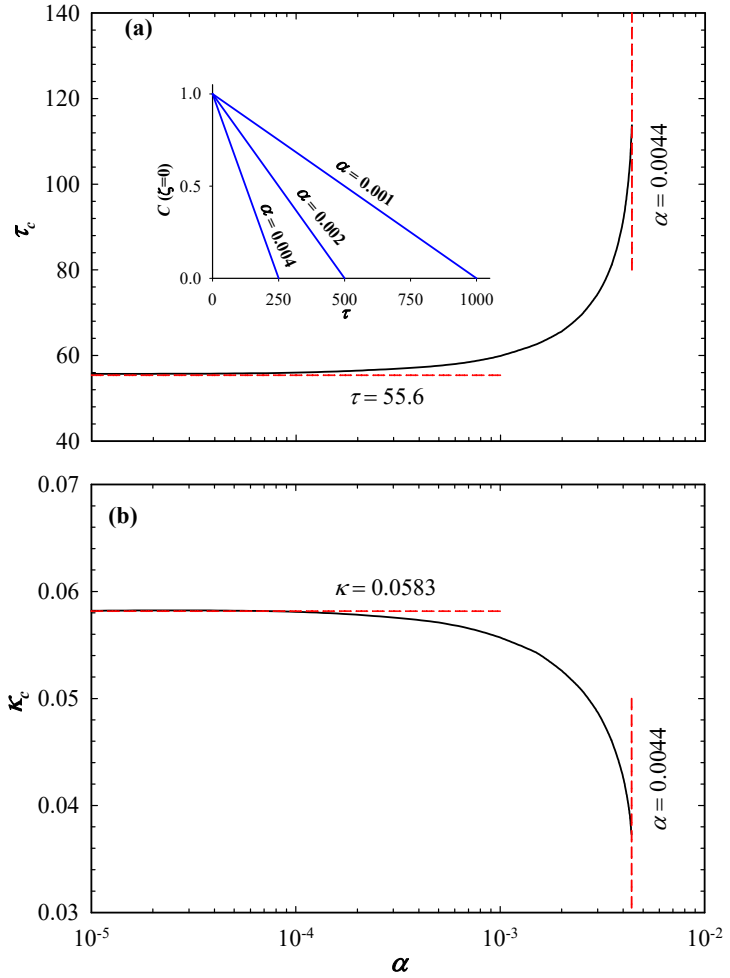


**Figure 7.7:** (a) Critical dimensionless time and (b) the corresponding wavenumber as functions of decline factor ($\alpha$) for a linearly declining top boundary. The inset plot shows the time dependent concentration boundary identified by linear decline factors of $\alpha$=0.001, 0.002 and 0.004.

### 7.5.1.2 Linear decline followed by constant concentration

We extended our analysis to study the effect of a boundary condition which is described by a linear decline followed by constant concentration ($\chi$>0). This stability analysis is important in understanding the stability behaviour of systems that experience a nearly uniform state after a temporal change in the upper boundary. The presented analysis finds application in many material processing and industrial settings where convection can be accelerated or delayed by proper tuning

of the boundary parameters. The neutral stability curves for decline factors of $\alpha$=0.01 and 0.1 at various concentrations of $\chi$=0.3, 0.5, and 0.7 are shown in Figure 7.8. The neutral curve for $\chi$=1 ($\alpha$=0) is also shown for comparison. It can be observed that the instability limit in the neutral stability curves shown in Figures 7.8 (a, c) shift upward significantly as the concentration decreases.

The result also shows that the neutral stability curves considerably shrinks as the concentration decreases suggesting a reduced instability region ($\sigma \geq 0$). It can be also observed that the loci of the critical points ($\kappa_c$, $\tau_c$) marked by filled symbols moves toward smaller wavenumbers as the concentration decreases. In general, a system with lower concentration leads to larger critical time, reduced unstable region, and much smaller dominant wavenumbers. This is attributed to the lower interface concentration, which negatively affects the growth of diffusive boundary layer.

Comparison of the neutral stability curves for systems with different decline factors, $\alpha$=0.01 and 0.1 shown in Figures 7.8(a) and 7.8(c), respectively, demonstrates that $\alpha$=0.1 leads to higher critical times than $\alpha$=0.01. This observation reflects the stabilizing effect of the decline factor.

Figures 7.8 (b) and 7.8(d) show the rescaled neutral stability curves where the transient time and the wavenumber are rescaled by $\chi$ as, $\tau \times \chi^2$ and $\kappa/\chi$, respectively. Interestingly, this rescaling collapses all neutral curves to a single one with unique critical point ($\kappa_c$, $\tau_c$) for systems with $\alpha$=0.1, suggesting a unified stability region as shown in Figure 7.8(d). This observation reveals that stability of a system with a large decline factor is controlled by the constant concentration portion of the boundary condition. In other words, the impact of decline factor on the stability of a system with linear decline followed by constant concentration decreases as the decline factor increases. In fact, as the decline factor increases the interface concentration reaches to the constant regime faster and consequently the behaviour of the system with the constant concentration boundary is recovered more quickly.

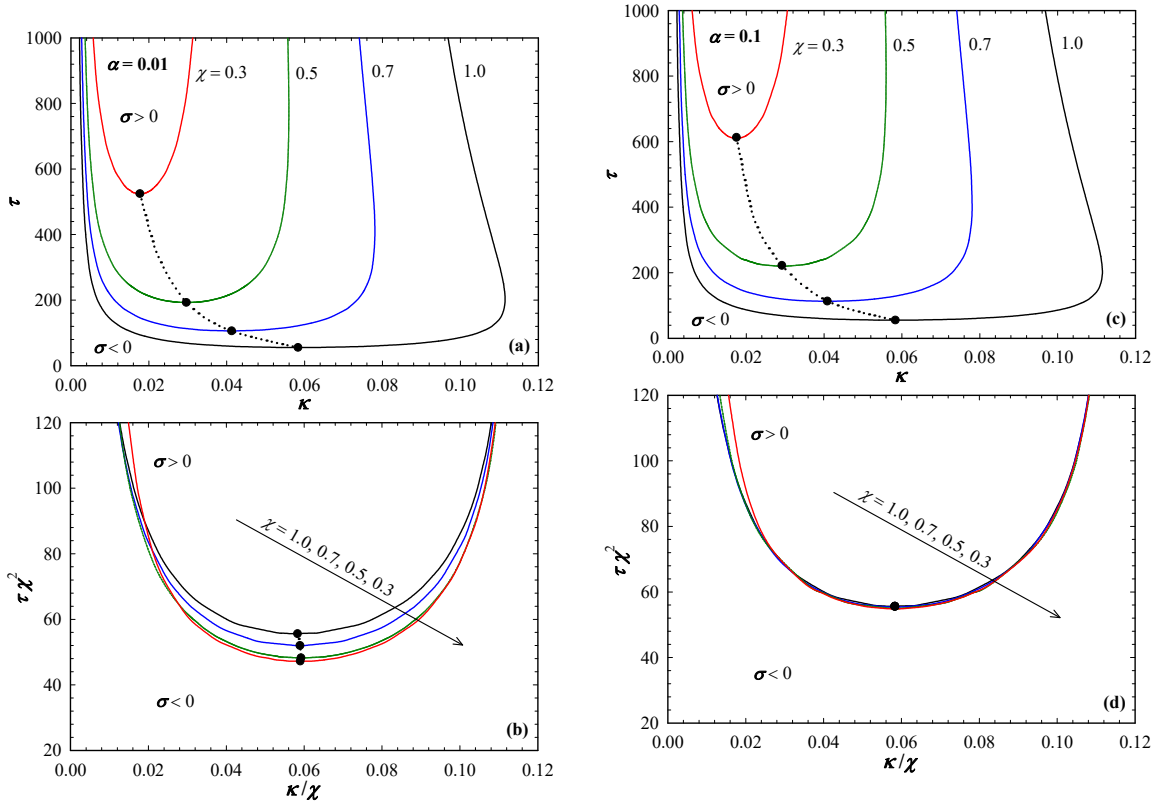


**Figure 7.8:** Neutral stability curves for systems with a linear decline followed by a constant concentration boundary (a, b) with decline factor $\alpha$=0.01, and (c, d) with decline factor $\alpha$=0.1 at different concentrations of $\chi$=0.3, 0.5, 0.7, and 1.0. The dotted lines show the temporal evolution of the dominant wavenumbers that maximize $\sigma$. Figures 8(b) and (d) represent the rescaled neutral curves for the cases shown in Figures 8(a) and (c), respectively.

The rescaled critical time and the corresponding wavenumber against the decline factor ($\alpha$) for various concentrations of $\chi$= 0.0, 0.3, 0.5, and 0.7 are shown in Figure 7.9. The results for the case of $\chi$= 1 ($\alpha$=0) is also shown for comparison. As expected, the system becomes more stable as the decline factor increases. The results reveal three regions of instability. In the first region ($\alpha \leq 10^{-4}$), the stability of the system is independent from the linear decline factor as well as the constant portion of the boundary condition. In fact, the drop of the interface concentration is so slow at small decline factors ($\alpha \leq 10^{-4}$) such that the onset is nearly unaffected by the decline of concentration at the upper boundary. In other words, stability of this region behaves similar to that

of a constant concentration case reported in the literature ( Meulenbroek et al., 2013; Tilton et al., 2013). This region is followed by a non-linear region ($10^{-4}\leq\alpha\leq10^{-2}$) where both the decline factor and the constant concentration portion of the boundary condition play a role. In the third region ($\alpha \geq 10^{-2}$), stability of the system is governed only by the constant concentration portion of the boundary condition. This is attributed to the quick transitions of the interface concentration to the constant concentration at large decline factors ($\alpha\geq10^{-2}$). The results shown in Figures 7.9 (c,d) reveal that for cases with $\chi<1$the rescaled critical time (and the corresponding wavenumbers) increases (decreases) and approaches the classical cases of constant concentration boundary condition (Jafari Raad and Hassanzadeh, 2015).

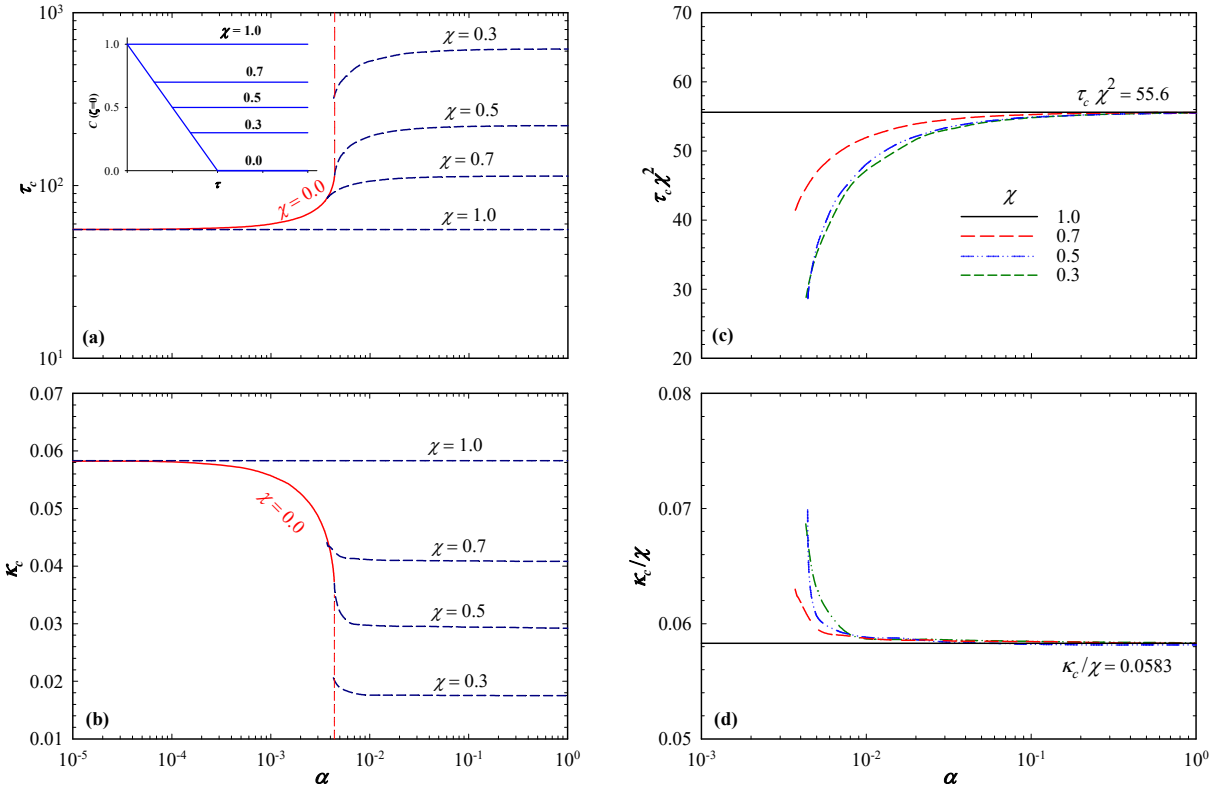


**Figure 7.9:** (a, c) Critical time and (b, d) the corresponding wavenumber versus decline factor. The inset plot in 7.9(a) shows the boundary condition. Figures 7.9(c) and (d) represent the rescaled critical time and the corresponding wavenumber.

#### 7.5.1.3 Symmetric flat floored valley shape boundary condition

A flat floored valley shape boundary condition is characterized by a linear decline, a constant concentration portion, followed by a linear rise. The stability analysis on the behaviour of the system with symmetric flat floored valley shape boundary condition provide fundamental understanding on the stability of the systems subject to cyclic boundary conditions in re-entry heating or/and periodic induced flow problems. Systems with re-entry heating and periodic boundary condition find application in many industrial and environmental settings, such as geothermal reservoir engineering, underground waste management and industrial emergency cooling systems. A controlled induced periodic boundary condition can also be used as a mechanism to control convection in the case of materials processing applications to attain higher efficiencies and to advance convection in achieving major enhancement of heat, mass and momentum transfer (Kwak and Hyun, 1996; Wu and Wang, 2017). Although, natural convection in porous media under periodic boundary conditions have been addressed in previous studies (Bhadauria et al., 2013; Caltaoirone, 1976; Chhuon and Caltagirone, 1979; Kwak and Hyun, 1996; Nield and Bejan, 2006; Steen and Aidun, 1988; Wu and Wang, 2017; Xie et al., 2010), to the best of our knowledge, this is the first parametric analysis that addresses the role of boundary parameters on the stability behaviour during each period of the boundary oscillation. This analysis provides useful insight into the stability behaviour of the system during each period and can be used as a tool for proper parameter tuning in an engineered natural convection problem.

The results of LSA for the scaled critical time and the corresponding wavenumber as a function of decline factor for this boundary condition are shown in Figure 7.10. Figures 7.10(a) and 7.10(b) show the critical time and the corresponding wavenumber for a case with $\chi$ = 0.7, respectively, for different $\theta$= 0.0, 0.1, 0.25, 0.5, and 1.0. Figures 7.10(c) and 7.10(d) show the same results for a case with $\chi$ = 0.5. It is worth noting that $\theta = \tau_1 / \tau_2$ is a measure of the duration of the constant boundary condition (flat portion of the valley) and thus smaller $\theta$ indicates longer duration of the flat portion. The behaviour of the critical time and the corresponding wavenumber for each case is shown. A case with linear decline followed by a zero concentration is also shown for comparison. The critical time and the corresponding wavenumber for this special case at a decline factor of ~$4\times10^{-3}$ approach infinity and zero, respectively, which are illustrated by the vertical dashed lines

and have been previously shown in Figures 7.5 and 7.9. In addition, a symmetric V shape boundary ($\theta$=1) is also shown for comparison.

For a boundary condition of interest, which is a symmetric flat floored valley shape boundary condition, the gradual increase of the onset time by increasing the decline factor shown by blue dashed line is partly due to the duration of the flat portion of the boundary condition. The maximum critical times shown by triangles mark the rise of concentration at the top boundary. The decline factor at which the onset time reaches a maximum depends on the duration of the flat portion of the boundary condition. A longer duration of the flat portion (smaller$\theta$) shows stronger stabilization effect of the boundary. The concentration rise at the boundary leads to decline of the critical time shown by brown dashed line that approaches the classical case ( $\tau_c$=55.6). The same observations can be made for the behaviour of the critical wavenumber.

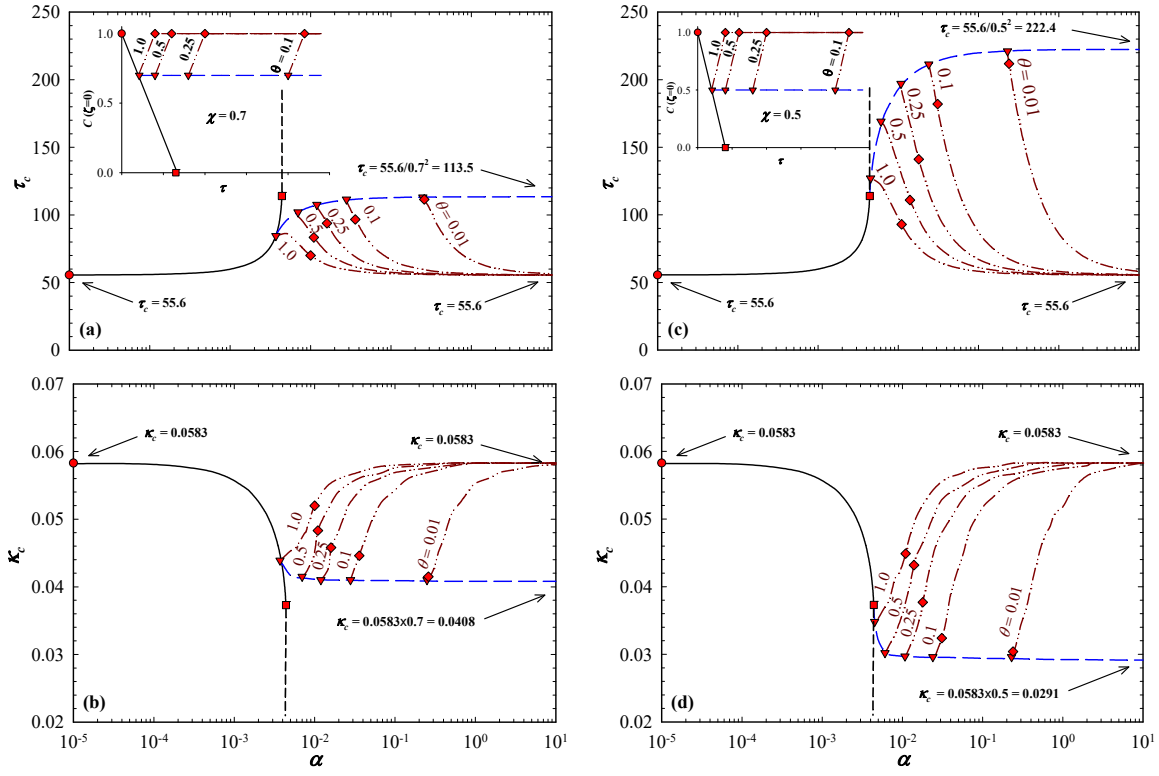


**Figure 7.10:** Critical time and the corresponding wavenumber versus decline factor for symmetric flat floored valley shape boundary condition where 7.10(a) and 7.10(b) show the critical time and the corresponding wavenumber for a case with $\chi$ = 0.7, respectively, for

different $\delta$= 0.0, 0.1, 0.25, 0.5, and 1.0, and 7.10(c) and 7.10(d) show the same results for a case with $\chi$ = 0.5. The inset plots show the shape of the boundary conditions for each case.

### 7.5.2 Numerical simulations

We have conducted full numerical simulations to gain further insight into the instability behaviour and the nonlinear dynamics of mixing beyond the onset. We solved the nonlinear problem with a high accuracy numerical model developed based on a well-known IMPEC approach where the implicit scheme is used to discretize flow Equations (3-4) while the transport Equations (2) are treated explicitly (Settari, 2001). The developed numerical model is based on a uniform Cartesian grid and second order finite difference discretization of the governing Equations (2-4).

The numerical model considers the physical domain and the boundary conditions described in Figure 7.1. One may refer to previous publications (Hassanzadeh et al., 2007) for further details on the numerical model and controls on the accuracy and convergence of the numerical solutions.

#### 7.5.2.1 Linear decline

We studied the effect of the linear decline factor on the onset of convective dissolution and the associated dynamics in systems with a linearly decreasing ramp concentration boundary. The concentration distributions, space-time concentration maps and the time-dependent Sherwood number as the most practical measures of convective dissolution are considered in analysis that follows.

The 2D numerical solutions were conducted to evaluate the concentration distribution associated with the convective dissolution. The domain size is chosen to ensure that the numerical solutions are independent from the domain aspect ratio and the lateral boundaries could not influence the evolution of convective fingers. Figure 7.11 shows the time evolution of concentration distribution for systems with time-dependent concentration boundary at different decline factors of $\alpha$=0, 0.00004, and 0.0004. It can be observed that these systems exhibit different instability behaviour followed by different fingering pattern. The results show that the systems with $\alpha$=0 results in faster development of the instabilities compared to the cases with declining concentration at the top boundary. These observations are in agreement with the results of stability analysis. As discussed earlier, this instability behaviour is attributed partly to the growth of the diffusive boundary layer

under the consequence of the time-dependent concentration at the upper boundary. As the decline factor increases, the interface concentration that supports the growth of boundary layer decreases faster leading to lower mass flux.

Figure 7.12 (a) shows space-time maps of the concentration of the solute along a horizontal slice below the interface ($z\approx+0$). Results of the space-time concentration maps show that lateral spreading and merging of the developed fingers in the system when $\alpha$=0 is more vigorous than those in the system with $\alpha$=0.0004. The results also show that the system with $\alpha$=0 leads to fingering pattern with shorter wavelength compared to the system with $\alpha$=0.0004. To gain a better understanding of the instability behaviour of the diffusive boundary layer and the dynamics of mixing process beyond the onset of instability, we analyzed the time-dependent Sherwood number as a measure of the dissolution process. Sherwood number is defined as the ratio of the total dissolution flux to the pure diffusion flux, $Sh = F_{total} / F_{diffusion}$ where the dissolution flux per unit area is define as:

$$F(\tau) = \frac{1}{A}\frac{d}{d\tau}\int_V C(\tau)dV \ , \tag{28}$$

where $V$ indicates the domain pore volume, $A$ is the cross-sectional area of the interface and $C$ is total concentration of the solute in the entire domain.

Figure 7.12(b) compares the time-dependent Sherwood number, Sh ($\tau$), at the early times for the three cases shown in Figure 7.12(a). It can be observed that the Sherwood number is unity at early times for all three cases suggesting a diffusion dominant mechanism. Figure 7.12(b) reveals that the Sherwood number for the system with α=0 deviates earlier from unity than that of $\alpha$=0.00004 implying an earlier onset of convection for systems with smaller decline factor. It is seen from Figure 7.12(b) that the diffusion is the dominant transport mechanism for the system with $\alpha$=0.0004. These results confirm the linear stability analysis predictions on the effect of decline factor on the instability behaviour of diffusive boundary layer in systems with a decreasing ramp concentration boundary.

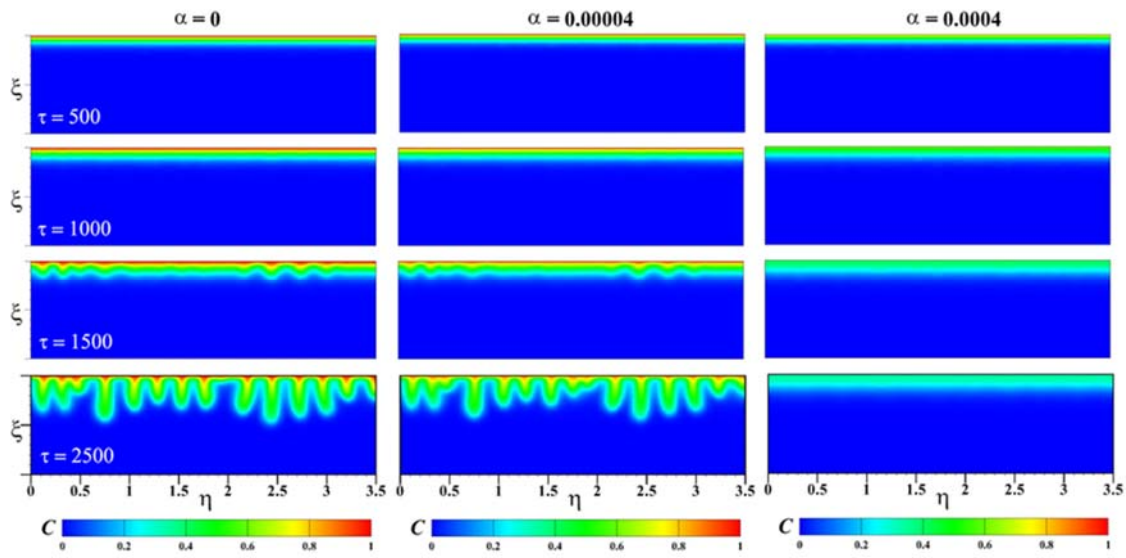


**Figure 7.11:** Temporal concentration distribution for a system imposed to a linear decline of concentration from top at different $\alpha$ = 0.0, 0.00004, and 0.0004 and a constant $\chi$=0.

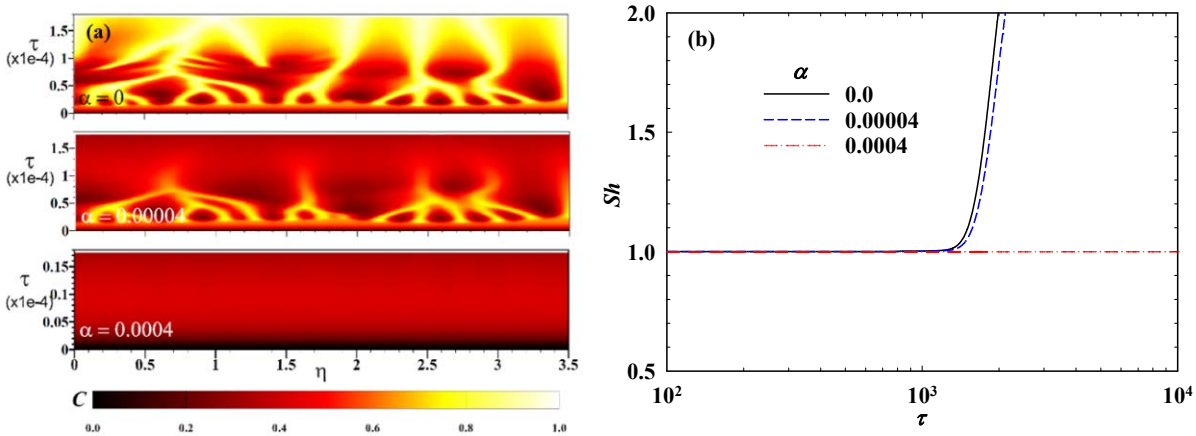


**Figure 7.12:** (a) Space-time maps of the concentration of the solute along a horizontal slice located just below the top boundary at $z \approx +0$ for the same cases shown in Figure 7.11 (b) Sherwood number versus time.

#### 7.5.2.2 Linear decline followed by constant concentration

Next, we considered the effect of linear decline followed by constant concentration on the onset of convection and the dynamics of convective dissolution. Figure 7.13 presents the time evolution of concentration distribution for different concentrations of $\chi$=0.7, 0.5, and 0.3, while the decline factor remained constant at $\alpha$=0.004. Results for a system with a constant concentration boundary ($\chi$ =1) is also shown for comparison.

Consistent with the result of LSA, Figure 7.13 demonstrates that a system with lower concentration results in weaker development of instability leading to delayed onset of free convection. Comparison of the developed fingering patterns show that systems with a smaller concentration result in sluggish form of fingers associated with low rate of convective dissolution due to the presence of less dense mixture on the upper layer. This is attributed to the fact that the flux of solute into the domain decreases when the concentration is lower at the interface, which suppresses the growth of convective fingers along the vertical direction. The results show that the magnitude of constant concentration following the linear decline significantly affects the wavelength of the density-driven fingers such that systems with higher concentration result in fingers with smaller wavelengths.

Figure 7.14 depicts space-time contour maps of the solute concentration along a horizontal slice located just below the interface at $z \approx +0$, as well as the time-dependent Sherwood number for the same cases, shown in Figure 7.13. The evolution of the fingers root concentration in Figure 7.14 (a), demonstrates that the growth of the diffusive boundary layer is significantly controlled by the magnitude of the constant concentration following the linear decline. It can be observed from these maps that systems with higher concentration lead to larger number of fingers associated with stronger finger roots. It is seen from the space-time map that finger interaction increases over time leading to a smaller number of dominant fingers. The finger root concentration significantly reduced in the system with $\chi$ =0.3 leading to a fading finger pattern.

Figure 7.14 (b) shows the numerical measurements of Sherwood number as a function of time. It can be observed that the magnitude of the constant concentration following the linear decline significantly influences the onset marked by the deviation of Sherwood number from unity. Numerical results confirm that systems with higher concentration lead to earlier onset time. Examination of the Sherwood number beyond the onset shows that a system with higher

concentration results in a larger Sherwood number, implying a stronger convective flux as compared to other cases with lower concentration. Higher convective dissolution rate in systems with higher concentration ratio is attributed to the strong interaction and merging of fingers as they propagate downward. These results show the important role of the constant concentration following the linear decline on evolution of the onset of convection and the dynamics of convective dissolution.

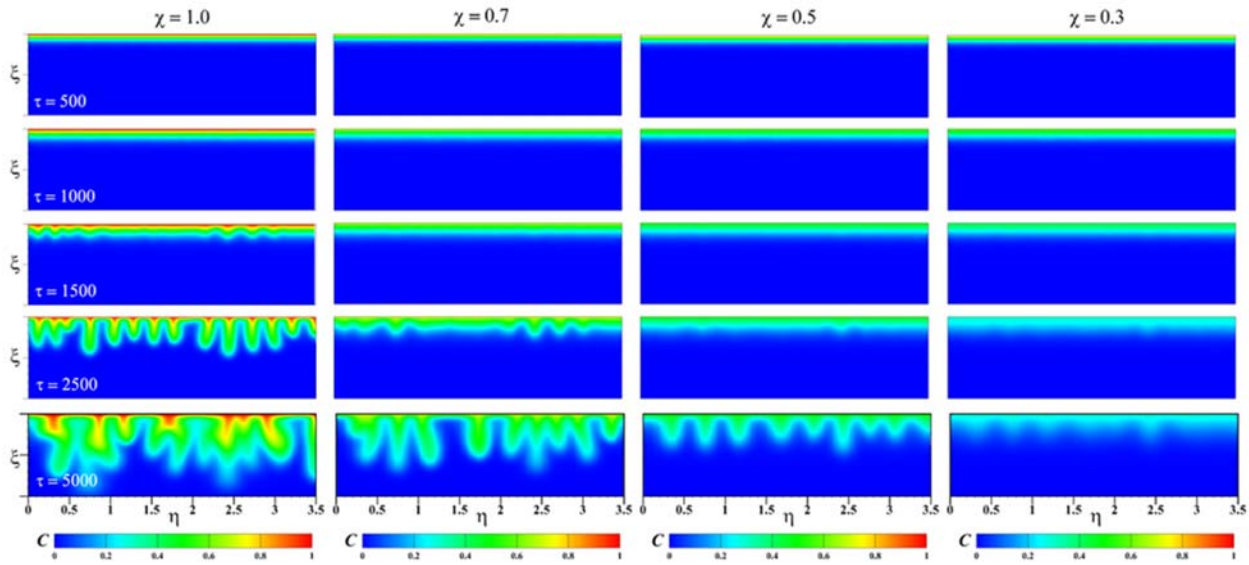


**Figure 7.13:** Temporal concentration distribution for a system exposed to linear decline followed by constant concentration at different $\chi$ =0.3, 0.5, and 0.7 with constant $\alpha$ = 0.004. A case with $\chi$ =1 is also show for comparison.

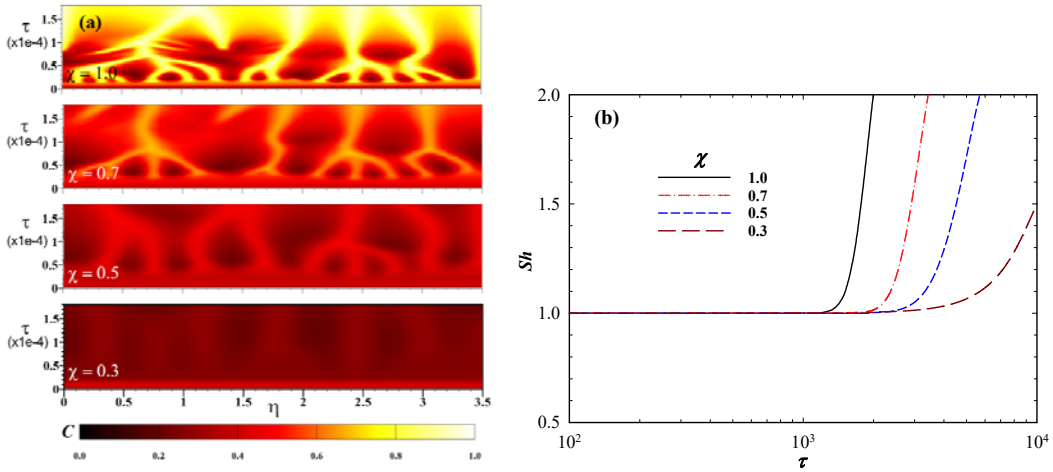


**Figure 7.14:** (a) Space-time maps of the concentration of the solute along a horizontal slice located just below the top boundary at z ≈ +0 for the same systems shown in Figure 7.13(b) Sherwood number versus time.

### 7.5.2.3 Symmetric flat floored valley shape boundary condition

As the last part of our analysis, the impact of a symmetric flat floored valley shape boundary condition on the onset of convection and the dynamics of mixing was investigated. In particular, we studied the effect of duration of the constant concentration (flat portion of the valley) by considering $\theta = 0.1, 0.25, 0.5$, and 1.0 while the decline factor and concentration remained constant at $\alpha = 0.004$ and $\chi = 0.5$, respectively. It is worthwhile noting that $\theta = \tau_1 / \tau_2$ and smaller $\theta$ indicates longer duration of the flat portion and $\theta = 1$ denotes a symmetric V shape boundary condition. The temporal concentration distributions, presented in Figure 7.15, demonstrates that a system with larger time ratio ($\theta$) results in faster development of instabilities in form of fingers. This is in agreement with the results of LSA. This observation is attributed to the fact that the as the time ratio increases the supporting flux for evolution of density-driven fingers is stronger leading to more vigorous fingering.

Careful review of the fingering patterns in systems with different $\theta$ shows that while the onset time and fingering patterns at the early times are different, they lead to almost similar fingering pattern at the later times ($\tau \geq 5000$). This behaviour can be credited to the same supporting flux into the

domain at the late times while a maximum interface concentration is established for all four considered cases. This can be also observed from the space-time maps, shown in Figure 7.16 (a), where almost the same fingering root patterns is seen for all cases at the late times ($\tau \geq 5000$). Numerical results of time-dependent Sherwood number, shown in Figure 7.16 (b), confirm that systems with shorter duration of the constant concentration (flat portion of the valley) lead to earlier onset time as well as stronger convective dissolution at early times beyond the onset.

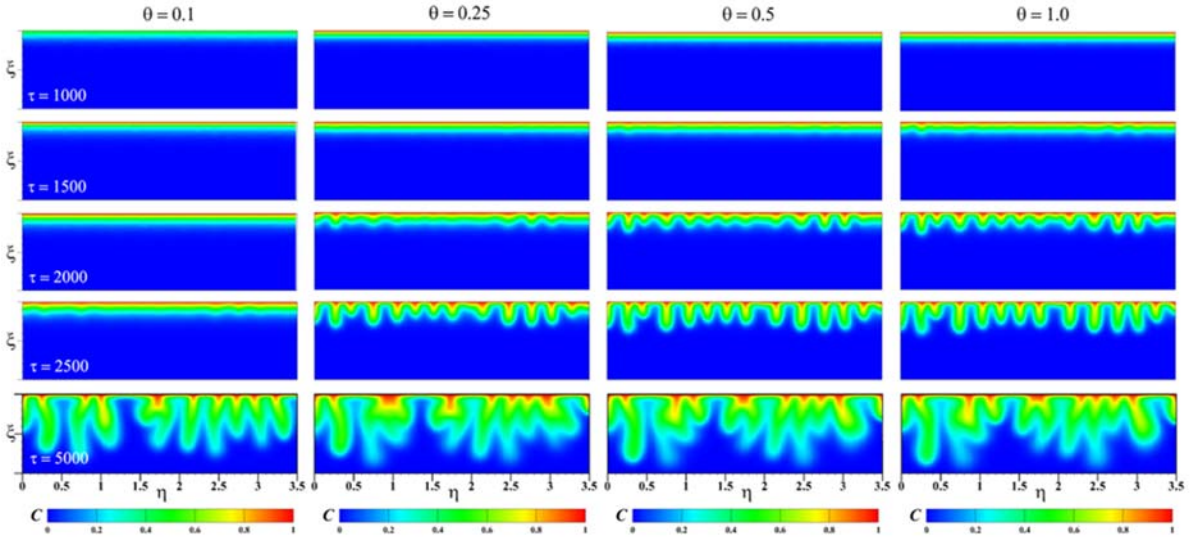


**Figure 7.15:** Temporal concentration distribution for the system exposed to the ramp-flat-ramp contact concentration boundary at different, $\theta = 0.1$, 0.25, 0.5, and 1.0 with constant $\alpha = 0.004$ and $\chi = 0.5$.

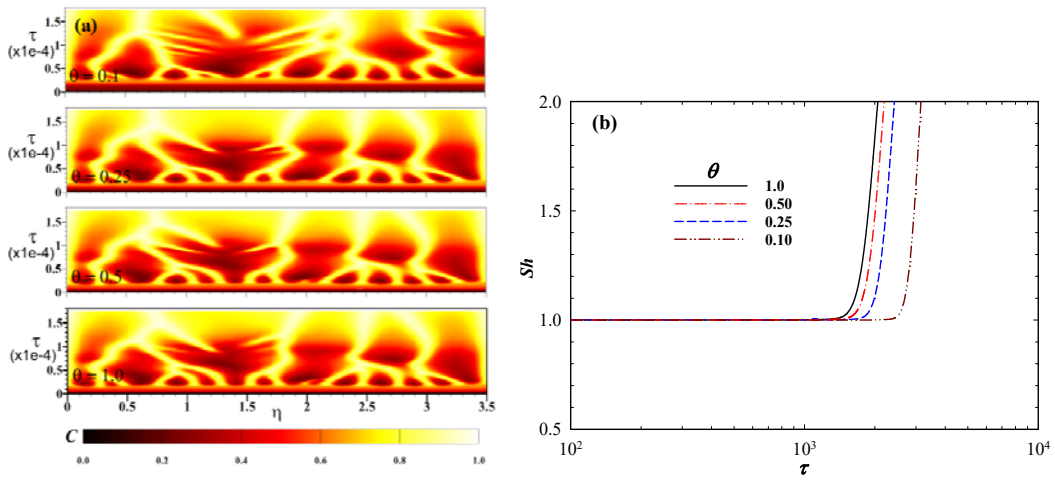


**Figure 7.16:** (a) Space-time maps of the concentration of the solute along a horizontal slice located just below the top boundary at z ≈ +0 for the same systems shown in Figure 15(b) Sherwood number versus time.

### 7.6 Summary and Conclusions

Linear stability analysis (LSA) and direct numerical simulations (DNS) were conducted to study the effect of interface boundary excitation on the onset of convection and associated dynamics of convective dissolution. Stability behaviour of the gravitational unstable diffusive boundary later were characterized as a function of parameters of a well-defined time-dependent interface concentration profile. It was found that for a system with a linear decline ($\alpha$) in concentration at the interface, the onset time monotonically increases for $10^{-4} \leq \alpha \leq 4.4\times10^{-3}$, beyond which the system turns to become unconditionally stable. The scaled critical time and the corresponding wavenumber were found as $\tau_c = 55.6$ and $\kappa_c = 0.0583$, respectively, for $\alpha < 10^{-4}$. It was also observed that the instability behaviour of systems with a linear decline followed by constant concentration is controlled by the constant concentration portion of the boundary condition such that the scaled critical times and the most dangerous wavenumbers lead to single scaling relations of $\tau_c = 55.6/\chi^2$ and $\kappa_c = 0.0583\chi$, respectively, for $\alpha \geq 10^{-1}$. It was shown that for a symmetric flat floored valley shape boundary condition the scaled critical time decreases by decreasing the duration of the flat portion of the boundary condition for the intermediate values of the decline factor, $3\times10^{-3} \leq \alpha \leq 10$. For the same interface boundary condition, it was observed that the scaling relations for the

critical time and the critical wavenumber at either large ($\alpha \geq 10^{1}$) or small ($\alpha \leq 10^{-4}$) decline factors can be described as those in the classical system with constant concentration of $\chi$=1. The dynamics of convective dissolution was also investigated using direct numerical simulations. The results of numerical simulations confirm the general stability criteria predicted by the linear stability analysis. The results also show that in addition to the onset time, the development of instabilities in form of density-driven fingers and the associated dynamics of convective dissolution are controlled by the interface boundary condition.

## 7.7 Acknowledgments

The authors would like to thank the anonymous reviewers for their constructive comments. This work was supported by a Discovery Grant from the Natural Sciences and Engineering Research Council of Canada (NSERC), Alberta Innovates - Technology Futures (AITF) and was enabled in part by support provided by WestGrid (www.westgrid.ca) and Compute Canada Calcul Canada (www.computecanada.ca). The first author also gratefully acknowledges the John and Willie Leone Family Department of Energy and Mineral Engineering at Pennsylvania State University for their hospitality.

## 7.8 Appendix 7.A: Comparison of Early Time Diffusive Flux

As discussed earlier, the linear decline boundary condition with small values of decline factor may find application in gas/liquid dissolution and absorption processes, especially in system with small dissolution capacity where the interface concentration varies linearly over time. Here, it is shown that the linear decline boundary condition with a low decline factor is able to reasonably resemble the diffusive flux the top boundary as compared to case when the boundary is coupled with a finite gas cap (Wen et al., 2018).

While the linear decline boundary condition does not resemble the pressure-dependent concentration of $CO_2$ at the interface when a $CO_2$ gas cap is coupled with the underlying brine, it can be shown that it recovers the flux at the top boundary for cases with small decline factor. The solutions for the pressure-dependent interface concentration (Wen et al., 2018) and the linear decline concentration boundary are given by:

$$C(z_D,t_D)=\frac{1}{1+\Pi}+\sum_{n=1}^{\infty}\frac{e^{-\mu_n^2\hat{t}}\left(2\Pi\cos\left(\mu_n z_D\right)-2\mu_n\sin\left(\mu_n z_D\right)\right)}{\mu_n^2+\Pi+\Pi^2}\quad,\ 0<z_D<1 \tag{A1}$$

where $\mu_n$ are the roots of the nonlinear equation $\tan(\mu_n)+\mu_n/\Pi=0$, n=1,2, …

$$C(z_D,t_D)=\left(1-a_D t_D\right)-\frac{4}{\pi}\sum_{n=1}^{\infty}\frac{1}{(2n-1)}\cos\left(\beta_n\left(1-z_D\right)\right)\left[e^{-\beta_n^2 t_D}+\frac{a_D}{\beta_n^2}\left(e^{-\beta_n^2 t_D}-1\right)\right],0<z_D<1 \tag{A2}$$

where $z$ (the height of the domain and positive downward) and time are scaled by height of domain, $H$ and the diffusive time scale, $H^2/D$, respectively. $B_n=(2n-1)\pi/2$ and, $\Pi$ and $a_D$ are dissolution capacity and the decline rate in the H-scale system, given by $\Pi=V_m K_h RT/V_g$ (Wen et al., 2018), and $a_D=\alpha\left(k\Delta\rho gH/\phi\mu D\right)^2$ (rescaled α in the this study), respectively.

We examined the diffusive flux, as the most important factor in controlling the onset of instability, for both pressure-dependent and the linear decline boundary condition as shown in Fig. A1. The results for constant concentration boundary ($\Pi=a_D=0$) is also shown for comparison. Fig. A1 shows that a system with the linear decline reasonably recovers the behaviour of diffusive flux in a $CO_2$/water system at early times for small dissolution capacities (i.e $\Pi<0.5\simeq a_D<0.5$).

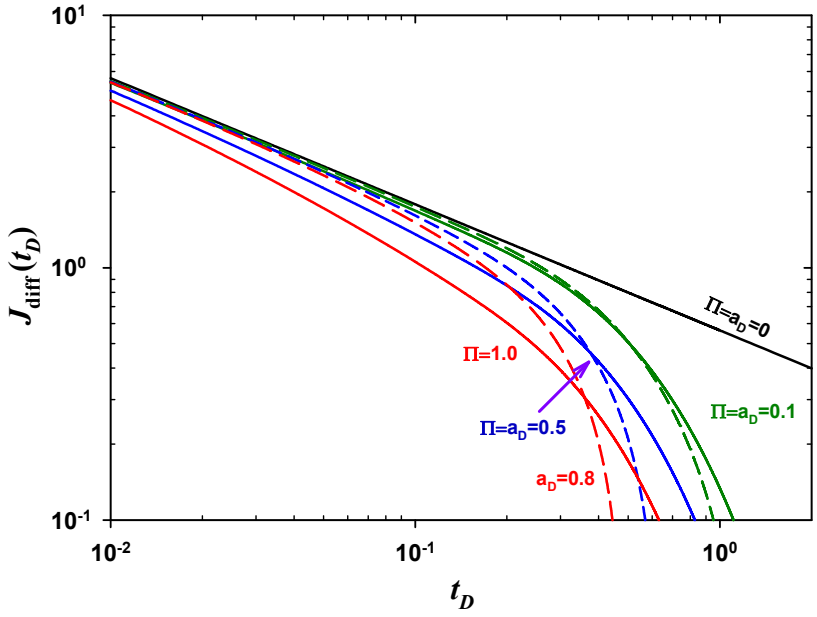


**Figure 7.A1:** Diffusive flux versus time for systems with (dashed line) linear decline and (solid line) pressure-dependent interface concentration in a $CO_2$/water system. The blue solid line represents the diffusive flux for cases with constant concentration boundary.

# Chapter 8: Onset of Density-driven Instabilities in Fractured Aquifers*

## 8.1 Abstract

Linear stability analysis is conducted to study the onset of density-driven convection involved in solubility trapping of $CO_2$ in fractured aquifers. The effect of physical properties of a fracture network on the stability of a diffusive boundary layer in a saturated fractured porous media is investigated using the dual porosity concept. Linear stability analysis results show that both fracture interporosity flow and fracture storativity play an important role in the stability behaviour of the system. It is shown that a diffusive boundary layer under the gravity field in fractured porous media with lower fracture storativity and/or higher fracture interporosity flow coefficient is more stable. We present scaling relations for the onset of convective instability in fractured aquifers with single and variable matrix block size distribution. These findings improve our understanding of density-driven flow in fractured aquifers and are important in the estimation of potential storage capacity, risk assessment, and storage site characterization and screening.

## 8.2 Introduction

Density-driven convection in porous media is of great importance for a wide range of applications related to groundwater, soil contamination, formation of ore deposits, carbon dioxide ($CO_2$)

* Jafari Raad, S. M., Hassanzadeh, H. (2018). Onset of density-driven instabilities in fractured aquifers. *Physical Review E*, *97*(4), 043109. https://doi.org/10.1103/PhysRevE.97.043109

sequestration, and petroleum and geothermal reservoirs (Alt-Epping and Zhao, 2010; Carballido-Landeira et al., 2013; Lindeberg and Wessel-Berg, 1997; Zhao et al., 2009). Natural convection can develop due to an unstable density profile in the gravity field, which can be attributed to either temperature or concentration gradient. Conceptual basis and general importance of both solutal and thermal density-driven convection in porous media have been comprehensively addressed in previous studies (Diersch and Kolditz, 2002; Nield and Bejan, 2006; Zhao et al., 2008). The conditions under which density-driven convection develops in the concentration field have received great attention in the past decade. Density-driven convection involved in geological sequestration of $CO_2$ in deep saline aquifers is a good example of the current interest (Jafari Raad and Hassanzadeh, 2015; Loodts et al., 2014; Trevelyan et al., 2011). Geological sequestration of $CO_2$ has been proposed as a short-term implementable option to reduce anthropogenic $CO_2$ emissions from the atmosphere (Lackner, 2003). Deep saline aquifers with their high storage capacity and worldwide accessibility have been identified as the best alternative for $CO_2$ storage (Lackner, 2003). Once $CO_2$ is injected into an aquifer it migrates upwards due to its buoyancy and spreads at the top of aquifers below a low permeability cap rock from where it gradually dissolves into the underlying brine (Lindeberg and Wessel-Berg, 1997). While most dissolved gases decrease fluid density, dissolution of $CO_2$ into brine slightly increases the density of the brine phase. The $CO_2$-rich brine phase sinks down due to gravitational instabilities that drive the convective dissolution. Convective dissolution enhances the mass transfer of $CO_2$ from the $CO_2$ free phase (plume) to the underlying brines. This process significantly decreases the volume of free-phase $CO_2$ under the cap rock, and consequently reduces risk of $CO_2$ leakage (Ennis-King and Paterson, 2005; Hassanzadeh et al., 2005). The onset of density-driven convection in porous media, in the context of the $CO_2$ sequestration process, has been the subject of several studies as it impacts the long-term storage security. The onset of density-driven convection has been often studied using linear stability theory and energy method in both isotropic (Ennis-King et al., 2005; Hassanzadeh et al., 2006; Riaz et al., 2006; Slim and Ramakrishnan, 2010) and anisotropic (Hong and Kim, 2008; Rapaka et al., 2008, 2009; Xu et al., 2006) porous media. This problem has been also addressed by a number of numerical studies (Andres and Cardoso, 2011; Chen and Zhang, 2010; Hassanzadeh et al., 2007; Hidalgo et al., 2013; Pau et al., 2010). These studies enhanced the understanding of the density-driven convection in the context of $CO_2$ sequestration in deep saline

aquifers. However, previous studies have been focused on $CO_2$ storage in nonfractured (single-porosity) deep saline aquifers.

Understanding the density-driven convection involved in dissolution of $CO_2$ in fractured formations is important since fractured aquifers are widespread and are gaining importance for their potential to host captured $CO_2$ for storage. Density-driven convection in fractured porous media has been the subject of several studies mostly related to geothermal energy, fractured petroleum reservoir exploration, hazardous waste disposal, formation of ore deposits, and groundwater applications. The onset of density-driven instabilities in fractured aquifers with a transient base state in the context of geological storage of $CO_2$ has not been studied sufficiently.

In the early studies on density-driven convection in fractured porous media, a single-fracture medium was approximated by a three-dimensional (3D) fluid-filled vertical slab or vertically oriented saturated porous box heated from below. This configuration was used for cases with either impermeable and nonconducting (Zebib and Kassoy, 1977) or impermeable conducting fracture walls (Kassoy and Cotte, 1985; V. I. Malkovsky and Pek, 2004; Murphy, 1979; Weidman and Kassoy, 1986; Zhao et al., 2005). Later, more complex models were considered to study this phenomenon either within a single fracture ( Graf and Therrien, 2008; Malkovsky and Pek, 2004; Malkovsky and Magri, 2016; Peaceman, 1976a, 1976b; Ruth, 1979; Yang et al., 1998; Zhao et al., 2004) or in a fracture network (Graf and Therrien, 2007; Saidi, 1987; Shikaze et al., 1998; Simmons et al., 2008; Vujević et al., 2014; Vujević and Graf, 2015; Yang, 2006) under various boundary conditions. Through these studies, it was shown that the density-driven flow within a single fracture with nonconducting walls is mostly governed by the stability criteria similar to those reported for stability of a diffusive boundary layer in vertically saturated porous medium (Davis, 1967; Nield, 1968; Zebib and Kassoy, 1977). It was reported that conducting fracture walls have a stabilizing effect on density-driven convection within the fracture (Alt-Epping and Zhao, 2010; Kassoy and Cotte, 1985; V. I. Malkovsky and Pek, 2004; Zhao et al., 2005). The stabilizing effect of conducting fracture walls is less distinct when the adjacent matrix blocks contribute to the transport process as compared to the cases when the fracture wall acts as a boundary (Alt-Epping and Zhao, 2010; Graf and Therrien, 2009; Malkovsky and Pek, 2004; Murphy, 1979; Zhao et al., 2006).

The stability of density-driven convection and the associated convective flow in fracture networks have been often studied using direct numerical simulations. Findings from previous studies show that fracture geometry and hydraulic properties play an important role in the stability of density-driven convection and the convective flow pattern within the fractured system. It has been observed that low fracture aperture, low matrix permeability, and high matrix porosity impede density-driven convection within the fracture network with orthogonal continuous or/and inclined discontinuous fractures (Graf and Therrien, 2007; Simmons et al., 2008). It was shown that the likelihood of continuous fracture circuits and thus the strength of density-driven convection in a fracture network increase as the fracture density and fracture length increase (Mourzenko et al., 2016; Vujević et al., 2014; Vujević and Graf, 2015).

Although significant achievements were made in the study of density-driven flow within fractured porous media, stability analysis of density-driven flows with transient temperature (or concentration) field in a fractured porous medium has not been studied sufficiently. The objectives of this study are to perform linear stability analysis of transient single-phase flow and transport in fractured rocks and develop scaling relations that relate the onset of density-driven instabilities to the key physical properties of the fractured rocks.

The common approach to study the stability of fluids in porous media is to use linear stability analysis. This approach is well accepted and has been widely used in the literature (Emami-Meybodi and Hassanzadeh, 2013; Jafari Raad and Hassanzadeh, 2015; Tan and Homsy, 1986; Trevelyan et al., 2015). In addition, we use the well-known dual porosity idealization of fractured porous media pioneered by Barenblatt et al. (Barenblatt et al., 1960), Warren and Root (Warren and Root, 1963), and Odeh (Odeh, 1965) to model single-phase flow in fractured media. The applicability of this elegant approach to model single-phase flow and transport in fractured porous media has been well accepted in the literature. However, while the dual porosity approach works very well for the single-phase flow situations, which is the subject of our study, it has some essential deficiencies when multiple phases are present. For instance, the gravity drainage process, capillarity, and reinfiltration phenomena are not easy to describe using the dual porosity approach. In this work, we deal with single-phase flow and transport of $CO_2$-saturated brine and therefore gravity drainage process, capillarity, and reinfiltration phenomena are not involved.

Based on the dual porosity concept, which is believed to be appropriate for single-phase flow and transport in fractured rocks, fractured porous systems are considered to be composed of two media, fracture networks with high permeability and low storativity and rock matrix blocks with low permeability and high storativity (Barenblatt et al., 1960; Saidi, 1987; Warren and Root, 1963). In this model, fractures with high permeability contribute to the main flow path for fluid in the fractured porous medium and matrix blocks act as sink or source. Thus, it is expected that density-driven flow develops in the brine-filled fracture networks. However, diffusive solute transport and hence density-driven flow within a fracture is strongly coupled with mass transfer in matrix blocks through the fracture-matrix interaction. The contrast between the dissolved $CO_2$ concentration in fractures and adjacent matrix blocks leads to mass transfer between matrix and fracture. Dissolved $CO_2$ mass transfer from the fracture to the matrix block can act as a sink for the accumulated $CO_2$ in the fissures (Zhou et al., 2017) and consequently affect the stability behaviour of the diffusive boundary layer developed in the fracture network.

Determination of the effect of the physical properties of the fractured porous media on the stability of a diffusive boundary layer requires a coupled model that takes into account the transient solute transport between the fracture and matrix blocks.

In this work, we performed linear stability analysis to study the instability behaviour of a gravitationally unstable diffusive boundary layer associated with dissolution of $CO_2$ in a saturated fractured porous medium. The effect of fracture physical properties and also fracture-matrix interaction on the instability behaviour of a diffusive boundary layer within the fractured porous medium was investigated. Scaling relationships that can be used to estimate the onset of density-driven instabilities were reported as a function of the most common physical properties of the fractured porous media.

## 8.3 Mathematical Formulation

### 8.3.1 Model description

An idealized picture of fractured rock is shown in Figure 8.1(a). We consider a two-dimensional (2D) fractured aquifer of thickness H with slab-shape matrix blocks saturated with quiescent brine as shown in Figure 8.1(b). No-flow boundary conditions are considered at the top and bottom of the domain. At the lower boundary, mass flux is set to zero, while constant concentration of $CO_2$

species is set at the top of the domain with respect to the mass transfer. Assuming single-phase flow and consequently in the absence of capillarity, the interface between $CO_2$ and water is considered sharp with a constant concentration of dissolved $CO_2$ (Riaz et al., 2006).

To study the problem, the coupled mass transfer between the fracture and matrix blocks is treated using the dual porosity model concept (Warren and Root, 1963). Based on this, the matrix blocks act as a sink for the fracture network.

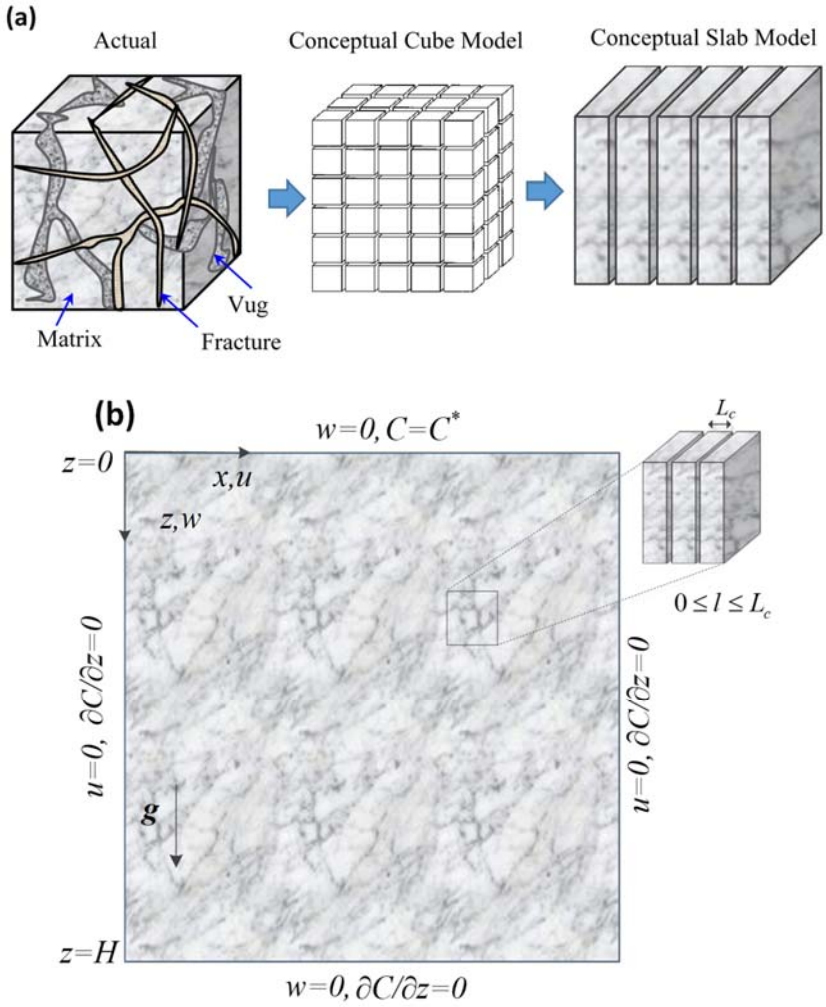


**Figure 8.1:** (a) Idealization of fractured rock with single-size block matrix and (b) geometry and boundary conditions considered in this study(Warren and Root, 1963). $C^*$ is the equilibrium concentration, and $C$ is the concentration of the diffusing species in the aqueous phase. $u$ and $w$ denote the horizontal and vertical components of the Darcy velocity in the fracture domain, respectively.

Using the Boussinesq approximation and in the absence of fluid compressibility, viscosity variation, and dispersion, the governing equations of nonreactive single-phase flow and transport in a fracture domain under the dual porosity concept can be written as follows:

$$\phi_f D_f(\nabla^2 C_f) - \vec{\mathbf{v}}.\nabla C_f = \phi_f \frac{\partial C_f}{\partial t} + \int_{L_{c\,\min}}^{L_{c\,\max}} Q(L_c) J(L_c) dL_c \; ; \tag{8.1}$$

$$\nabla \cdot \vec{\mathbf{v}} = 0 \; ; \tag{8.2}$$

$$\vec{\mathbf{v}} = -\frac{k}{\mu}(\nabla p - \rho \mathbf{g} \nabla z) ; \tag{8.3}$$

$$\phi_m D_m \frac{\partial^2 C_m}{\partial \ell^2} = \phi_m \frac{\partial C_m}{\partial t} , \tag{8.4}$$

where $\mathbf{v}(u,w)$ is the vector of Darcy velocity, $p$ is the pressure, $l$ denotes the spatial coordinate in the matrix block domain with $0 \le l \le L_c$, and $L_c$ is the characteristic thickness of the matrix block. $C_f(x,z,t)$ and $C_m(\ell,t)$ are the concentrations of $CO_2$ in fracture and matrix, respectively; $\mu$ is the viscosity; $k$ is the permeability; $\phi$ is the porosity; and $\boldsymbol{g}$ is the gravitational acceleration. $D$ is the effective molecular diffusion coefficient and is assumed to be independent of concentration for dilute solutions. Subscripts $m$ and $f$ stand for matrix and fracture, respectively. $\rho$ is the brine density defined as $\rho = \rho_b(1+\beta C)$ where $\rho_b$ is the density of fresh brine, $\beta$ is the coefficient of density variation with concentration, and $C$ is the concentration of dissolved $CO_2$ in water. The integral term (or sink) in Equation (8.1) accounts for the mass transfer of dissolved $CO_2$ between matrix blocks and the fractures, and $L_{c\,\min}$ and $L_{c\,\max}$ are minimum and maximum matrix block sizes, respectively.

$Q(L)$ is the rate of mass transfer from the fracture to the adjacent matrix blocks. For matrix block with slab-shape geometry the rate of mass transfer from the fracture to the adjacent matrix block is expressed as

$$Q(L_c) = \frac{\phi_m D_m}{L_c} \frac{\partial C_m}{\partial \ell}\bigg|_{\ell = L_c} . \tag{8.5}$$

Function *J(L)* in Equation (8.1) is the probability density function (PDF) describing the size distribution function for the matrix blocks. For a fractured porous medium with a single size-matrix block of thickness $L_c$ the sink term in Equation (8.1) is reduced to $Q(L_c)$.

A fractured porous medium may be classified as an intensely or sparsely fractured system depending on the skewness of the block length probability density function (PDF) (Johns and Jalali, 1991). Linear and exponential probability density functions are the two most common continuous block size distributions used in the modelling of dual porosity media (Segall, 1981). In this study, we use exponential probability density as the most general function to characterize the matrix block size distribution. The corresponding function for an exponential block size distribution is given by (Jelmert, 1995)

$$J(L_c) = \frac{me^{-mL_c}}{me^{-mL_{c\min}} - me^{-mL_{c\max}}}\ , \tag{8.6}$$

where $m$ is an exponential distribution constant; $L_{c\,\min}$ and $L_{c\,\max}$ are minimum and maximum matrix block sizes existing in the distribution, respectively.

It has been observed that a collection of continuous matrix blocks with different characteristic lengths can be interpreted using a single-matrix block with an equivalent length (Zimmerman and Bodvarsson, 1995), where the equivalent length is obtained based on the matrix block size distribution.

In other words, the sink term in fracture conservation mass Equation (8.1) is equivalent to the fracture interporosity flow with an equivalent length $L_{ce}$ as given by

$$\int_{L_{c\min}}^{L_{c\max}} Q(L_c)J(L_c)dL_c \cong \frac{\phi_m D_m}{L_{ce}} \left.\frac{\partial C_m}{\partial \ell}\right|_{\ell=L_{ce}}\ . \tag{8.7}$$

In the following, the above formulation is used to perform the linear stability analysis.

### 8.3.2 Base state solution

At the early times and prior to the onset of convection, molecular diffusion is the dominant mechanism involved in transport of dissolved $CO_2$. In this case, the dimensionless equations governing the mass transfer within the fractured porous media can be written as follows:

$$\frac{\partial^2 \hat{C}_{0f}}{\partial \hat{z}^2} - \frac{\lambda}{\hat{L}_e}\frac{1-\omega}{\omega}\frac{\partial \hat{C}_{0m}}{\partial \hat{\ell}}\bigg|_{\hat{\ell}=\hat{L}_e} = \frac{\partial \hat{C}_{0f}}{\partial \hat{t}}, \tag{8.8}$$

$$\frac{\partial^2 \hat{C}_{0m}}{\partial \hat{\ell}^2} = \frac{1}{\lambda}\frac{\partial \hat{C}_{0m}}{\partial \hat{t}}, \tag{8.9}$$

where subscript 0 stands for the base state. We use $H$, $L_{c\,max}$, $C^*$, and $H^2/D_f$ to scale the spatial coordinates in the fracture domain ($x,z$), the spatial coordinate in the matrix block domain ($l$), concentration, and time, respectively. Using these scalings the governing equations are nondimensionalized. In the above equations $\omega=\phi_f/\phi_t$ is the storativity, $\lambda = D_m H^2/D_f L_{c\max}^2$ is the interporosity flow coefficient, and $\hat{L}_e = L_{ce}/L_{c\max}$ is the dimensionless matrix block equivalent thickness. The storativity coefficient, $\omega=\phi_f/\phi_t$, is defined as the pore volume of the fracture per total pore volume of the fractured porous medium where subscripts $f$ and $t$ refer to the fracture and the total system (both fracture and matrix domains), respectively.

In the case of exponential distribution, the equivalent thickness in dimensionless form is expressed as (Ranjbar et al., 2012):

$$\hat{L}_e = \frac{(\alpha F_h + 1)e^{-\alpha F_h} - (\alpha + 1)e^{-\alpha}}{\alpha\,(e^{-\alpha F_h} - e^{-\alpha})}, \tag{8.10}$$

where $F_h = L_{c\min}/L_{c\max}$, and $\alpha$ is a dimensionless exponential distribution constant.

The following initial and boundary conditions are used to close the formulation.

For fracture: $\hat{C}_{0f}(\hat{z},\hat{t}=0)=0$, $\hat{C}_{0f}(0,\hat{t})=1$, and $\partial \hat{C}_{0f}(0,\hat{t})/\partial \hat{z}=0$, (8.11)

For matrix: $\hat{C}_{0m}(\hat{\ell},\hat{t}=0)=0$, $\hat{C}_{0m}(\hat{L}_e,\hat{t})=\hat{C}_{0f}$, and $\partial \hat{C}_{0m}(0,\hat{t})/\partial \hat{\ell}=0$. (8.12)

The base state solution for the concentration field in the fracture domain can be obtained by using Laplace transform and inverted to the time domain using residue theorem (Carslaw and Jaeger, 1959) as given by

$$\hat{C}_{0f}(\hat{z},\hat{t}) = 1 + \sum_{n=1}^{\infty}(-1)^{n+1}\frac{(2n-1)\pi}{\eta f'}\cos\left(\frac{(2n-1)\pi}{2}(1-\hat{z})\right)\exp\left(\eta_n \hat{t}\right), \tag{8.13}$$

Where

$$f(\eta_n) = \eta_n + \frac{\lambda}{\hat{L}_e}\frac{1-\omega}{\omega}\sqrt{\frac{\eta_n}{\lambda}}\tanh\left(\sqrt{\frac{\eta_n}{\lambda}}\hat{L}_e\right), \tag{8.14}$$

and $f' = df(\eta_n)/d\eta_n$, and $\eta_n$ are roots of the following nonlinear equation:

$$f(\eta_n) + \frac{(2n-1)^2\pi^2}{4} = 0. \tag{8.15}$$

Figure 8.2(a) shows the base state concentration profiles versus depth in the fracture domain with different fracture storativity coefficients ($\omega$) and constant fracture interporosity flow coefficient ($\lambda$) at a given time ($\hat{t} = 0.08$). It can be observed that diffusive mass transfer of $CO_2$ in a fracture is much slower when the fracture storativity decreases. This is due to the fact that the matrix blocks act as a sink for the dissolved $CO_2$. Note that $\omega$=1 denotes the single-porosity system with properties of the fracture domain. A low storativity implies larger matrix pore volume per unit bulk volume of the fractured media and hence a much stronger sink for the dissolved $CO_2$.

Figure 8.2(b) shows the time-dependent diffusive flux at the upper interface ($z$ = 0). The results for diffusive flux versus time clearly indicate that the flux of $CO_2$ at the interface into the domain is higher for a system with lower fracture storativity during the early time and later throughout the shutdown period when the effect of concentration reaches the bottom boundary.

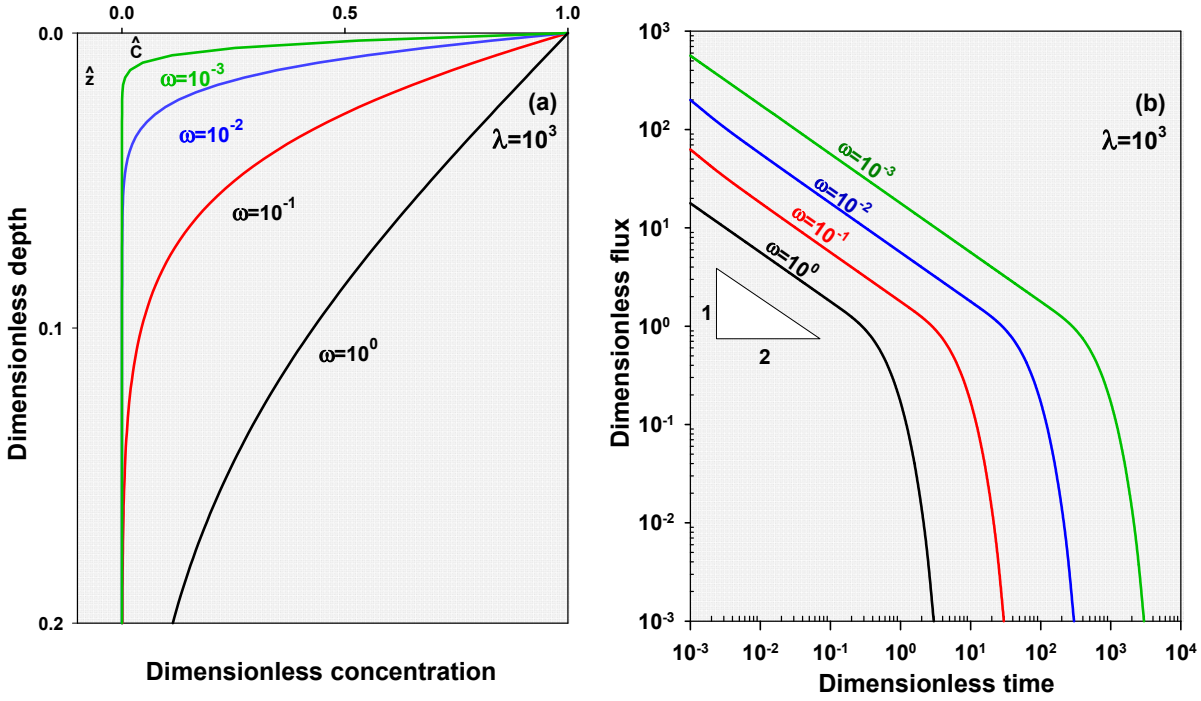


**Figure 8.2:** (a) Base state concentration profiles versus depth at $\hat{t} = 0.08$ and (b) $CO_2$ diffusive flux at the upper interface for fracture domain with a constant fracture interporosity flow coefficient of $\lambda = 10^3$ and different fracture storativity coefficients $\omega = 1$, $\omega = 10^{-1}$, $\omega = 10^{-2}$, and $\omega = 10^{-3}$.

Figure 8.3 shows the dependency of the base state concentration profile on the fracture interporosity flow coefficient. It can be observed that increase of the fracture interporosity flow coefficient at a constant fracture storativity retards the propagation of $CO_2$ concentration in the fracture domain. Solution of the base state concentration also shows that for a fractured porous medium with fracture interporosity flow coefficients larger than $\lambda > 10^3$, the concentration within the fracture domain is less sensitive to the fracture interporosity flow coefficient. Later, we will show how the dependency of the concentration profile on the physical properties of the system may impact the onset of density-driven instabilities.

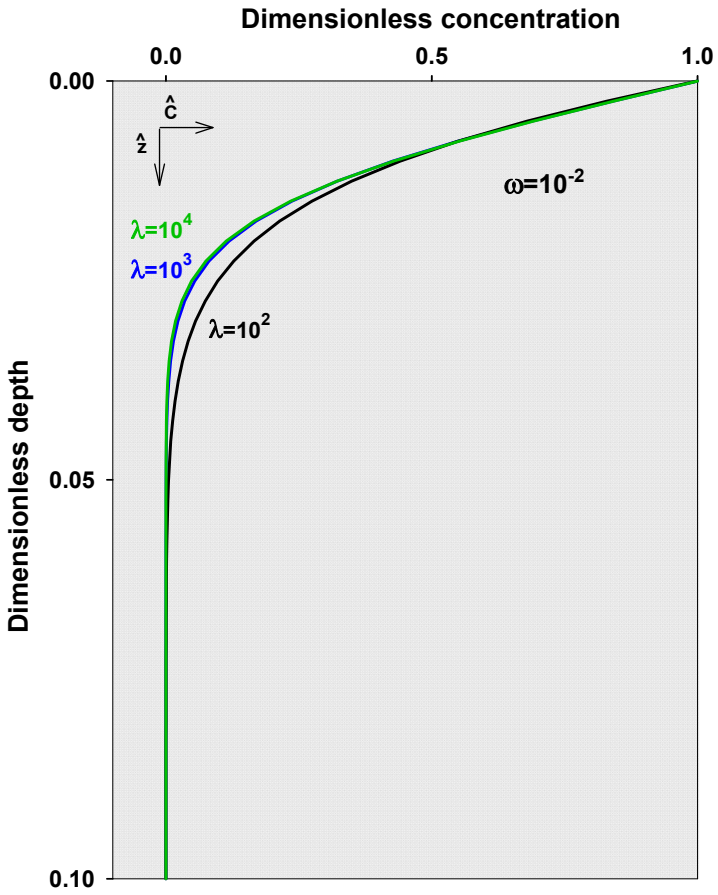


**Figure 8.3:** Base state concentration profiles versus depth in fracture domain with fracture storativity $\omega = 10^{-2}$, and different fracture interporosity flow coefficients of $\lambda = 10^{2}, 10^{3}$, and $10^{4}$ at $\hat{t} = 0.08$ .

### 8.3.3 Linear stability analysis

The linear stability analysis determines the time at which the diffusive boundary layer becomes unstable leading to convective mixing of $CO_2$. As discussed earlier, convective mixing plays an important role in the rate of $CO_2$ solubility trapping. We performed the linear stability analysis under quasi steady-state approximation (QSSA) (Tan and Homsy, 1986) to study the growth of instabilities of a diffusive boundary layer involved in $CO_2$ sequestration into a fractured aquifer.

To conduct a linear stability analysis, the governing equations of flow and transport given in Equations (8.1)-(8.4) are linearized. Pressure, velocity, concentration and density fields are

subjected to infinitesimal perturbations as $\mathbf{s} = \mathbf{s}_0 + \mathbf{s}'$ where **s**=**s**[p,**v**,C,ρ]; $s_0$ and s' are the base state and perturbations, respectively.

Substituting the perturbed variables into the flow and transport equations, implementing the base state quantities, taking the curl of Equation (8.3), and, after simplification, we obtain the following perturbed equations.

$$\frac{\partial^2 C_f'}{\partial z^2} - w' \frac{\partial C_{0f}}{\partial z} = \frac{\partial C_f'}{\partial t}, \tag{8.16}$$

$$\frac{\partial^2 C_m'}{\partial \ell^2} = \frac{1}{\lambda} \frac{\partial C_m'}{\partial t}, \tag{8.17}$$

$$\nabla^2 w' = \mathrm{Ra} \nabla^2 C_f', \tag{8.18}$$

where the velocity perturbation is scaled by $(\phi D)_f/H$, $\nabla^2 = \nabla_{xy}^2$, $\mathrm{Ra} = kg\beta C^* H / \mu(\phi D)_f$, and the hats (^) are dropped for convenience. $w'$ denotes the vertical component of the Darcy velocity perturbation, and $C^*$ is the equilibrium concentration (maximum concentration) of the diffusing species in the aqueous phase.

By using the Fourier decomposition method, the perturbed velocity and concentration are expressed as

$$[C_f', C_m', w'] = [C_f^*, C_m^*, w^*](z, t_0) e^{-i\kappa x + \sigma t}, \tag{8.19}$$

where $\kappa$ and $\sigma$ are the perturbation wave number and growth rate, respectively. Using Equation (8.19) the decomposed perturbed equations can be written as

$$\frac{d^2 C_f^*}{dz^2} - \kappa^2 C_f^* - w^* \frac{\partial C_{0f}}{\partial z} = (\sigma) C_f^*, \tag{8.20}$$

$$\frac{d^2 w^*}{dz^2} - \kappa^2 w^* = \mathrm{Ra}(-\kappa^2) C_f^*, \tag{8.21}$$

with the boundary conditions $w^*(z=0) = w^*(z=1) = 0, C^*(z=0) = 0$, and $\partial C^*(z=1)/\partial z = 0$.

To find the growth rate $\sigma$ as a function of wave number $\kappa$, Equations (8.20) and (8.21) are solved numerically using the finite difference method. The following eigenvalue problem can be obtained using the discretized perturbed Equations (8.20) and (8.21).

$$\{\mathbf{A}_c - \mathrm{Ra}\left(-\kappa^2\right)\mathbf{A}_w^{-1}\frac{\partial C_{0f}}{\partial z}\}[C^*]=[\sigma][C^*], \tag{8.22}$$

where $\mathbf{A}_w=(\mathbf{D}_w-\kappa^2\mathbf{I})$, $\mathbf{A}_c=(\mathbf{D}_c-\kappa^2\mathbf{I})$; $\mathbf{D}_w$ and $\mathbf{D}_c$ are coefficient matrices based on central discretization of the second derivatives and c and *w* are subscripts for concentration and velocity, respectively.

The above eigenvalue problem is solved numerically for a range of system physical properties at a certain diffusive time. The same numerical procedure addressed in the previous studies (Emami-Meybodi and Hassanzadeh, 2013) is employed to solve the eigenvalue problem. The maximum eigenvalue of the coefficient matrix is considered as the growth rate $\sigma$, corresponding to the assigned wave number $\kappa$, and *Ra* at a certain time. The time at which the growth rate turns positive at the given Ra number represents the onset of instability.

### 8.4 Results and Discussion

Linear stability analysis was conducted to study the effect of the physical properties of fractured porous media and interaction of matrix and fracture on the onset of density-driven convection. In the following, the stability criterion of the diffusive boundary layer in a fractured porous medium is examined for a wide range of dual porosity parameters.

Figure 8.4 shows the growth rate of perturbations for a system with different fracture storativity and interporosity flow coefficients at a constant Ra number and $\hat{t}_0=18\times10^3$. Linear stability analysis results reveal different growth rates for these systems, suggesting different instability behaviour. Results of perturbation growth rates for systems with a constant interporosity flow coefficient $\lambda$, shown in Figure 8.4(a) indicate that systems with larger fracture storativity ω lead to higher perturbation growth rates. This may imply that systems with larger fracture storativity are gravitationally less stable than those with smaller ω.

Results of growth rates for systems with a constant fracture storativity and Ra number are shown in Figure 8.4(b) for different interporosity flow coefficients. It can be observed that increase of interporosity flow coefficient leads to lower perturbations growth rates, suggesting a more stable diffusive boundary layer. In other words, the fracture to matrix mass transfer has a stabilizing effect. To further clarify these findings, results of onset of the convective instabilities versus Ra for various fracture storativity and interporosity flow properties are shown in Figure 8.5.

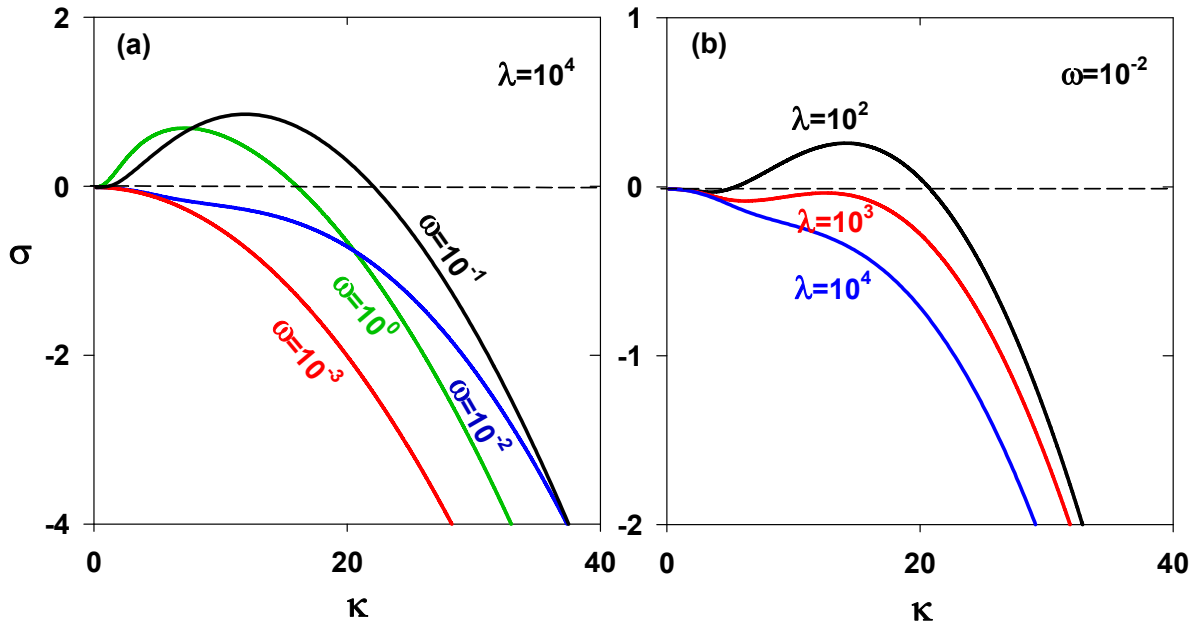


**Figure 8.4:** Perturbation growth rates versus wave number for systems with different fracture storativity and interporosity flow coefficients at a constant Ra=500 and $\hat{t}_0 = 1.8\times10^{-3}$.

Figure 8.5 shows the onset of instabilities as a function of Rayleigh number for fractured systems with single-size matrix blocks at different fracture storativity and interporosity flow coefficients. Results show that in all cases the onset time of instability is inversely promotional to the square of the Rayleigh nimber, implying that the onset time is independent of the porous layer thickness, which is in agreement with previous findings (Ennis-King et al., 2005; Hassanzadeh et al., 2006; Meulenbroek et al., 2013; Slim, 2014). Results of stability analysis shown in Figure 8.5(a) clearly indicate the important role of fracture storativity on the onset of instability. For a given Ra number and fracture interporosity flow coefficient, it is observed that a fractured system with larger fracture storativity shows the earlier onset time. This is in agreement with previous findings for

the effect of fracture density and storativity on the onset and dynamics of density-driven flow in fractured porous media (Graf and Therrien, 2007; Mourzenko et al., 2016; Vujević et al., 2014). For the case of a single-porosity system with fracture properties ($\omega$=1), linear stability analysis results in a scaling prefactor value of $a$ ~56 for the dimensionless onset time as a function of Ra number. This is in agreement with previous studies (Jafari Raad et al., 2016; Jafari Raad and Hassanzadeh, 2015, 2016; Riaz et al., 2006). Scaling results also show that the value of prefactor $a$, representing the onset of density-driven instability at constant Ra and interporosity flow coefficient, significantly increases as the fracture storativity factor decreases. Comparison of scaling onset results for systems with different fracture interporosity flow coefficients also shows that the onset of instability is delayed as the fracture to matrix interporosity flow coefficient increases. This observation is in agreement with those reported in the literature (Alt-Epping and Zhao, 2010; Graf and Therrien, 2009; V. I. Malkovsky and Pek, 2004; Murphy, 1979; Chongbin Zhao et al., 2006). This instability behaviour is attributed to the stabilizing effect of fracture to matrix mass transfer on the growth rate of perturbations in the diffusive boundary layer.

Careful review of the onset time results for a system with constant Ra number and fracture interporosity flow coefficient shows that the rescaling of the onset time as a function of Ra number leads to a single scaling with unique prefactor $a/\omega$ for cases with fracture storativity coefficients less than 0.1. It is worth noting that most of the natural fractured systems have fracture storativity below 0.1. The new scaling onset time is shown in Figure 8.6.

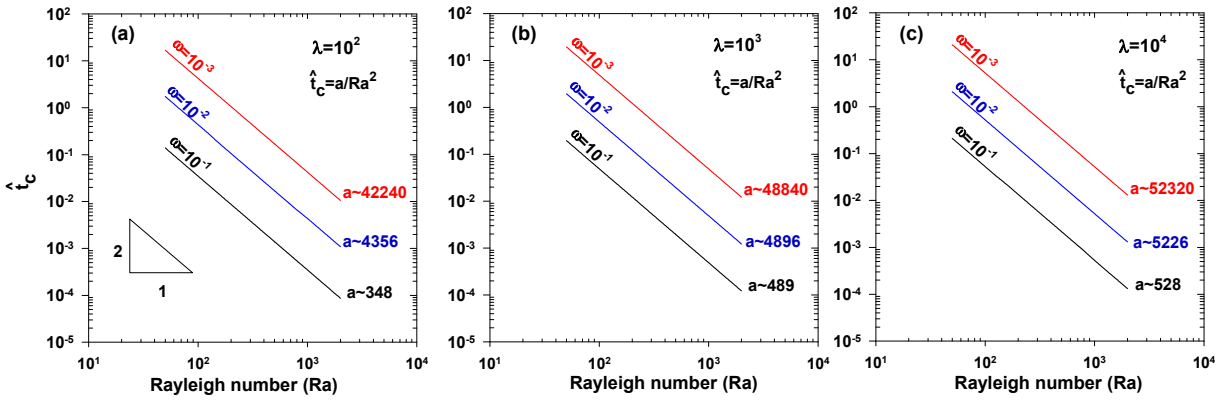


**Figure 8.5:** Onset of instability scaled with Ra for fractured systems with single-size matrix blocks at different fracture storativity and interporosity flow coefficients.

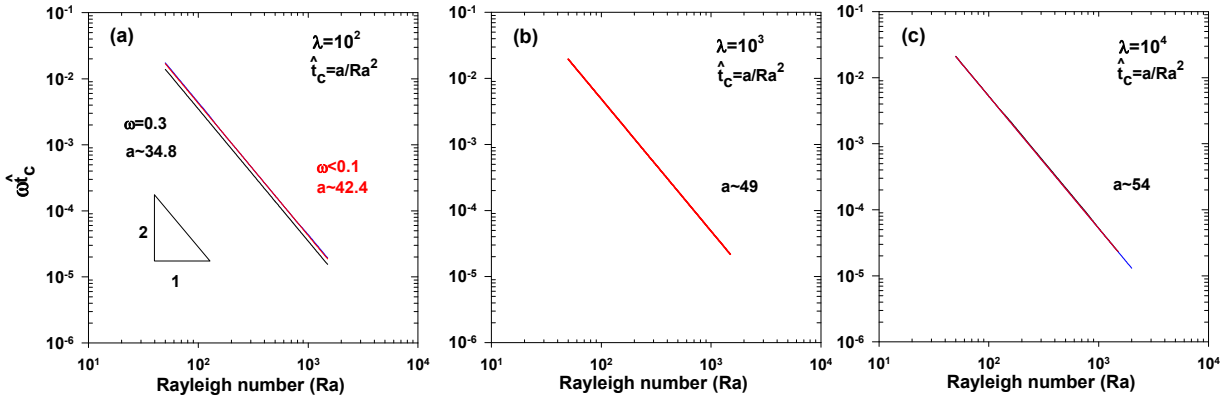


**Figure 8.6:** Onset of instability scaled with Ra for fractured systems with single-size matrix blocks at different fracture interporosity flow coefficients.

Figure 8.7 shows the effect of fracture storativity on the neutral stability curves for fractured systems with a constant interporosity flow coefficient, $\lambda$ =100. The results clearly show that the instability limit in the neutral stability curves significantly shifts upward as fracture storativity decreases. This observation suggests that the system turns more stable at smaller fracture storativities. Rescaling the transient time by multiplying it by the fracture storativity coefficient leads to a single neutral curve suggesting a unified stability limit for a constant interporosity flow coefficient as shown in Figure 8.7(b).

The neutral stability curves for the fractured systems with constant fracture storativity ω=0.1, at different fracture interporosity flow coefficients $\lambda$ =100, 1000 and 10000 are also shown in Figure 8.8. The neutral curves show that as the interporosity flow coefficient increases the system turns more stable. It can be observed that the regions of instability (σ>0) move upward as the fracture interporosity flow coefficients increase.

The QSSA formulation of the dual porosity problem does not allow explicit parametric analysis of the stability problem. In Appendix A, we use the Galerkin technique (Hassanzadeh et al., 2006; Xu et al., 2006) to convert the linearized perturbation equations [Equations (8.16)-(8.18)] to a system of ordinary differential equations, which allows analysis of the stability criterion for the special limiting cases of dual porosity parameters ($\lambda$ and $\omega$).

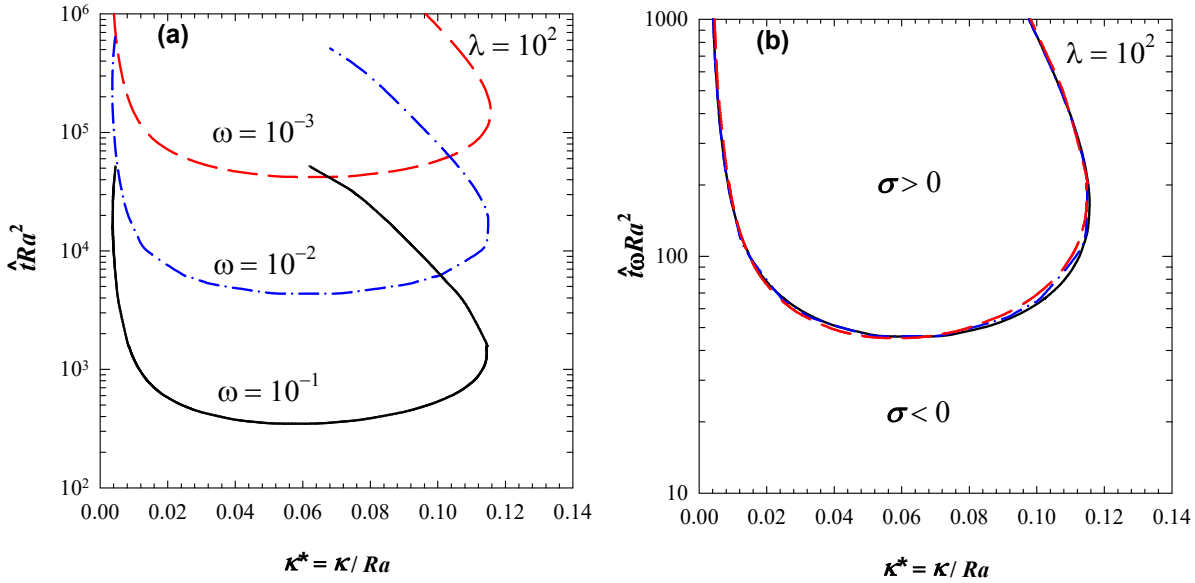


**Figure 8.7:** Neutral stability curves for fractured systems with single-size matrix blocks and a constant fracture interporosity flow coefficient $\lambda$ =100, at different fracture storativity coefficients.

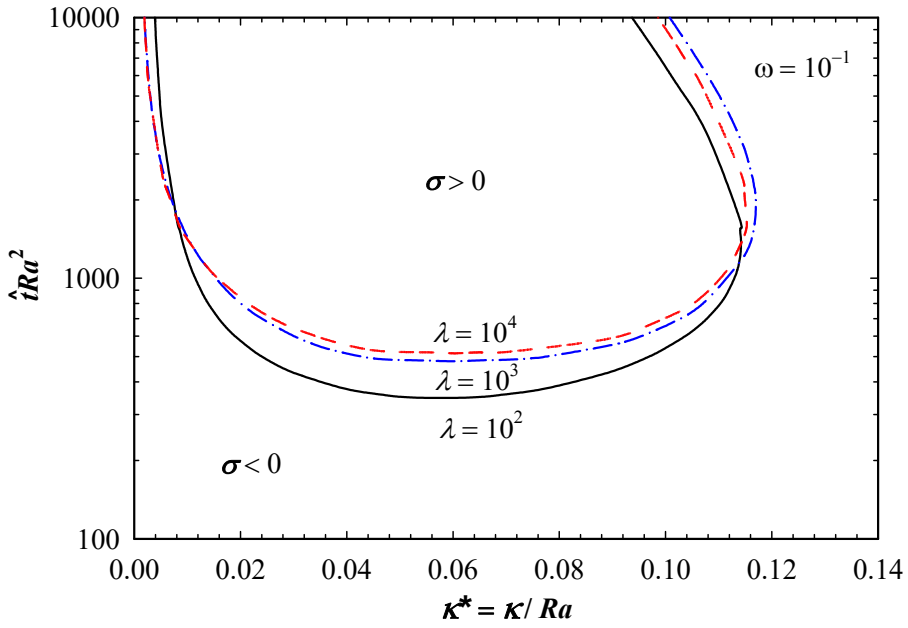


**Figure 8.8:** Neutral stability curves for fractured systems with single-size matrix blocks and a constant fracture storativity ω=0.1, at different fracture interporosity flow coefficients.

It is of interest to find out how the variability of matrix block sizes in the fracture aquifers may influence the instability behaviour of the diffusive boundary layer. Figure 8.9 shows the scaling of the onset time as a function of Rayleigh number for fractured systems with different fracture intensities at constant storativity and interporosity flow coefficients. The exponential probability density function with four different common values of α=-20, -5, 5, and 20 at the constant fracture uniformity $F_h$=0.1 was employed to represent the matrix block size distribution (Rodriguez et al., 2001). For an exponential probability density function [see Equations (8.6) and (8.10)], positive values of *m* (*α* in dimensionless form) imply higher fracture intensity and negative values of *m* infer sparse fracturing. Scaling results for the onset time versus Ra number show that increase of fracture intensity (positively increasing of α value) stabilizes the diffusive boundary layer leading to higher onset time. This suggests that the diffusive boundary layer for an intensively fractured system is more stable than the sparse one. This instability behaviour is expected since for an intensely fractured system mass transfer between matrix and fracture is higher, thus promoting stability of the boundary layer.

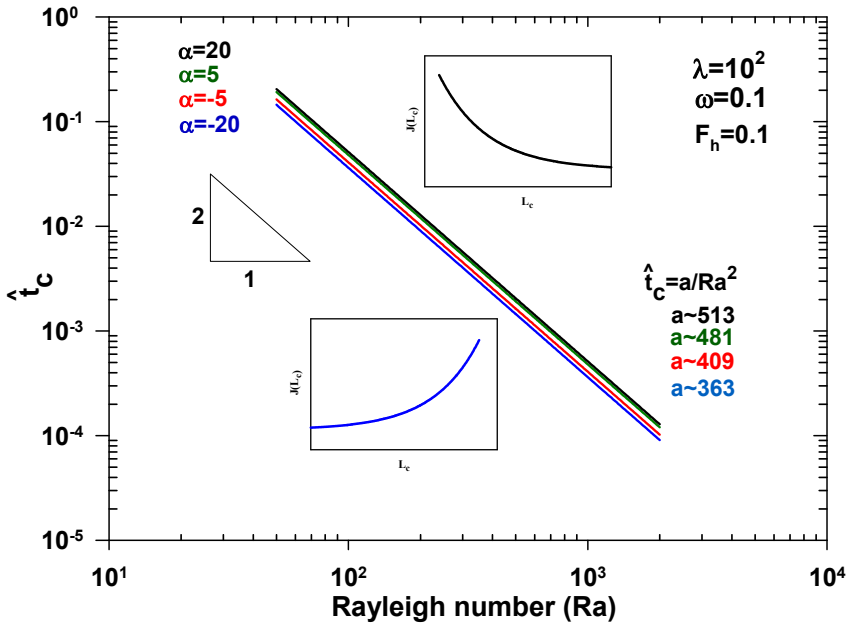


**Figure 8.9:** Onset of instability as a function of Ra number for fractured systems with different matrix block sizes represented by exponential probability density function at constant fracture storativity and interporosity flow coefficients. The inset plots show the matrix block size probability distribution.

Figure 8.10 shows the scaling of the onset time as a function of Ra number for a fractured system with exponential matrix block size distribution at different fracture storativity and interporosity flow coefficients. It can be observed that the onset time can be rescaled as a unique scaling for systems with fracture storativity coefficients less than 0.1. The results shown in Figures 8.10(a)-8.10(c) also indicate that the impact of matrix block size distribution on the onset of instability decreases as the fracture interporosity flow coefficient increases.

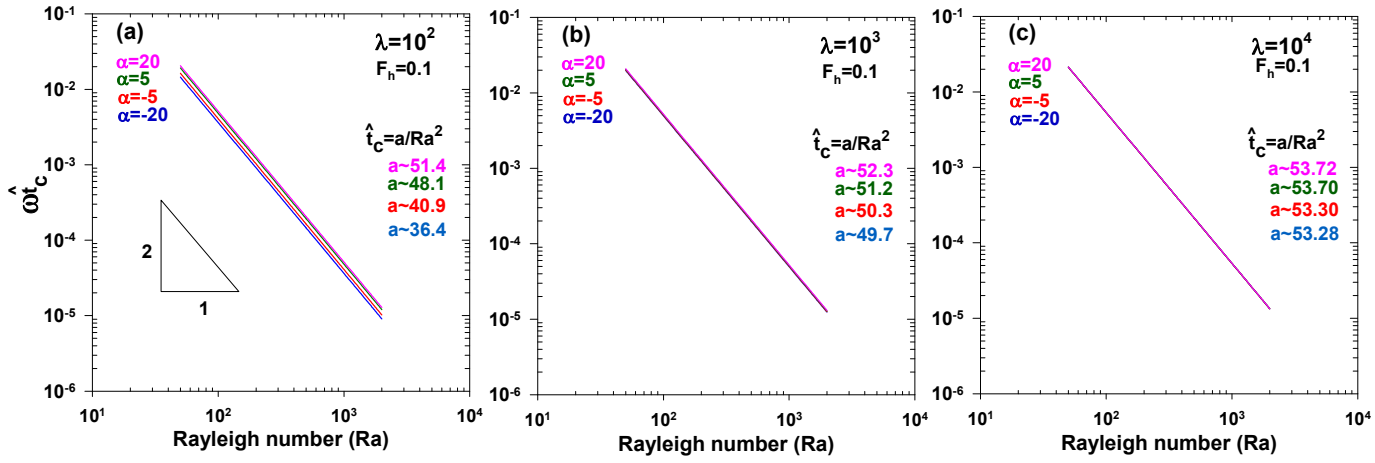


**Figure 8.10:** Scaled onset time of instability for fractured systems with variable matrix block size at different fracture interporosity flow coefficients.

## 8.5 Summary and Conclusions

We have conducted a linear stability analysis to investigate the onset of natural convection involved in the $CO_2$ sequestration process in fractured saline aquifers. The dual porosity model was employed to describe the solute transport in fractured media. The effect of physical properties of the fractured porous media on the stability of a transient diffusive boundary was investigated. It was shown that increase of the interporosity flow coefficient leads to a more stable diffusive boundary layer. It was also shown that a diffusive boundary layer under the gravity field in a fractured porous medium with a higher fracture storativity coefficient is less stable. We also examined the effect of matrix block size distribution on the stability behaviour of the diffusive boundary layer using an exponential probability density function. It was observed that increase of

fracture intensity stabilizes the diffusive boundary layer leading to a delayed onset time. In general, it was shown that the diffusive boundary layer for an intensively fractured system is more stable than the sparse one. Results of the onset time show that the impact of matrix block size distribution on the onset of instability decreases as the fracture interporosity flow coefficient increases. The scaling relation for the onset of convection as a function of Rayleigh number, fracture interporosity and storativity coefficients, and matrix block size distribution properties were developed. It was shown that the onset time as a function of Ra number for cases with fracture storativity coefficients less than 0.1 can be presented using a single scaling relation with unique prefactor $a/\omega$. Such scaling relationships are of great importance in characterization of the fate of the injected $CO_2$, risk assessment, and site screening purposes.

Finally, we used an idealization of the dual porosity formulation. The behaviour of mixing beyond the onset of convection in complex fractured formations in the presence of heterogeneity calls for further studies. The current study paves the way for further studies in this area.

### 8.6 Acknowledgments

The authors would like to thank the anonymous reviewers for their constructive comments. This work was supported by the Natural Sciences and Engineering Research Council of Canada (NSERC) Discovery Grant and Alberta Innovates - Technology Futures (AITF) and was enabled in part by the computing support provided by WestGrid and Compute Canada Calcul Canada.

### 8.7 Appendix 8.A: Semi-analytical Treatment of The Linear Stability for Special Cases

The detailed linear stability analysis in the main text was conducted using the QSSA, which does not allow explicit representation of the special cases. Here, we use the Galerkin technique (Hassanzadeh et al., 2006; Xu et al., 2006), which allows explicit parametric analysis of the stability problem for some limiting cases.

The linearized Equations (8.16)-(8.18) can be transformed into ordinary differential equations (ODEs) using the Galerkin technique (Hassanzadeh et al., 2006; X. Xu et al., 2006). The resulting ODEs can be rearranged to find the Rayleigh numbers as a function of the dual porosity parameters ($\lambda$ and $\omega$) as given by

$$\mathrm{Ra}=\left(\frac{da_l}{d\hat{t}}+\left(\kappa^2+\left(l-\frac{1}{2}\right)^2\pi^2\right)a_l\right)\frac{\left(\left(l\pi\right)^2+\kappa^2\right)\left(1-4l\right)}{2\kappa^2 l\pi a_l\left[\frac{\left(4l-1\right)^2}{\eta_{2l}f'_{\eta_{2l}}}e^{\eta_{2l}\hat{t}}+\frac{1}{\eta_1 f'_{\eta_1}}\mathrm{e}^{\eta_1\hat{t}}\right]}, \tag{8.A1}$$

where $a$ is the time-dependent amplitude of concentration perturbation in the fracture domain; $l$=1,2,….,N is the summation index in the Fourier expansion of the concentration perturbation; and other parameters have been defined in Sec. 8.3. Equation (8.A1) allows explicit parametric analysis of the stability problem for special cases as described in the following.

**Special cases**

**Case (i)** $\lambda\to\infty$**.** The relation given for the Rayleigh number in Equation (8.A1) reduces to the following equation when $\lambda\to\infty$:

$$\mathrm{Ra}=\left(\frac{\omega+1}{\omega}\right)\frac{\pi\left(\frac{da_l}{d\hat{t}}+\left(\kappa^2+\left(l-\frac{1}{2}\right)^2\pi^2\right)a_l\right)\left(\left(l\pi\right)^2+\kappa^2\right)\left(4l-1\right)}{16\kappa^2 la_l\left(e^{-\frac{(4l-1)^2\pi^2}{4}\hat{t}}+e^{-\frac{\pi^2}{4}\hat{t}}\right)}. \tag{8.A2}$$

This equation indicates that the onset time is independent of $\lambda$ when $\lambda\to\infty$. The detailed analysis using QSSA also shows that for $\lambda\geq 10^4$ the onset time is independent of $\lambda$.

**Case (ii)** $\omega\to 1$. The relation given for Rayleigh number in Equation (8.A1) reduces to the following equation when $\omega\to 1$:

$$\mathrm{Ra}=\frac{\pi\left(\frac{da_l}{d\hat{t}}+\left(\kappa^2+\left(l-\frac{1}{2}\right)^2\pi^2\right)a_l\right)\left(\left(l\pi\right)^2+\kappa^2\right)\left(4l-1\right)}{8\kappa^2 la_l\left(e^{-\frac{(4l-1)^2\pi^2}{4}\hat{t}}+e^{-\frac{\pi^2}{4}\hat{t}}\right)}, \tag{8.A3}$$

which is equivalent to Case i ( $\lambda\to\infty$) when $\omega$=1.

**Case (iii)** $\omega\to 0$. The relation given for the Rayleigh number in Equation (8.A1) reduces to $\mathrm{Ra}=\infty$ when $\omega\to 0$, which indicates an unconditionally stable state. It is worth noting that

this conclusion has been reached as a result of the dual porosity assumption where the transport mechanism in the matrix is pure diffusion.

**Case (iv).** When $\tanh\sqrt{\eta_n/\lambda} \approx 1$ or $\sqrt{\eta_n/\lambda} \geq 4$ it can be shown that

$$Ra = \frac{\pi}{4\kappa^2 l a_l g_l}\left(\frac{da_l}{d\hat{t}} + \left(\kappa^2 + \left(l-\frac{1}{2}\right)^2\pi^2\right)a_l\right)\left((l\pi)^2+\kappa^2\right)(4l-1). \tag{8.A4}$$

where $g_l$ is only a function of $(1-\omega)\sqrt{\lambda}/\omega, \hat{t}$. This indicates that for a constant Ra, the onset time is only a function of $\kappa$ and $(1-\omega)\sqrt{\lambda}/\omega$. In other words, $t_c = \wp(Ra, \kappa, 1-\omega)\sqrt{\lambda}/\omega)$

**Case (v).** $\lambda \to 0$ while $\omega > 0$: The relation given for the Rayleigh number in Equation (8.A1) reduces to Equation (A3) in this case.

# Chapter 9: Conclusions and Recommendations

## 9.1 Conclusions

This dissertation has presented analytical and numerical analyses on stability criteria of buoyancy-driven convection and hydrodynamics of the associated convective mixing in porous media with applications to the geological storage of $CO_2$ in deep saline aquifers. This study has firstly investigated the dynamics of concentration dependent base state density profile evolve during dissolution process for different fluid pair systems. Mathematical models have been developed to characterize the role of the base state density profile on the stability criteria of the buoyancy-driven convection and the dynamics of the associated convective mixing in the considered fluid pair systems.

The analysis on the role of the base state density profile has been extended to problems with application to $CO_2$ sequestration process. In particular, stability criterion of the buoyancy-driven convection and the dynamics of associated convective dissolution in fluid systems involved in impure $CO_2$ sequestration process and also analogue fluid systems used in experiments of convective dissolution of $CO_2$ in brine have been addressed.

This study has also presented a theoretical analysis on stability criterion of the buoyancy-driven convection and the dynamics of convective mixing in porous media subjected to time-dependent boundaries. This research has also offered a mathematical model describing stability behaviour of diffusive boundary layer involved $CO_2$ storage in fractured saline aquifers. It has also investigated the effect of physical properties of fracture network on the stability criterion of the buoyancy-driven convection and consequently dynamics of mixing process.

This dissertation has provided fundamental understanding of the hydrodynamics of buoyancy-driven flow and convective mixing. In particular, scaling laws derived from this study, which can be used to design experiments and incorporated into storage site screening and selection models, are of great importance and are key novel contribution of this study. The results from this study also provide insight into a wide range of applications in various aspects of mixing encountered in engineering and science. In the following, the contributions of this dissertation are described in more details followed by recommendations for future study.

### 9.1.1 Role of the base state density profile in hydrodynamics of the buoyancy-driven convection

Using analytical and numerical developments, I have characterized the role of the base state density profile evolved during dissolution process on the onset of buoyancy-driven instabilities and the dynamics of the associated convective mixing in binary and ternary fluid pair systems. Using linear stability analysis (LSA), I have parameterized the role of non-monotonic density profile in the stability criteria of the fluid systems. LSA results revealed the important role of the characteristic shape of the base state density profile in the stability criterion of the system. Universal scaling relations, which allows estimation of the onset of the convective instabilities and generalization of the non-monotonic dependence of the growth of the instabilities were presented based on the results obtained from LSA of the diffusive boundary layer in different fluid pair systems.

I have extended this analysis to typical analogue fluid systems used in experiments of convective dissolution of $CO_2$. In particular, I have studied the stability criterion of the buoyancy-driven convection and the dynamic of associated convective mixing in EGMeOH/water and water/propylene glycol fluid pair systems.

Using both linear stability analysis and direct numerical simulations, I have provided new evidences that neither EG-MeOH nor PPG analogue systems do resemble the dynamics of convective instabilities associated with dissolution of $CO_2$ in water. It was found that there are fundamental differences in the evolution of the buoyancy-driven instability and dynamics of convective mixing between $CO_2$/water and these analogue systems. Results revealed that for a constant Rayleigh number the onset of convective instabilities for these analogue fluids can be

lower (or higher) by an order of magnitude as compared to $CO_2$/water. It was shown that the base state density behaviour of analogue systems has a significant effect on the stability characteristics of the diffusive boundary layer and the convective mixing beyond the onset of instability. According to the results of this study, the choice of the analogue system is critically important in the design of experiments for proper representation of the convective instabilities in $CO_2$/water system. Results of this study form a basis for proper selection of an analogue system and are necessary to interpret $CO_2$ convective dissolution experiments.

### 9.1.2 Dynamic of the buoyancy-driven convection associated with impure $CO_2$ storage

I have studied the effect of impurities in a $CO_2$ stream on the onset of buoyancy-driven convection and subsequent dynamics of convective mixing associated with impure carbon dioxide ($CO_2$) storage in deep saline aquifers. I have shown that the contrast in diffusion coefficients of $CO_2$ and permitted impurities may give rise to a non-monotonic density profile during the dissolution process depending on the solute buoyancy ratio and equilibrium concentration of the gas. I have suggested that the buoyancy-driven convection modes can be systematically classified in the ($r_\beta r_c$, $r_D$) parameter space based on the type of the developed base state density profile.

Using LSA and with the help of the developed parameter space classification, I have shown that an impurity such as $H_2S$ has a potential to accelerate the buoyancy-driven instabilities. The LSA results clearly indicated the important role of the composition of the injected stream on the onset of buoyancy-driven convection. Using direct numerical simulation, it was shown that the dynamic of the system at the onset of convective dissolution does not hold beyond the onset, such that an impure stream with an earlier onset of convective dissolution develops a slower dynamic at the late time of the process. While an impurity such as $H_2S$ is prone to impede the convective dissolution, it was shown that an informed choice of impurity can lead to similar convective dissolution as of pure $CO_2$ stream. These findings suggest that an impure $CO_2$ stream can be engineered to improve the rate of dissolution and thus solubility trapping of $CO_2$ leading to higher storage security and efficiency.

### 9.1.3 Role of diffusivity contrasts in dynamics of buoyancy-driven convection in multi-component fluid systems

Using investigation of time evolving base state density profiles in a two-component partially miscible fluid mixture, analytical and numerical experiments, I have classified various instability mechanisms in a parameter space characterized by the relative contribution of solutes to the density and their diffusion coefficient ratio. I have examined both stabilizing and destabilizing effects of the diffusion coefficient contrast on Rayleigh–Bénard (RB) instabilities and the associated convective dissolution in systems with different diffusivity ratios and opposing contribution of dissolving solutes to the mixture density. A parametric analysis indicated eight distinct instability regions. Using linear stability analysis (LSA) and direct numerical simulation (DNS), I have quantified the interplay of double diffusive (DD) instabilities and Rayleigh–Bénard (RB) convection in terms of the onset time and convective dissolution flux. In particular, I have studied two important categories of fluid systems with positive and negative net density contribution of the solutes. In both cases, it was shown that the diffusion contrast effect has a potential to accelerate or slow down the convective instabilities depending on the solutes diffusion contrast. The parametric analysis for systems with negative net density contribution of the solutes revealed a transition from pure DD instabilities to RB convection at relatively high diffusion contrast, leading to significantly earlier onset of convective instability and higher dissolution flux.

It was shown that the key point to distinguish whether the diffusion contrast has a stabilizing or destabilizing effect on buoyancy-driven instabilities depends on the relative contribution of the two species to the density. The relevance of the base state density profile in the control of onset was characterized by analyzing the favorable driving density difference in systems with different diffusivity contrasts. I have proposed scaling relations for the onset as a function of the driving density difference. The presented parametric analysis provides new insights into differential diffusion effects and can be used to control instabilities in partially miscible systems.

### 9.1.4 Boundary excitation effects on buoyancy-driven flows in porous media

I have performed an inclusive analysis of the instability and the associated dynamics of solutal natural convection in saturated porous media in the presence of boundary excitation. I have used a time-dependent boundary condition to simulate the concentration excitation at the interface.

Using linear stability analysis (LSA), I have provided a detailed parametric analysis on the stability of a diffusive boundary layer in porous media subject to three different types of linear decline, linear decline followed by constant concentration, and symmetric flat floored valley shape boundary conditions.

The LSA results showed that the boundary excitation influences the stability behaviour and evolution of the subsequent convective instabilities. I have proposed scaling relations based on results of LSA to describe the critical time and the associated wavenumber of convective instabilities that incorporate the effect of the characteristics of the boundary condition and the physical properties of the porous layer. The dynamics of the system beyond the onset time has also been studied using direct numerical simulations. The results of DNS revealed that the dynamics of the buoyancy-driven mixing is significantly influenced by the temporal variation of concentration at the boundary. These findings improve our understanding of buoyancy-driven instabilities in the presence of boundary excitation and finds applications in thermal and solutal convection in porous media.

### 9.1.5 Buoyancy-driven instabilities in fractured porous media

I have performed linear stability analysis (LSA) to study the instability behaviour of a gravitationally unstable diffusive boundary layer associated with dissolution of $CO_2$ in a saturated fractured porous medium. I have studied the effect of fracture physical properties and fracture-matrix interaction on the instability behaviour of a transient diffusive boundary layer in a dual porosity porous medium. LSA results revealed that both fracture interporosity flow and fracture storativity play an important role in the stability behaviour of the system. Results showed that a diffusive boundary layer under the gravity field in fractured porous media with lower fracture storativity and/or higher fracture interporosity flow coefficient is more stable.

I have also studied the effect of matrix block size distribution on the stability behaviour of the diffusive boundary layer using an exponential probability density function. LSA results showed that the diffusive boundary layer for an intensively fractured system is more stable than the sparse one. Results also revealed that the impact of matrix block size distribution on the onset of instability decreases as the fracture interporosity flow coefficient increases. Based on the results of LSA, I have proposed scaling relations for the onset of convection as a function of the most

common physical properties of the fractured porous media. Such scaling relationships are of great importance in characterization of the fate of the injected $CO_2$, risk assessment, and site screening purposes.

## 9.2 Recommendations for Future Research

The above-mentioned theoretical and numerical analyses enhanced our understanding of transport phenomena in porous media and provided useful tools for application in geological $CO_2$ storage and waste disposal in subsurface formations and groundwater resource engineering. Significant challenges remain in this field and represent exciting opportunities for future experimental and theoretical investigations. In the following, some of these challenges as a potential for future research is briefly described.

### 9.2.1 Two-phase flow effects associated with impure $CO_2$ storage

Studies of two-phase $CO_2$ convective dissolution and the two-phase flow effects therein have thus far focused almost solely on pure $CO_2$/brine system. Two-phase flow effects are expected to be important in stability behaviour and the dynamics of convective dissolution impure $CO_2$/brine system. It is essential to study two-phase flow effects such as capillarity on the stability criterion of the buoyancy-driven convection and the hydrodynamics of convective dissolution involved in geological storage of impure $CO_2$.

### 9.2.2 Gas phase fractional composition change associated with impure $CO_2$ storage

In the case of impure gas injection, the fractional composition of the free phase gas can rarely remain constant during the whole span of the sequestration process due to either small gas/brine volume ratio or the solubility and diffusivity contrast of $CO_2$ and impurities. In this case, the fractional portion of $CO_2$ in the gas phase region may decrease or increase with time depending on the $CO_2$/impurity solubility and diffusivity ratio as dissolution progresses. This suggests a time-dependent aqueous $CO_2$/impurity concentration at the gas/brine interface affecting the density difference driving convective dissolution. This important physical behaviour of the fractional gas composition in the gas phase region and its role in the gas/brine concentration interface and subsequently the dynamics of convective dissolution has been not well understood and need to be investigated.

### 9.2.3 Reactive convective mixing associated with impure $CO_2$ storage

Upon dissolution of impure $CO_2$ stream in brine, a variety of geochemical reactions may occur between the dissolved gas species (e.g., $CO_2$, $H_2S$, $NO_2$ and $SO_2$) and reactants dissolved in the brine. These reactions can severely complicate the situation by interacting with the transport phenomena, altering the hydrodynamic instability and the spatio-temporal convection patterns. The impact of these reactive processes on the trapping mechanisms; in particular, convective dissolution and consequently overall trapping of impure $CO_2$ is, however, poorly understood and needs to be investigated. Understanding the effects of chemical reaction on the dynamics of dissolution and consequently effectiveness of $CO_2$ trapping is of great importance for long-term storage and risk assessment.

### 9.2.4 Dynamics of convective dissolution in fractured aquifers

The impact of fracture networks on the dynamics of convective mixing involved in $CO_2$ storage in fractured aquifers is poorly understood. The effect of fracture-matrix mass transfer interaction and fracture network geometry on dynamics of convective dissolution is expected to be significant. The hydrodynamic of $CO_2$ convective dissolution in fractured aquifers is less discussed and worthy of further investigation.

## References


Agartan, E., Trevisan, L., Cihan, A., Birkholzer, J., Zhou, Q., and Illangasekare, T. H. (2015). Experimental study on effects of geologic heterogeneity in enhancing dissolution trapping of supercritical $CO_2$. Water Resources Research, 51(3), 1635–1648. https://doi.org/10.1002/2014WR015778

Akhbari, D., and Hesse, M. A. (2017). Causes of underpressure in natural $CO_2$ reservoirs and implications for geological storage. Geology, 45(1), 47–50. https://doi.org/10.1130/G38362.1

Alt-Epping, P., and Zhao, B. C. (2010). Reactive mass transport modelling of a three-dimensional vertical fault zone with a finger-like convective flow regime. Journal of Geochemical Exploration, 106, 8–23.

Andres, J. T. H., and Cardoso, S. (2011). Onset of convection in a porous medium in the presence of chemical reaction. Physical Review E, 83(4), 046312. https://doi.org/10.1103/PhysRevE.83.046312

Bachu, S. (2008). $CO_2$ storage in geological media: role, means, status and barriers to deployment. Progress in Energy and Combustion Science, 34(2), 254–273. https://doi.org/10.1016/j.pecs.2007.10.001

Bachu, S., and Carroll, J. J. (2005). In-situ phase and thermodynamic properties of resident brine and acid gases ($CO_2$ and $H_2S$) injected into geological formations in western Canada. Greenhouse Gas Control Technologies 7, I, 449–457. https://doi.org/10.1016/B978-008044704-9/50046-X

Bachu, S., and Gunter, W. (2005). Overview of acid-gas injection operations in Western Canada. In Greenhouse Gas Control Technologies 7 (pp. 443–448). Elsevier. https://doi.org/10.1016/B978-008044704-9/50045-8

Bachu, S., Adams, J. J., Michael, K., and Buschkuehle, B. E. (2003). Acid gas injection in the alberta basin: a commercial-scale analogue for $CO_2$ geological sequestration in sedimentary basins. In: Proceedings of the second national conference on carbon dioxide sequestration. Alexandria.

Bachu, S., Haug, K., and Michael, K. (2008). Stress regime at acid-gas injection operations in western canada; energy resources coservation board. Edmonton, Alberta, Canada.

Backhaus, S., Turitsyn, K., and Ecke, R. E. (2011). Convective instability and mass transport of diffusion layers in a Hele-shaw geometry. Physical Review Letters, 106(10), 104501(1-4). https://doi.org/10.1103/PhysRevLett.106.104501

Barenblatt, G., Zheltov, I., and Kochina, I. (1960). Basic concepts in the theory of seepage of homogeneous liquids in fissured rocks. Journal of Applied Mathematics and Mechanics, 24(5), 1286–1303. https://doi.org/10.1016/0021-8928(60)90107-6

Bear, J. (1972). Dynamics of fluids in porous media. New York: Elsevier.

Benson, S. M., and Cole, D. R. (2008). $CO_2$ Sequestration in Deep Sedimentary Formations. Elements, 4(5), 325–331. https://doi.org/10.2113/gselements.4.5.325

Bestehorn, M., and Firoozabadi, A. (2012). Effect of fluctuations on the onset of density-driven convection in porous media. Physics of Fluids, 24(11), 114102(1-30). https://doi.org/10.1063/1.4767467

Bhadauria, B. S., Hashim, I., and Siddheshwar, P. G. (2013). Effects of time-periodic thermal boundary conditions and internal heating on heat transport in a porous medium. Transport in Porous Media, 97(2), 185–200. https://doi.org/10.1007/s11242-012-0117-7

Bird, R. B., Stewart, W. E., and Lightfoot, E. N. (2002). Transport phenomena (Second). New York: J. Wiley. Retrieved from https://books.google.ca/books/about/Transport Phenomena.

Blake, K. R., Bejan, A., and Poulikakos, D. (1984). Natural convection near 4°C in a water saturated porous layer heated from below. International Journal of Heat and Mass Transfer, 27(12), 2355–2364. https://doi.org/10.1016/0017-9310(84)90094-2

Boot-Handford, M. E., Abanades, J. C., Anthony, E. J., Blunt, M. J., Brandani, S., Mac Dowell, N., et al. (2014). Carbon capture and storage update. Energy Environ. Sci., 7(1), 130–189. https://doi.org/10.1039/C3EE42350F

Caltaoirone, J. (1976). Stability of a horizontal porous layer under periodical boundary conditions. International Journal of Heat and Mass Transfer, 19(8), 815–820. https://doi.org/10.1016/0017-9310(76)90193-9

Carballido-Landeira, J., Trevelyan, P. M. J., Almarcha, C., and De Wit, A. (2013). Mixed-mode instability of a miscible interface due to coupling between Rayleigh-Taylor and double-diffusive convective modes. Physics of Fluids, 25(2), 024107. https://doi.org/10.1063/1.4790192

Cardoso, S., and Andres, J. T. H. (2014). Geochemistry of silicate-rich rocks can curtail spreading of carbon dioxide in subsurface aquifers. Nature Communications, 5, 5743(1-6). https://doi.org/10.1038/ncomms6743

Carroll, J. J., and Maddocks, J. R. (1999). Design considerations for acid gas injection. In: Laurance Reid Gas Conditioning Conference. Norman Oklahoma.

Carslaw, H. S., and Jaeger, J. C. (1959). Conduction of Heat in Solids. Clarendon Press.

Chan Kim, M., and Kyun Choi, C. (2012). Linear stability analysis on the onset of buoyancy-driven convection in liquid-saturated porous medium. Physics of Fluids, 24(4), 044102. https://doi.org/10.1063/1.3703330

Chen, C., and Zhang, D. (2010). Pore-scale simulation of density-driven convection in fractured porous media during geological $CO_2$ sequestration. Water Resources Research, 46(11), 1–9. https://doi.org/10.1029/2010WR009453

Chhuon, B., and Caltagirone, J. P. (1979). Stability of a horizontal porous layer with timewise periodic boundary conditions. Journal of Heat Transfer, 101(2), 244. https://doi.org/10.1115/1.3450954

Coats, K. H.(1969). Elements of reservoir simulation. University of Texas, College of Engineerin, Engineering Institutes. INTERCOMP Resource Development [Houston, Texas 77027].

Conrad, F. H., Flint, M. C., Meyer, R. H., and Sjoberg, J. W. (1952). Analysis of system methanol-ethylene glycol-water. Analytical Chemistry, 24(5), 837–840. https://doi.org/10.1021/ac60065a021

Coumou, D., Driesner, T., and Heinrich, C. A. (2008). The structure and dynamics of mid-ocean ridge hydrothermal systems. Science (New York), 321(5897), 1825–8. https://doi.org/10.1126/science.1159582

Van Dam, R. L., Simmons, C. T., Hyndman, D. W., and Wood, W. W. (2009). Natural free convection in porous media: First field documentation in groundwater. Geophysical Research Letters, 36(11), L11403. https://doi.org/10.1029/2008GL036906

Daniel, D., and Riaz, A. (2014). Effect of viscosity contrast on gravitationally unstable diffusive layers in porous media. Physics of Fluids, 26(11), 116601. https://doi.org/10.1063/1.4900843

Davis, S. H. (1967). Convection in a box: linear theory. Journal of Fluid Mechanics, 30(03), 465. https://doi.org/10.1017/S0022112067001545

Derlacki, Z. J., Easteal, A. J., Edge, A. V. J., Woolf, L. A., and Roksandic, Z. (1985). Diffusion coefficients of methanol and water and the mutual diffusion coefficient in methanol-water solutions at 278 and 298 K. The Journal of Physical Chemistry, 89(24), 5318–5322. https://doi.org/10.1021/j100270a039

Diersch, H.-J. G., and Kolditz, O. (2002). Variable-density flow and transport in porous media: approaches and challenges. Advances in Water Resources, 25(8–12), 899–944. https://doi.org/10.1016/S0309-1708(02)00063-5

Eckert, K., and Grahn, A. (1999). Plume and Finger Regimes Driven by an Exothermic Interfacial Reaction. Physical Review Letters, 82(22), 4436–4439. https://doi.org/10.1103/PhysRevLett.82.4436

Eckert, K., Acker, M., and Shi, Y. (2004). Chemical pattern formation driven by a neutralization reaction. I. Mechanism and basic features. Physics of Fluids, 16(2), 385–399. https://doi.org/10.1063/1.1636160

Elder, J. W., and W., J. (1967). Steady free convection in a porous medium heated from below. Journal of Fluid Mechanics, 27(01), 29. https://doi.org/10.1017/S0022112067000023

Elenius, M. T., Nordbotten, J. M., and Kalisch, H. (2012). Effects of a capillary transition zone

on the stability of a diffusive boundary layer. IMA Journal of Applied Mathematics, 77(6), 771–787. https://doi.org/10.1093/imamat/hxs054

Elenius, M. T., Nordbotten, J. M., and Kalisch, H. (2014). Convective mixing influenced by the capillary transition zone. Computational Geosciences, 18(3–4), 417–431. https://doi.org/10.1007/s10596-014-9415-1

Emami-Meybodi, H., and Hassanzadeh, H. (2015). Two-phase convective mixing under a buoyant plume of $CO_2$ in deep saline aquifers. Advances in Water Resources, 76, 55–71. https://doi.org/10.1016/j.advwatres.2014.11.011

Emami-Meybodi, H., Hassanzadeh, H., Green, C. P., and Ennis-King, J. (2015). Convective dissolution of $CO_2$ in saline aquifers: Progress in modelling and experiments. International Journal of Greenhouse Gas Control, 40, 238–266. https://doi.org/10.1016/j.ijggc.2015.04.003

Emami Meybodi, H., and Hassanzadeh, H. (2013). Stability analysis of two-phase buoyancy-driven flow in the presence of a capillary transition zone. Physical Review E, 87(3), 033009. https://doi.org/10.1103/PhysRevE.87.033009

Ennis-King, J., Preston, I., and Paterson, L. (2005). Onset of convection in anisotropic porous media subject to a rapid change in boundary conditions. Physics of Fluids, 17(8), 084107. https://doi.org/10.1063/1.2033911

Ennis-King, J. P., and Paterson, L. (2005). Role of convective mixing in the long-term storage of carbon dioxide in deep saline formations. SPE Journal, 10(03), 349–356. https://doi.org/10.2118/84344-PA

EPA. (2014). Climate change indicators in the United States. U.S. Environmental protection agency.

Farajzadeh, R., Salimi, H., Zitha, P. L. J., and Bruining, H. (2007). Numerical simulation of density-driven natural convection in porous media with application for $CO_2$ injection projects. International Journal of Heat and Mass Transfer, 50(25–26), 5054–5064. https://doi.org/10.1016/j.ijheatmasstransfer.2007.08.019

Fernández-Sempere, J., Ruiz-Beviá, F., Colom-Valiente, J., and Más-Pérez, F. (1996). Determination of diffusion coefficients of glycols. Journal of Chemical and Engineering Data, 41(1), 47–48. https://doi.org/10.1021/je950193j

Firoozabadi, A., and Cheng, P. (2010). Prospects for subsurface $CO_2$ sequestration. AIChE Journal, 56(6), 1398–1405. https://doi.org/10.1002/aic.12287

Firoozabadi, A., and Myint, P. C. (2010). Prospects for subsurface $CO_2$ sequestration. AIChE Journal, 56(6), 1398–1405. https://doi.org/10.1002/aic.12287

Gao, G., Fu, B., Zhan, H., and Ma, Y. (2013). Contaminant transport in soil with depth-dependent reaction coefficients and time-dependent boundary conditions. Water Research,

47(7), 2507–2522. https://doi.org/10.1016/j.watres.2013.02.021

Gaus, I., Audigane, P., André, L., Lions, J., Jacquemet, N., Durst, P., et al. (2008). Geochemical and solute transport modelling for $CO_2$ storage, what to expect from it? International Journal of Greenhouse Gas Control, 2(4), 605–625. https://doi.org/10.1016/J.IJGGC.2008.02.011

Ghesmat, K., Hassanzadeh, H., and Abedi, J. (2011). The impact of geochemistry on convective mixing in a gravitationally unstable diffusive boundary layer in porous media: $CO_2$ storage in saline aquifers. Journal of Fluid Mechanics, 673, 480–512. https://doi.org/10.1017/S0022112010006282

Gilfillan, S. M. V, Lollar, B. S., Holland, G., Blagburn, D., Stevens, S., Schoell, M., et al. (2009). Solubility trapping in formation water as dominant $CO_2$ sink in natural gas fields. Nature, 458(7238), 614–618. https://doi.org/10.1038/nature07852

Gopalakrishnan, S. S., Carballido-Landeira, J., Knaepen, B., and De Wit, A. (2018). Control of Rayleigh-Taylor instability onset time and convective velocity by differential diffusion effects. Physical Review E, 98(1), 011101. https://doi.org/10.1103/PhysRevE.98.011101

Graf, T., and Therrien, R. (2007). Variable-density groundwater flow and solute transport in irregular 2D fracture networks. Advances in Water Resources, 30(3), 455–468. https://doi.org/10.1016/j.advwatres.2006.05.003

Graf, T., and Therrien, R. (2008). A test case for the simulation of three-dimensional variable-density flow and solute transport in discretely-fractured porous media. Advances in Water Resources, 31(10), 1352–1363. https://doi.org/10.1016/j.advwatres.2008.07.003

Graf, T., and Therrien, R. (2009). Stable-unstable flow of geothermal fluids in fractured rock. Geofluids, 9(2), 138–152. https://doi.org/10.1111/j.1468-8123.2008.00233.x

Griffiths, R. W. (1981). Layered double-diffusive convection in porous media. Journal of Fluid Mechanics, 102(1), 221. https://doi.org/10.1017/S0022112081002619

Hassanzadeh, H., Pooladi-Darvish, M., and Keith, D. W. (2005). Modelling of convective mixing in $CO_2$ storage. Journal of Canadian Petroleum Technology, 44(10), 43–50.

Hassanzadeh, H., Pooladi-Darvish, M., and Keith, D. W. (2006). Stability of a fluid in a horizontal saturated porous layer: effect of non-linear concentration profile, initial, and boundary conditions. Transport in Porous Media, 65(2), 193–211. https://doi.org/10.1007/s11242-005-6088-1

Hassanzadeh, H., Pooladi-Darvish, M., and Keith, D. W. (2007). Scaling behaviour of convective mixing, with application to geological storage of $CO_2$. AIChE Journal, 53(5), 1121–1131. https://doi.org/10.1002/aic.11157

Hewitt, D. R., Neufeld, J. A., and Lister, J. R. (2013). Convective shutdown in a porous medium at high Rayleigh number. Journal of Fluid Mechanics, 719, 551–586.

https://doi.org/10.1017/jfm.2013.23

Hidalgo, J. J., Fe, J., Cueto-Felgueroso, L., and Juanes, R. (2012). Scaling of convective mixing in porous media. Physical Review Letters, 109(26), 264503. https://doi.org/10.1103/PhysRevLett.109.264503

Hidalgo, J. J., MacMinn, C. W., and Juanes, R. (2013). Dynamics of convective dissolution from a migrating current of carbon dioxide. Advances in Water Resources, 62, 511–519. https://doi.org/10.1016/j.advwatres.2013.06.013

Holness, M. B., Nielsen, T. F. D., and Tegner, C. (2006). Textural maturity of cumulates: a record of chamber filling, liquidus assemblage, cooling rate and large-scale convection in mafic layered intrusions. Journal of Petrology, 48(1), 141–157. https://doi.org/10.1093/petrology/egl057

Hong, J. S., and Kim, M. C. (2008). Effect of anisotropy of porous media on the onset of buoyancy-driven convection. Transport in Porous Media, 72(2), 241–253. https://doi.org/10.1007/s11242-007-9147-y

Horton, C. W., and Rogers, F. T. (1945). Convection currents in a porous medium. Journal of Applied Physics, 16(6), 367. https://doi.org/10.1063/1.1707601

Huppert, H. E., and Sparks, R. S. J. (1984). Double-Diffusive Convection Due to Crystallization in Magmas. Annual Review of Earth and Planetary Sciences, 12(1), 11–37. https://doi.org/10.1146/annurev.ea.12.050184.000303

Huppert, H. E., and Turner, J. S. (1981). Double-diffusive convection. Journal of Fluid Mechanics, 106(1), 299. https://doi.org/10.1017/S0022112081001614

IEAGHG. (2011). Effect of impurities on geological storage of $CO_2$. IEAGHG.

Ingham, D. B., and Pop, I. I. (2005). Transport Phenomena in Porous Media. Volume III. Elsevier.

Islam, A., and Sun, A. Y. (2015). Quantification of $CO_2$ masses trapped through free convection process in isothermal brine saturated reservoir. International Journal of Heat and Mass Transfer, 87, 128–137. https://doi.org/10.1016/j.ijheatmasstransfer.2015.03.083

Jafari Raad, S. M., and Hassanzadeh, H. (2015). Onset of dissolution-driven instabilities in fluids with nonmonotonic density profile. Physical Review E, Statistical, Nonlinear, and Soft Matter Physics, 92(5–1), 053023. https://doi.org/10.1103/PhysRevE.92.053023

Jafari Raad, S. M., and Hassanzadeh, H. (2016). Does impure $CO_2$ impede or accelerate the onset of convective mixing in geological storage? International Journal of Greenhouse Gas Control, 54, 250–257. https://doi.org/10.1016/j.ijggc.2016.09.011

Jafari Raad, S. M., and Hassanzadeh, H. (2017). Prospect for storage of impure carbon dioxide streams in deep saline aquifers—A convective dissolution perspective. International Journal of Greenhouse Gas Control, 63, 350–355. https://doi.org/10.1016/J.IJGGC.2017.06.011

Jafari Raad, S. M., Fatehi, R., Azin, R., Osfouri, S., and Bahadori, A. (2015). Linear perturbation analysis of density change caused by dissolution of carbon dioxide in saline aqueous phase. Journal of Molecular Liquids, 209, 539–548. https://doi.org/10.1016/j.molliq.2015.06.034

Jafari Raad, S. M., Emami-Meybodi, H., and Hassanzadeh, H. (2016). On the choice of analogue fluids in $CO_2$ convective dissolution experiments. Water Resources Research, 52(6), 4458–4468. https://doi.org/10.1002/2015WR018040

Jelmert, T. A. (1995). The effect of a distributed block length function on double porosity transitions during linear flow. Journal of Petroleum Science and Engineering, 12(4), 277–293. https://doi.org/10.1016/0920-4105(94)00042-3

Ji, X., and Zhu, C. (2013). Predicting possible effects of $H_2S$ impurity on $CO_2$ transportation and geological storage. Environmental Science and Technology, 47(1), 55–62.

Johns, R. T., and Jalali, Y. (1991). Comparison of Pressure-Transient Response in Intensely and Sparsely Fractured Reservoirs. SPE Formation Evaluation, 6(04), 513–518. https://doi.org/10.2118/18800-PA

Kassoy, D. R., and Cotte, B. (1985). The effects of sidewall heat loss on convection in a saturated porous vertical slab. Journal of Fluid Mechanics, 152(1), 361. https://doi.org/10.1017/S0022112085000738

Kim, M. C. (2014). Miscible gravitational instability of initially stable horizontal interface in a porous medium: Non-monotonic density profiles. Physics of Fluids, 26(11), 114102. https://doi.org/10.1063/1.4900859

Kim, M. C., and Choi, C. K. (2014). Density maximum effects on the onset of buoyancy-driven convection in a porous medium saturated with cold water. International Journal of Heat and Mass Transfer, 71, 313–320. https://doi.org/10.1016/j.ijheatmasstransfer.2013.12.025

Kuritani, T., Yokoyama, T., and Nakamura, E. (2007). Rates of thermal and chemical evolution of magmas in a cooling magma chamber: a chronological and theoretical study on basaltic and andesitic lavas from rishiri volcano, Japan. Journal of Petrology, 48(7), 1295–1319. https://doi.org/10.1093/petrology/egm018

Kwak, H. S., and Hyun, J. M. (1996). Natural convection in an enclosure having a vertical sidewall with time-varying temperature. Journal of Fluid Mechanics, 329(1), 65. https://doi.org/10.1017/S0022112096008828

Lackner, K. S. (2003). Climate change. A guide to $CO_2$ sequestration. Science, 300(5626), 1677–8. https://doi.org/10.1126/science.1079033

Landau, L. D., and Lifshitz, E. M. (2004). Fluid Mechanics. Elsevier/Butterworth-Heinemann.

Lee, H., Hong, W.-H., and Kim, H. (1990). Excess volumes of binary and ternary mixtures of water, methanol, and ethylene glycol. Journal of Chemical and Engineering Data, 35(3), 371–374. https://doi.org/10.1021/je00061a040

Lee, Y. E., and Li, S. F. Y. (1991). Binary diffusion coefficients of the methanol/water system in the temperature range 30-40 ºC. Journal of Chemical and Engineering Data, 36(2), 240–243. https://doi.org/10.1021/je00002a024

Lei, H., Li, J., Li, X., and Jiang, Z. (2016). Numerical modelling of co-injection of $N_2$ and $O_2$ with $CO_2$ into aquifers at the Tongliao CCS site. International Journal of Greenhouse Gas Control, 54, 228–241. https://doi.org/10.1016/j.ijggc.2016.09.010

Lemaigre, L., Budroni, M. A., Riolfo, L. A., Grosfils, P., and De Wit, A. (2013). Asymmetric Rayleigh-Taylor and double-diffusive fingers in reactive systems. Physics of Fluids, 25(1), 014103. https://doi.org/10.1063/1.4774321

Li, D., Jiang, X., Meng, Q., and Xie, Q. (2015). Numerical analyses of the effects of nitrogen on the dissolution trapping mechanism of carbon dioxide geological storage. Computers and Fluids. https://doi.org/10.1016/j.compfluid.2015.02.014

Li, Q., Liu, X., Du, L., Bai, B., Fang, Z., Jing, M., and Li, X. (2013). Economics of Acid Gas Injection with Comparison to Sulfur Recovery in China. Energy Procedia, 37, 2505–2510. https://doi.org/10.1016/j.egypro.2013.06.132

Lindeberg, E., and Wessel-Berg, D. (1997). Vertical convection in an aquifer column under a gas cap of $CO_2$. Energy Conversion and Management, 38, S229–S234. https://doi.org/10.1016/S0196-8904(96)00274-9

Liu, H., and Dane, J. (1996). A criterion for gravitational instability in miscible dense plumes. Journal of Contaminant Hydrology, 23(3), 233–243. https://doi.org/10.1016/0169-7722(95)00098-4

Loodts, V., Thomas, C., Rongy, L., and De Wit, A. (2014). Control of convective dissolution by chemical reactions: General classification and application to $CO_2$ dissolution in reactive aqueous solutions. Physical Review Letters, 113(11), 114501. https://doi.org/10.1103/PhysRevLett.113.114501

Loodts, V., Rongy, L., De Wit, A., Avnir, D., Kagan, M., Citri, O., et al. (2015). Chemical control of dissolution-driven convection in partially miscible systems: theoretical classification. Phys. Chem. Chem. Phys., 17(44), 29814–29823. https://doi.org/10.1039/C5CP03082J

Loodts, V., Saghou, H., Knaepen, B., Rongy, L., De Wit, A., Loodts, V., et al. (2018). Differential diffusivity effects in reactive convective dissolution. Fluids, 3(4), 83. https://doi.org/10.3390/fluids3040083

MacMinn, C. W., and Juanes, R. (2013). Buoyant currents arrested by convective dissolution. Geophysical Research Letters, 40(10), 2017–2022. https://doi.org/doi:10.1002/grl.50473

MacMinn, C. W., Neufeld, J. A., Hesse, M. A., and Huppert, H. E. (2012). Spreading and convective dissolution of carbon dioxide in vertically confined, horizontal aquifers. Water

Resources Research, 48(11), W11516(1-11). https://doi.org/10.1029/2012WR012286

Malkovsky, V. I., and Magri, F. (2016). Thermal convection of temperature-dependent viscous fluids within three-dimensional faulted geothermal systems: Estimation from linear and numerical analyses. Water Resources Research, 52(4), 2855–2867. https://doi.org/10.1002/2015WR018001

Malkovsky, V. I., and Pek, A. A. (2004). Onset of thermal convection of single-phase fluid in open vertical faults. Phys. Solid Earth, 40(8), 672–9. Retrieved from http://adsabs.harvard.edu/abs/2002EGSGA..27.1835M

Mao, X., Prommer, H., Barry, D., Langevin, C., Panteleit, B., and Li, L. (2006). Three-dimensional model for multi-component reactive transport with variable density groundwater flow. Environmental Modelling and Software, 21(5), 615–628. https://doi.org/10.1016/J.ENVSOFT.2004.11.008

Markewitz, P., Kuckshinrichs, W., Leitner, W., Linssen, J., Zapp, P., Bongartz, R., et al. (2012). Worldwide innovations in the development of carbon capture technologies and the utilization of $CO_2$. Energy and Environmental Science, 5(6), 7281. https://doi.org/10.1039/c2ee03403d

Metz, B., Davidson, O., de Coninck, H., Loos, M., Meyer, L., and IPCC. (2005). Special report on carbon dioxide capture and storage, prepared by working group III of the intergovernmental panel on climate change. Cambridge, United Kingdom and New York, NY, USA.

Metz, B., Davidson, O., Bosch, P., Dave, R., Meyer, L., and IPCC. (2007). Climate change: mitigation of climate change. contribution of working group III to the fourth assessment report of the intergovernmental panel on climate change. Cambridge, United Kingdom and New York, NY, USA.

Meulenbroek, B., Farajzadeh, R., and Bruining, H. (2013). The effect of interface movement and viscosity variation on the stability of a diffusive interface between aqueous and gaseous $CO_2$. Physics of Fluids, 25(7), 074103(1-22). https://doi.org/10.1063/1.4813072

Mikhail, S. Z., and Kimel, W. R. (1961). Densities and viscosities of methanol-water mixtures. Journal of Chemical and Engineering Data, 6(4), 533–537. https://doi.org/10.1021/je60011a015

Moore, D. R., and Weiss, N. O. (1973). Nonlinear penetrative convection. Journal of Fluid Mechanics, 61(03), 553–581. https://doi.org/10.1017/S0022112073000868

Moshfeghian, M., Johannes, A. H., and Maddox, R. N. (2002). Thermodynamic properties are important in predicting pipeline operations accurately. Oil and Gas Journal, 100(5), 56–62.

Mourzenko, V., Mezon, C., Thovert, J.-F., Antoine, R., Fontaine, F., Finizola, A., and Adler, P. (2016). 3D convection in a fractured porous medium : influence of fracture network

parameters. In 13èmes Journéess d'études des Milieux Poreux 2016. Anglet, France. Retrieved from https://hal.archives-ouvertes.fr/hal-01394555

Murphy, H. D. (1979). Convective instabilities in vertical fractures and faults. Journal of Geophysical Research, 84(B11), 6121. https://doi.org/10.1029/JB084iB11p06121

Myint, P. C., and Firoozabadi, A. (2013). Onset of convection with fluid compressibility and interface movement. Physics of Fluids, 25(9), 094105. https://doi.org/10.1063/1.4821743

NACAP. (2012). The north american carbon storage atlas. The U.S. department of energy (DOE), natural resources canada (NRCan), and the mexican ministry of energy (SENER).

Neufeld, J. A., Hesse, M. A., Riaz, A., Hallworth, M. A., Tchelepi, H. A., and Huppert, H. E. (2010). Convective dissolution of carbon dioxide in saline aquifers. Geophysical Research Letters, 37(22), 1–5. https://doi.org/10.1029/2010GL044728

Nicot, J.-P., Solano, S., Lu, J., Mickler, P., Romanak, K., Yang, C., and Zhang, X. (2013). Potential subsurface impacts of $CO_2$ stream impurities on geologic carbon storage. Energy Procedia, 37, 4552–4559. https://doi.org/10.1016/j.egypro.2013.06.362

Nield, D. A. (1968). Onset of Thermohaline Convection in a Porous Medium. Water Resources Research, 4(3), 553–560. https://doi.org/10.1029/WR004i003p00553

Nield, D. A., and Bejan, A. (2006). Convection in porous media (Third Edit). New York: Springer.

Nield, D. A., and Bejan, A. (2013). Convection in Porous Media. New York: Springer. https://doi.org/10.1007/978-1-4614-5541-7

Odeh, A. S. (1965). Unsteady-State Behaviour of Naturally Fractured Reservoirs. Society of Petroleum Engineers Journal, 5(01), 60–66. https://doi.org/10.2118/966-PA

Orr, F. M. (2009a). Onshore geologic storage of $CO_2$. Science, 325(5948), 1656–8. https://doi.org/10.1126/science.1175677

Orr, F. M. (2009b). $CO_2$ capture and storage: are we ready? Energy and Environmental Science, 2(5), 449. https://doi.org/10.1039/b822107n

Pacala, S., and Socolow, R. (2004). Stabilization Wedges: Solving the Climate Problem for the Next 50 Years with Current Technologies. Science, 305(5686), 968–972.

Pau, G. S. H., Bell, J. B., Pruess, K., Almgren, A. S., Lijewski, M. J., and Zhang, K. (2010). High-resolution simulation and characterization of density-driven flow in $CO_2$ storage in saline aquifers. Advances in Water Resources, 33(4), 443–455. https://doi.org/10.1016/j.advwatres.2010.01.009

Peaceman, D. W. (1976a). Convection in fractured reservoirs - the effect of matrix-fissure transfer on the instability of a density inversion in a vertical Fissure. Society of Petroleum Engineers Journal, 16(05), 269–280. https://doi.org/10.2118/5523-PA

Peaceman, D. W. (1976b). Convection in Fractured Reservoirs Numerical Calculation of Convection in a Vertical Fissure, Including the Effect of Matrix-Fissure Transfer. Society of Petroleum Engineers Journal, 16(05), 281–301. https://doi.org/10.2118/5959-PA

Pop, I. I., and Ingham, D. B. (2001). Convective heat transfer : mathematical and computational modelling of viscous fluids and porous media. Pergamon.

Pringle, S., and Glass, R. J. (2002). Double-diffusive finger convection: influence of concentration at fixed buoyancy ratio. Journal of Fluid Mechanics, 462, 161–183. https://doi.org/10.1017/S0022112002008522

Radko, T. (2013). Double-Diffusive Convection. Cambridge: Cambridge University Press. https://doi.org/10.1017/CBO9781139034173

Rahimi, N., and Griffin, P. J. (2004). Potential for Acid Gas Injection at Kharg Island. In Sour Oil and Gas Advanced Technology International Conference (p. E6). Doha.

Ranjbar, E., Hassanzadeh, H., and Chen, Z. (2012). One-dimensional matrix-fracture transfer in dual porosity systems with variable block size distribution. Transport in Porous Media, 95(1), 185–212. https://doi.org/10.1007/s11242-012-0039-4

Rapaka, S., Chen, S., Pawar, R. J., Stauffer, P. H., and Zhang, D. (2008). Non-modal growth of perturbations in density-driven convection in porous media. Journal of Fluid Mechanics, 609, 285–303. https://doi.org/10.1017/S0022112008002607

Rapaka, S., Pawar, R. J., Stauffer, P. H., Zhang, D., and Chen, S. (2009). Onset of convection over a transient base-state in anisotropic and layered porous media. Journal of Fluid Mechanics, 641, 227. https://doi.org/10.1017/S0022112009991479

Ray, A., and Nemethy, G. (1973). Densities and partial molal volumes of water-ethylene glycol mixtures. Journal of Chemical and Engineering Data, 18(3), 309–311. https://doi.org/10.1021/je60058a031

Riaz, A., Hesse, M., Tchelepi, H. A., and Orr, F. M. (2006). Onset of convection in a gravitationally unstable diffusive boundary layer in porous media. Journal of Fluid Mechanics, 548(1), 87. https://doi.org/10.1017/S0022112005007494

Rodriguez-N., R., Cinco-L., H., and Samaniego-V., F. (2001). A variable block size model for the characterization of naturally fractured reservoirs. In SPE Annual Technical Conference and Exhibition. Society of Petroleum Engineers. https://doi.org/10.2118/71570-MS

Saidi, A. M. (1987). Reservoir Engineering of Fractured Reservoirs : Fundamental and Practical Aspects. Total.

Schincariol, R. A., and Schwartz, F. W. (1990). An experimental investigation of variable density flow and mixing in homogeneous and heterogeneous media. Water Resources Research, 26(10), 2317–2329. https://doi.org/10.1029/WR026i010p02317

Schmitt, R. W. (1994). Double Diffusion in Oceanography. Annual Review of Fluid Mechanics,

26(1), 255–285. https://doi.org/10.1146/annurev.fl.26.010194.001351

Segall, P. (1981). The development of joints and faults in granitic rocks. Stanford University.

Settari, A. (2001). Topics in Reservoir Simulation. Calgary, Alberta, Canada: TAURUS Reservoir Solutions Ltd.

Shen, C., and Chengji. (2015). Effects of salinity variations on subsurface flow in salt marshes. The University of Queensland. https://doi.org/10.14264/uql.2015.783

Shikaze, S. G., Sudicky, E., and Schwartz, F. (1998). Density-dependent solute transport in discretely-fractured geologic media: is prediction possible? Journal of Contaminant Hydrology, 34(3), 273–291. https://doi.org/10.1016/S0169-7722(98)00080-1

Simmons, C. T. (2005). Variable density groundwater flow: From current challenges to future possibilities. Hydrogeology Journal, 13(1), 116–119. https://doi.org/10.1007/s10040-004-0408-3

Simmons, C. T., Sharp, J. M., and Nield, D. A. (2008). Modes of free convection in fractured low-permeability media. Water Resources Research, 44(3), W03431. https://doi.org/10.1029/2007WR006551

Slim, A. C. (2014). Solutal-convection regimes in a two-dimensional porous medium. Journal of Fluid Mechanics, 741, 461–491. https://doi.org/10.1017/jfm.2013.673

Slim, A. C., and Ramakrishnan, T. S. (2010). Onset and cessation of time-dependent, dissolution-driven convection in porous media. Physics of Fluids, 22(12), 124103. https://doi.org/10.1063/1.3528009

Slim, A. C., Bandi, M. M., Miller, J. C., and Mahadevan, L. (2013). Dissolution-driven convection in a Hele–Shaw cell. Physics of Fluids, 25(2), 024101(1-20). https://doi.org/10.1063/1.4790511

Steen, P. H., and Aidun, C. K. (1988). Time-periodic convection in porous media: transition mechanism. Journal of Fluid Mechanics, 196(1), 263. https://doi.org/10.1017/S0022112088002708

Sun, T., and Teja, A. S. (2004). Density, Viscosity and Thermal Conductivity of Aqueous Solutions of Propylene Glycol, Dipropylene Glycol, and Tripropylene Glycol between 290 K and 460 K. Journal of Chemical and Engineering Data, 49(5), 1311–1317. https://doi.org/10.1021/je049960h

Talman, S. (2015). Subsurface geochemical fate and effects of impurities contained in a $CO_2$ stream injected into a deep saline aquifer: What is known. International Journal of Greenhouse Gas Control, 40, 267–291. https://doi.org/10.1016/J.IJGGC.2015.04.019

Tamimi, A., Rinker, E. B., and Sandall, O. C. (1994). Diffusion coefficients for hydrogen sulfide, carbon dioxide, and nitrous oxide in water over the temperature range 293-368 K. Journal of Chemical and Engineering Data, 39(2), 330–332.

https://doi.org/10.1021/je00014a031

Tan, C. T., and Homsy, G. M. (1986). Stability of miscible displacements in porous media: Rectilinear flow. Physics of Fluids, 29(11), 3549–3556. https://doi.org/10.1063/1.865832

Ternström, G., Sjöstrand, A., Aly, G., and Jernqvist, Å. (1996). Mutual diffusion coefficients of water + ethylene glycol and water + glycerol mixtures. Journal of Chemical and Engineering Data, 41(4), 876–879. https://doi.org/10.1021/je9501705

Tilton, N., Daniel, D., and Riaz, A. (2013). The initial transient period of gravitationally unstable diffusive boundary layers developing in porous media. Physics of Fluids, 25(9), 092107. https://doi.org/10.1063/1.4821225

Trevelyan, P. M. J., Almarcha, C., and De Wit, A. (2011). Buoyancy-driven instabilities of miscible two-layer stratifications in porous media and Hele-Shaw cells. Journal of Fluid Mechanics, 670, 38–65. https://doi.org/10.1017/S0022112010005008

Trevelyan, P. M. J., Almarcha, C., and De Wit, A. (2015). Buoyancy-driven instabilities around miscible A+B→C reaction fronts: A general classification. Physical Review E, 91(2), 023001(1-8). https://doi.org/10.1103/PhysRevE.91.023001

Truex, M., Oostrom, M., and Tartakovsky, G. (2015). Evaluating transport and attenuation of inorganic contaminants in the vadose zone for aqueous waste disposal sites. Richland, Washington.

Tsai, P. A., Riesing, K., and Stone, H. A. (2013). Density-driven convection enhanced by an inclined boundary: Implications for geological $CO_2$ storage. Physical Review E, 87(1), 011003. https://doi.org/10.1103/PhysRevE.87.011003

Tsierkezos, N. G., and Molinou, I. E. (1999). Densities and Viscosities of Ethylene Glycol Binary Mixtures at 293.15 K. Journal of Chemical and Engineering Data, 44(5), 955–958. https://doi.org/10.1021/je990059p

Tsivintzelis, I., Kontogeorgis, G. M., Michelsen, M. L., and Stenby, E. H. (2010). Modelling phase equilibria for acid gas mixtures using the CPA equation of state. I. Mixtures with H2S. AIChE Journal, 56(11), 2965–2982. https://doi.org/10.1002/aic.12207

Turner, J. S. (1979). Buoyancy Effects in Fluids. Cambridge: Cambridge University Press. https://doi.org/10.1017/CBO9780511608827

Vafai, K. (Ed.). (2005). Handbook of Porous Media, Second Edition. CRC Press. https://doi.org/10.1201/9780415876384

Vujević, K., and Graf, T. (2015). Combined inter- and intra-fracture free convection in fracture networks embedded in a low-permeability matrix. Advances in Water Resources, 84, 52–63. https://doi.org/10.1016/j.advwatres.2015.07.014

Vujević, K., Graf, T., Simmons, C. T., and Werner, A. D. (2014). Impact of fracture network geometry on free convective flow patterns. Advances in Water Resources, 71, 65–80.

https://doi.org/10.1016/j.advwatres.2014.06.001

W. Ruth, D. (1979). On the stability of density inversion in a vertical fissure with and without matrix-fissure interchange. Society of Petroleum Engineers Journal, 1–30. https://doi.org/SPE-8147-MS

Wall, R. A., and Kenefake, D. A. (2005). Acid Gas Injection Facilities for Gas Disposal at the Shute Creek Treating Facility. In International Petroleum Technology Conference (pp. 1–5). Doha: International Petroleum Technology Conference. https://doi.org/10.2523/10944-MS

Wang, J., Ryan, D., Anthony, E. J., Wildgust, N., and Aiken, T. (2011). Effects of impurities on $CO_2$ transport, injection and storage. Energy Procedia, 4, 3071–3078. https://doi.org/10.1016/j.egypro.2011.02.219

Warren, J. E., and Root, P. J. (1963). The behaviour of naturally fractured reservoirs. Society of Petroleum Engineers Journal, 3(03), 245–255. https://doi.org/10.2118/426-PA

Weidman, P. D., and Kassoy, D. R. (1986). The influence of side wall heat transfer on convection in a confined saturated porous medium. Physics of Fluids, 29(2), 349. https://doi.org/10.1063/1.865718

Weir, G., White, S., and Kissling, W. (1996). Reservoir storage and containment of greenhouse gases, II: Vapour-entry pressures. Transport in Porous Media, 23(1), 61–82. https://doi.org/10.1007/BF00145266

Weir, G. J., White, S. P., and Kissling, W. M. (1995). Reservoir storage and containment of greenhouse gases. Energy Conversion and Management, 36(6–9), 531–534. https://doi.org/10.1016/0196-8904(95)00060-Q

Wen, B., Akhbari, D., Zhang, L., and Hesse, M. A. (2018). Convective carbon dioxide dissolution in a closed porous medium at low pressure. Journal of Fluid Mechanics, 854, 56–87. https://doi.org/10.1017/jfm.2018.622

Whatley, L. (2000). Acid-gas injection proves economic for West Texas gas plant. Oil and Gas Journal, 98(21), 58–61.

Wong, S., Keith, D., Wichert, E., Gunter, B., and Mccann, T. (2003). Economics of acid gas reinjection an innovative $CO_2$ storage opportunity. In Greenhouse Gas Control Technologies - 6th International Conference (pp. 1661–1664). Elsevier. https://doi.org/10.1016/B978-008044276-1/50270-1

Wooding, R. A. (1969). Growth of fingers at an unstable diffusing interface in a porous medium or Hele-Shaw cell. Journal of Fluid Mechanics, 39(03), 477. https://doi.org/10.1017/S002211206900228X

Worster, M. G., Huppert, H. E., and Sparks, R. S. J. (1990). Convection and crystallization in magma cooled from above. Earth and Planetary Science Letters, 101(1), 78–89. https://doi.org/10.1016/0012-821X(90)90126-I

Wu, F., and Wang, G. (2017). Numerical simulation of natural convection in an inclined porous cavity under time-periodic boundary conditions with a partially active thermal side wall. RSC Advances, 7(28), 17519–17530. https://doi.org/10.1039/C6RA28333K

Wylock, C., Rednikov, A., Haut, B., and Colinet, P. (2014). Nonmonotonic Rayleigh-Taylor Instabilities Driven by Gas–Liquid $CO_2$ Chemisorption.

Xie, Y., Simmons, C. T., Werner, A. D., and Ward, J. D. (2010). Effect of transient solute loading on free convection in porous media. Water Resources Research, 46(11). https://doi.org/10.1029/2010WR009314

Xu, T., Apps, J. A., Pruess, K., and Yamamoto, H. (2004). Injection of $CO_2$ with $H_2S$ and $SO_2$ and Subsequent Mineral Trapping in Sandstone-Shale Formation. Lawrence Berkeley National Laboratory.

Xu, T., Apps, J. A., Pruess, K., and Yamamoto, H. (2007). Numerical modelling of injection and mineral trapping of $CO_2$ with $H_2S$ and $SO_2$ in a sandstone formation. Chemical Geology, 242(3), 319–346. https://doi.org/10.1016/j.chemgeo.2007.03.022

Xu, X., Chen, S., and Zhang, D. (2006). Convective stability analysis of the long-term storage of carbon dioxide in deep saline aquifers. Advances in Water Resources, 29(3), 397–407. https://doi.org/10.1016/j.advwatres.2005.05.008

Yang, C., and Gu, Y. (2006). Accelerated Mass Transfer of $CO_2$ in Reservoir Brine Due to Density-Driven Natural Convection at High Pressures and Elevated Temperatures. Industrial and Engineering Chemistry Research, 45(8), 2430–2436. https://doi.org/10.1021/ie050497r

Yang, J. (2006). Finite element modelling of transient saline hydrothermal fluids in multifaulted sedimentary basins: implications for ore-forming processes. Canadian Journal of Earth Sciences, 43(9), 1331–1340. https://doi.org/10.1139/e06-021

Yang, J., and Edwards, R. N. (2000). Predicted groundwater circulation in fractured and unfractured anisotropic porous media driven by nuclear fuel waste heatgeneration. Canadian Journal of Earth Sciences, 37(9), 1301–1308. https://doi.org/10.1139/e00-031

Yang, J., Latychev, K., and Edwards, R. N. (1998). Numerical computation of hydrothermal fluid circulation in fractured Earth structures. Geophysical Journal International, 135(2), 627–649. https://doi.org/10.1046/j.1365-246X.1998.00669.x

Zebib, A., and Kassoy, D. R. (1977). Onset of natural convection in a box of water-saturated porous media with large temperature variation. Physics of Fluids, 20(1), 4. https://doi.org/10.1063/1.861695

Zhang, W., Xu, T., and Li, Y. (2011). Modelling of fate and transport of coinjection of H2S with $CO_2$ in deep saline formations. Journal of Geophysical Research, 116(B2), B02202. https://doi.org/10.1029/2010JB007652

Zhao, C., Hobbs, B. E., Ord, A., Peng, S., Mühlhaus, H. B., and Liu, L. (2004). Theoretical investigation of convective instability in inclined and fluid-saturated three-dimensional fault zones. Tectonophysics, 387(1–4), 47–64. https://doi.org/10.1016/j.tecto.2004.06.007

Zhao, C., Hobbs, B. E., Ord, A., Peng, S., Mühlhaus, H. B., and Liu, L. (2005). Double diffusion-driven convective instability of three-dimensional fluid-saturated geological fault zones heated from below. Mathematical Geology, 37(4), 373–391. https://doi.org/10.1007/s11004-005-5954-2

Zhao, C., Hobbs, B. E., Ord, A., Kühn, M., Mühlhaus, H. B., and Peng, S. (2006). Numerical simulation of double-diffusion driven convective flow and rock alteration in three-dimensional fluid-saturated geological fault zones. Computer Methods in Applied Mechanics and Engineering, 195(19–22), 2816–2840. https://doi.org/10.1016/j.cma.2005.07.008

Zhao, C., Hobbs, B. E., and Ord, A. (2008). Convective and advective heat transfer in geological systems. Berlin: Springer.

Zhao, C., Hobbs, B. E., and Ord, A. (2009). Fundamentals of computational geoscience: numerical methods and algorithms. Berlin: Springer.

Zhou, Q., Oldenburg, C. M., Spangler, L. H., and Birkholzer, J. T. (2017). Approximate solutions for diffusive fracture-matrix transfer: Application to storage of dissolved $CO_2$ in fractured rocks. Water Resources Research, 53, 1746–1762. https://doi.org/10.1002/2016WR019868

Ziabakhsh-Ganji, Z., and Kooi, H. (2012). An Equation of State for thermodynamic equilibrium of gas mixtures and brines to allow simulation of the effects of impurities in subsurface $CO_2$ storage. International Journal of Greenhouse Gas Control, 11, S21–S34. https://doi.org/10.1016/j.ijggc.2012.07.025

Ziabakhsh-Ganji, Z., and Kooi, H. (2014a). Sensitivity of Joule–Thomson cooling to impure $CO_2$ injection in depleted gas reservoirs. Applied Energy, 113, 434–451. https://doi.org/10.1016/j.apenergy.2013.07.059

Ziabakhsh-Ganji, Z., and Kooi, H. (2014b). Sensitivity of the $CO_2$ storage capacity of underground geological structures to the presence of SO2 and other impurities. Applied Energy, 135, 43–52. https://doi.org/10.1016/j.apenergy.2014.08.073

Zimmerman, R. W., and Bodvarsson, G. S. (1995). Effective block size for imbibition or absorption in dual-porosity media. Geophysical Research Letters, 22(11), 1461–1464. https://doi.org/10.1029/95GL01496

Zirrahi, M., Azin, R., Hassanzadeh, H., and Moshfeghian, M. (2012). Mutual solubility of $CH_4$, $CO_2$, $H_2S$, and their mixtures in brine under subsurface disposal conditions. Fluid Phase Equilibria, 324, 80–93. https://doi.org/10.1016/j.fluid.2012.03.017

Zirrahi, M., Hassanzadeh, H., and Abedi, J. (2015). Prediction of $CO_2$ solubility in bitumen using the cubic-plus-association equation of state (CPA-EoS). The Journal of Supercritical Fluids, 98, 44–49. https://doi.org/10.1016/j.supflu.2015.01.001

## Appendix: Reuse and Permissions License

# American Physical Society
# Reuse and Permissions License

07-Apr-2019

This license agreement between the American Physical Society ("APS") and SEYED MOSTAFA JAFARI RAAD ("You") consists of your license details and the terms and conditions provided by the American Physical Society and SciPris.

## Licensed Content Information

| | |
|---|---|
| **License Number:** | **RNP/19/APR/013664** |
| **License date:** | 07-Apr-2019 |
| **DOI:** | 10.1103/PhysRevE.97.043109 |
| **Title:** | Onset of density-driven instabilities in fractured aquifers |
| **Author:** | Seyed Mostafa Jafari Raad and Hassan Hassanzadeh |
| **Publication:** | Physical Review E |
| **Publisher:** | American Physical Society |
| **Cost:** | USD $ 0.00 |

## Request Details

**Does your reuse require significant modifications**: No

| | |
|---|---|
| **Specify intended distribution locations:** | Worldwide |
| **Reuse Category:** | Reuse in a thesis/dissertation |
| **Requestor Type:** | Author of requested content |
| **Items for Reuse:** | Whole Article |
| **Format for Reuse:** | Print and Electronic |
| **Total number of print copies:** | Up to 10000 |

## Information about New Publication:

| | |
|---|---|
| **University/Publisher:** | University of Calgary |
| **Title of dissertation/thesis:** | Buoyancy Driven Flows in Porous Media with Applications to Geological Storage of Carbon Dioxide |
| **Author(s):** | Seyed Mostafa Jafari Raad |
| **Expected completion date:** | Apr. 2019 |

## License Requestor Information

| | |
|---|---|
| **Name:** | SEYED MOSTAFA JAFARI RAAD |
| **Affiliation:** | Individual |
| **Email Id:** | seyedmostafa.jafarir@ucalgary.ca |
| **Country:** | Canada |

# American Physical Society
# Reuse and Permissions License

**TERMS AND CONDITIONS**

The American Physical Society (APS) is pleased to grant the Requestor of this license a non-exclusive, non-transferable permission, limited to Print and Electronic format, provided all criteria outlined below are followed.

1. You must also obtain permission from at least one of the lead authors for each separate work, if you haven't done so already. The author's name and affiliation can be found on the first page of the published Article.

2. For electronic format permissions, Requestor agrees to provide a hyperlink from the reprinted APS material using the source material's DOI on the web page where the work appears. The hyperlink should use the standard DOI resolution URL, http://dx.doi.org/{DOI}. The hyperlink may be embedded in the copyright credit line.

3. For print format permissions, Requestor agrees to print the required copyright credit line on the first page where the material appears: "Reprinted (abstract/excerpt/figure) with permission from [(FULL REFERENCE CITATION) as follows: Author's Names, APS Journal Title, Volume Number, Page Number and Year of Publication.] Copyright (YEAR) by the American Physical Society."

4. Permission granted in this license is for a one-time use and does not include permission for any future editions, updates, databases, formats or other matters. Permission must be sought for any additional use.

5. Use of the material does not and must not imply any endorsement by APS.

6. APS does not imply, purport or intend to grant permission to reuse materials to which it does not hold copyright. It is the requestor's sole responsibility to ensure the licensed material is original to APS and does not contain the copyright of another entity, and that the copyright notice of the figure, photograph, cover or table does not indicate it was reprinted by APS with permission from another source.

7. The permission granted herein is personal to the Requestor for the use specified and is not transferable or assignable without express written permission of APS. This license may not be amended except in writing by APS.

8. You may not alter, edit or modify the material in any manner.

9. You may translate the materials only when translation rights have been granted.

10. APS is not responsible for any errors or omissions due to translation.

11. You may not use the material for promotional, sales, advertising or marketing purposes.

12. The foregoing license shall not take effect unless and until APS or its agent, Aptara, receives payment in full in accordance with Aptara Billing and Payment Terms and Conditions, which are incorporated herein by reference.

13. Should the terms of this license be violated at any time, APS or Aptara may revoke the license with no refund to you and seek relief to the fullest extent of the laws of the USA. Official written notice will be made using the contact information provided with the permission request. Failure to receive such notice will not nullify revocation of the permission.

14. APS reserves all rights not specifically granted herein.

15. This document, including the Aptara Billing and Payment Terms and Conditions, shall be the entire agreement between the parties relating to the subject matter hereof.

# American Physical Society
# Reuse and Permissions License

07-Apr-2019

This license agreement between the American Physical Society ("APS") and SEYED MOSTAFA JAFARI RAAD ("You") consists of your license details and the terms and conditions provided by the American Physical Society and SciPris.

## Licensed Content Information

| | |
|---|---|
| **License Number:** | **RNP/19/APR/013665** |
| **License date:** | 07-Apr-2019 |
| **DOI:** | 10.1103/PhysRevE.92.053023 |
| **Title:** | Onset of dissolution-driven instabilities in fluids with nonmonotonic density profile |
| **Author:** | Seyed Mostafa Jafari Raad and Hassan Hassanzadeh |
| **Publication:** | Physical Review E |
| **Publisher:** | American Physical Society |
| **Cost:** | USD $ 0.00 |

## Request Details

**Does your reuse require significant modifications**: No

| | |
|---|---|
| **Specify intended distribution locations:** | Worldwide |
| **Reuse Category:** | Reuse in a thesis/dissertation |
| **Requestor Type:** | Author of requested content |
| **Items for Reuse:** | Whole Article |
| **Format for Reuse:** | Print and Electronic |
| **Total number of print copies:** | Up to 10000 |

## Information about New Publication:

| | |
|---|---|
| **University/Publisher:** | University of Calgary |
| **Title of dissertation/thesis:** | Buoyancy Driven Flows in Porous Media with Applications to Geological Storage of Carbon Dioxide |
| **Author(s):** | Seyed Mostafa Jafari Raad |
| **Expected completion date:** | Apr. 2019 |

## License Requestor Information

| | |
|---|---|
| **Name:** | SEYED MOSTAFA JAFARI RAAD |
| **Affiliation:** | Individual |
| **Email Id:** | seyedmostafa.jafarir@ucalgary.ca |
| **Country:** | Canada |

# American Physical Society
# Reuse and Permissions License

**TERMS AND CONDITIONS**

The American Physical Society (APS) is pleased to grant the Requestor of this license a non-exclusive, non-transferable permission, limited to Print and Electronic format, provided all criteria outlined below are followed.

1. You must also obtain permission from at least one of the lead authors for each separate work, if you haven't done so already. The author's name and affiliation can be found on the first page of the published Article.

2. For electronic format permissions, Requestor agrees to provide a hyperlink from the reprinted APS material using the source material's DOI on the web page where the work appears. The hyperlink should use the standard DOI resolution URL, http://dx.doi.org/{DOI}. The hyperlink may be embedded in the copyright credit line.

3. For print format permissions, Requestor agrees to print the required copyright credit line on the first page where the material appears: "Reprinted (abstract/excerpt/figure) with permission from [(FULL REFERENCE CITATION) as follows: Author's Names, APS Journal Title, Volume Number, Page Number and Year of Publication.] Copyright (YEAR) by the American Physical Society."

4. Permission granted in this license is for a one-time use and does not include permission for any future editions, updates, databases, formats or other matters. Permission must be sought for any additional use.

5. Use of the material does not and must not imply any endorsement by APS.

6. APS does not imply, purport or intend to grant permission to reuse materials to which it does not hold copyright. It is the requestor's sole responsibility to ensure the licensed material is original to APS and does not contain the copyright of another entity, and that the copyright notice of the figure, photograph, cover or table does not indicate it was reprinted by APS with permission from another source.

7. The permission granted herein is personal to the Requestor for the use specified and is not transferable or assignable without express written permission of APS. This license may not be amended except in writing by APS.

8. You may not alter, edit or modify the material in any manner.

9. You may translate the materials only when translation rights have been granted.

10. APS is not responsible for any errors or omissions due to translation.

11. You may not use the material for promotional, sales, advertising or marketing purposes.

12. The foregoing license shall not take effect unless and until APS or its agent, Aptara, receives payment in full in accordance with Aptara Billing and Payment Terms and Conditions, which are incorporated herein by reference.

13. Should the terms of this license be violated at any time, APS or Aptara may revoke the license with no refund to you and seek relief to the fullest extent of the laws of the USA. Official written notice will be made using the contact information provided with the permission request. Failure to receive such notice will not nullify revocation of the permission.

14. APS reserves all rights not specifically granted herein.

15. This document, including the Aptara Billing and Payment Terms and Conditions, shall be the entire agreement between the parties relating to the subject matter hereof.